Title

Theoretical Investigations of the Stereoselectivities and Mechanisms of Organic Reactions Catalyzed by Vicinal Diamines and Transition Metal Complexes

Author

Simon, Adam

Publication Date

2018

Peer reviewed|Thesis/dissertation

UNIVERSITY OF CALIFORNIA

Los Angeles

Theoretical Investigations of the Stereoselectivities and Mechanisms of Organic Reactions Catalyzed by Vicinal Diamines and Transition Metal Complexes

A dissertation submitted in partial satisfaction of the requirements for the degree Doctor of Philosophy in Chemistry

by

Adam Simon

2018

ABSTRACT OF THE DISSERTATION

Theoretical Investigations of the Stereoselectivities and Mechanisms of Organic Reactions Catalyzed by Vicinal Diamines and Transition Metal Complexes

by

Adam Simon

Doctor of Philosophy in Chemistry

University of California, Los Angeles, 2018

Professor Kendall N. Houk, Chair

This dissertation describes the elucidation of reaction mechanisms and the sources of asymmetric induction in organic reactions with density functional theory. Modern density functional theory is used to develop and propose models for the stereoselectivity of complex organocatalytic reactions. Computations of reactions catalyzed by vicinal diamines, which involve a broad scope of substrates and reactivity, are described in Chapters 1-3. A series of collaborations with experimental research groups are elaborated on in Chapters 4-7.

Chapter 1 describes a computational study of aldol reactions catalyzed by the vicinal diamine class of organocatalysts. The computations and DFT benchmark of the entire transition state landscape of a theoretical model for the simplest aldol reaction catalyzed by ethylene diamine were performed. In addition, the first successful experimental report of a vicinal diamine-catalyzed aldol reaction was studied computationally. The computations revealed a nine-membered cyclic transition state in well-defined conformations of cyclooctane. We identified that the crown (chair-chair) conformation accounted for the observed stereoselectivity in these aldol reactions.

Chapter 2 elaborates on the findings in Chapter 1 of the dissertation by exploring five modern and complex examples of aldol chemistry involving elaborate vicinal diamine catalysts by density functional theory. The computations revealed the sources of stereoselectivity, reactivity, and substituent effects both in catalyst and substrates for aldol reactions catalyzed by vicinal diamines. We proposed a stereoselectivity model based on the conformations of cyclooctane that serves as a predictive model for further aldol chemistry, as well as for the design of new reactions.

Chapter 3 continues the exploration of vicinal diamine catalysis in the realm of Nazarov chemistry. Density functional theory was used to determine the mechanism, stereoselectivity, and source of product inhibition in Nazarov reactions of ketoenones catalyzed by vicinal diamines. The formation of an enamine-iminium ion was determined, and the stereoselectivity was found to be caused by the cyclohexane conformation formed in the enamine-iminium complex. The dihedral angle of the diamine preferred one helicity of the electrocyclization transition state.

Chapter 4 summarizes a collaboration between our group and the research group of Prof. Patrick Harran, where they developed new methods to synthesize macrocyclic pyrroloindolines by alkylating tryptophan-based oligopeptides. Computations were performed to understand the regiodivergent nature of the macrocyclization reactions. We determined that both the *endo*- and

exo-pyrroloindolines form, but the exclusive observation of *endo*-pyrroloindolines is due to the propensity for the *exo*-intermediates to rapidly rearrange to thermodynamically preferred C2-linked isomers.

In Chapter 5, a collaboration between our group and Prof. Neil Garg's research group on the arylations of chiral enamines with arynes. The Garg lab discovered and developed the synthetic methodology for arylating the alpha position of chiral enamines to form stereodefined quaternary centers. We performed density functional theory calculations to understand the mechanism and source of stereoselectivity in the reaction of benzyne and chiral enamines, as well as predict better-performing substituents.

Chapter 6 describes a collaboration between our group and Prof. Karl Anker Jørgensen's research group in Aarhus, Denmark. The Jørgensen group discovered and developed hetero-[6+4] and [6+2] reactions of heteroaromatic compounds to yield highly complex scaffolds from simple pyrrole aldehydes and olefins. With density functional theory calculations, we determined the nature of the [6+4] and [6+2] reaction mechanisms to be stepwise zwitterionic pathways. The enantio-controlling step was identified as the cyclization step. DFT was used to predict better-performing catalysts for the hetero-[6+2] reaction.

In Chapter 7, we describe a collaboration with Prof. Scott Denmark on the Soai reaction. Prof. Denmark's group has discovered a new autocatalytic reaction system where detailed kinetics and mechanistic investigations revealed the intricacies of the autocatalytic Soai mechanism. We performed density functional theory calculations to probe the transition state model of enantioselectivity in the autocatalytic mechanism, and the source of autocatalysis.

The dissertation of Adam Simon is approved.

Patrick G. Harran

Jennifer M. Murphy

Kendall N. Houk, Committee Chair

University of California, Los Angeles

2018

DEDICATION

To friends and family.

TABLE OF CONTENTS

List of Schemes

(blue). The connectivity and relative stereochemistry of bridged pyrroloindolines **8d**, **9d** and **11e** was assigned by ^{1}H-^{13}C-HMBC and ^{1}H-^{1}H-NOESY (red arrows), respectively.

Scheme 4.3. Cyclization scan of oligomers having Trp(5-Br) shifted along the chain (P1→P4). Pyrroloindoline formation is sensitive to sequence composition and ring size, but favored by 5-bromotryptophan. No pyrroloindoline is formed from P1 isomer **12**, whereas P2 and P3 variants **13** and **14** lead to pyrroloindolines **17e** and **18c**, respectively, as major products. Internal C3 alkylation of the P4 variant leads instead to cyclization of the terminal carboxamide to *exo*-pyridoindoline **19b**.

Scheme 4.4. Selective synthesis of pyrroloindoline 9d. Bimolecular Pd^{0}-catalyzed C3-selective cinnamylation of 5-fluoro-L-tryptophan promoted by Et_3B sets up to form the bridging 15-membered ring by lactamization. ^{1}H NMR spectra (500 MHz, DMSO-d_6) of **9d** obtained by this route match that of material isolated from the acid-promoted cyclization. Key resonance annotations in blue. * Denotes contaminant signals.

Scheme 4.5. Combining trifunctional template 28 with Trp-Trp-Tyr rapidly forms complex polycycles. Initial amidation and Pictet-Spengler cyclization of Trp1 (i.e. **29**) followed by acid-promoted cyclization leads to macrocycle isomers **31a**–**f** substituting the periphery of Trp2. Polycycle **31e**, results from indole C3 alkylation and cyclization to the *endo*-pyrroloindoline, analogously to related products obtained from template 1. *Note: Peak **31d** contained two product isomers that were not identified.

Scheme 6.1. *N*- versus *C*- asymmetric functionalization of pyrrole derivatives.

Scheme 6.2. Biologically-relevant scaffolds A-E based on products 4, 6 and 8 in Scheme 7.1

Scheme 6.3. Scope of the hetero-[6+4] cycloaddition of imidazoles and pyrazole 1g-i with electron-deficient dienes 2

List of Figures

PCM//B3LYP/6-31G(d)–IEF-PCM (1,4-dioxane)). The free energies of activation ($\Delta\Delta G^{\ddagger}$), relative to **TS-2a**, are reported in kcal/mol.

Figure 2.3. Lowest-energy transition structures **TS-3a** and **TS-3b** for the aldol addition of isatin and the enamine formed by **2b** and acetaldehyde (M06-2X/def2-TZVPP–IEF-PCM//B3LYP/6-31G(d)–IEF-PCM (THF)). The free energies of activation ($\Delta\Delta G^{\ddagger}$), relative to **TS-3a**, are reported in kcal/mol.

Figure 2.4. Model aldol system where the amide functional group of isatin was replaced with methylenes. The transition structures **TS-4a** and **TS-4b** are modified structures from **TS-3a** and **TS-3b**, which were calculated at the M06-2X/def2-TZVPP–IEF-PCM//B3LYP/6-31G(d)–IEF-PCM (THF) level of theory. The free energies of activation ($\Delta\Delta G^{\ddagger}$), relative to **TS-4b**, are reported in kcal/mol.

Figure 2.5. Lowest-energy transition structures **TS-5a–d** for the aldol addition of *p*-nitrobenzaldehyde and the enamine formed by **3** and cyclohexanone (M06-2X/def2-TZVPP–IEF-PCM//B3LYP/6-31G(d)–IEF-PCM (cyclohexanone)). The free energies of activation ($\Delta\Delta G^{\ddagger}$), relative to **TS-5a**, are reported in kcal/mol.

Figure 3.1. Lowest-energy transition structures for the Nazarov cyclization of the enamine-iminium intermediate **3a** derived from substrate **1** and diamine **I** leading to the major (*S*) and minor (*R*) products (M06-2X/def2-TZVPP–IEF-PCM//B3LYP/6-31G(d)–IEF-PCM (MeCN). Newman projections through C3 and C4 are shown below **TS-1M** and **TS-1P**. The cyclohexyl rings are transparent in the Newman projections for clarity. The relative free energies of activation compared with **TS-1M** are reported in kcal/mol.

Figure 3.2. **TS-2M** and **TS-2aP** are the (enantiomeric) lowest-energy transition structures for the model Nazarov cyclization of the enamine-iminium intermediate derived from substrate **1** and

diamine **II**. (M06-2X/def2-TZVPP–IEF-PCM//B3LYP/6-31G(d)–IEF-PCM (MeCN). **TS-2bP** is a higher energy transition structure similar to the geometry of **TS-1P**. The transition structures are illustrated as Newman projections through C6 and C7. The relative free energies of activation compared with **TS-2M** are reported in kcal/mol.

Figure 3.3. Lowest-energy transition structures for the Nazarov cyclization of the enamine-iminium intermediate for Entry 2 in Scheme 1 leading to the major (*S*) and minor (*R*) products (M06-2X/def2-TZVPP–IEF-PCM//B3LYP/6-31G(d)–IEF-PCM (MeCN). The relative free energies of activation compared with **TS-3M** are reported in kcal/mol.

Figure 4.1. A. Pyrroloindoline synthesis and biosynthesis typically proceed via bimolecular electrophilic substitution of indole at C3 and capture of the resulting indolenium ion by a proximal nitrogen nucleophile. The reaction of tryptophan is often *exo*-selective. Tautomerization of tryptophan by acid equilibrates to the C2-*endo* pyrroloindoline. **B.** Intramolecular *C–C* bond formation at C3 leads to *ansa*-bridged macrocyclic pyrroloindolines.

Fig. 4.2. Rearrangement of pyrroloindoline 18c. **A.** Time-course HPLC-UV (254 nm) analysis showing rearrangement of isolated **18c** to isomer **18a** in TFA/$MeNO_2$ solution. Trace regioisomers (labelled) also form in this reaction. **B.** Proposed mechanism for 1,2-rearrangement. **C.** Kinetic plot showing pseudo-first-order reaction of **18c** and accumulation of major product **18a**

Fig. 4.3. *exo*-Pyrroloindolines rearrange more readily than *endo*-pyrroloindolines. **A.** Under acidic conditions, C3a-cinnamyl pyrroloindolines undergo ring-chain tautomerism and 1,2-rearrangement to indole C2-linked isomers. The kinetic plot for rearrangement of **21a** and **21b** in 20 vol% TFA at 5 °C shows the faster rate of reaction for *exo*-pyrroloindoline **21b**. From Eyring analysis, the free energy of activation was 1.9 kcal•mol^{-1} higher for *exo*-**21b** relative to *endo*-**21a**. **B.** DFT calculations indicate that *endo*-pyrroloindoline **21a** is the thermodynamically more stable

Figure 5.4. Variation of the nucleophilic component **30** in the trapping with **11**. Conditions unless otherwise stated: i. enamine **30** (1.0 equiv), silyl triflate **11** (1.5 equiv), CsF (7.5 equiv), DME (0.1 M), 30 °C, 3 h; ii. 1 M $HCl_{(aq)}$, 23 °C, 30 min. Yields reflect the average of two isolation experiments. [a] Aryne trapping performed for 6 h.

Figure 5.5. One-pot, mmol-scale arylation reaction to furnish **36**. Conditions for enamine formation: ketoester **39** (1.0 equiv), amine **23** (1.0 equiv), benzene (0.7 M), 80 °C, 16 h, followed by evaporation of benzene solvent. Conditions for arylation: i. silyl triflate **11** (1.5 equiv), CsF (7.5 equiv), DME (0.1 M), 30 °C, 6 h; ii. 1 M $HCl_{(aq)}$, 23 °C, 12 h.

Figure 5.6. Lowest-energy transition structures **TS1** and **TS2** for the addition of benzyne and the chiral enamine derived from amine **20** (M06-2X/def2-TZVPP–SMD (diethylether)//B3LYP/6-31+G(d,p)). Free energy activation barriers ($\Delta G^{\ddagger}$) are compared to separated intermediates. The difference in free energies of activation ($\Delta\Delta G^{\ddagger}$), relative to **TS1**, are reported in kcal/mol.

Figure 5.7. Lowest-energy transition structures **TS3** and **TS4** for the addition of benzyne and chiral enamine **25** (M06-2X/def2-TZVPP–SMD (diethylether)//B3LYP/6-31+G(d,p)). Free energy activation barriers ($\Delta G^{\ddagger}$) are compared to separated intermediates. The difference in free energies of activation ($\Delta\Delta G^{\ddagger}$), relative to **TS1**, are reported in kcal/mol.

Figure 6.1. Consumption of pyrrole **1b** (graph A); amount of catalyst **3b** over time (graph B); the development of iminium-ion **I** over time (graph C) and cycloadduct **4be** formation (graph D) as a function of time. Reaction conditions: Pyrrole **1b** (1 equiv.), electron-deficient diene **2e** (1 equiv.), catalyst **3b** (20 mol%) and benzoic acid (20 mol%) in $CDCl_3$ (0.17 M), in the presence of MS. Integrations have been normalized towards TES as internal standard.

Figure 6.2. Optimized ground-state structures for two conformations of the catalyst and lowest-energy conformations for the *cis*- and *trans*-arrangements of intermediates **I** and **II** (M06-2X/def2-TZVPP–SMD//B3LYP/6-31G(d)–SMD ($CHCl_3$).

Figure 6.3. Computed free energy reaction pathway profile for the hetero-[6+4] cycloaddition involving hetero-6-π-intermediate *trans*-**II** derived from catalyst **3b** and model of substrate **2** (M06-2X/def2-TZVPP–SMD//B3LYP/6-31G(d)–SMD ($CHCl_3$). The starting point is the computed free energy of the separated *trans*-**II** and substrate and all following energies are compared to them. All structures are lowest-energy conformations of transition states or ground states.

Figure 6.4. Computed free energy reaction pathway profile for the hetero-[6+2] cycloaddition involving hetero-6-π-intermediate *trans*-**II** derived from catalyst **3b** and model of substrate **7** (M06-2X/def2-TZVPP–SMD//B3LYP/6-31G(d)–SMD ($CHCl_3$). The starting point is the computed free energy of the separated *trans*-**II** and substrate and all following energies are compared to them. All structures are lowest-energy conformations of transition states or ground states.

Figure 7.1: a. The Soai reaction system. **b.** Current state of structural and mechanistic understanding. **c.** Structural idiosyncrasies. **d.** Unsolved challenges and open questions.

Figure 7.2: a. Asymmetric autocatalysis with chiral amplification in alkylation of **3** with diisopropylzinc. **b.** Observation of sigmoidal aldehyde consumption profiles and non-linear autocatalysis upon monitoring aldehyde consumption by *in-situ* IR spectroscopy **c** Qualitative comparison of catalytic activities and non-linear effect of alkoxides **Py*XX*** in dialkylzinc addition to **3** by ReactIR monitoring of aldehyde consumption.

Figure 7.3: Partial ^{1}H-NMR spectra (750 MHz) of zinc alkoxides in toluene-d_8 at 23 ^{0}C. *tol* = residual toluene, *prop* = propane, *eth* = ethane. **a.** Enantioenriched zinc alkoxides with signature chemical shifts for species **a** (black boxed) and species **b-d** (red boxed) **b.** Diastereomeric species possible in a racemic cubic tetramer with their relative peak distributions. ^{1}H NMR of the aryl and TMS region for racemic **PhEI** displays this predicted quadruplet pattern.

Figure 7.4: a. Sterically weakened PhXX cubic tetramers are disrupted by pyridine. **b.** A conceptually similar 'cube escape' occurs in the PyXX alkoxides with intramolecular pyridine coordination yielding the Soai tetramer. **c.** The predicted identity of the cube-escaped PyII Soai tetramer based on analogy with Soai's crystal structure.

Figure 7.5*:* a. *In-situ* IR profiles for aldehyde consumption in diisopropylzinc alkylations catalyzed by scalemic **PyII. b.** Rate law and thermodynamic parameters for the non-autocatalytic reaction as measured using initial rate kinetic analysis.

Figure 7.6: DFT studies for floor-to-floor substrate docking and alkyl transfer by the **PyII** tetramer. Transition structures **TS-3a–3b** and **TS-5a–5b**, and optimized minima **int-3a** and **int-5a–5b** calculated at the M06-2X/def2-TZVPP–SMD (toluene)//B3LYP/6-31G(d) level of theory. Energies reported in kcal/mol. Purple, zinc; yellow, silicon; red, oxygen; blue, nitrogen; gray, carbon. Hydrogens are hidden for clarity. ΔG, free energy of activation. $\Delta\Delta G^{\ddagger}$, relative free energy activation barrier.

List of Tables

Acknowledgements

I would like to express my gratitude to my doctoral advisor, Professor Kendall N. Houk, for his guidance and mentorship throughout the years of my dissertation research. I am thankful to have been a part of Prof. Houk's research group, and have grown tremendously because of it. With his guidance, I have had the opportunity to collaborate with research groups around the world on significant projects – even travelling to Aarhus, Denmark for our collaborations with the Jørgensen group. Indeed, I must acknowledge my esteemed collaborators: Prof. Karl Anker Jørgensen, Prof. Scott Denmark, Prof. Neil Garg, Prof. Patrick Harran, Prof. Yi Tang, Dr. Ed Sherer, Prof. Wolfgang Kroutil, and Prof. Justin Mohr. Also, Prof. Heather Maynard for running an excellent CBI program.

Dr. Colin Lam was my mentor upon arriving in Prof. Houk's research group for our shared interest in studying organocatalysis, and I must acknowledge that all of the work described herein was enabled by Colin's mentorship in performing computations, their analysis, and their presentation. From Colin, I learned the basics of programming and working efficiently. I learned how to study and carry out a project with completeness, and prepare those results in a manuscript with rigour. In combination with Prof. Houk's mentorship, I learned to frame such completeness succinctly.

In addition, I would like to thank all the members of the lab from which I learned plenty of tips and tricks whether about computations, academia, or life in general when I first started in the group: Dr. Ashay Patel, Dr. Matt Grayson, Dr. Mareike Holland, Dr. Steven Lopez, Dr. Brian Levandowski, Dr. Cyndi He, Dr. Jason Fell, Dr. Janice Lin, Dr. Marc Garcia Borrás, Dr. Peiyuan Yu, and Dr. Song Yang. I also have to thank the younger crowd, including Katherine Bay, Kersti

Caddell Haatveit, Xiangyang Chen, Meng Duan, Cooper Jamieson, and Tyler Benton for our fun conversations and being awesome people.

I must thank my parents for their unconditional support, and Qi Wang for her endless patience.

Chapter 1 is a modified version of the publication, "Transition States of Vicinal Diamine-Catalyzed Aldol Reactions." Simon, A.; Lam, Y. h-.; Houk, K. N. *J. Am. Chem. Soc.* **2016**, *138*, 503.

Chapter 2 is a modified version of the publication, "Origins of Stereoselectivity of Chiral Vicinal Diamine-Catalyzed Aldol Reactions." Simon, A.; Yeh, A. J.; Lam, Y. h-; Houk, K. N. *J. Org. Chem.* **2016**, *81*, 14039.

Chapter 3 is a modified version of the publication, "Origins of Stereoselectivity of Enamine–Iminium-Activated Nazarov Cyclizations by Vicinal Diamines." Simon, A.; Lam, Y. h-; Houk, K. N. *J. Org. Chem.* **2017**, *82*, 8186.

Chapter 4 is a modified version of the publication, "On the Prevalence of Bridged Macrocyclic Pyrroloindolines Formed in Regiodivergent Alkylations of Tryptophan." Rose, T. E.; Curtin, B. H.; Lawson, K. V.; Simon, A.; Houk, K. N.; Harran, P. G. *Chem. Sci.* **2016**, *7*, 4158. Dr. Tristin Rose, Dr. Brice Curtin, and Dr. Kenneth Lawson conducted the experiments under the supervision of Prof. Patrick Harran. I performed the DFT computations under the supervision of Prof. Kendall N. Houk.

Chapter 5 is a modified version of the publication, "Arynes and Cyclic Alkynes as Synthetic Buillding Blocks for Stereodefined Quaternary Centers." Picazo, E.; Anthony, S. M.; Giroud, M.; Simon, A.; Miller, M. A.; Houk, K. N.; Garg, N. K. *J. Am. Chem. Soc.* **2018**, *140*, 7605. Dr. Picazo, Sarah, Anthony, Dr. Giroud, and Margeaux Miller performed the experiments under the

supervision of Prof. Neil Garg. I performed the DFT computations under the supervision of Prof. Kendall N. Houk.

Chapter 6 describes a collaboration between the Jørgensen group and our group titled: "Catalytic Enantioselectivity Hetero-[6+4] and [6+2] Cycloadditions of Heteroaromatic Compounds." Giulio Bertuzzi, Mathias Thøgersen, Maxime Giardinetti, Dr. Andreu Vidal-Albalat performed the experiments under the supervision of Prof. Karl Anker Jørgensen. I performed the DFT calculations under the supervision of Prof. Kendall N. Houk.

Chapter 7 describes a collaboration between the Denmark group and our group titled: "Demystifying the Soai Reaction." Soumitra V. Athavale conducted the experiments under the supervision of Prof. Scott E. Denmark, and I performed the DFT calculations under the supervision of Prof. Kendall N. Houk.

VITA

Education

University of California, Los Angeles — December 2018

University of California, San Diego — June 2014
B.S. in Chemistry
Phi Beta Kappa
High Distinction

Publications

1. Simon, A.; Lam, Y. h-.; Houk, K. N. Transition States of Vicinal Diamine-Catalyzed Aldol Reactions. *J. Am. Chem. Soc.* **2016**, *138*, 503.

2. Lin, H. C.; McMahon, T. C.; Patel, A.; Corsello, M.; Simon, A.; Xu, W.; Zhao, M.; Houk, K. N.; Garg, N. K.; Tang, Y. P450-Mediated Coupling of Indole Fragments to Forge Communesin and Unnatural Isomers. *J. Am. Chem. Soc.* **2016**, *138*, 4002.

3. Lam, Y. h-.; Grayson, M. N.; Holland, M. C.; Simon, A; Houk, K. N. Theory and Modeling of Asymmetric Catalytic Reactions. *Acc. Chem. Res.* **2016**, *49*, 750.

4. Rose, T. E.; Curtin, B. H.; Lawson, K. V.; Simon, A.; Houk, K. N.; Harran, P. G. On the Prevalence of Bridged Macrocyclic Pyrroloindolines Formed in Regiodivergent Alkylations of Tryptophan. *Chem. Sci.* **2016**, *7*, 4158

5. Vogel, P.; Lam, Y. h-.; Simon, A.; Houk, K. N. Organocatalysis: Fundamentals and Comparisons to Medal and Enzyme Catalysis. *Catalysts*, **2016**, *6*, Article 128.

6. Simon, A.; Yeh, A. J.; Lam, Y. h-; Houk, K. N. Origins of Stereoselectivity of Chiral Vicinal Diamine-Catalyzed Aldol Reactions. *J. Org. Chem.* **2016**, *81*, 14039.

7. Simon, A.; Lam, Y. h-; Houk, K. N. Origins of Stereoselectivity of Enamine–Iminium-Activated Nazarov Cyclizations by Vicinal Diamines. *J. Org. Chem.* **2017**, *82*, 8186.

8. He, C. Q.; Simon, A.; Lam, Y. h-.; Brunskill, A. P. J.; Yasuda, N.; Tan, J.; Hyde, A. M.; Sherer, E. C.; Houk, K. N. Model for the Enantioselectivity of Asymmetric Intramolecular Alkylations by Bis-Quaternized Cinchona Alkaloid-Derived Catalysts. *J. Org. Chem.* **2017**, *82*, 8645–8650.

9. Picazo, E.; Anthony, S. M.; Giroud, M.; Simon, A.; Miller, M. A.; Houk, K. N.; Garg, N. K. Arynes and Cyclic Alkynes as Synthetic Buillding Blocks for Stereodefined Quaternary Centers. *J. Am. Chem. Soc.* **2018**, *140*, 7605.

10. Yu, P.; He, C. Q.; Simon, A.; Li, W.; Mose, R.; Thøgersen, M. K.; Jørgensen, K. A.; Houk, K. N. Organocatalytic [6+4] Cycloadditions via Zwitterionic Intermediates: Chemo-, Regio-, and Stereoselectivities. *J. Am. Chem. Soc.* **2018**, *140*, 13726.

Awards and Honors

Dissertation Year Fellowship, 2018-2019
Christopher S. Foote Fellowship, 2017 Senior Fellow
Chemistry and Biology Interface Trainee, 2015-2018

Chapter 1. Transition States of Vicinal Diamine-Catalyzed Aldol Reactions

1.1 Abstract

The transition states of aldol reactions catalyzed by vicinal diamines are characterized with density functional calculations. It was found that a cyclic transition state involving a nine-membered hydrogen bonded ring is preferred. The crown (chair-chair) conformations of the transition state account for the observed stereoselectivity of these reactions.

1.2 Introduction

Vicinal diamines such as **1**-**5** are effective organocatalysts for aldol reactions (Scheme 1.1).[1-4] The pioneering work by Yamamoto with catalyst **1** was one of the first examples of chiral diamines in direct aldol reactions.[5] Luo followed this with the first effective chiral primary-tertiary diamine catalyst **2**.[6] Zhang computationally investigated the stereoselectivity of aldol reactions with diamine **2**.[7] The origins of stereoselectivities in these reactions were explained by *ad hoc* models with steric clashes between the substrate and the catalyst moieties. The nature of the transition states in these reactions, and their role in determining stereocontrol have received little attention.

Scheme 1.1. Example Diamines in Aldol Catalysis

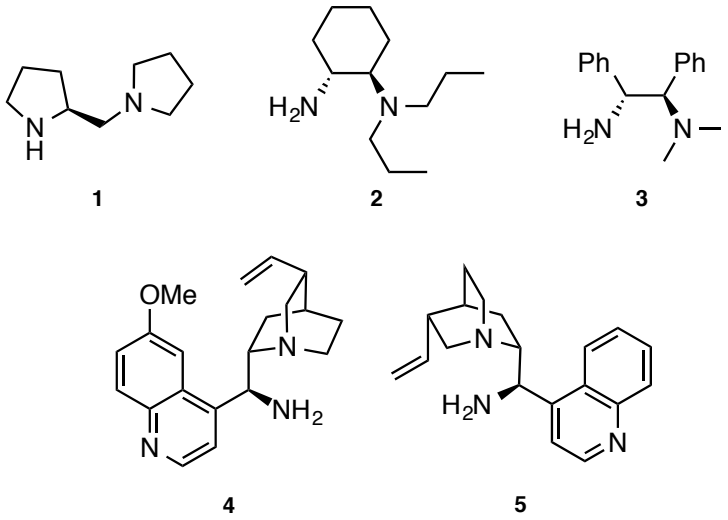

We recently studied the origins of enantiocontrol in the organocatalyzed fluorination[8,9] and an intramolecular aldol condensation,[10,11] both catalyzed by cinchona alkaloid-derived primary amines that contain a chiral vicinal diamine. We showed that these reactions proceed through cyclic transition states with well-defined conformations. We have now investigated the origins of stereoselectivity in intermolecular aldol reactions catalyzed by vicinal diamines. Here, we propose cyclic transition structures for these reactions, and show how their conformational preferences underlie the high levels of stereoselectivity in a manner that is reminiscent of the seminal Zimmerman–Traxler model.[12]

The model by Zimmerman and Traxler was a breakthrough in the understanding of stereocontrol in aldol additions. The stereochemical outcomes of metal-catalyzed aldol reactions are governed by the conformation of a six-membered cyclic transition state (Figure 1.1A).[12,13] The conformational preference of cyclic transition states has since then been the basis of stereocontrol in a wide variety of asymmetric reactions. In the Houk–List model for proline-catalyzed aldol reactions, the stereochemistry-determining C–C bond-forming step involves a partial Zimmerman–Traxler-like transition state acquiring a chair configuration of the enamine and the electrophilic carbonyl group (Figure 1.1B).[14] The intramolecular fluorine transfer in Figure 1.1C

acquires a chair conformation of the seven-membered stereocontrolling cyclic transition state.[8] The transition state models summarized in Figure 1 highlight the chair transition states of these asymmetric reactions.

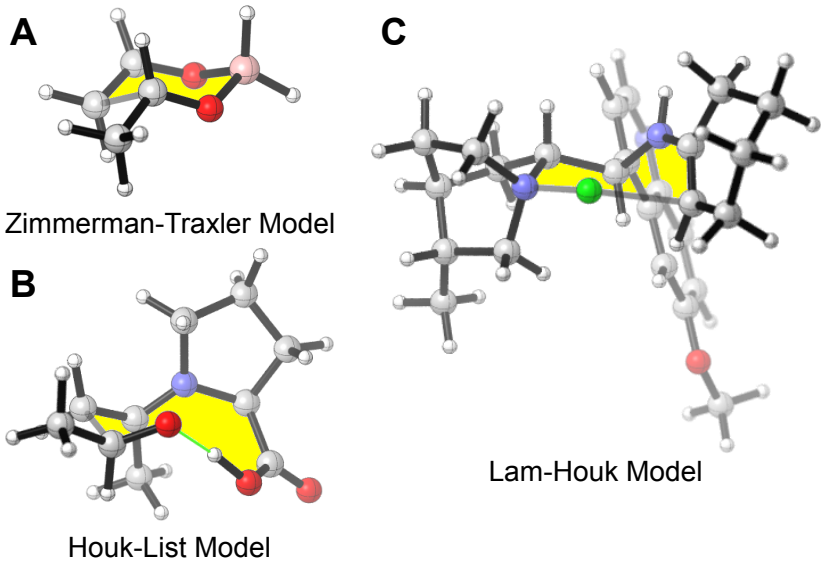

Figure 1.1. Example of the Zimmerman-Traxler model (A), the Houk-List model with L-proline (B), and the Lam-Houk model with cinchona alkaloid-primary amine (C).

We first explored the simplest possible example of aldol transition states for the aldol reaction acetaldehyde and formaldehyde catalyzed by ethylenediamine, the parent vicinal diamine (Scheme 1.2). We also studied the experimental system of acetone and *p*-nitrobenzaldehyde catalyzed by diamine **1**.

Scheme 1.2. Model Aldol Reaction and Yamamoto's Reported Aldol Addition Catalyzed by L-Proline Derived Catalyst.

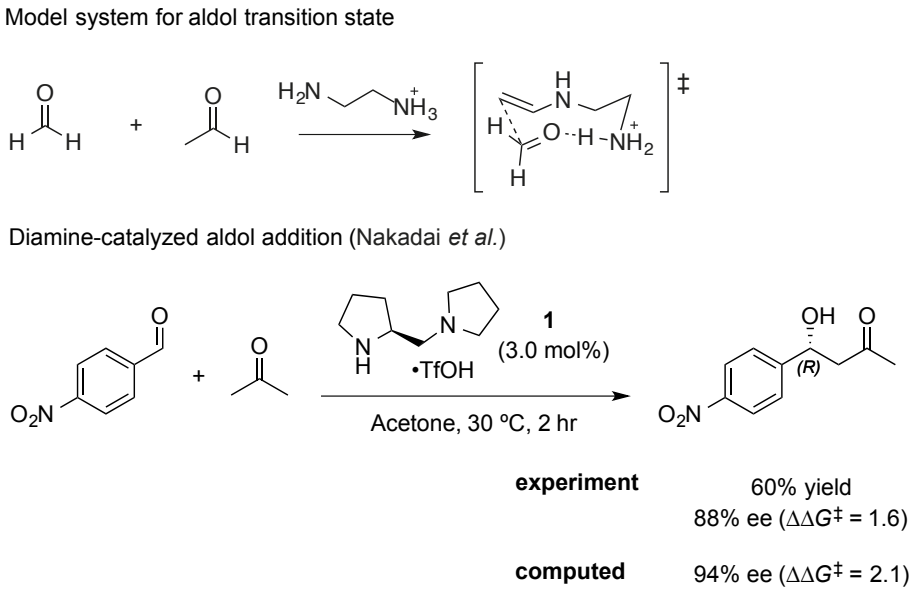

1.3 Computational Methods

Conformational searches were performed with OPLS-2005 force-fields in Maestro/Macromodel.[15] Quantum chemical calculations were performed using *Gaussian 09*.[16] Geometry optimizations and frequency calculations were performed at the B3LYP/6-31G(d) level of theory.[17] Single-point energies of the aldol transition structures were also calculated using B3LYP,[17] ωB97X-D,[18] and M06-2X[19] with the def2-TZVPP[20] basis set in conjunction with the IEF-PCM[21] solvation model for the experimental system. The M06-2X/def2-TZVPP//B3LYP/6-31G(d) level of theory, including IEF-PCM (acetone) for the experimentally used solvent, has been shown to efficiently yield accurate energies for stereoisomeric transition states in organocatalytic systems,[22] and the results using this method are presented in the main text. All other DFT methods yielded the same trends and magnitudes in the relative free energies of activation ($\Delta\Delta G^{\ddagger}$) of the stereoisomeric transition structures.

1.4 Results and Discussion

The four lowest-energy transition structures for the aldol reaction of formaldehyde and acetaldehyde catalyzed by protonated ethylenediamine are shown in Figure 1.2. These four are

(+)-gauche diamines. There are four enantiomeric structures with (-)-gauche diamine conformers as well.

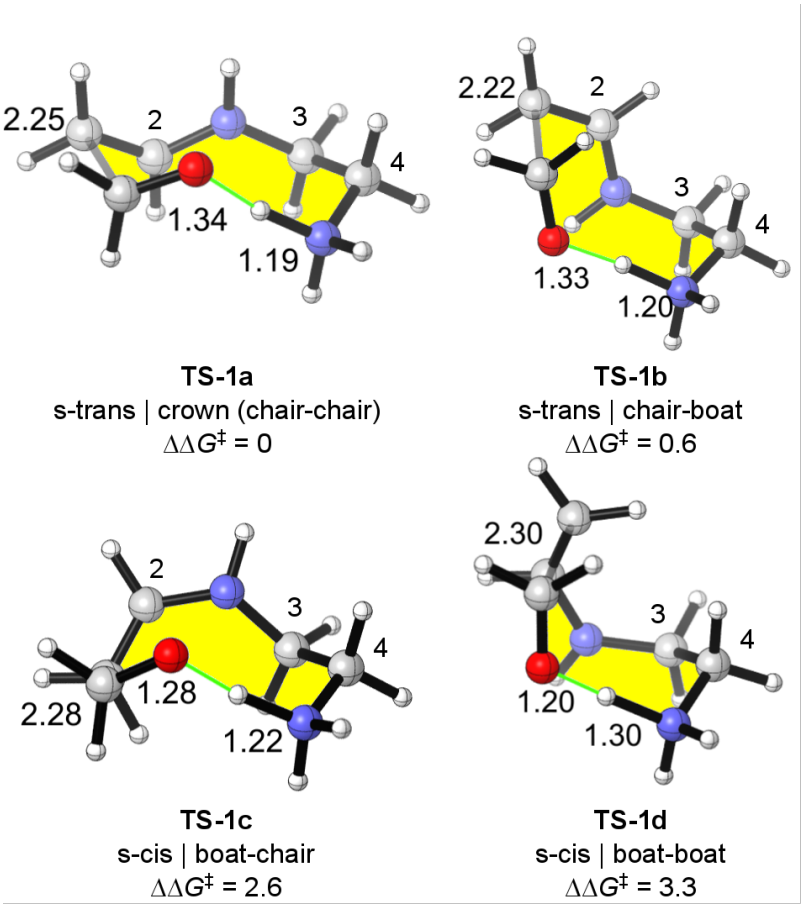

Figure 1.2. Lowest-energy transition structures **TS-1a–d** for the aldol addition of formaldehyde and the enamine formed by (+)-gauche ethylenediamine and acetaldehyde (M06-2X/def2-TZVPP//B3LYP/6-31G(d)). The free energies of activation ($\Delta\Delta G^{\ddagger}$), relative to **TS-1a**, are reported in kcal/mol.

The cyclic transition structures are highlighted in yellow. As in the intramolecular aldol study,[10] the eight heavy atoms of the aldol transition state resemble low-energy conformers of cyclooctane.[23] **TS-1a** is the crown conformation (chair-chair) and is the lowest-energy transition structure. **TS-1b** is the chair-boat and is higher in energy than **TS-1a** by only 0.6 kcal/mol. **TS-1a**

and **TS-1b** both acquire Zimmerman-Traxler chair conformations,[12] but **TS-1b** is a boat on the catalyst side. The dihedral angle of the N-C3-C4-N bond is 58º for **TS-1a** and 55º for **TS-1b**, corresponding to a favorable conformation of the catalyst. The minor difference in energy between the two transition structures arises from an eclipsed H-H interaction in **TS-1b** between the N–H of the enamine and the axial C–H of C3. Both **TS-1a** and **TS-1b** have s-trans configurations of the enamine and staggered approaches along the forming C–C bond.

TS-1c is in a boat-chair conformation and is 2.6 kcal/mol higher in energy than **TS-1a**. **TS-1d** is in a boat-boat conformation and is 3.3 kcal/mol higher in energy compared to **TS-1a**. Both transition structures have s-cis configurations of the enamine and are higher in energy than the s-trans transition structures, in agreement with the Houk-List model.[14] The destabilization of both **TS-1c** and **TS-1d** is due to eclipsing about the forming C–C bond, a type of torsional steering.[24] The presence of 1,2-allylic strain of the enamine NH and vinyl hydrogen of C2 also contributes to their higher energies. Additionally, the dihedral angle of the N-C3-C4-N bond is 75° for **TS-1c** and 46° for **TS-1d**. Both transition structures have boat conformations at the forming C–C bond and are higher in energy compared to the chairs (**TS-1a** and **TS-1b**), as in the Zimmerman-Traxler model.[12] In addition to these four transition structures, four higher-energy conformations were located.

These results show that there are strongly preferred crown (chair-chair) and chair-boat conformations. For the experimental catalysts **1-5** the (+)- or (-)-gauche preference is determined by the chirality of the catalyst, which excludes the possibility of enantiomeric conformations. We explored if the conformational preferences observed in the model system are maintained in more substituted systems with catalyst **1**.

We studied the Yamamoto catalyst **1** that attained reasonable stereoselectivity in an intermolecular aldol addition of *p*-nitrobenzaldehyde and acetone (Scheme 1.2). Enantioselectivity in this reaction is 88% ee, which corresponds to a difference in activation free energies ($\Delta\Delta G^{\ddagger}$) of 1.6 kcal/mol. The two lowest-energy transition structures leading to the major (**TS-2a**) and minor (**TS-2b**) products are illustrated in Figure 1.3. **TS-2a** and **TS-2b** have (+)-gauche conformations of the catalyst and are both crown conformations. They differ in the facial selectivity of the aldehyde; **TS-2a** has an equatorial aryl group, and **TS-2b** has an axial aryl group. The geometry of the enamine-catalyst is very similar in both transition structures. Thus the enantioselectivity arises from the equatorial versus axial position of the aldehyde substituent on a cyclic transition state in the crown conformation.

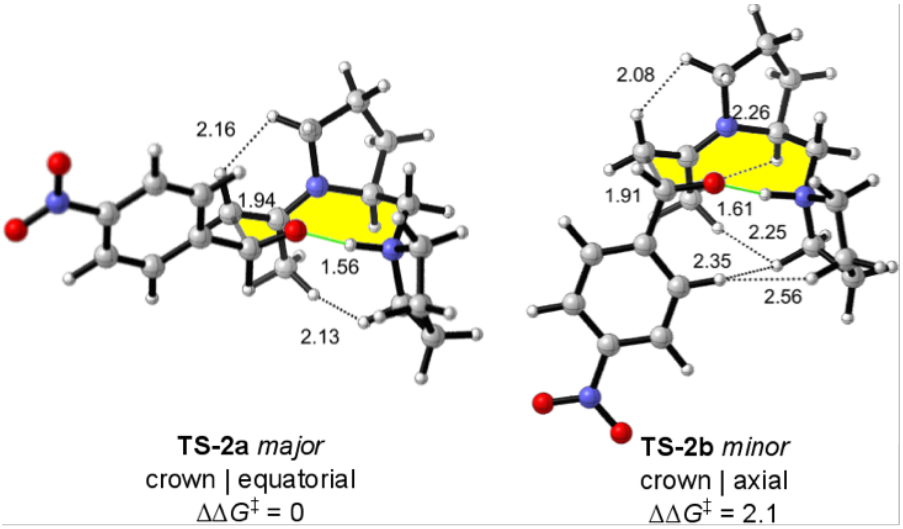

Figure 1.3. Lowest-energy transition structures **TS-2a** and **TS-2b** for the aldol addition of *p*-nitrobenzaldehyde and the enamine formed by catalyst **1** and acetone (M06-2X/def2-TZVPP–IEF-PCM(acetone)//B3LYP/6-31G(d)–IEF-PCM(acetone)). The free energies of activation ($\Delta\Delta G^{\ddagger}$), relative to **TS-2a**, are reported in kcal/mol.

In addition to **TS-2a** and **TS-2b**, 7 stereoisomeric transition structures **TS-2c–i** were located (Figure 1.4). **TS-2c**, **TS-2e**, and **TS-2g** lead to the major (*R*) enantiomer, while **TS-2d**, **TS-2f**, **TS-2h**, and **TS-2i** lead to the minor (*S*) enantiomer. **TS-2c**, **TS-2f**, and **TS-2g** have (-)-gauche conformations at the NCCN bond of the diamine, and the pyrrolidine rings are axial relative to the cyclic aldol transition state. **TS-2d**, **TS-2f**, **TS-2g**, and **TS-2h** are destabilized due to eclipsed forming C–C bonds. **TS-2e** is higher in energy than **TS-2a** by 2.1 kcal/mol and is in the boat-chair conformation that is destabilized by a slightly eclipsed forming C–C bond and a wide 79° NCCN dihedral angle of the catalyst. **TS-2i**, a chair-boat but with a highly distorted pyrrolidine ring, is 10.4 kcal/mol higher in energy.

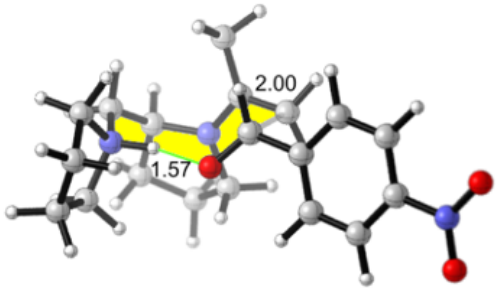

TS-2c
chair-boat
$\Delta\Delta G^{\ddagger}$ = 1.7

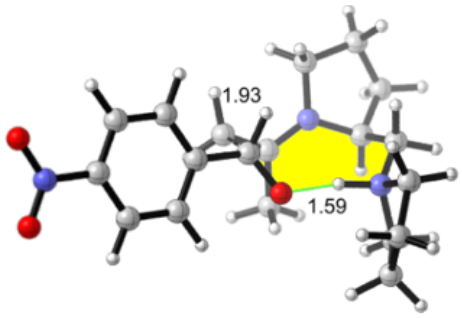

TS-2d
twist-crown
$\Delta\Delta G^{\ddagger}$ = 2.2

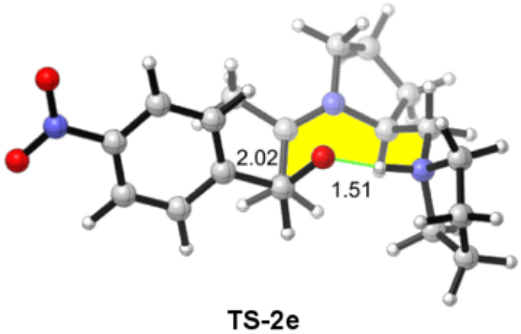

TS-2e
boat-chair
$\Delta\Delta G^{\ddagger}$ = 2.1

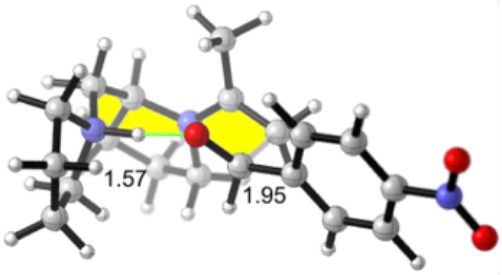

TS-2f
twist-chair-boat
$\Delta\Delta G^{\ddagger}$ = 3.9

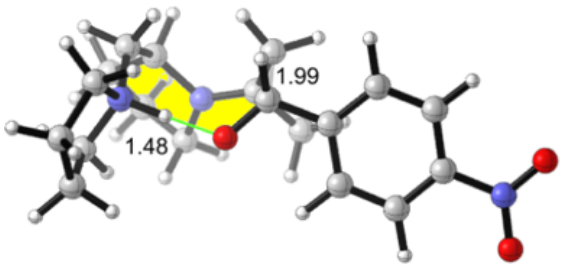

TS-2g
boat-boat
$\Delta\Delta G^{\ddagger}$ = 3.3

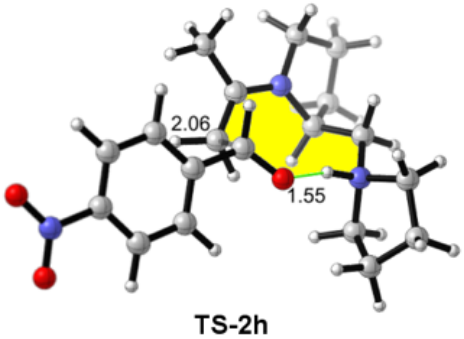

TS-2h
twist-boat-chair
$\Delta\Delta G^{\ddagger}$ = 5.1

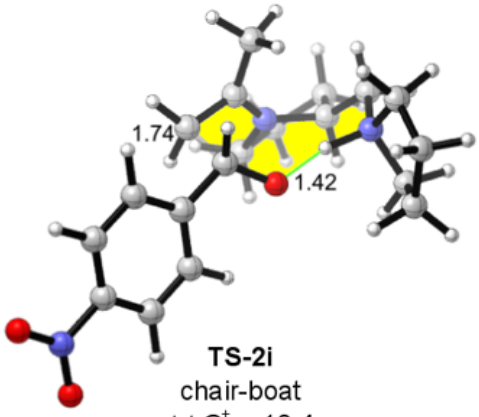

TS-2i
chair-boat
$\Delta\Delta G^{\ddagger}$ = 10.4

Figure 1.4. Transition structures **TS-2c–i** for the aldol reaction of *p*-nitrobenzaldehyde and the enamine formed by catalyst **1** and acetone (M06-2X/def2-TZVPP–IEF-PCM(acetone)//B3LYP/6-31G(d)–IEF-PCM(acetone)). Stereoisomeric transition structures that lead to the major (*R*) product are on the left side of the figure. Stereoisomeric transition structures that lead to the minor (*S*) product are on the right side of the figure. The relative free energies of activation compared with **TS-2a** are reported in kcal/mol.

We have found that the lowest-energy transition structures, i.e. the crown (chair-chair) conformations, acquire matching (+)-gauche conformations at both the forming C–C bond and the NCCN bond of the catalyst. The catalyst is able to occupy both (+)- and (-)-gauche conformations at the NCCN bond, however the (+)-gauche conformations were found to be more stable in this case because the (-)-gauche conformer has an axial pyrrolidine ring. The transition structures with mismatching (+)- and (-)-gauche conformations are higher in energy. The model system is quite transferable to the experimental system. The RMSD between the skeleton of the crown in the model and experimental system was 0.13 Å.

1.5 Conclusions

The stereoselectivity of intermolecular aldol additions catalyzed by vicinal diamines can be explained by the model in Scheme 1.3. The hydrogen-bonded transition state prefers a crown conformation, although the chair-boat is only slightly higher in energy. Both the crown and the chair-boat contain a chair arrangement of the enamine and carbonyl atoms that is consistent with the Zimmerman-Traxler model. These preferences are found in the model system, and are amplified in substituted systems with additional steric interactions. In the intramolecular aldol condensation[10] we found that the stereocontrolling transition structure was the boat-chair. In that

case, the presence of a tether between the enamine and carbonyl affected the approaching C–C bond configurations, which led to the boat-chair acquiring a more favorable staggered conformation.

Scheme 1.3. Stereoselectivity Model for Vicinal Diamine-Catalyzed Aldol Reactions.

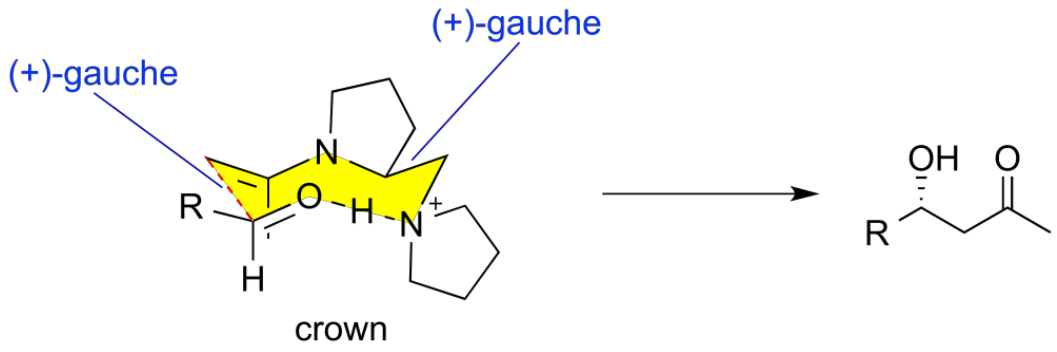

1.6 References

(1) Li, J.; Fu, N.; Li, X.; Luo, S.; Cheng, J.-P. *J. Org. Chem.* **2010**, *75*, 4501–4507.

(2) Chen, L.; Luo, S.; Li, J.; Li, X.; Cheng, J.-P. *Org. Biomol. Chem.* **2010**, *8*, 2627–2632.

(3) Gao, J.; Bai, S.; Gao, Q.; Liu, Y.; Yang, Q. *Chem. Commun.* **2011**, *47*, 6716–6718.

(4) Kumar, A.; Singh, S.; Kumar, V.; Chimni, S. S. *Org. Biomol. Chem.* **2011**, *9*, 2731–2742.

(5) Nakadai, M.; Saito, S.; Yamamoto, H. *Tetrahedron* **2002**, *58*, 8167–8177.

(6) (a) Luo, S.; Xu, H.; Li, J.; Zhang, L. A.; Cheng, J.-P. *J. Am. Chem. Soc.* **2007**, *129*, 3074–3075. (b) Zhang, L.; Fu, N.; Luo, S. *Acc. Chem. Res.* **2015**, *48*, 986−997.

(7) Sun, X.; Zhu, R.; Gao, J.; Zhang, D.; Feng, D. *J. Phys. Chem. A.* **2012**, *116*, 7082–7088.

(8) Lam, Y.-h.; Houk, K. N. *J. Am. Chem. Soc.* **2014**, *136*, 9556–9559.

(9) Kwiatkowski, P.; Beeson, T. D.; Conrad, J. C.; MacMillan, D. W. C. *J. Am. Chem. Soc.* **2011**, *133*, 1738–1741.

(10) Lam, Y.-h.; Houk, K. N. *J. Am. Chem. Soc.* **2015**, *137*, 2116–2127.

(11) Zhou, J.; Wakchaure, V.; Kraft, P.; List, B. *Angew. Chem. Int. Ed.* **2008**, *47*, 7656–7658.

(12) Zimmerman, H. E.; Traxler, M. D. *J. Am. Chem. Soc.* **1957**, *79*, 1920–1923.

(13) Li, Y.; Paddon-Row, M. N.; Houk, K. N. *J. Am. Chem. Soc.* **1988**, 110, 3684–3686.

(14) Bahmanyar, S.; Houk, K. N.; Martin, H. J.; List, B. *J. Am. Chem. Soc.* **2003**, *125*, 2475–2479.

(15) (a) Banks, J.L.; Beard, H.S.; Cao, Y.; Cho, A.E.; Damm, W.; Farid, R.; Felts, A.K.; Halgren, T.A.; Mainz, D.T.; Maple, J.R.; Murphy, R.; Philipp, D.M.; Repasky, M.P.; Zhang, L.Y.; Berne, B.J.; Friesner, R.A.; Gallicchio, E.; Levy. R.M. *J. Comp. Chem.* **2005**, *26*, 1752. (b) Schrödinger Release 2015-3: MacroModel, version 10.9, Schrödinger, LLC, New York, NY, 2015.

(16) Frisch, M. J.; Trucks, G. W.; Schlegel, H. B.; Scuseria, G. E.; Robb, M. A.; Cheeseman, J. R.; Scalmani, G.; Barone, V.; Mennucci, B.; Petersson, G. A.; Nakatsuji, H.; Caricato, M.; Li, X.; Hratchian, H. P.; Izmaylov, A. F.; Bloino, J.; Zheng, G.; Sonnenberg, J. L.; Hada, M.; Ehara, M.; Toyota, K.; Fukuda, R.; Hasegawa, J.; Ishida, M.; Nakajima, T.; Honda, Y.; Kitao, O.; Nakai, H.; Vreven, T.; Montgomery, J. A., Jr.; Peralta, J. E.; Ogliaro, F.; Bearpark, M.; Heyd, J. J.; Brothers, E.; Kudin, K. N.; Staroverov, V. N.; Keith, T.; Kobayashi, R.; Normand, J.; Raghavachari, K.; Rendell, A.; Burant, J. C.; Iyengar, S. S.; Tomasi, J.; Cossi, M.; Rega, N.; Millam, J. M.; Klene, M.; Knox, J. E.; Cross, J. B.; Bakken, V.; Adamo, C.; Jaramillo, J.; Gomperts, R.; Stratmann, R. E.; Yazyev, O.; Austin, A. J.; Cammi, R.; Pomelli, C.; Ochterski, J. W.; Martin, R. L.; Morokuma, K.; Zakrzewski, V. G.; Voth, G. A.; Salvador, P.; Dannenberg, J. J.; Dapprich, S.; Daniels, A. D.; Farkas, O.; Foresman, J. B.; Ortiz, J. V.; Cioslowski, J.; Fox, D. J. Gaussian 09, Rev. D.01; Gaussian, Inc.: Wallingford, CT, 2013.

(17) (a) Becke, A. D. *J. Chem. Phys.* **1993**, *98*, 5648. (b) Lee, C.; Yang, W.; Parr, R. G. *Phys. Rev. B* **1988**, *37*, 785. (c) Vosko, S. H.; Wilk, L.; Nusair, M. Can. *J. Phys.* **1980**, *58*, 1200. (d) Stephens, P. J.; Devlin, F. J.; Chabalowski, C. F.; Frisch, M. J. *J. Phys. Chem.* **1994**, *98*, 11623.

(18) Chai, J.-D.; Head-Gordon, M. *Phys. Chem. Chem. Phys.* **2008**, *10*, 6615.

(19) Zhao, Y.; Truhlar, D. *Theor. Chem. Acc.* **2008**, *120*, 215.

(20) Weigend, F.; Ahlrichs, R. *Phys. Chem. Chem. Phys.* **2005**, *7*, 3297.

(21) Tomasi, J.; Mennucci, B.; Cammi, R. *Chem. Rev.* **2005**, *105*, 2999.

(22) Simoń, L.; Goodman, J. M. *Org. Biomol. Chem.* **2011**, *9*, 689− 700.

(23) Wiberg, K. B. *J. Org. Chem.* **2003**, *68*, 9322−9329.

(24) Wang, H.; Houk, K. N. *Chem. Sci.* **2014**, *5*, 462-470.

Chapter 2. Origins of Stereoselectivity of Chiral Vicinal Diamine-Catalyzed Aldol Reaction

2.1 Abstract

The sources of asymmetric induction in aldol reactions catalyzed by cinchona alkaloid-derived amines, and chiral vicinal diamines in general, have been determined by density functional theory calculations. Four vicinal diamine-catalyzed aldol reactions were examined. The cyclic transition states of these reactions involve nine-membered hydrogen-bonded rings in distinct conformations. Using nomenclature from eight-membered cycloalkanes, the heavy atoms of the low-energy transition states are in crown (chair-chair) and chair-boat conformations. The factors that control which of these are favored have been identified.

2.2 Introduction

The functionalization of carbonyl compounds by asymmetric aminocatalysis has proven to have considerable synthetic utility.[1] Proline and its derivatives are widely used chiral amines for enantioselective reactions.[2] The collaborations of experimentalists and computational chemists have revealed the mechanistic intricacies of asymmetric aldol reactions catalyzed by proline.[3] Vicinal diamines are another general class of related catalysts and are alternatives to proline.[4]

Both vicinal diamines and proline rely on enamine and iminium chemistry. Proline has a carboxylic acid while one of the amines of a diamine can be protonated and function as a general acid. These catalysts vary from simple 1,2-diaminocyclohexanes (**3**) to more complex cinchona alkaloid-derived amines **1** and **2** (Scheme 2.1). The vicinal diamines, **3** and **4**, are important catalysts for aldol reactions. A summary of aldol reactions involving chiral vicinal diamine catalysts is shown in Scheme 2. Yamamoto, using diamine **4**, reported one of the first examples of vicinal diamine-catalyzed aldol reactions (Scheme 2.2, eq. 1).[4] They used acetone, as well as cyclic ketones, with *p*-nitrobenzaldehyde as the aldol acceptor and reported good to excellent

enantioselectivity. Luo reported a successful and robust series of aldol reactions catalyzed by **3** (Scheme 2.2, eq. 2).[5] Catalyst **3** works with linear aliphatic ketone donors with excellent stereocontrol, and gives unprecedented *syn* diastereoselectivity for ethyl ketones.[5]

Scheme 2.1. Examples of Vicinal Diamines

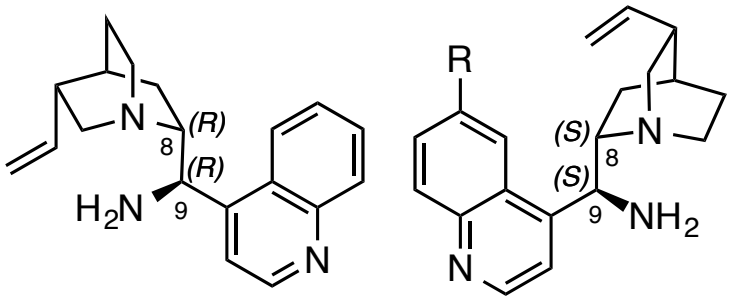

1 **2a R = H** **2b R = OMe**

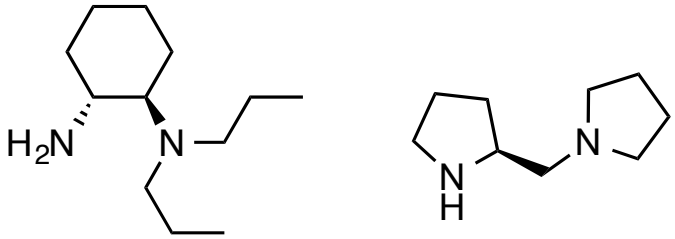

3 **4**

The cinchona alkaloid-derived primary amine catalysts **1** and **2** are pseudoenantiomers because the important stereogenic centers at C8 and C9 are inverted. These cinchona alkaloid-derived primary amines have been studied spectroscopically and computationally.[6-8] While **1** and **2** are conformationally flexible, both the ground state and transition states of the reactions that they catalyze have a common conformational preference.[7-9]

The use of cinchona-derived amine catalysts both complemented and expanded the synthetic utility of chiral pyrrolidine-based secondary amines in aldol chemistry.[10-13] Cinchona alkaloid-derived primary amines are advantageous over secondary amine catalysts for reactions involving sterically demanding functional groups.[14] The first example of asymmetric

intermolecular aldol reactions catalyzed by cinchonine- and cinchonidine-based primary amines (**1** and **2a**) was reported in 2007 (Scheme 2.2, eq. 3).[10] Later, these catalysts, including quinine-derived primary amines (**2b**), were shown to perform well with more complex substrates, which sometimes reacted overly slow with secondary amine-based catalysts (Scheme 2.2, eq. 4-5).[12,13]

Scheme 2.2. Examples of Aldol Reactions Catalyzed by Chiral Vicinal Diamines

eq. 1 (Yamamoto *et al.*)

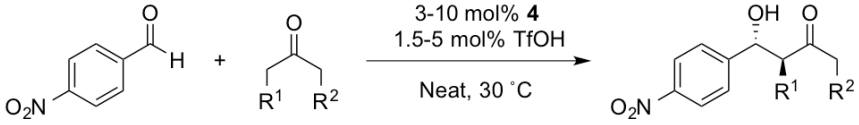

R^1 = H, R^2 = H	88% ee
R^1 = R^2 = $(CH_2)_2$	84% ee
R^1 = R^2 = $(CH_2)_3$	96% ee

eq. 2 (Luo *et al.*)

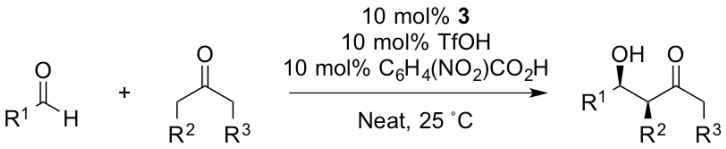

R^1 = 1-Napth	R^2 = H, R^3 = H	97% ee
R^1 = 4-NO_2Ph	R^2 = Me, R^3 = H	96% ee
R^1 = 4-NO_2Ph	R^2 = Me, R^3 = Me	96% ee
R^1 = 4-NO_2Ph	R^2 = R^3 = $(CH_2)_3$	98% ee

eq. 3 (Liu *et al.*)

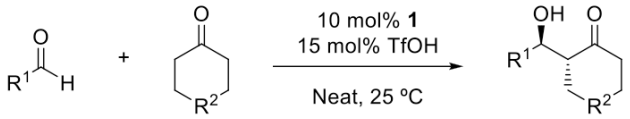

R^1 = 4-NO_2Ph	R^2 = CH_2	99% ee
R^1 = 4-NO_2Ph	R^2 = O	91% ee
R^1 = 4-NO_2Ph	R^2 = S	94% ee
R^1 = 4-NO_2Ph	R^2 = —	86% ee

eq. 4 (Chimni *et al.*)

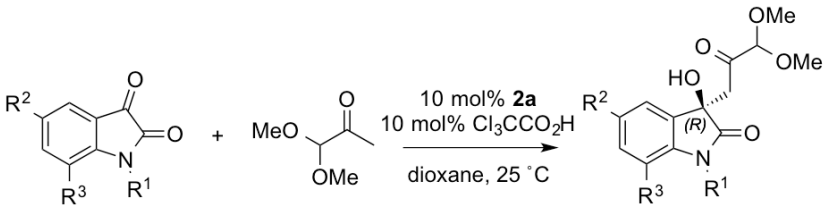

R^1 = H, R^2 = H, R^3 = H	92% ee
R^1 = Me, R^2 = H, R^3 = H	94% ee
R^1 = Bn, R^2 = Br, R^3 = H	92% ee
R^1 = H, R^2 = Br, R^3 = Br	82% ee

eq. 5 (Zhao *et al.*)

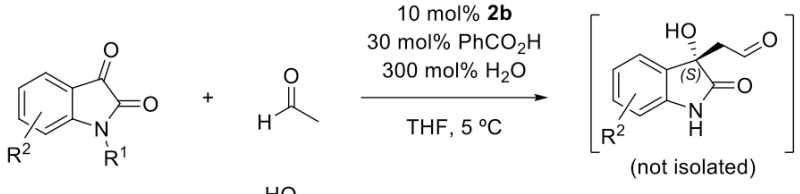

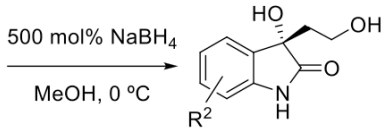

R^1 = H, R^2 = H	92% ee
R^1 = H, R^2 = 5-MeO	92% ee
R^1 = H, R^2 = 4-Br	88% ee
R^1 = Bn, R^2 = H	92% ee

The sources of asymmetric induction in the reactions by Liu,[10] Chimni,[13] and Zhao[12] (Scheme 2.2, eq. 3-5) are not well known, and they have mostly been explained by *ad hoc* models in the original reports. The origins of asymmetric induction of vicinal diamine-catalyzed aldol reactions were only recently explored by our group[9,15] and the Zhang group.[16] Our efforts have shown that the stereoselectivities of intra- and intermolecular aldol reactions are determined by favored conformations of cyclic transition states.[9,15]

We now present quantum chemical calculations of transition states for the more complex examples of these reactions reported by Liu,[10] Chimni,[13] and Zhao[12] in Scheme 2.2. The privileged cinchona alkaloid-derived primary amines are examined with classical substrates, *i.e.* cyclohexanone and *p*-nitrobenzaldehyde, and pharmaceutically-relevant isatin-based substrates. Additionally, we revisit computations by the Zhang group[16] for the sources of stereoselectivity in the aldol reactions reported by Luo (Scheme 2.2, eq. 2).[5] A general method to explain the source of asymmetric induction in vicinal diamine-catalyzed reactions is proposed.

2.3 Computational Methods

All quantum chemical calculations were performed with *Gaussian 09*.[17] Geometry optimizations and frequencies were calculated with the B3LYP[18] density functional with the 6-31G(d) basis set in conjunction with the IEF-PCM implicit solvation model.[19] Optimized geometries were verified by frequency calculations as minima (zero imaginary frequencies) or transition structures (a single imaginary frequency). Free energy corrections were calculated using Truhlar's quasiharmonic approximation.[20] Single point energy calculations were performed on optimized geometries with the M06-2X[21] density functional and def2-TZVPP[22] basis set with the IEF-PCM model for the experimental solvent reported. The thermal corrections evaluated from the unscaled vibrational frequencies at the B3LYP/6-31G(d)–IEF-PCM level on the optimized

geometries were then added to the M06-2X/def2-TZVPP–IEF-PCM electronic energies to obtain the free energies. We previously tested how several density functionals perform with the model system[15] and found that the M06-2X/def2-TZVPP–IEF-PCM//B3LYP/6-31G(d)–IEF-PCM provided accurate energies while being relatively efficient in terms of computational times.[23] B3LYP/6-31G(d) provides appropriate geometry structures, but dispersion-inclusive methods with larger basis sets are required for accurate energies.[9a]

Monte Carlo conformational searches were performed on the enamines formed by the protonated catalysts and aldol donors in the presence of the aldol acceptors to identify reactive conformations with the OPLS_2005 force field[24] in *Maestro*/*Macromodel*.[25] Reactive conformations with the distance between the bond-forming atoms shorter than 4.0 Å were used as input geometries for transition structure optimizations. Structure graphics were generated using *CYLView*.[26]

2.4 Results and Discussion

We previously studied the origins of stereoselectivity in intramolecular aldol condensations catalyzed by cinchona alkaloid-derived primary amine **2b**.[9a,11,27] The stereochemistry-determining transition structures by Lam and Houk are shown in Scheme 2.3. These reactions proceed through a nine-membered hydrogen bonded cyclic transition state, where the eight heavy atoms adopt conformations that resemble low-energy conformations of cyclooctane.[28] The lowest-energy transition structure adopts the boat-chair conformation, and leads to the major enantiomer. The minor product was predicted to form via the cyclic transition structure in the crown conformation.

Scheme 2.3. Stereo-Determining Transition Structures by Lam and Houk[9a]

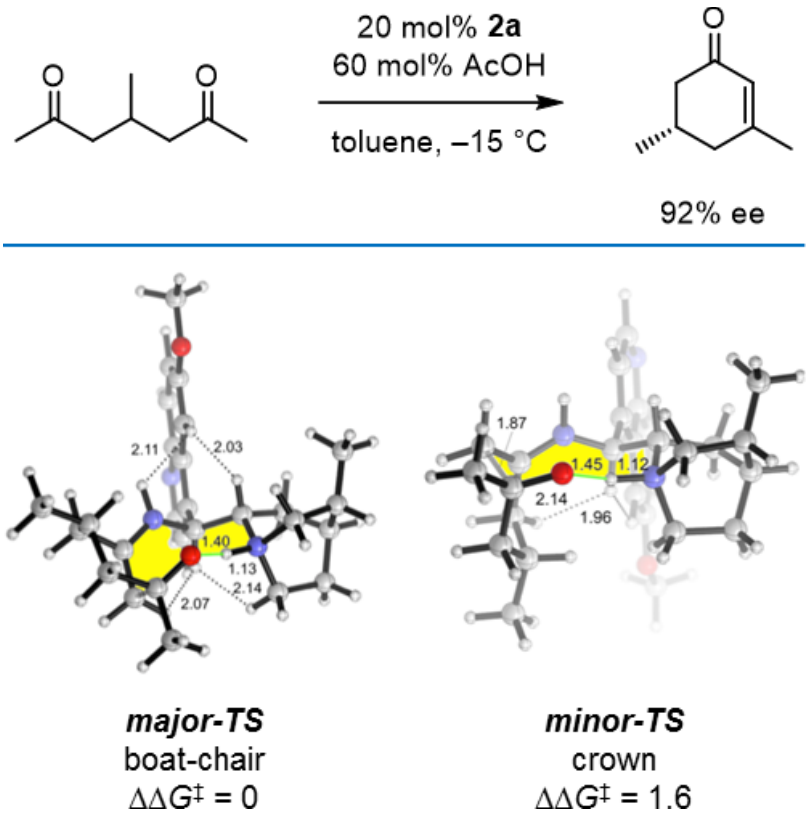

The transition states of intermolecular aldol reactions catalyzed by the parent vicinal diamine were also reported in an earlier communication.[15] The prototypical vicinal diamine-catalyzed aldol transition structures (Scheme 2.4) display well-defined conformations, with a preference for the crown conformation. Chair conformations about the forming C–C bonds were found in the low-energy crown and chair-boat conformations. The s-trans enamines (crown and chair-boat) were found to be preferred over s-cis enamines (boat-chair and boat-boat). We also explained Yamamoto's vicinal diamine-catalyzed aldol reaction shown in Scheme 2.5.[4] The crown with an equatorial aryl substituent formed the observed major product, while the crown with an axial aryl substituent formed the minor enantiomeric product, reminiscent of the Zimmerman-Traxler model.[29]

Scheme 2.4. Prototypical Vicinal-Diamine Catalyzed Aldol Transition Structures[15]

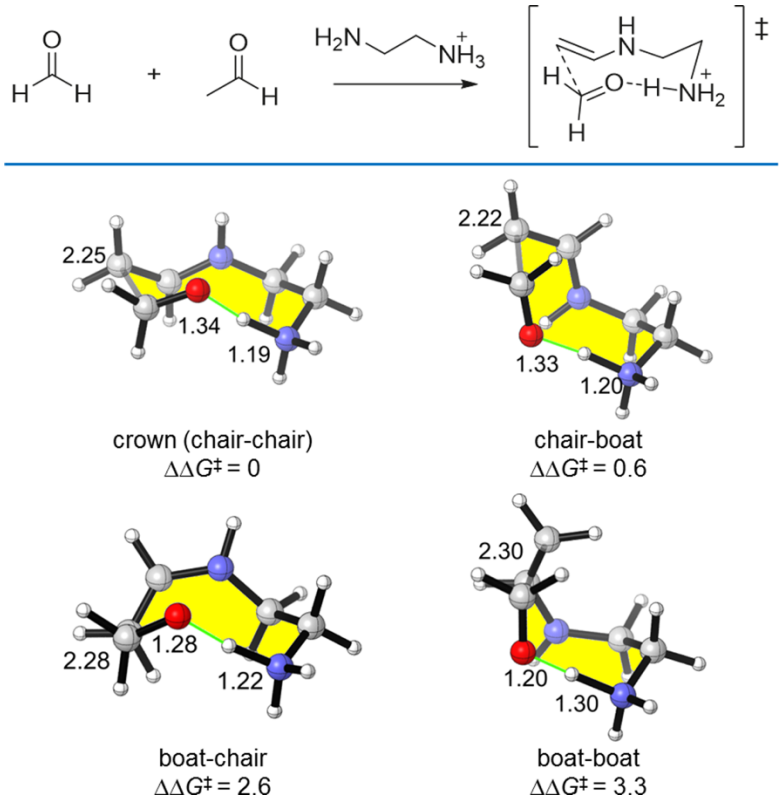

Scheme 2.5. Stereo-Determining Transition Structures for Yamamoto's Aldol Reaction[15]

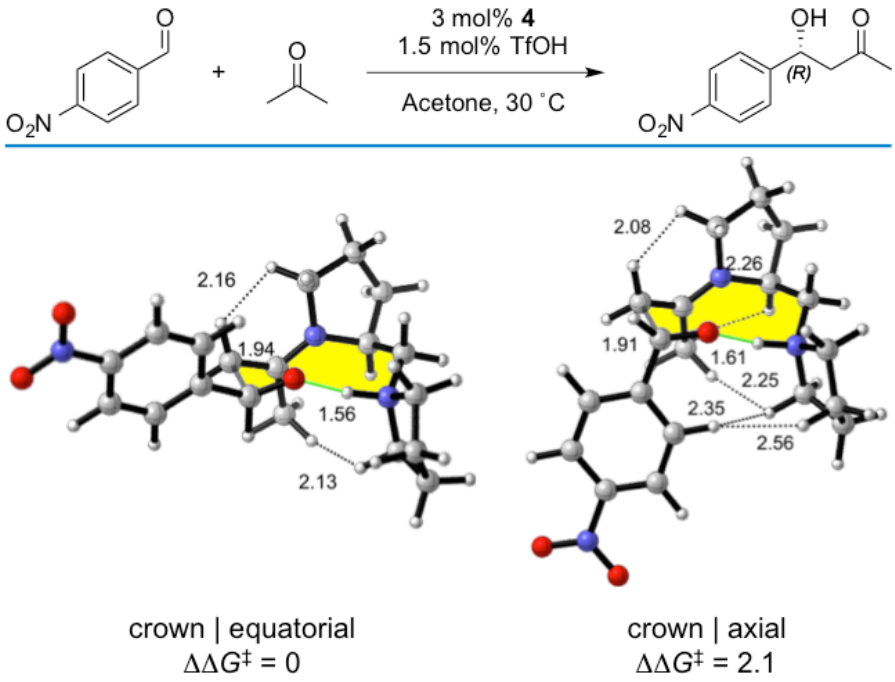

In 2007, Liu reported that the aldol reactions of cyclohexanones and substituted benzaldehydes were effectively catalyzed by the cinchona alkaloid-derived vicinal diamine **1**

(Scheme 2.6).[10] They observed 99% ee, with a diastereomeric ratio of 9.2:1 for the example in Scheme 2.6. This corresponds to a difference in free energies of activation ($\Delta\Delta G^{\ddagger}$) of ≥2.9 kcal/mol for enantioselectivity and 1.2 kcal/mol for diastereoselectivity.

Scheme 2.6. Example Aldol Reaction Reported by Liu

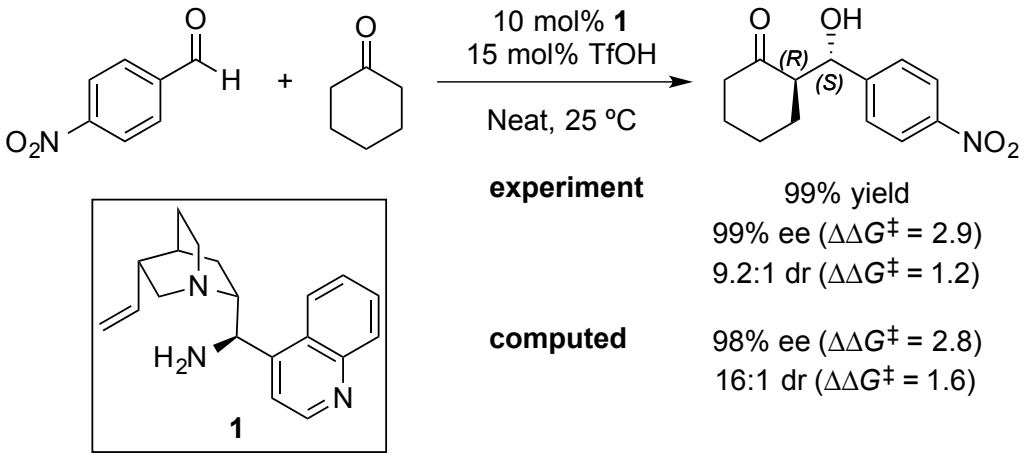

Four transition structures for the aldol reaction of *p*-nitrobenzaldehyde and the enamine formed by **1** and cyclohexanone were located (Figure 2.1). As reported earlier,[15] the transition structures are nine-membered hydrogen-bonded rings that have heavy atoms resembling conformations of cyclooctane.[28] The quinoline ring is equatorial in the favored transition structures.

TS-1a leads to the major (*R*,*S*) *anti*-product and is the lowest-energy transition structure. The (*R*,*R*) *syn*-diastereomer is formed from **TS-1b** and is higher in energy by 1.6 kcal/mol compared with **TS-1a**. Both **TS-1a** and **TS-1b** are crown conformations, have staggered conformations about the forming C–C bond, and have s-trans enamine conformations of the catalyst. These two transition structures differ by the equatorial and axial nature of the *p*-nitrobenzaldehyde group. **TS-1c** also leads to a *syn*-diastereomer, but with the (*S*,*S*) absolute configuration. This transition structure is higher in energy by 2.8 kcal/mol. **TS-1c** is in a boat-chair conformation, and contains a steric interaction between the s-cis enamine and the quinoline ring

of the catalyst. The proximal H•••H interaction is at 2.73 Å. The forming C–C bond is rather eclipsed with a dihedral angle of 36° at the OC–CC bond. The absolute configuration of the minor diastereomer has not been reported,[10] but we predict that the (*R*,*R*) *syn*-product is preferred via **TS-1b**, in close agreement with experimental diastereoselectivity.

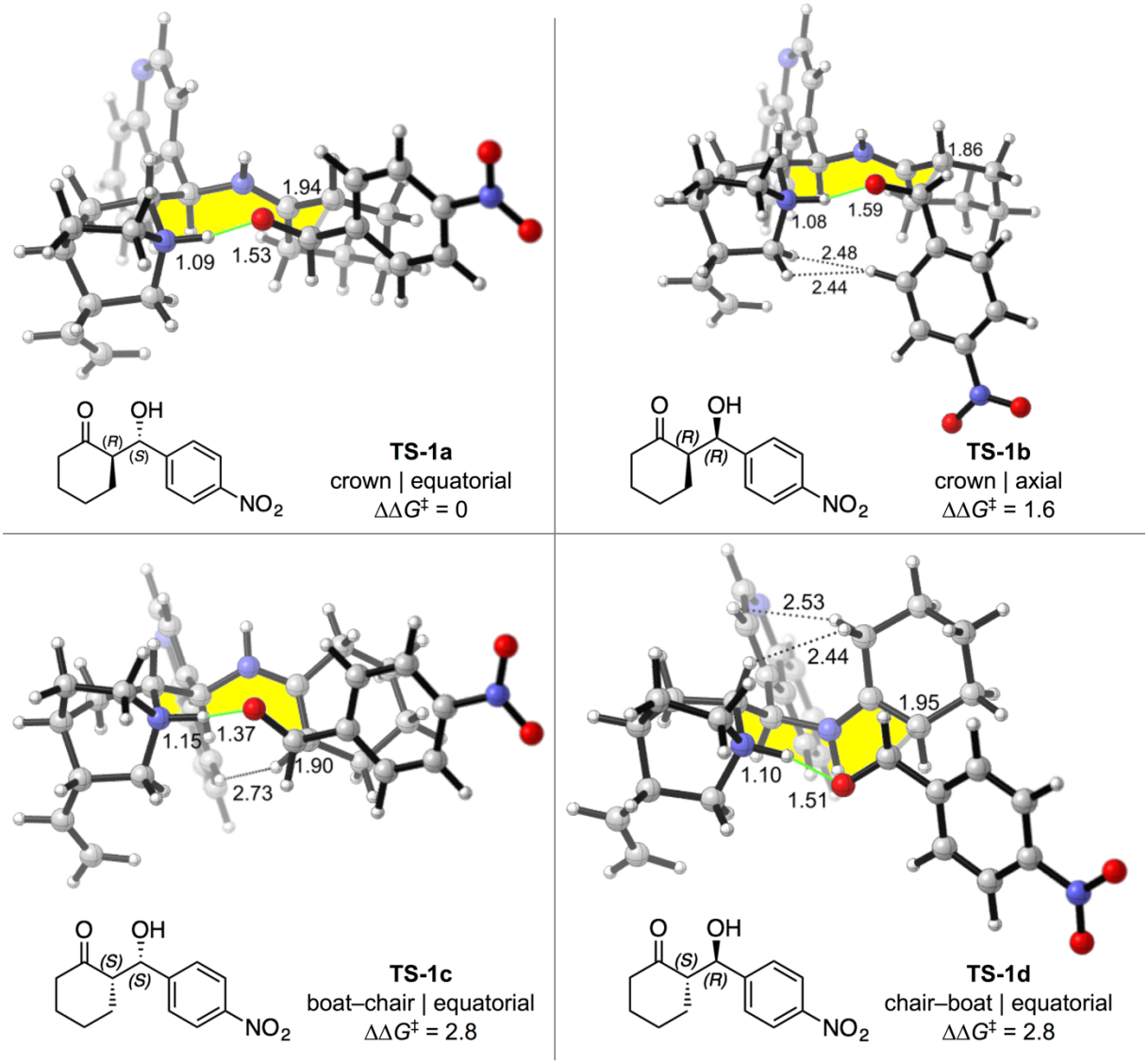

Figure 2.1. Lowest-energy transition structures **TS-1a–d** for the aldol addition of *p*-nitrobenzaldehyde and the enamine formed by **1** and cyclohexanone (M06-2X/def2-TZVPP–IEF-PCM//B3LYP/6-31G(d)–IEF-PCM (cyclohexanone)). The free energies of activation ($\Delta\Delta G^{\ddagger}$), relative to **TS-1a**, are reported in kcal/mol.

The minor (*S*,*R*) enantiomer is formed by **TS-1d**, which is higher in energy than **TS-1a** by 2.8 kcal/mol, also in close agreement with experimental enantioselectivity. **TS-1d** is in the chair-boat conformation, which has a staggered arrangement at the forming C–C bond between the s-trans enamine and electrophilic carbonyl carbon. **TS-1d** contains steric interactions between the axial alkyl group of the enamine and the quinoline ring of the catalyst. These H•••H interactions in the chair-boat are 2.44 and 2.53 Å. Thus, the destabilization of the chair-boat results from steric repulsions between the axial methylene of the cyclohexanone and the quinoline ring of the catalyst.

We also studied the aldol reactions reported by Chimni[13] and Zhao[12] to explore how complex substrates affected the conformational preferences of the aldol transition state (Scheme 2.7). Catalysts **2a** and **2b** possess the same absolute configuration at C8 and C9, yet the senses of stereoselectivity of the two reactions are opposite. The (*R*) product reported by Chimni is formed from the addition to the *Si* face of isatin by the enamine derived from **2a** and pyruvic aldehyde dimethyl acetal in 92% ee ($\Delta\Delta G^{\ddagger}$ = 1.9 kcal/mol). The reaction reported by Zhao, however, yields the (*S*) product requiring *Re* selectivity at the isatin by the enamine derived from **2b** and acetaldehyde also in 92% ee ($\Delta\Delta G^{\ddagger}$ = 1.8 kcal/mol).

Scheme 2.7. Aldol Reactions Reported by Chimni and Zhao

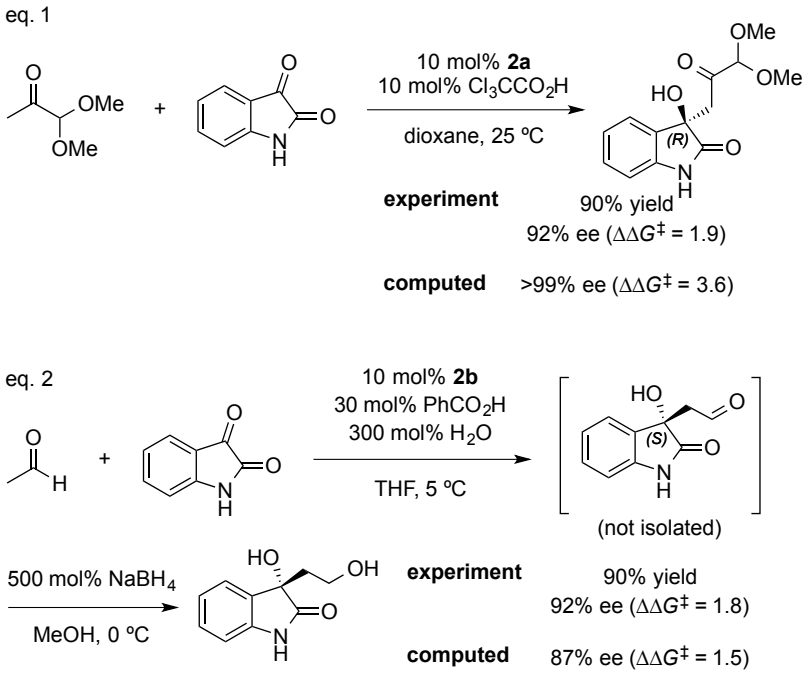

For Chimni's aldol reaction (Scheme 2.7, eq. 1), the two lowest-energy stereocontrolling transition structures are shown in Figure 2.2. **TS-2a** leads to the major (*R*) product and is the lowest-energy transition structure. The minor (*S*) enantiomer forms from **TS-2b**. The difference in free energy of activation ($\Delta\Delta G^{\ddagger}$) between **TS-2a** and **TS-2b** is 3.6 kcal/mol, which overestimates the reported enantioselectivity.

TS-2a and **TS-2b** have similar conformations at the cinchona alkaloid-derived primary amine catalyst. Both enamines are s-trans and the quinoline rings are equatorial. The chair-boat is destabilized by a steric clash between the axial dimethoxymethyl group of the enamine and quinoline ring of the catalyst. The major H•••H interactions are 2.50 and 2.40 Å between the axial CH of the enamine, quinoline ring, and C8-H of the catalyst.

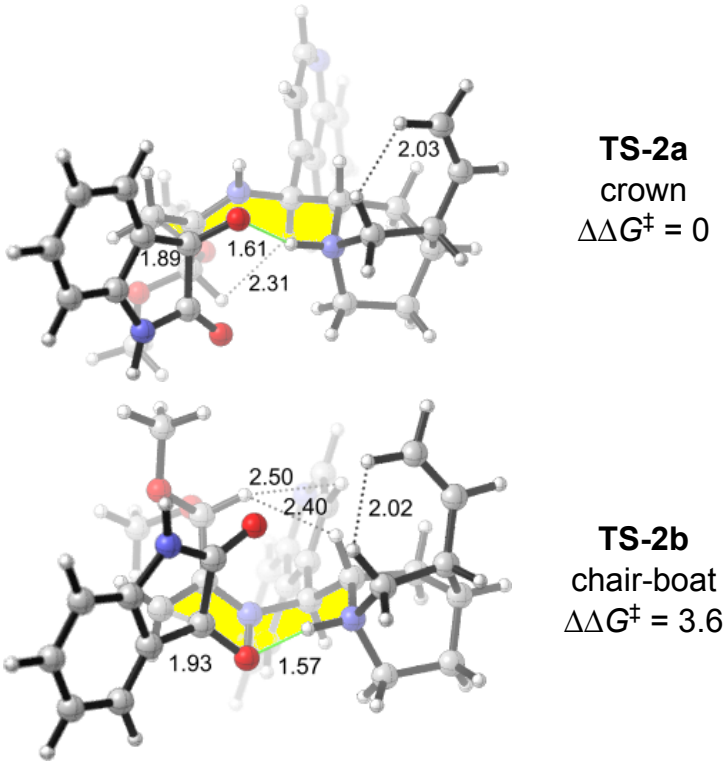

Figure 2.2. Lowest-energy transition structures **TS-2a** and **TS-2b** for the aldol addition of isatin and the enamine formed by **2a** and pyruvic aldehyde dimethyl acetal (M06-2X/def2-TZVPP–IEF-PCM//B3LYP/6-31G(d)–IEF-PCM (1,4-dioxane)). The free energies of activation ($\Delta\Delta G^{\ddagger}$), relative to **TS-2a**, are reported in kcal/mol. The two lowest-energy transition structures for Zhao's aldol reaction (Scheme 2.7, eq. 2) are shown in Figure 2.3. **TS-3a**, the favored transition structure, is in the chair-boat conformation, with an s-trans enamine and equatorial quinoline ring. With an aldehyde aldol donor, there is no steric interaction between the axial substituent of the enamine and quinoline ring in the chair-boat. **TS-3b** is in the crown conformation with both an s-trans enamine and equatorial quinoline ring. We found that the distances between the amide carbonyl oxygen and the polarized CH's adjacent to the protonated quinuclidinium nitrogen are quite close in both **TS-3a** and **TS-3b**.

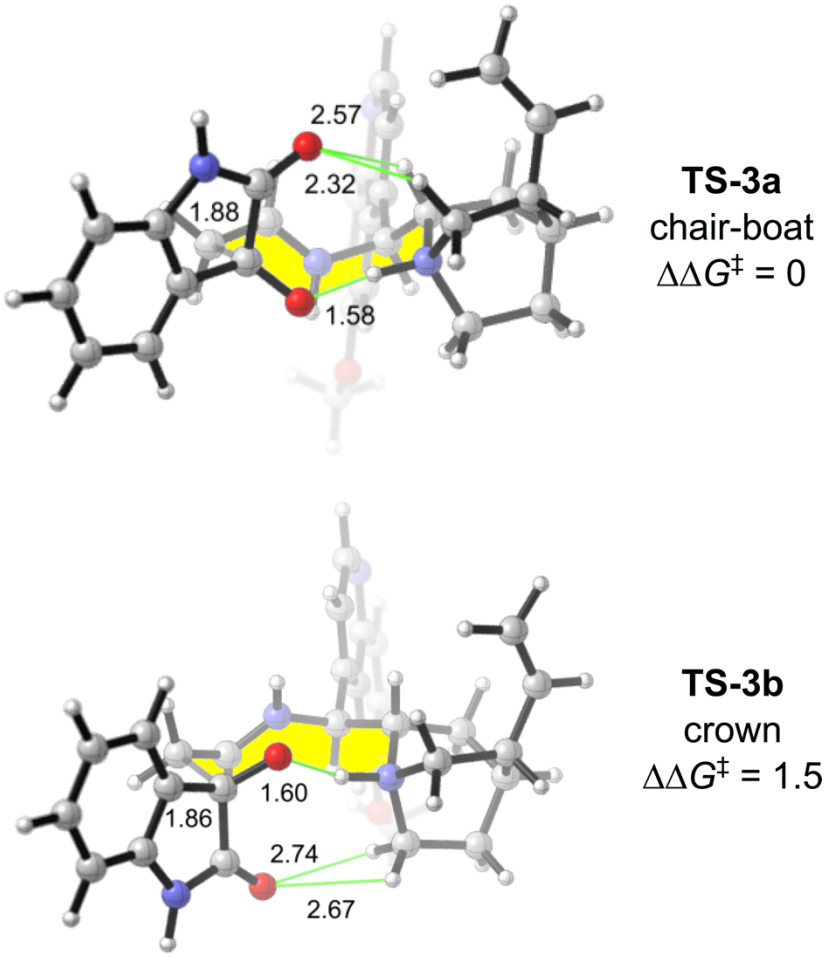

Figure 2.3. Lowest-energy transition structures **TS-3a** and **TS-3b** for the aldol addition of isatin and the enamine formed by **2b** and acetaldehyde (M06-2X/def2-TZVPP–IEF-PCM//B3LYP/6-31G(d)–IEF-PCM (THF)). The free energies of activation ($\Delta\Delta G^{\ddagger}$), relative to **TS-3a**, are reported in kcal/mol.

In **TS-3a** there are two $^{+}$NCH•••O$^{\delta-}$ interactions at 2.57 and 2.32 Å. In the crown, **TS-3b**, these are further apart at 2.74 and 2.67 Å. Thus, there are hydrogen-bonding interactions between the amide carbonyl oxygen and the polarized alkyl groups adjacent to the quinuclidinium nitrogen, which are stronger in the chair-boat conformation. Electrostatic $^{+}$NCH•••O$^{\delta-}$ interactions are also present in the Houk-List model for proline-catalyzed aldol additions.[3a]

To test the importance of this electrostatic interaction, we computed a model of the reaction, where the amide functional group in the aldol transition structures **TS-4a** and **TS-4b** is replaced with methylene groups. The crown and chair-boat conformations with the model reactant are shown in Figure 2.4. **TS-4a**, the chair-boat, is higher in energy than **TS-4b**, the crown, by 1.1 kcal/mol. Thus, hydrogen bonding between the amide carbonyl oxygen and polarized alkyl groups overcome the intrinsic conformational preferences of the aldol transition state in Zhao's aldol reaction with aldehyde aldol donors. These results explain the difference in facial selectivities of the enamine additions to isatin in the reactions reported by Chimni[13] and Zhao.[12]

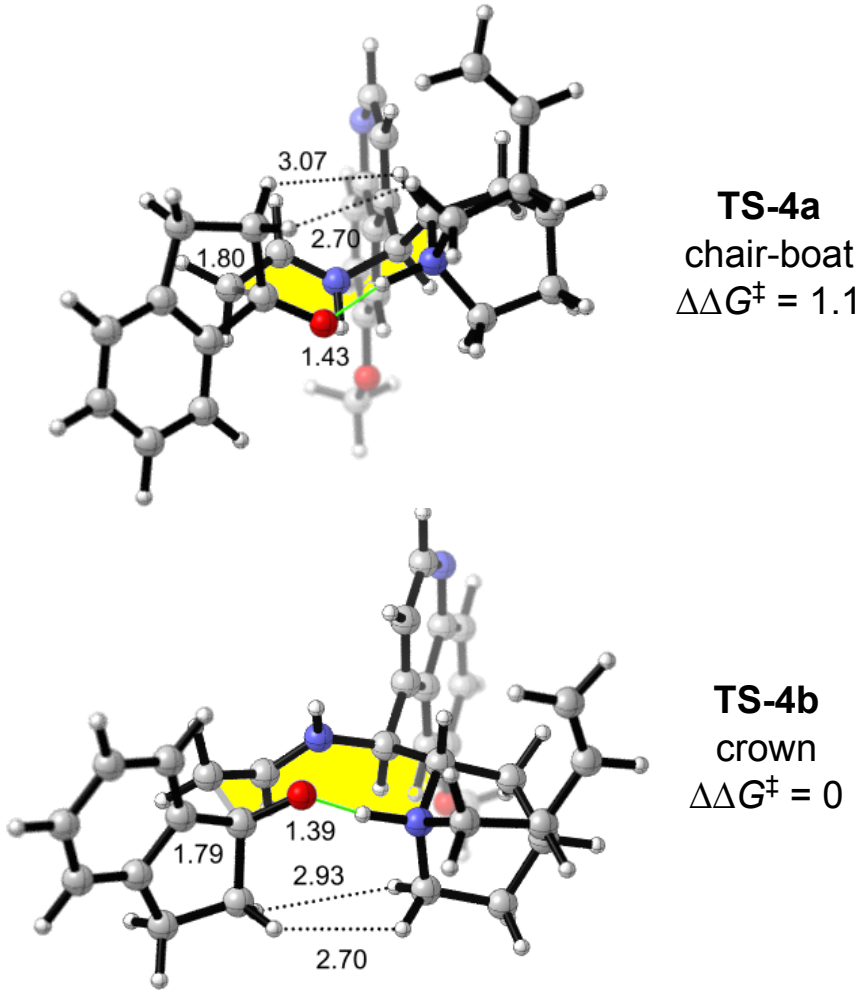

Figure 2.4. Model aldol system where the amide functional group of isatin was replaced with methylenes. The transition structures **TS-4a** and **TS-4b** are modified structures from **TS-3a** and

TS-3b, which were calculated at the M06-2X/def2-TZVPP–IEF-PCM//B3LYP/6-31G(d)–IEF-PCM (THF) level of theory. The free energies of activation ($\Delta\Delta G^{\ddagger}$), relative to **TS-4b**, are reported in kcal/mol.

Luo reported a robust methodology for bimolecular aldol reactions catalyzed by the vicinal diamine **3**.[5a] One example, similar to the reaction reported by Liu[10] in the same year, is the aldol addition of *p*-nitrobenzaldehyde and cyclohexanone catalyzed by **3** (Scheme 2.8). The reaction achieved 98% ee with 9:1 dr, corresponding to difference in free energies of activation of 2.7 kcal/mol and 1.2 kcal/mol, respectively.

Scheme 2.8. Example Aldol Reaction Reported by Luo

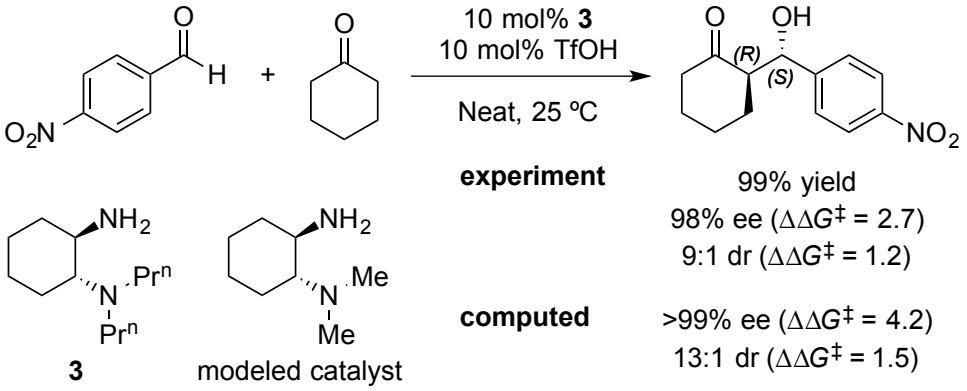

In 2012, the Zhang group reported computational studies of three aldol reactions reported by Luo, including the reaction in Scheme 2.8.[16] They calculated the transition structures for the reactions at the B3LYP/6-311+G(d,p)//B3LYP/6-31G(d) level of theory and explained the reported enantioselectivities and diastereoselectivities. Their chemical analysis involves the conformations of the enamines and using Newman projections down the forming C–C bond, reminiscent of the Houk-List model. The differences in energy between the stereoisomeric

transition structures were rationalized by the degree of planarity of the enamine and dihedral angle of the forming C–C bonds. The model proposed by the Zhang group illustrates the conformations of the enamine and aldol acceptor, but ignores conformations of the catalyst.

We recalculated their transition structures at the M06-2X/def2-TZVPP–IEF-PCM//B3LYP-6-31G(d)–IEF-PCM (cyclohexanone) level of theory. The four lowest-energy transition structures are shown in Figure 2.5. **TS-5a**, **TS-5c**, and **TS-5d** are consistent with the transition structures reported by Zhang. However, we located a new low-energy stereoisomer, **TS-5b**. **TS-5a** leads to the major (*R*,*S*) *anti*-product and is the lowest-energy transition structure. **TS-5b** leads to the (*R*,*R*) *syn*-diastereomer and is higher in energy by 1.5 kcal/mol compared with **TS-5a**, in close agreement with the experimental diastereoselectivity. **TS-5c** leads to the (*S*,*S*) *syn*-diastereomer and is higher in energy by 3.6 kcal/mol. **TS-5d**, which forms the minor (*S*,*R*) stereoisomer, is higher in energy by 4.2 kcal/mol. The energy difference between **TS-5a** and **TS-5d** reproduces the enantioselectivity found by Zhang.

We found that the transition structures again have heavy atoms arranged in conformations resembling those of cyclooctane,[28] and are analogous to the results of the cinchona alkaloid-catalyzed reaction of cyclohexanone and *p*-nitrobenzaldehyde in their relative trend of energies (Figure 2.1). The lowest-energy transition structure, **TS-5a**, is in the crown conformation. **TS-5b** is also in a crown conformation but has an axial aryl group of the aldehyde. **TS-5c** is in the boat-chair conformation, and is destabilized due to an eclipsed forming C–C bond and steric interactions between the enamine and catalyst. **TS-5d** is in the chair-boat conformation. Both **TS-5a** and **TS-5d** contain staggered chair conformations at the forming C–C bond and have enamines in s-trans conformations. The source of destabilization of **TS-5d** is due to the steric H•••H interactions between the axial methylene of cyclohexanone and the catalyst. Shown in Figure 2.5, the H•••H

distances are 1.95 and 2.38 Å, which are not present in **TS-5a** because the axial methylene is distant from the cyclohexyl portion of the catalyst.

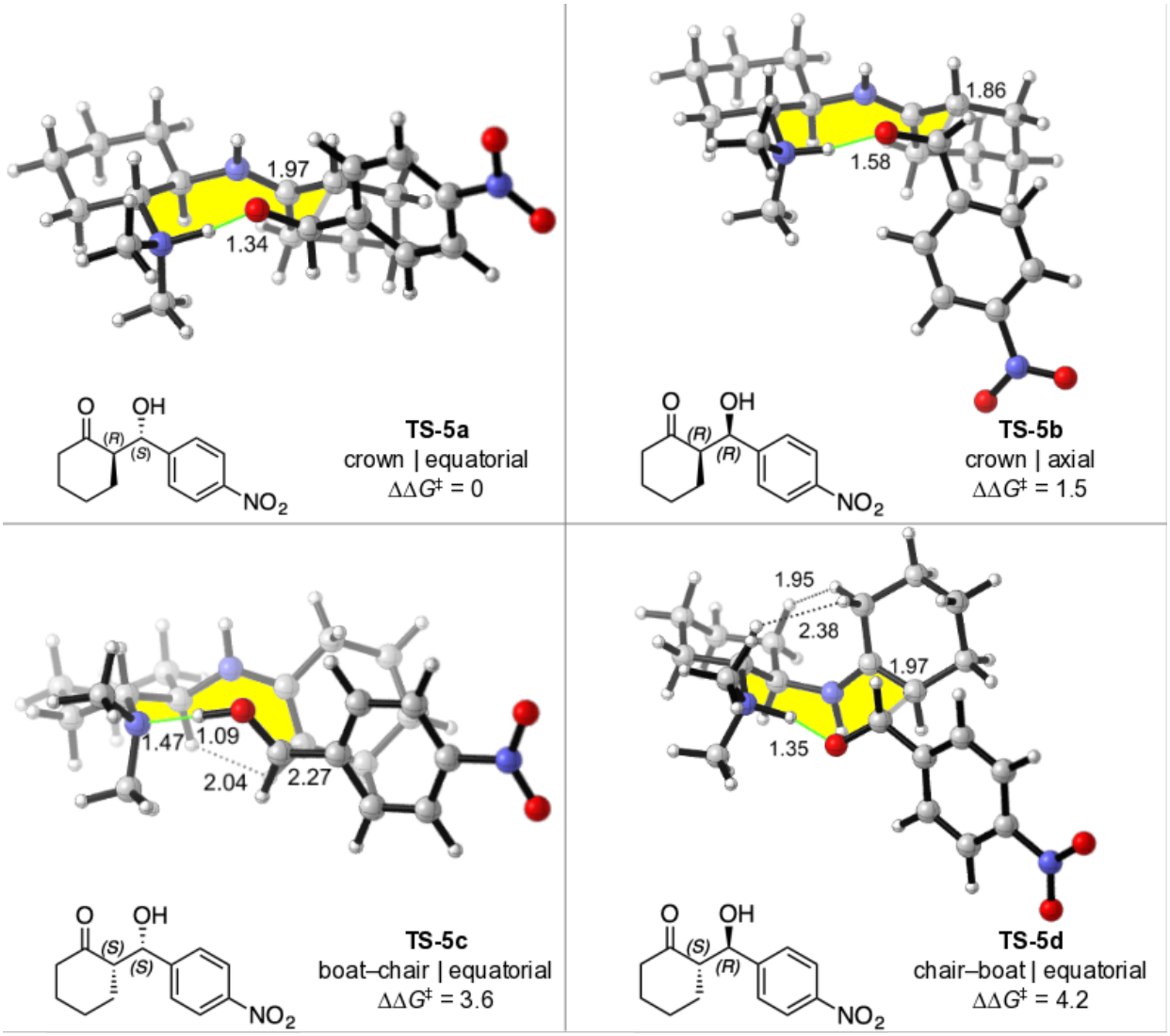

Figure 2.5. Lowest-energy transition structures **TS-5a–d** for the aldol addition of *p*-nitrobenzaldehyde and the enamine formed by **3** and cyclohexanone (M06-2X/def2-TZVPP–IEF-PCM//B3LYP/6-31G(d)–IEF-PCM (cyclohexanone)). The free energies of activation ($\Delta\Delta G^{\ddagger}$), relative to **TS-5a**, are reported in kcal/mol.

In the studies of Yamamoto's catalyst,[15] we found that the lowest-energy transition structure, *i.e.* the crown, acquired (+)-gauche conformations about both the forming C–C bond and the NCCN dihedral of the catalyst. In contrast, the higher-energy transition structures were in various combinations of (+)- and (-)-gauche conformations about these two bonds.

The lowest-energy transition structures for the Chimni, Liu, and Luo reactions either have matching (+)- or (-)-gauche conformations at both the forming C–C bonds and NCCN dihedrals. In these systems, the NCCN dihedral of the catalyst is fixed either due to rigidity (1,2-diaminocyclohexane) or conformational preference (cinchona alkaloid-derived primary amines). When the diamine is (+)-gauche, then the major product has a (+)-gauche arrangement about the forming bond. These results are summarized in Scheme 2.9. The NCCN dihedral of the vicinal diamines is a predictable measure for the gauche conformation about the forming C–C bond in the crown conformation.

2.5 Conclusions

Cyclic transition structures are preferred for vicinal-diamine catalyzed aldol reactions. The crown conformer is consistently the lowest-energy transition structure in bimolecular systems, unless secondary interactions destabilize the crown or stabilize the chair-boat (e.g. Figure 2.3). The crown has trans-enamine and staggered chair arrangements of both the forming bond and catalyst. The gauche conformations about the NCCN bond and forming C–C bond of the catalyst are both (+) or (-) for the crown conformations. We have found this to be the case in five examples (Scheme 9). In addition, we have predicted the preferences of the minor enantiomer, being either a chair-boat or crown with an axial substituent depending on the system. Diastereoselectivity relies on the difference in energy between the two crown conformations, analogous to the Zimmerman-

Traxler model.[29] In intramolecular aldol reactions, the boat-chair conformation is preferred (Scheme 2.9).[9a]

Scheme 2.9. Summary of Results

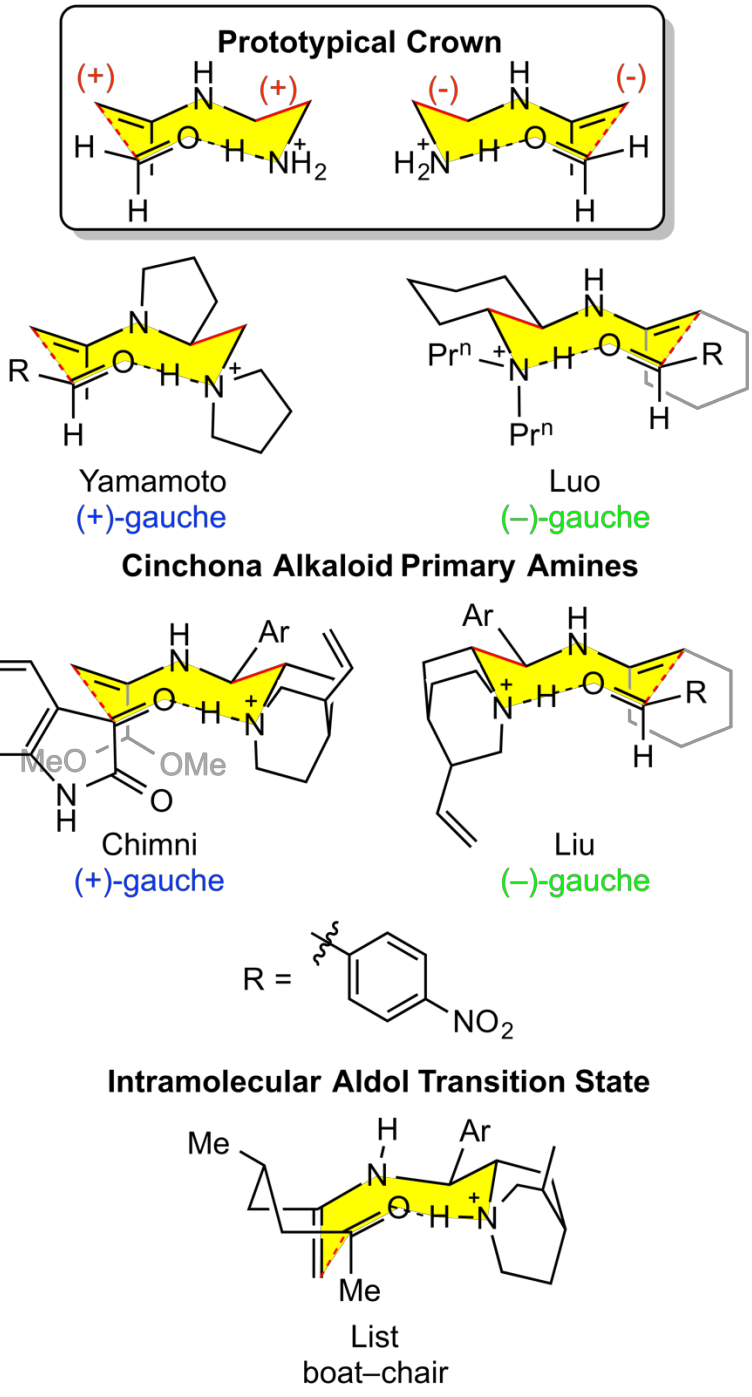

The model proposed here explains the source of asymmetric induction for aldol reactions catalyzed by both simple and complex vicinal diamines. The general features of this system have been invoked to explain other vicinal diamine-catalyzed reactions.[30] The predictability and reliability of these mechanistic insights should assist in the rational design of vicinal diamine-catalyzed reactions of aldol, Mannich, and other carbonyl functionalizing reactions.

2.6 References

(1) (a) Bertelsen, S.; Jørgensen, K. A. *Chem. Commun.* **2009**, 2178–2189. (b) Melchiorre, P.; Marigo, M.; Carlone, A.;. Bartoli, G. *Angew. Chem. Int. Ed.* **2008**, *47*, 6138–6171. (c) Mukherjee, S.; Yang, J. W.; Hoffmann, S.; List, B. *Chem. Rev.* **2007**, *107*, 5471–5569. (d) Lelais, G.; MacMillan, D. W. C. *Aldrichimica Acta* **2006**, *39*, 79–87. (e) Melchiorre, P. *Angew. Chem. Int. Ed.* **2012**, *51*, 9748–9770.

(2) (a) List, B.; Lerner, R. A.; Barbas, C. F., III. *J. Am. Chem. Soc.* **2000**, *122*, 2395–2396. (b) List, B. *Tetrahedron* **2002**, *58*, 5573–5590. (c) Movassaghi, M.; Jacobsen, E. N. *Science* **2002**, *298*, 1904–1905.

(3) (a) Bahmanyar, S.; Houk, K. N. *J. Am. Chem. Soc.* **2001**, *123*, 12911–12912. (b) Bahmanyar, S.; Houk, K. N.; Martin, H. J.; List, B. *J. Am. Chem. Soc.* **2003**, *125*, 2475–2479.

(4) (a) Nakadai, M.; Saito, S.; Yamamoto, H. *Tetrahedron* **2002**, *58*, 8167–8177. (b) Saito, S.; Yamamoto, H. *Acc. Chem. Res.* **2004**, *37*, 570–579.

(5) (a) Luo, S.; Xu, H.; Li, J.; Zhang, L. A.; Cheng, J.-P. *J. Am. Chem. Soc.* **2007**, *129*, 3074–3075. (b) Zhang, L.; Fu, N.; Luo, S. *Acc. Chem. Res*. **2015**, *48*, 986–997.

(6) (a) Dijkstra, G. D. H.; Kellogg, R. M.; Wynberg, H.; Svendsen, J. S.; Marko, I.; Sharpless, K. B. *J. Am. Chem. Soc.* **1989**, *111*, 8069−8076. (b) Dijkstra, G. D. H.; Kellogg, R. M.; Wynberg,

H. *J. Org. Chem.* **1990**, *55*, 6121−6131. (c) Bürgi, T.; Baiker, A. *J. Am. Chem. Soc.* **1998**, *120*, 12920−12926.

(7) Moran, A.; Hamilton, A.; Bo, C.; Melchiorre, P. *J. Am. Chem. Soc.* **2013**, *135*, 9091−9098.

(8) Olsen, R. A.; Borchardt, D.; Mink, L.; Agarwal, A.; Mueller, L. J.; Zaera, F. *J. Am. Chem. Soc.* **2006**, *128*, 15594−15595.

(9) (a) Lam, Y.-h.; Houk, K. N. *J. Am. Chem. Soc.* **2015**, *137*, 2116–2127. (b) Lam, Y.-h.; Houk, K. N. *J. Am. Chem. Soc.* **2014**, *136*, 9556–9559.

(10) Zheng, B.-L.; Liu, Q.-Z.; Guo, C.-S.; Wang, X.-L.; He, L. *Org. Biomol. Chem.* **2007**, *5*, 2913–2915.

(11) Zhou, J.; Wakchaure, V.; Kraft, P.; List, B. *Angew. Chem. Int. Ed.* **2008**, *47*, 7656–7658.

(12) Guo, Q.; Zhao, J. C.-G. *Tetrahedron Lett.* **2012**, *53*, 1768-1771.

(13) Kumar, A.; Chimni, S. S. *Eur. J. Org. Chem.* **2013**, 4780–4786.

(14) McCooey, S. H.; Connon, S. J. *Org. Lett.* **2007**, *9*, 599–602.

(15) Simon, A.; Lam, Y.-h.; Houk, K. N. *J. Am. Chem. Soc.* **2016**, *138*, 503–506.

(16) Sun, X.; Zhu, R.; Gao, J.; Zhang, D.; Feng, D. *J. Phys. Chem. A* **2012**, *116*, 7082–7088.

(17) Frisch, M. J.; Trucks, G. W.; Schlegel, H. B.; Scuseria, G. E.; Robb, M. A.; Cheeseman, J. R.; Scalmani, G.; Barone, V.; Mennucci, B.; Petersson, G. A.; Nakatsuji, H.; Caricato, M.; Li, X.; Hratchian, H. P.; Izmaylov, A. F.; Bloino, J.; Zheng, G.; Sonnenberg, J. L.; Hada, M.; Ehara, M.; Toyota, K.; Fukuda, R.; Hasegawa, J.; Ishida, M.; Nakajima, T.; Honda, Y.; Kitao, O.; Nakai, H.; Vreven, T.; Montgomery, J. A., Jr.; Peralta, J. E.; Ogliaro, F.; Bearpark, M.; Heyd, J. J.; Brothers, E.; Kudin, K. N.; Staroverov, V. N.; Keith, T.; Kobayashi, R.; Normand, J.; Raghavachari, K.; Rendell, A.; Burant, J. C.; Iyengar, S. S.; Tomasi, J.; Cossi, M.; Rega, N.; Millam, J. M.; Klene, M.; Knox, J. E.; Cross, J. B.; Bakken, V.; Adamo, C.; Jaramillo, J.; Gomperts, R.; Stratmann, R.

E.; Yazyev, O.; Austin, A. J.; Cammi, R.; Pomelli, C.; Ochterski, J. W.; Martin, R. L.; Morokuma, K.; Zakrzewski, V. G.; Voth, G. A.; Salvador, P.; Dannenberg, J. J.; Dapprich, S.; Daniels, A. D.; Farkas, O.; Foresman, J. B.; Ortiz, J. V.; Cioslowski, J.; Fox, D. J. Gaussian 09, Rev. D.01; Gaussian, Inc.: Wallingford, CT, 2013.

(18) (a) Vosko, S. H.; Wilk, L.; Nusair, M. *Can. J. Phys.* **1980**, *58*, 1200−1211. (b) Lee, C.; Yang, W.; Parr, R. G. *Phys. Rev. B* **1988**, *37*, 785−789. (c) Becke, A. D. *J. Chem. Phys.* **1993**, *98*, 5648−5652. (d) Stephens, P. J.; Devlin, F. J.; Chabalowski, C. F.; Frisch, M. J. *J. Phys. Chem.* **1994**, *98*, 11623−11627.

(19) Tomasi, J.; Mennucci, B.; Cammi, R. *Chem. Rev.* **2005**, *105*, 2999–3094.

(20) (a) Ribeiro, R. F.; Marenich, A. V.; Cramer, C. J.; Truhlar, D. G. *J. Phys. Chem. B* **2011**, *115*, 14556−14562. (b) Zhao, Y.; Truhlar, D. G. *Phys. Chem. Chem. Phys.* **2008**, *10*, 2813−2818.

(21) Zhao, Y.; Truhlar, D. *Theor. Chem. Acc.* **2008**, *120*, 215–241.

(22) Weigend, F.; Ahlrichs, R. *Phys. Chem. Chem. Phys.* **2005**, *7*, 3297−3305.

(23) Simón, L.; Goodman, J. M. *Org. Biomol. Chem.* **2011**, *9*, 689−700.

(24) Banks, J. L.; Beard, H. S.; Cao, Y.; Cho, A. E.; Damm, W.; Farid, R.; Felts, A. K.; Halgren, T. A.; Mainz, D. T.; Maple, J. R.; Murphy, R.; Philipp, D. M.; Repasky, M. P.; Zhang, L. Y.; Berne, B. J.; Friesner, R. A.; Gallicchio, E.; Levy. R. M. *J. Comput. Chem.* **2005**, *26*, 1752–1780.

(25) Schrödinger Release 2015-3: MacroModel, version 10.9, Schrödinger, LLC, New York, NY, 2015.

(26) *CYLview*, 1.0b; Legault, C. Y. Université de Sherbrooke, 2009 (http://www.cylview.org).

(27) Lam, Y.-h.; Grayson, M. N.; Holland, M. C.; Simon, A.; Houk, K. N. *Acc. Chem. Res.* **2016**, *49*, 750–762.

(28) Wiberg, K. B. *J. Org. Chem.* **2003**, *68*, 9322−9329.

(29) Zimmerman, H. E.; Traxler, M. D. *J. Am. Chem. Soc.* **1957**, *79*, 1920–1923.

(30) Mose, R.; Jensen, M. E.; Preegel, G.; Jørgensen, K. A. *Angew. Chem. Int. Ed.* **2015**, *54*, 13630–13634.

Chapter 3. Origins of Stereoselectivity of Enamine-Iminium Activated Nazarov Cyclizations by Vicinal Diamines

3.1 Abstract

The mechanism and sources of asymmetric induction in Nazarov reactions reported by Tius and coworkers have been determined with quantum chemical calculations. A chiral vicinal diamine forms an enamine-iminium adduct with α-ketoenones, and this undergoes a cationic conrotatory electrocyclization. The chiral diamine imparts stereocontrol in the enamine-iminium complex by forming a six-membered ring that favors one helicity of the electrocyclization transition state.

3.2 Introduction

Nazarov cyclizations are synthetically important reactions that generate cyclopentenones via a cationic 4π electrocyclization of a protonated dienone; up to three new contiguous carbon stereocenters can be generated in this reaction.[1] Nazarov reactions have achieved high levels of stereoselectivity by chiral Lewis acid catalysts,[2] chiral auxiliaries,[3] and recently organocatalysts.[4] Vicinal diamines are successful organocatalysts, because of their bifunctional and tunable behavior.[5] Tius reported that simultaneous enamine and iminium activation by a chiral vicinal diamine for stereoselective Nazarov reactions of α-ketoenones gave 11-63% yield and 90:10 to >99:1 enantiomeric ratios (Scheme 3.1).[6]

Scheme 3.1. Chiral diamine-mediated Nazarov cyclizations.[6]

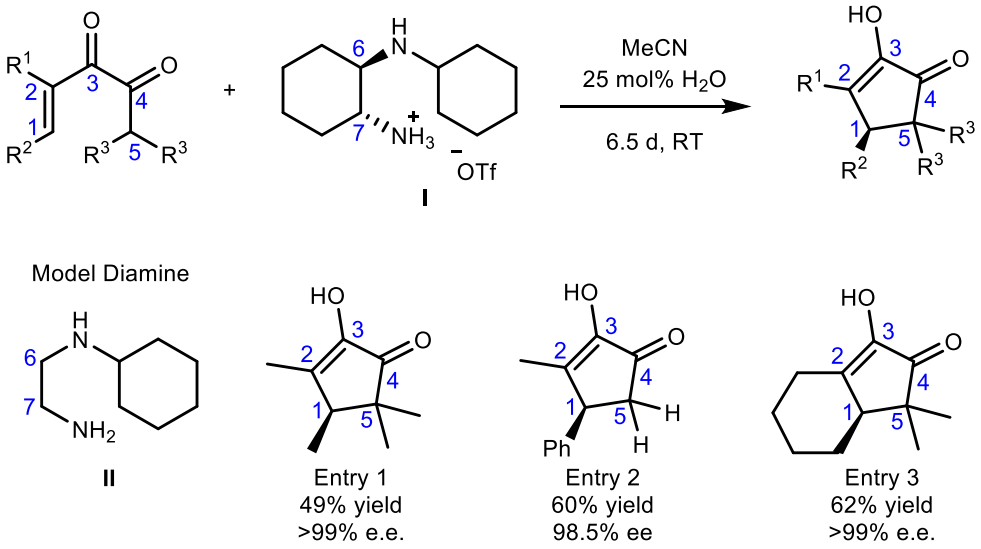

Computational modeling of stereoselectivity has been accomplished for many Nazarov reactions.[7,8] The first stereochemical model for an organocatalyzed Nazarov reaction was recently reported by our group.[8] These computational results explained the induction of asymmetry by a thiourea–primary amine catalyst,[4b] which favored one helical conformation in the Nazarov cyclization transition state. In the thiourea system, the electrocyclization occurred via an enol intermediate with hydrogen-bonding catalysis by the thiourea–primary amine. Enamine formation was unlikely due to the nonpolar conditions of the reaction. By contrast, the mechanism and source of stereoselectivity, as well as the cause of product inhibition in the diamine-mediated Nazarov reaction by Tius has not been studied computationally.[6] Tius proposed a simultaneous enamine-iminium intermediate that undergoes cyclization. We used density functional theory calculations to predict transition states for three pathways: two combinations of enamine-iminium activation at the two carbonyls, and an enamine intermediate that undergoes a Michael addition. The thermodynamics of the intermediates along the reaction coordinate were calculated to determine the source of product inhibition. The factors that control stereoselectivity, as well as a stereochemical model, are proposed.

3.2 Computational Methods

The quantum chemical calculations were performed with Gaussian 09.[9] The geometries were fully optimized at the B3LYP[10]/6-31G(d) level of theory in conjunction with the IEF-PCM implicit solvation model[11] to account for solvation effects of acetonitrile (MeCN), the solvent used experimentally. All optimized geometries were verified by frequency computations as minima (zero imaginary frequencies) or transition structures (a single imaginary frequency). Free energy corrections were calculated using Truhlar's quasiharmonic approximation.[12] Free energies were obtained by performing single-point energy calculations on the optimized geometries with the density functional method M06-2X[13]/def2-TZVPP[14] with the IEF-PCM model (MeCN). We found that the M06-2X/def2-TZVPP–IEF-PCM//B3LYP/6-31G(d)–IEF-PCM level of theory provides accurate geometries and energies, while being relatively efficient in computational times.[15] The lowest-energy transition structures were also optimized at the M06-2X/6-31G(d,p) level of theory in conjunction with single point energies calculated using various dispersion-inclusive DFT methods. These methods qualitatively agree with the experimental results.

3.3 Results and Discussion

The reaction proceeds experimentally by exposing the α-ketoenone substrate to a full equivalent of diamine salt **I** in wet acetonitrile at room temperature for 6-7 days.[6] An unidentified intermediate forms containing the product. Acidic work-up liberates the cyclopentenone from the intermediate with extremely high optical purity and modest yields. The free energy profile of the Nazarov cyclization involving **1** and diamine salt **I** (Entry 1, Scheme 1) was calculated with the M06-2x/def2-TZVPP–IEF-PCM//B3LYP/6-31G(d)–IEF-PCM(MeCN) level of theory (Scheme 3.2). We predict the diamine forms an enamine at C4, which is the electrophilic carbonyl, to form **2a** or **2b**. Either the primary or the secondary amine can react at this position. The primary amine

as the enamine nitrogen in **2a** is more stable by 6.8 kcal/mol because the cyclohexyl group is far from the methyl groups of the α-ketoenone. Enamine **2** can either undergo a Michael addition to form the product directly, or proceed to the enamine-iminium intermediate **3**. The predicted barrier for the Michael addition is 15.8 kcal/mol for **2a** and 24.5 kcal/mol for **2b**. The equilibrium formation of the intermediate **3** should occur readily, although we did not compute barriers for this equilibrium, which involve a number of proton shuffling processes with water. The enamine-iminium intermediate **3** is more stable than reactants by 2.6 kcal/mol and 3.0 kcal/mol for **3a** and **3b**, respectively. Either **3a** or **3b** reacts via the 4π electrocyclization with a barrier of only 10.5 kcal/mol for **3a** and 11.8 kcal/mol for **3b**. We predict that the electrocyclization mechanism is significantly lower in energy than the Michael addition mechanism, and is the dominant pathway. The electrocyclization forms the highly stable enamine-iminium products **5a** and **5b**, which are 26.2 and 23.2 kcal/mol lower in energy than separated **1** and diamine **I**-H^+, respectively. The hydrolysis product, **6**, is 14.8 kcal/mol lower in energy. This agrees with the observed product inhibition when diamine **I** is used in substoichiometric quantities. Intermediate **5** requires acidic work-up to release **6** via hydrolysis.

Scheme 3.2. Proposed mechanism of the Nazarov reaction

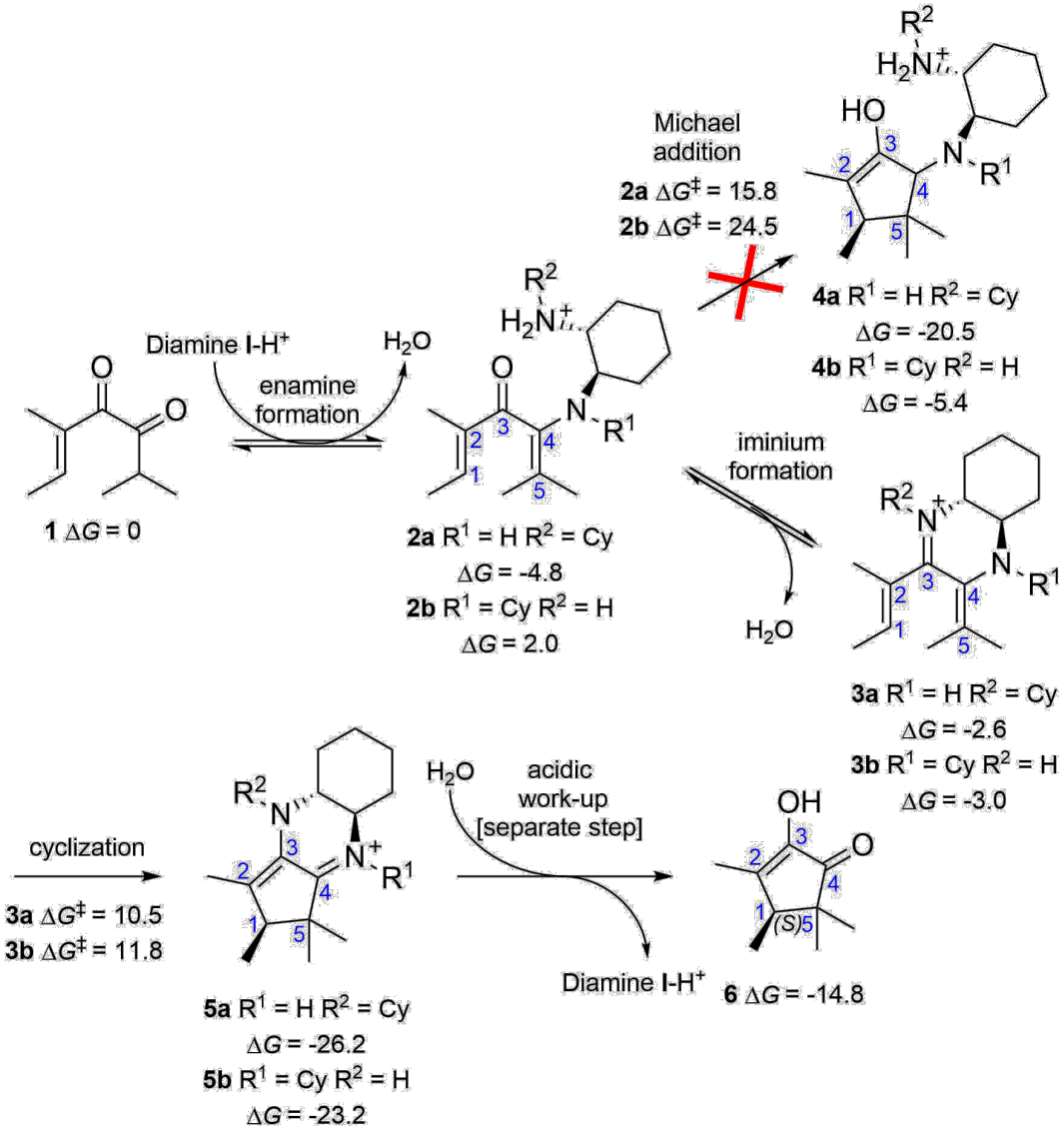

The electrocyclization transition state determines the stereochemistry. Entry 1, as reported by Tius, yields electrocyclization product **6** with (*S*) configuration at the newly formed chiral center with greater than 99% enantiomeric excess. We predict that diamine **I** forms the enamine with substrate **1** to give the enamine-iminium **3a** as the reactive complex; the primary amine first attacks the carbonyl of **1**. The lowest-energy transition structures for the electrocyclization of **3a** are shown in Figure 3.1.

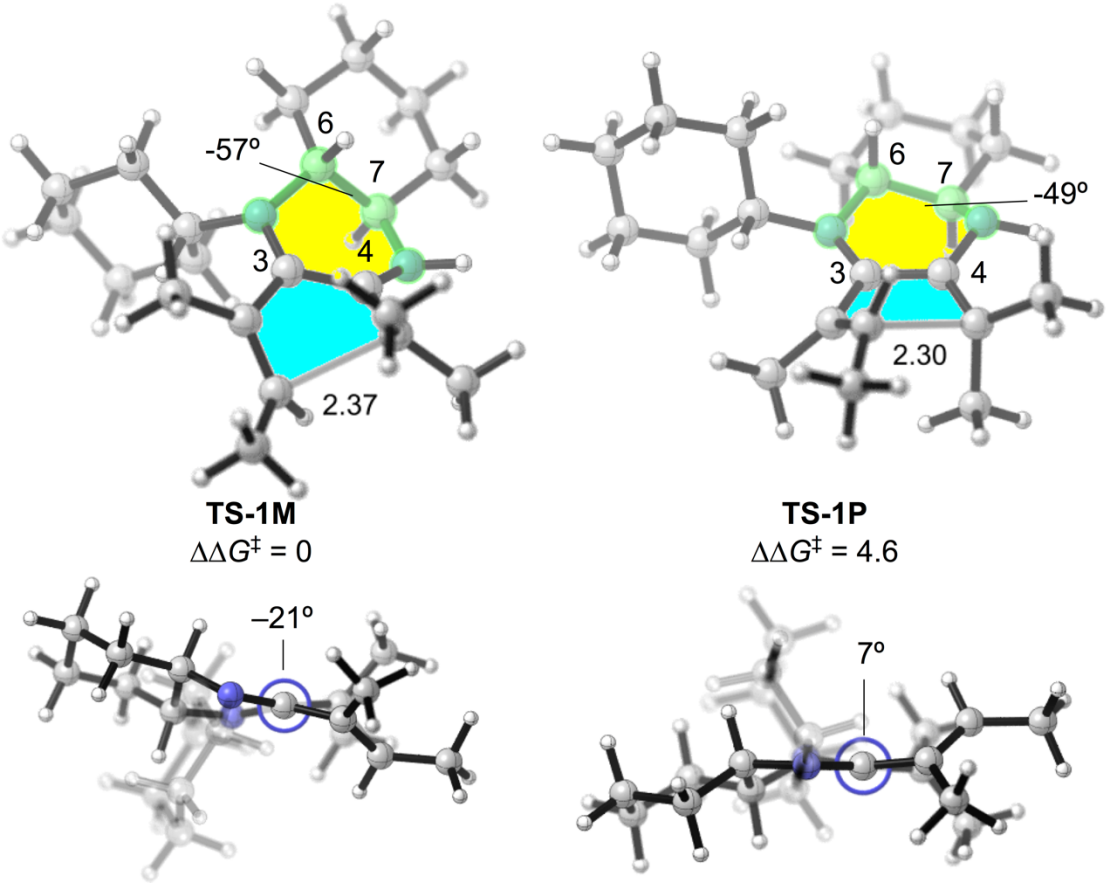

Figure 3.1. Lowest-energy transition structures for the Nazarov cyclization of the enamine-iminium intermediate **3a** derived from substrate **1** and diamine **I** leading to the major (*S*) and minor (*R*) products (M06-2X/def2-TZVPP–IEF-PCM//B3LYP/6-31G(d)–IEF-PCM (MeCN). Newman projections through C3 and C4 are shown below **TS-1M** and **TS-1P**. The cyclohexyl rings are transparent in the Newman projections for clarity. The relative free energies of activation compared with **TS-1M** are reported in kcal/mol.

The transition structure **TS-1M** leads to the major (*S*)-product. **TS-1P** yields the unobserved minor (*R*)-product, and is higher in energy by 4.6 kcal/mol. The **M** and **P** (left- and right-handed helicity, respectively) in the **TS-**series refer to the helical chirality of the forming five-membered ring that is highlighted in blue. The differences from those in Figure 1 are the

disposition and conformations of the cyclohexyl ring and the conformations of the two six-membered rings. The difference in activation barriers between **TS-1M** and **TS-1P** ($\Delta\Delta G^{\ddagger}$ = 4.6 kcal/mol) agrees with the experimentally observed enantioselectivity (>99.5% e.e. (*S*), $\Delta\Delta G^{\ddagger}$ >3.6 kcal/mol).

The stereocontrolling factor that differs between **TS-1M** and **TS-1P** is the helical chirality of the forming five-membered ring. The internal six-membered ring, highlighted in yellow, resembles a half–chair conformation in the transition structures. It is fused to an additional chair six-membered ring and resembles a trans-decalin. The N-C6-C7-N dihedral angle is –57º in **TS-1M** and –49º in **TS-1P**. Also shown in Figure 1 are Newman projections through C3 and C4 of the transition structures. The dihedral angle N-C3-C4-N is –21º in **TS-1M**, and 7º in **TS-1P**. **TS-1P** is more planar than **TS-1M**.

In order to understand what causes the difference in energy between transition structures **TS-1M** and **TS-1P**, a model system was studied with the external six-membered ring removed. This allows free rotation of the diamine, and removes the chirality of C6 and C7. Computations of the enamine-iminium intermediate formed by **1** with achiral diamine **II** (Scheme 3.1) were performed. They reveal what transition state geometry is favored in the absence of chiral auxiliary constraints. The lowest-energy transition structures **TS-2M** and **TS-2aP**, as well as a higher energy transition structure **TS-2bP**, are illustrated in Figure 3.2.

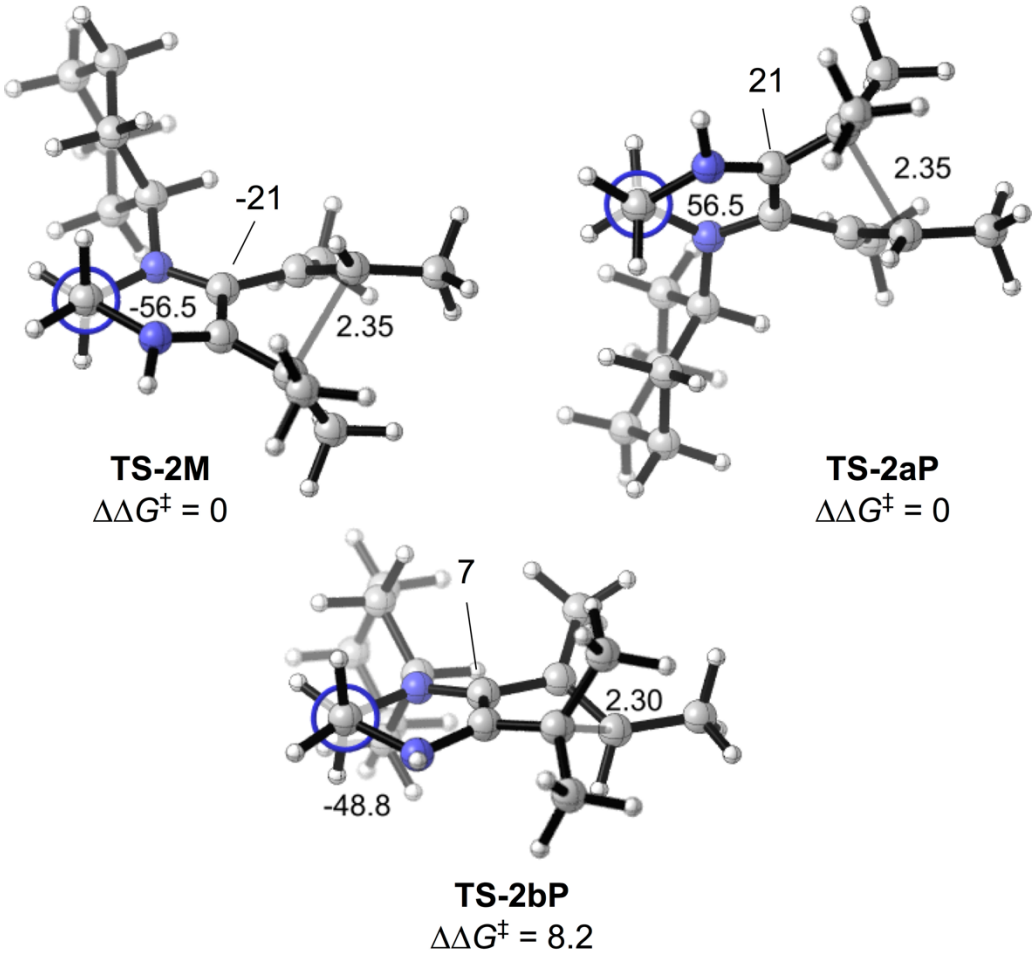

Figure 3.2. **TS-2M** and **TS-2aP** are the (enantiomeric) lowest-energy transition structures for the model Nazarov cyclization of the enamine-iminium intermediate derived from substrate **1** and diamine **II**. (M06-2X/def2-TZVPP–IEF-PCM//B3LYP/6-31G(d)–IEF-PCM (MeCN). **TS-2bP** is a higher energy transition structure similar to the geometry of **TS-1P**. The transition structures are illustrated as Newman projections through C6 and C7. The relative free energies of activation compared with **TS-2M** are reported in kcal/mol.

Figure 3.2 displays the Newman projections across C6 and C7 of the achiral diamine. **TS-2M** and **TS-2aP** are enantiomeric and isoenergetic in this model system. The dihedrals about C3 and C4 are –21° and 21° respectively, due to the clockwise and counter-clockwise twists of the

cyclizing termini. In turn, this causes the N-C6-C7-N dihedral angles of **TS-2M** and **TS-2aP** to be –57º and 57º, respectively, in the half-chairs. **TS-2bP** is a higher-energy transition structure that leads to the minor (*R*)-product with a –49° N-C6-C7-N dihedral angle. **TS-2bP** is 8.2 kcal/mol higher in energy than **TS-2M**. The –49° dihedral forces the cyclization transition state to be nearly planar at C3-C4, resulting in the higher energy **TS-2aP**. The uncatalyzed parent Nazarov transition state has a 31° dihedral at C3-C4, and locking the C6-C7 conformation into the (–)-gauche conformation favors the left-handed **M** helix of the cyclization transition state.

The transition structures (Figure 3.3) were calculated for the Nazarov cyclization of Entry 2 (Scheme 3.1). In this case, the preferred enamine-iminium intermediate has a secondary nitrogen for the enamine and primary nitrogen for the iminium. However, this does not change the conformation of the amines, which are (–)-gauche. This preference is opposite of the enamine-iminium intermediate we calculated from Entry 1. In this case, the enamine is unsubstituted. In Entry 1, the enamine is substituted with methyl groups, which have closed-shell repulsions with the cyclohexyl ring. In each case, the difference in energy between the two arrangements in the electrocyclization transition state is less than 2 kcal/mol. The factors that control the stereoselectivity remain the same. The predicted difference in activation barrier ($\Delta\Delta G^{\ddagger}$) is 3.1 kcal/mol, which agrees closely with the experimentally observed enantioselectivity of 98.5% ($\Delta\Delta G^{\ddagger}$ = 2.9 kcal/mol).

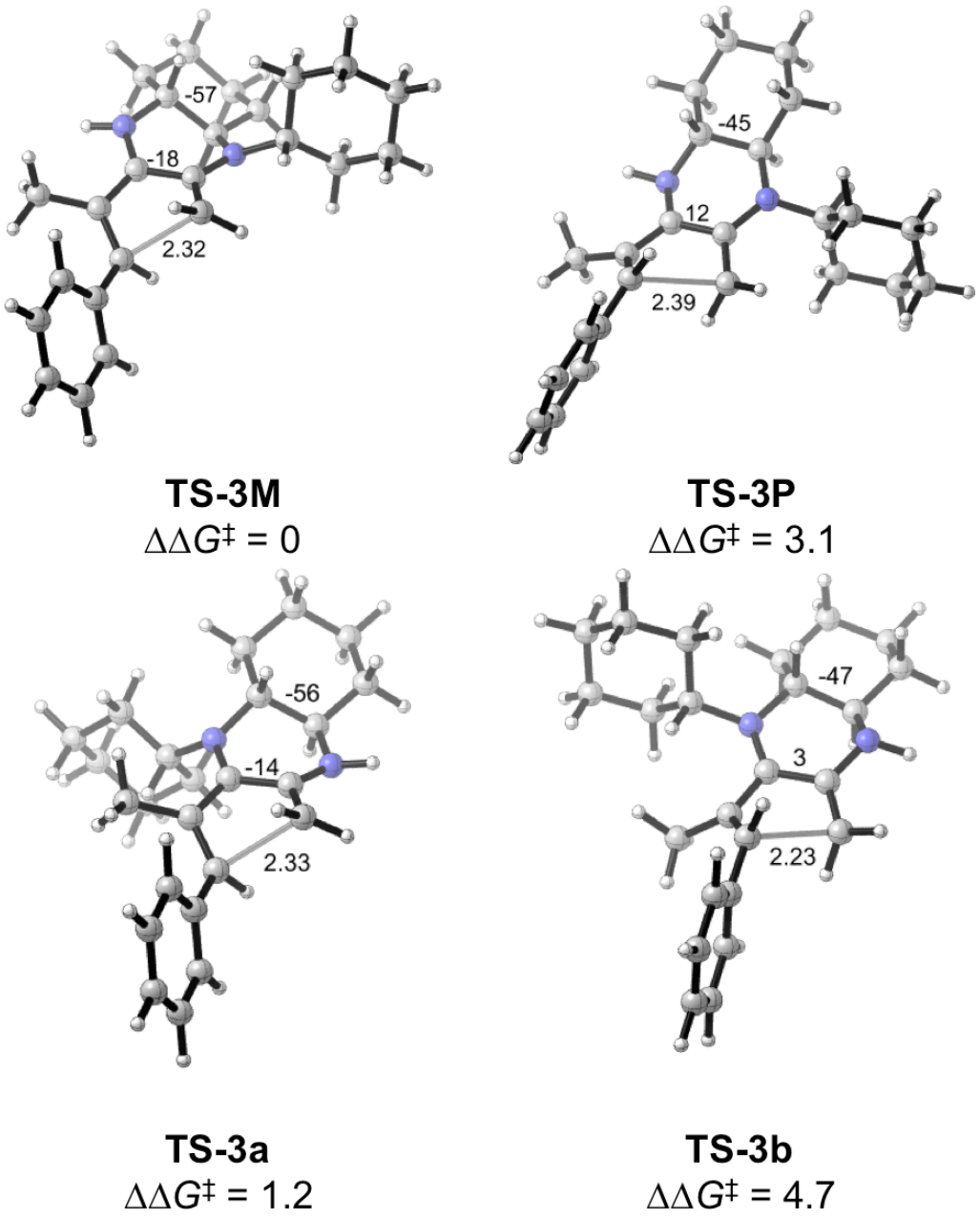

Figure 3.3. Lowest-energy transition structures for the Nazarov cyclization of the enamine-iminium intermediate for Entry 2 in Scheme 3.1 leading to the major (*S*) and minor (*R*) products (M06-2X/def2-TZVPP–IEF-PCM//B3LYP/6-31G(d)–IEF-PCM (MeCN). The relative free energies of activation compared with **TS-3M** are reported in kcal/mol.

3.5 Conclusions

The mechanism, source of product inhibition, and origins of stereoselectivity have been explained with density functional theory calculations. The reaction forms the enamine-iminium intermediate originally predicted by Tius.[6] The product inhibition occurs because the enamine-iminium cyclopentenone-intermediate following cyclization is extremely stable, and requires acidic conditions for hydrolysis to occur.

The diamine is locked into the (–)-gauche conformation, which favors left-handed helicity in the Nazarov transition state. The (–)-gauche diamine yields cyclizations with M helicity, and the (+)-gauche diamine is predicted to yield P helicity (Scheme 3.3). Torquoselectivity is achieved through the newly formed ring of the diamine and α-ketoenone. This six-membered ring favors one helical chirality of the cyclizing moiety of the Nazarov transition state. If product inhibition can be solved, this would provide another organocatalytic method for Nazarov cyclizations with high optical purity.

Scheme 3.3. Summary of Stereoselectivity Model

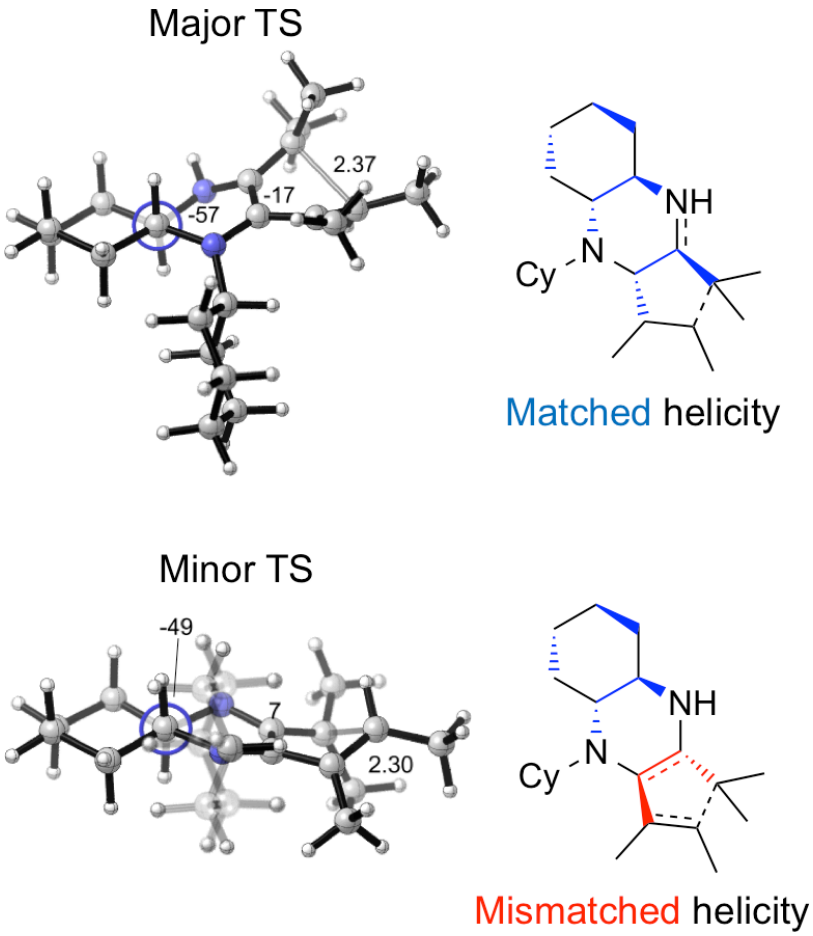

3.6 References

(1) (a) Nazarov, I. N.; Zaretskaya, I. I. *Izv. Akad. Nauk SSSR, Ser. Khim*. **1941**, 211–224.; (b) Nazarov, I. N.; Zaretskaya, I. I. Zh. Obshch. Khim. **1957**, *27*, 693–713.; (c) Nazarov, I. N.; Zaretskaya, I. I.; Sorkina, T. I. Zh. Obshch. Khim. **1960**, *30*, 746–754.; (c) Shimada, N.; Stewart, C.; Tius, M. A. *Tetrahedron* **2011**, *67*, 5851-5870.; (d) Tius, M. A. *Chem. Soc. Rev*. **2014**, *43*, 2979−3002.; (e) West, F. G.; Scadeng, O.; Wu, Y.-K.; Fradette, R. J.; Joy, S. The Nazarov Cyclization. In *Comprehensive Organic Synthesis II*, 2nd ed.; Knochel, P., Molander, G. A., Eds.; Elsevier: The Netherlands, 2014; Vol. 5, pp 827−866.

(2) (a) Liang, G.; Trauner, D. *J. Am. Chem. Soc.* **2004**, *126*, 9544–9545.; (b) Liang, G.; Gradl, S. N.; Trauner, D. *Org. Lett.* **2003**, *5*, 4931–4934.; (c) Nie, J.; Zhu, H.-W.; Cui,H.-F.;Hua,M.-Q.;Ma, J.-A. *Org. Lett.* **2007**, *9*, 3053–3056. .

(3) (a) Pridgen, L. N.; Huang, K.; Shilcrat, S.; Tickner-Eldridge, A.; DeBrosse, C.; Haltiwanger, R. C. *Synlett* **1999**, 1612–1614.; (b) Kerr, D. J.; Metje, C.; Flynn, B. L. *Chem. Commun.* **2003**, *39*,1380–1381.; (c) Banaag, A. R.; Tius, M. A. *J. Org. Chem*. **2008**, *73*, 8133-8141.; (d) Kerr, D. J.; White, J. M.; Flynn, B. L. *J. Org. Chem.* **2010**, *75*, 7073–7084; (e) Wu, Y.-K.; Niu, T.; West, F. G. *Chem. Commun*. **2012**, *48*, 9186−9188.

(4) (a) Rueping, M.; Ieawsuwan, W.; Antonchick, A. P.; Nachtsheim, B. J. *Angew. Chem., Int. Ed.* **2007**, *46*, 2097–2100.; (b) Basak, A. K.; Shimada, N.; Bow, W. F.; Vicic, D. A.; Tius, M. A. *J. Am. Chem. Soc.* **2010**, *132*, 8266–8267.; (c) Huang, Y.-W.; Frontier, A. J. *Tetrahedron Lett*. **2015**, *56*, 3523− 3526.

(5) (a) Notz, W.; Tanaka, F.; Barbas, C. F. III. *Acc. Chem. Res.* **2004**, *37*, 580–591.; b) Trost, B. M.; Brindle, C. S. *Chem Soc Rev.* **2010**, *39*, 1600–1632.

(6) Bow, W. F.; Basak, A. K.; Jolit, A.; Vicic, D. A.; Tius, M. A. *Org. Lett.* **2010**, *12*, 440–443

(7) (a) Smith, D. A.; Ulmer, C. W., II. *Tetrahedron Lett*. **1991**, *32*, 725−728.; (b) Shi, F.-Q.; Li, X.; Xia, Y.; Zhang, L.; Yu, Z.-X. *J. Am. Chem. Soc.* **2007**, *129*, 15503−15512.; (c) Marcus, A. P.; Lee, A. S.; Davis, R. L.; Tantillo, D. J.; Sarpong, R. *Angew. Chem., Int. Ed*. **2008**, *47*, 6379−6383.; (d) Lebœuf, D.; Huang, J.; Gandon, V.; Frontier, A. J. *Angew. Chem., Int. Ed*. **2011**, *50*, 10981−10985.; (e) Kitamura, K.; Shimada, N.; Atesin, A. C.; Ateşin, T. A.; Tius, M. A. *Angew. Chem., Int. Ed*. **2015**, *54*, 6288−6291.; (f) Lovie-Toon, J. P. Tram, C. M.; Flynn, B. L.; Krenske, E. H. *ACS Catal.* **2017**, *7*, 3466−3476.

(8) Asari, A. H.; Lam, Y.-h.; Tius, M. A.; Houk, K. N. *J. Am. Chem. Soc.* **2016**, *137*, 13191−13199.

(9) Frisch, M. J.; Trucks, G. W.; Schlegel, H. B.; Scuseria, G. E.; Robb, M. A.; Cheeseman, J. R.; Scalmani, G.; Barone, V.; Mennucci, B.; Petersson, G. A.; Nakatsuji, H.; Caricato, M.; Li, X.; Hratchian, H. P.; Izmaylov, A. F.; Bloino, J.; Zheng, G.; Sonnenberg, J. L.; Hada, M.; Ehara, M.; Toyota, K.; Fukuda, R.; Hasegawa, J.; Ishida, M.; Nakajima, T.; Honda, Y.; Kitao, O.; Nakai, H.; Vreven, T.; Montgomery, J. A., Jr.; Peralta, J. E.; Ogliaro, F.; Bearpark, M.; Heyd, J. J.; Brothers, E.; Kudin, K. N.; Staroverov, V. N.; Keith, T.; Kobayashi, R.; Normand, J.; Raghavachari, K.; Rendell, A.; Burant, J. C.; Iyengar, S. S.; Tomasi, J.; Cossi, M.; Rega, N.; Millam, J. M.; Klene, M.; Knox, J. E.; Cross, J. B.; Bakken, V.; Adamo, C.; Jaramillo, J.; Gomperts, R.; Stratmann, R. E.; Yazyev, O.; Austin, A. J.; Cammi, R.; Pomelli, C.; Ochterski, J. W.; Martin, R. L.; Morokuma, K.; Zakrzewski, V. G.; Voth, G. A.; Salvador, P.; Dannenberg, J. J.; Dapprich, S.; Daniels, A. D.; Farkas, O.; Foresman, J. B.; Ortiz, J. V.; Cioslowski, J.; Fox, D. J. Gaussian 09, Rev. D.01; Gaussian, Inc.: Wallingford, CT, 2013.

(10) (a) Vosko, S. H.; Wilk, L.; Nusair, M. *Can. J. Phys.* **1980**, *58*, 1200−1211. (b) Lee, C.; Yang, W.; Parr, R. G. *Phys. Rev. B* **1988**, *37*, 785−789. (c) Becke, A. D. *J. Chem. Phys.* **1993**, *98*, 5648−5652. (d) Stephens, P. J.; Devlin, F. J.; Chabalowski, C. F.; Frisch, M. J. *J. Phys. Chem.* **1994**, *98*, 11623−11627.

(11) Tomasi, J.; Mennucci, B.; Cammi, R. *Chem. Rev.* **2005**, *105*, 2999−3094.

(12) (a) Ribeiro, R. F.; Marenich, A. V.; Cramer, C. J.; Truhlar, D. G. *J. Phys. Chem. B* **2011**, *115*, 14556−14562. (b) Zhao, Y.; Truhlar, D. G. *Phys. Chem. Chem. Phys.* **2008**, *10*, 2813−2818.

(13) Zhao, Y.; Truhlar, D. *Theor. Chem. Acc.* **2008**, *120*, 215−241.

(14) Weigend, F.; Ahlrichs, R. *Phys. Chem. Chem. Phys.* **2005**, *7*, 3297−3305.

(15) (a) Simoń, L.;Goodman, J. M. *Org. Biomol. Chem.* **2011**, *9*, 689− 700.; (b) Simon, A.; Lam, Y.-h.; Houk, K. N. *J. Am. Chem. Soc.* **2016**, *138*, 503–506.; (c) Lam, Y.-h.; Grayson, M. N.; Holland, M. C.; Simon, A.; Houk, K. N. *Acc. Chem. Res*. **2016**, *49*, 750−762.

Chapter 4. On the Prevalence of Bridged Macrocyclic Pyrroloindolines Formed in Regiodivergent Alkylations of Tryptophan.

4.1 Abstract

A Friedel-Crafts alkylation is described that efficiently transforms tryptophan-containing peptides into macrocycles of varying ring connectivity. Factors are surveyed that influence the distribution of regioisomers, with a focus on indole C3-alkylations leading to bridged *endo*-pyrroloindolines. We probe the stability and stereochemistry of these pyrroloindolines, study their rearrangement to C2-linked indolic macrocycles, and demonstrate a scalable, stereoselective synthesis of this compound class. Placing the macrocyclization in sequence with further template-initiated annulation leads to extraordinary polycyclic products and further demonstrates the potential for this chemistry to drive novel peptidomimetic lead discovery programs

4.2 Introduction

The pyrroloindoline (hexahydropyrrolo[2,3-*b*]indole) motif is present in numerous tryptophan- and tryptamine-derived natural products. Methods to synthesize this ring system typically parallel biosynthetic schemes, wherein an indolic precursor is activated by substitution at its C3 position by an external electrophile.[1] The incipient indolenium ion is then captured internally by a proximal nitrogen nucleophile (Fig. 4.1A). Bimolecular reactions of tryptophan in this manner often proceed without diastereoselectivity.[2] Where achievable, kinetically diastereoselective transformations typically favor an *exo* disposition of the C2-carboxyl group,[3] the extent of which depends strongly on the nature of the electrophile and on N_α- and carboxyl substitution.[4] Significant advances in enantioselective synthesis of pyrroloindolines have been recently reported,[5] including catalyst systems that can override the inherent substrate bias of

tryptophan.[6] Here, we investigate a different modality wherein the indole activation step is itself a ring-forming reaction (Fig. 4.1B).

Acid-promoted Friedel-Crafts alkylation enables procedurally straightforward, protecting group-free access to densely functionalized macrocycles.[1] The indolic side chain of tryptophan is a powerful partner in this chemistry, because its multident nucleophilicity leads to diverse ring structures.

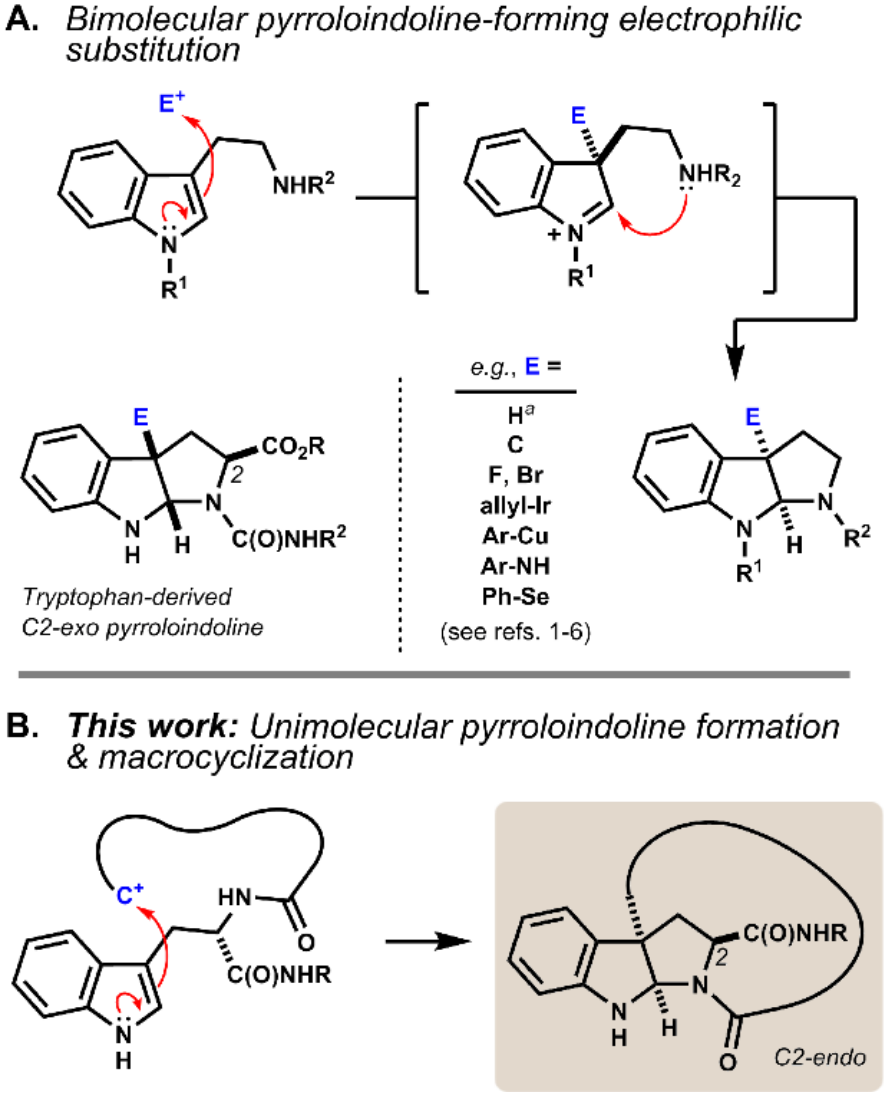

Figure 4.1. A. Pyrroloindoline synthesis and biosynthesis typically proceed via bimolecular electrophilic substitution of indole at C3 and capture of the resulting indolenium ion by a proximal

nitrogen nucleophile. The reaction of tryptophan is often *exo*-selective. [a] Tautomerization of tryptophan by acid equilibrates to the C2-*endo* pyrroloindoline.[4e,10] **B.** Intramolecular *C–C* bond formation at C3 leads to *ansa*-bridged macrocyclic pyrroloindolines.

Competing alkylation of indole C3 is particularly interesting as it embeds an *endo*-pyrroloindoline segment directly into an angularly linked, *ansa*-bridged peptidyl macrocycle.[2] Pyrroloindolines bearing a C3a-linked macrocycle are rare, having been identified in only two classes of natural products, the chaetocochins,[7] and nocardioazines.[8] To our knowledge, synthesis of macrocyclic pyrroloindolines by intramolecular indole C3 substitution is limited to one example in an initial communication by us (*vide infra*).[9] The present study accesses six new products bearing these motifs, as well as thirty-nine additional indolic macrocycle isomers, and characterizes their structures and reactivity in detail.

In a recent study of internal alkylations of tryptophan-containing peptides, we characterized the products derived from acidolysis of composite oligomer **2** (Scheme 4.1).[9] When treated with Brønsted or Lewis acid, degradation of the cinnamyl carbonate in **2** led to competing internal Friedel-Crafts alkylations of proximal tryptophan and tyrosine side chains. The distribution of products was sensitive to acid promoter, solvent and temperature. Major products resulted from substitution at indole C5 of both tryptophan residues (**4**, **5**, Scheme 4.1). The least polar isomer, a minor product of the reaction, was assigned as *ansa*-bridged polycycle **3**, wherein the macrocyclization had formed an angular *C–C* linkage to a newly-formed *endo*-pyrroloindoline. The connectivity and relative stereochemistry of **3** was assigned by correlation NMR spectroscopy (HMBC, NOESY). Within limits of preparative isolation and analysis, a single diastereomer of **3** was identified in the product mixture.

Scheme 4.1. Initial unoptimized discovery (see ref. 9). Oligomer **2**, derived from template **1** and Trp-Trp-Tyr, forms isomeric macrocycles by direct internal Friedel-Crafts alkylation under acidic conditions (e.g. MeSO3H, MeNO2). Major products **4** and **5** result from substitution at indole C5. Bridged endo-pyrroloindoline **3** was obtained as a minor product.

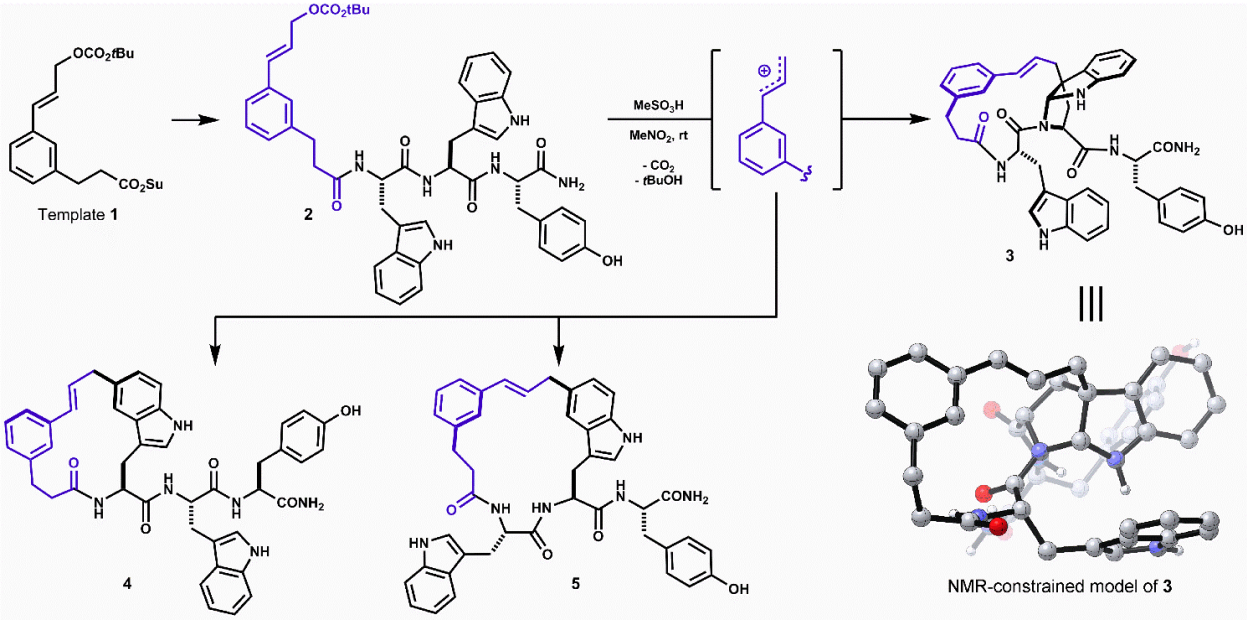

Large ring-forming alkylations of this type were designed to generate topologically varied macrocycles with the intent of studying how ring connectivity and side chain rotational freedom influence pharmacological properties. Macrocyclization alone often improves performance relative to linear counterparts by restricting conformation and masking polar functional groups.[11] Recent efforts have focused on confronting the pharmacokinetic limitations typically faced by macrocycles.[11a,c,12] In particular, stereochemistry and backbone *N*-methylation patterns have been identified in cyclic penta- and hexapeptide lactams,[11d,13] and of related analogs,[11b,14] that enable passive diffusion through membranes and enhance oral bioavailability. More general means to affect these changes would be highly desirable. Along these lines, the increased rigidity and fewer main chain *N–H* bonds in **3** made this compound particularly interesting.

Here, we carefully examine the structure and stability of *ansa*-bridged pyrroloindolines related to **3**. We survey their prevalence in mixtures of isomeric macrocycles generated by internal Friedel-Crafts alkylations of tryptophan. We evaluate structural features and reaction conditions that influence pyrroloindoline formation, and examined the origin of the observed diastereoselectivity. In addition, we have prepared a member of this new structural class using conventional target-based synthesis, thereby confirming structure and establishing a scalable route to the group in general. Lastly, we show that this new unimolecular pyrroloindoline formation also proceeds in more complex settings.

4.3 Computational Methods

All quantum chemical calculations were performed with Gaussian 09. Geometry optimizations and frequencies were calculated with the ωB97x-D (*in vacuo*) density functional with the 6-31G(d,p) basis set. Optimized geometries were verified by frequency calculations as minima (zero imaginary frequencies) or transition structures (a single imaginary frequency). Free energy corrections were determined using unscaled ωB97x-D/6-31G(d,p) vibrational frequencies assuming a standard state of 1 atm and 298.15 K. Errors in the treatment of low modes as harmonic oscillations were mitigated by use of the quasiharmonic approximation proposed by Truhlar and coworkers. Single point energy calculations were performed on optimized geometries with ωB97x-D/6-311+G(d,p). The free energies reported herein were determined by adding zero-point energy and thermal correction determined using ωB97x-D/6-31G(d,p) to electronic energies computed at the ωB97x-D/6-311+G(d,p) level of theory.

Monte Carlo conformational searches were performed on the intermediates using the OPLS-2005 force field in Maestro/Macromodel. Reactive conformations with the distance between the bond-forming atoms shorter than 4.0 Å were used as input geometries for transition structure optimizations.

4.4 Results and Discussion

Analogs of linear oligomer **2** were designed to block major pathways of C5 alkylation in an attempt bias macrocyclization towards electrophilic substitution at indole C3. Substrates **6** and **7** bearing 5-methyl- and 5-fluoro-L-tryptophan, respectively, blocked C5 alkylation and removed competing side chain nucleophiles of Trp1 and Tyr3 (Scheme 4.2). Treating **6** or **7** with either methanesulfonic acid or triflimide in nitromethane‡ led to complete conversion to a mixture of isomeric products within minutes at room temperature. Abundant products were isolated and characterized as *C–C* and *C–N* linked macrocycles **8a-d** and **9a-d**. Bridged pyrroloindolines **8d** and **9d** were assigned as *endo*-22*S*,24*R*,25*R* on the basis of sequential NOE correlations about the newly formed pyrrolidine ring (see Scheme 4.2A). However, these materials were again obtained only as minor products. While using triflimide (4–6 eq.) as the acid promoter increased overall yield and remarkably shortened reaction times (1-2 min), it did not appreciably alter product distribution as had been observed for parent substrate **2**.[9] Blocking C5 with an electron-donating substituent (i.e. $–CH_3$) had not suppressed reaction at the benzenoid ring or enhanced pyrroloindoline formation as intended, but an electron-withdrawing substituent (i.e. –F) was somewhat more effective in this regard. Both, however, shifted reactivity at the benzenoid ring from C5 to C4. Nonetheless, the formation of 15-membered macrocyclic *endo*-pyrroloindoline products in substrates bearing P2 tryptophan residues appeared to be generally diastereoselective.

Scheme 4.2. Pyrroloindoline-forming macrocyclizations of 5-substituted tryptophans. A, B. Acidolysis of oligomers **6**, **7** or **10** promotes internal substitution at indole N1, C2, C3, C4 or C6 (blue). The connectivity and relative stereochemistry of bridged pyrroloindolines **8d**, **9d** and **11e** was assigned by ^{1}H-^{13}C-HMBC and ^{1}H-^{1}H-NOESY (red arrows), respectively.

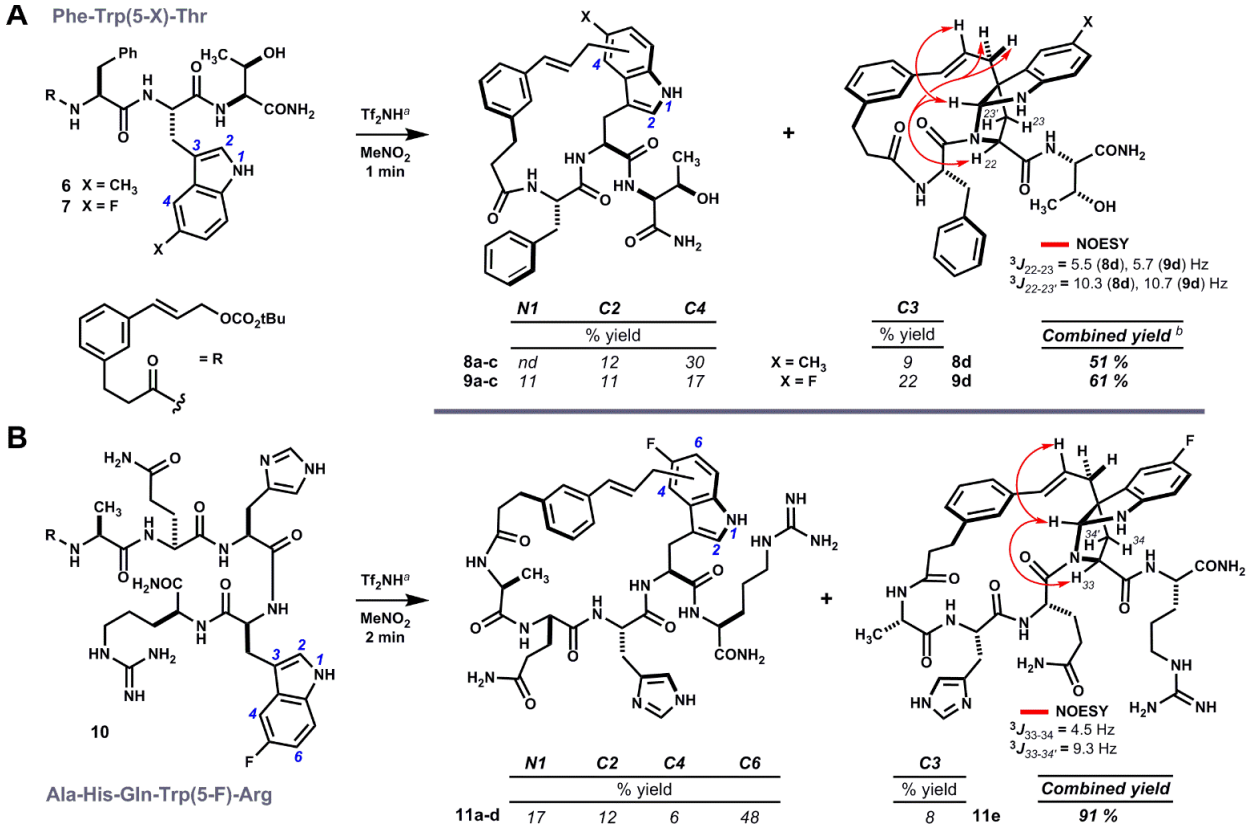

[a]Tf_2NH 4-6 eq., $MeNO_2$, 5 mM in substrate, rt. [b]Additional products were detected by HPLC; combined yield underestimates actual yield due to characterization of only major products, shown. *nd* = not determined.

Accordingly, we next surveyed substrates varying in the position of tryptophan and in composition of the surrounding peptide. Substrate **10**, bearing 5-fluoro-L-tryptophan at P4, underwent rapid cyclization unimpeded by the basic guanidine or imidazole side chains of arginine

and histidine, respectively (Scheme 4.2B). Triflimide improved reaction yield considerably in this case, and afforded 21-membered ring bridged *endo*-pyrroloindoline **11e** and isomeric macrocycles **11a–d** in 91% combined yield. Notably, the major product resulted from alkylation at indole C6 (i.e. **11d**), rather than C4 as had been observed in reactions of **6** and **7**. Taken together, these data suggest that regioselectivity tracks the inherent indole reactivity, which can be influenced by substitution of the indole nucleus. However, unlike bimolecular variants, the course of these cyclizations also depends on the geometry attainable by a given substrate and therefore the sequence of the embedded peptide. Thus, blocking the highly reactive C5 position of native tryptophan offers a useful means to finely tune the topology of macrocyclic products by shifting ring connectivity to adjacent positions C4 and C6.

To further test the effect of chain length on reaction regioselectivity and pyrroloindoline formation, we examined cyclizations of isomeric substrates **12–15** bearing 5-bromo-L-tryptophan in positions 1 through 4 (Scheme 4.3). Acidolysis of P1 variant **12** resulted primarily in cyclization at indole C6 (i.e. **16a**) and, to a lesser extent, at N1 and C7. No pyrroloindoline was observed in this case, presumably due to unfavorable strain associated with formation of a 13-memered ring by C3 substitution. As expected, P2 isomeric sequence **13** led to the pyrroloindoline **17e** bearing the core 15-membered ring shared by products **3**, **8d** and **9d**. Surprisingly, however, **17e** was

Scheme 4.3. Cyclization scan of oligomers having Trp(5-Br) shifted along the chain (P1→P4). Pyrroloindoline formation is sensitive to sequence composition and ring size, but favored by 5-bromotryptophan. No pyrroloindoline is formed from P1 isomer **12**, whereas P2 and P3 variants **13** and **14** lead to pyrroloindolines **17e** and **18c**, respectively, as major products. Internal C3

alkylation of the P4 variant leads instead to cyclization of the terminal carboxamide to *exo*-pyridoindoline **19b**.

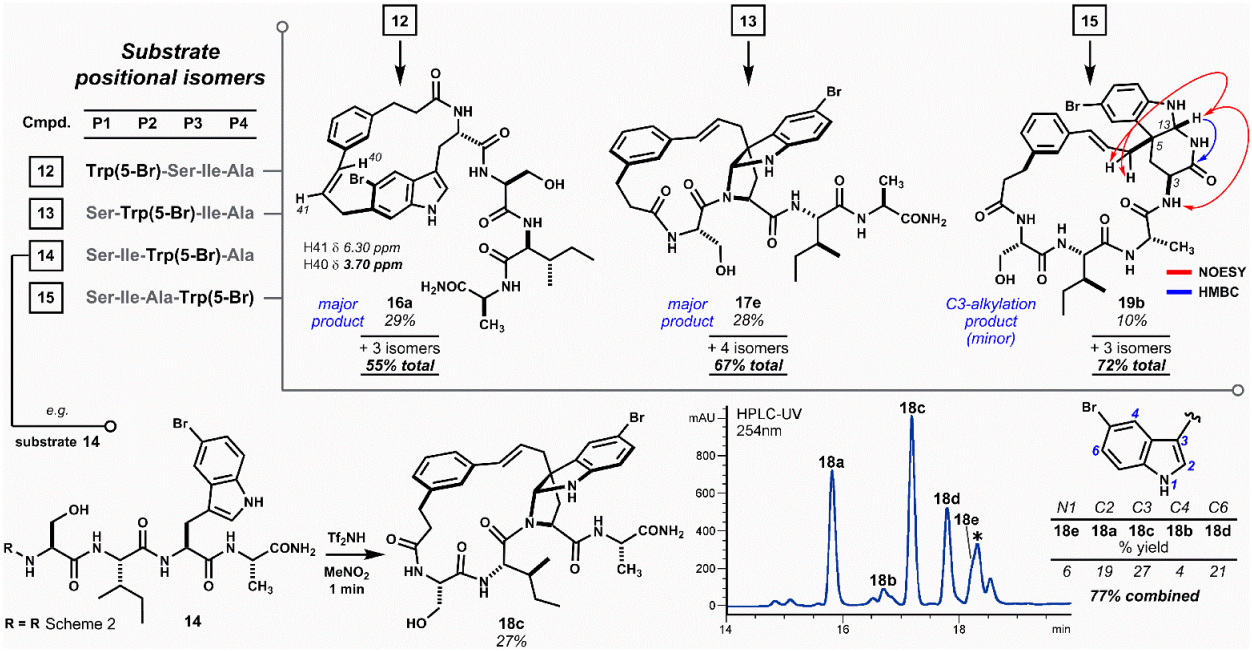

formed as the major product in 28% yield. It is not yet known whether this improved yield reflects the inherent reactivity of 5-bromoindole. Regioselectivity for C3 alkylation may also benefit from the smaller steric bulk of the serine side chain in **17e** relative to tryptophan in **3** or to phenylalanine in **8d** and **9d**. Intriguingly, acidolysis of isomeric P3 sequence (**14**) also led to C3 alkylation and cyclization giving *endo*-pyrroloindoline **18c** as the major product in 27% yield. The final P4 variant (**15**), however, did not give an analogous pyrroloindoline but instead afforded *exo*-pyridoindoline **19b** by cyclization of the terminal carboxamide subsequent to C3 cinnamylation. Interestingly, the observed *exo* configuration had resulted from initial *pro-R* substitution, a facial bias identical to that observed for the pyrroloindoline outcomes. In another case, however, a substrate bearing 5-bromotryptophan at P4 yielded both *exo*- and *endo*-pyridoindolines (1.8:1 dr). This suggests that the mechanism for diastereoselection leading to *exo*-**19b** is distinct from pyrroloindoline outcomes (*vide infra*). The substrates surveyed here indicate that regioselectivity

in tryptophan-based macrocyclizations is sensitive to oligomer composition, but bridged *endo*-pyrroloindoline and pyridoindoline products appear to form frequently.

While facial bias offers one potential rationale for the observed diastereoselectivity, we remained cognizant of the possibility for rearrangement of C3-linked macrocycles to other isomers under the reaction conditions.[15] Indeed, bimolecular electrophilic substitution at indole C2 often proceeds by initial C3 addition and 1,2-migration.[16] When isolated pyrroloindoline **18c** was re-subjected to the reaction conditions with Tf_2NH (4 eq.) in $MeNO_2$, partial 1,2-rearrangement to the corresponding C2-linked isomer **18a** was observed over a period of several hours. Consistent with previous observations, this slow equilibration of pyrroloindoline products suggests that large ring-forming cinnamylations proceed under kinetic control.[17] Under forcing conditions with 20 vol% TFA in $MeNO_2$, complete rearrangement of **18c** to **18a** was observed within 3 hours ($t_{1/2}$ = 44 min, Fig. 2). Trace formation of other macrocycle isomers indicates that 1,2-rearrangement competes with reversion to a cinnamyl carbocation. The formation of C2-linked **18a** in brief acidolysis reactions of linear substrate **14** may result from direct substitution at C2.[16b,18] Alternatively, **18a** may result from initially unselective C3 alkylation and rapid 1,2-rearrangement of one diastereomer, that corresponding to the *exo*-pyrroloindoline (i.e. *pro-S* addition at C3).[19] Though a discrete *exo* diastereomer has not been observed, the latter possibility is supported by the near equal ratio of C3- to C2-linked products in the aforementioned seven examples. In two additional acid-promoted cyclizations, however, indole C2-linked macrocycles were obtained in the absence of pyrroloindoline products. Yet, in the case of **2→3** (Scheme 4.1), the product of C3 alkylation was obtained without concurrent C2 alkylation.[9]

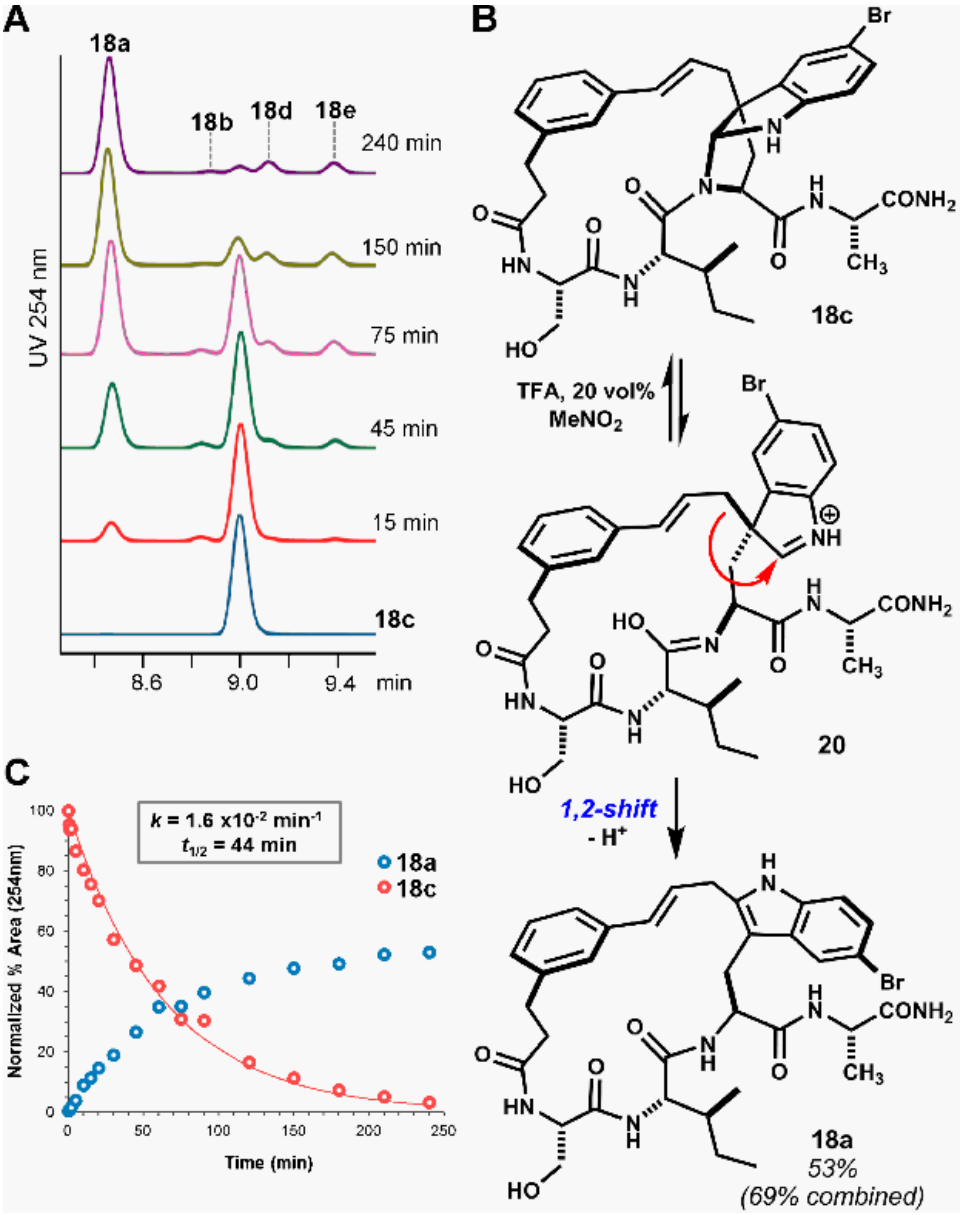

Fig. 4.2. Rearrangement of pyrroloindoline 18c. A. Time-course HPLC-UV (254 nm) analysis showing rearrangement of isolated **18c** to isomer **18a** in TFA/$MeNO_2$ solution. Trace regioisomers (labelled) also form in this reaction. **B.** Proposed mechanism for 1,2-rearrangement.[18] **C.** Kinetic plot showing pseudo-first-order reaction of **18c** and accumulation of major product **18a**

To further probe the origin of diastereoselectivity in pyrroloindoline-forming macrocyclizations, we examined the 1,2-rearrangement of model *exo*- and *endo*-pyrroloindolines

21a and **21b** (Fig. 4.3A). Under pseudo-first-order conditions using 20 vol% TFA in $MeNO_2$, rearrangement of *exo*-**21b** to indole C2-linked product **22** proceeded at a rate nearly 30-times faster than that of *endo*-**21a** (Fig. 4.3B). An Eyring plot was constructed from rate data at five different temperatures, which revealed activation energies $\Delta G^{\ddagger}_{exo}$ = 20.5 kcal•mol^{-1} and $\Delta G^{\ddagger}_{endo}$ = 22.4 kcal•mol^{-1} for these processes at 22 °C. We next explored this reaction computationally in order to better understand this kinetic difference. Using density functional theory (DFT), *endo*-pyrroloindoline **21a** (R = Me) was calculated to be 1.0 kcal•mol^{-1} more stable than the corresponding *exo* diastereomer **21b**. This finding is consistent with reported thermodynamic preferences of related pyrroloindolines.[3b,4e,19] Preference for the *endo*-pyrroloindoline in this case is primarily due to 1,3-allylic strain resulting from the tertiary amide. DFT was also used to calculate the free energy profiles for the reactions of **21a** and **21b** (Fig. 4.4-4.5). In each case, 1,2-shift of the cinnamyl group from an intermediate indolium ion (*i.e.* **23a**,**b**) was found to be rate limiting. Diastereomeric transition structures **TS-2a** and **TS-2b** bear nearly enantiomeric geometries with respect to the indole ring and migrating cinnamyl group, but differ in orientation of the *S*-alanyl moiety relative to the indolic nucleus. This leads to greater stabilization of transition state **TS-2b** relative to **TS-2a** ($\Delta\Delta G^{\ddagger}_{calc}$ = 2.9 kcal•mol^{-1}), in agreement with the experimentally observed difference in activation energy ($\Delta\Delta G^{\ddagger}_{exp}$ = 1.9 kcal•mol^{-1}). Thus, the more rapid rearrangement of *exo*-pyrroloindoline **21b** results both from the higher energy of **21b** relative to **21a**, and from the lower kinetic barrier for the reaction **21b**→**22** relative to **21a**→**22**. These findings suggest that the diastereoselectivity observed in pyrroloindoline-forming macrocyclizations arises, at least in part, from the facility of *exo*-pyrroloindolines to rearrange to the corresponding indole C2-linked isomers.

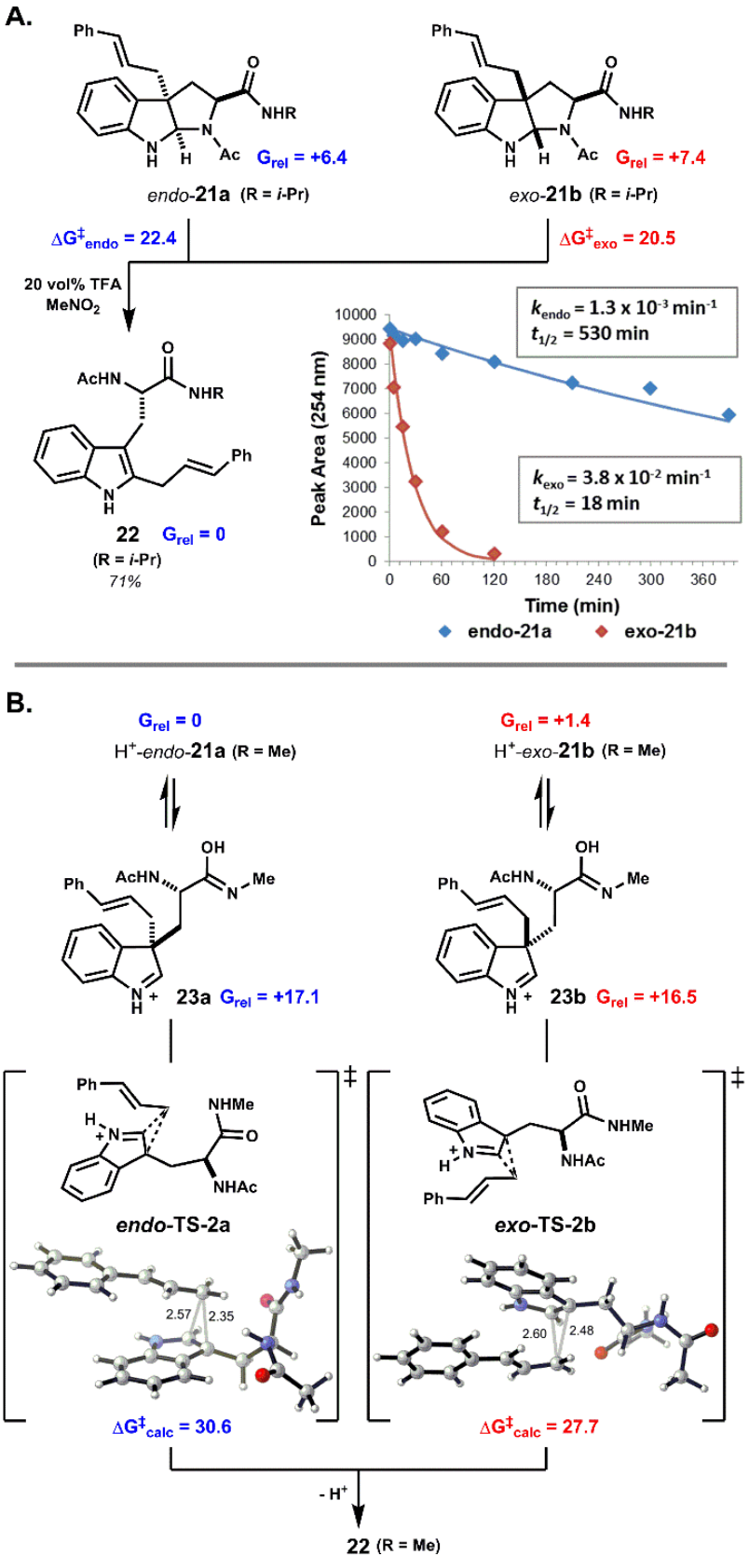
A.
Ph
O
NHR
N
H
H
Ac
G_{rel} = +6.4
endo-21a (R = i-Pr)
G_{rel} = +7.4
exo-21b (R = i-Pr)
$\Delta G^{\ddagger}_{endo}$ = 22.4
$\Delta G^{\ddagger}_{exo}$ = 20.5
20 vol% TFA
$MeNO_2$
AcHN
22 G_{rel} = 0
(R = i-Pr)
71%
k_{endo} = 1.3 x 10^{-3} min^{-1}
$t_{1/2}$ = 530 min
k_{exo} = 3.8 x 10^{-2} min^{-1}
$t_{1/2}$ = 18 min
Peak Area (254 nm)
Time (min)
endo-21a
exo-21b
B.
G_{rel} = 0
H^+-endo-21a (R = Me)
G_{rel} = +1.4
H^+-exo-21b (R = Me)
OH
Me
23a G_{rel} = +17.1
23b G_{rel} = +16.5
NHMe
NHAc
endo-TS-2a
exo-TS-2b
2.57
2.35
2.60
2.48
$\Delta G^{\ddagger}_{calc}$ = 30.6
$\Delta G^{\ddagger}_{calc}$ = 27.7
- H^+
22 (R = Me)

Fig. 4.3. *exo*-Pyrroloindolines rearrange more readily than *endo*-pyrroloindolines. A. Under acidic conditions, C3a-cinnamyl pyrroloindolines undergo ring-chain tautomerism and 1,2-rearrangement to indole C2-linked isomers. The kinetic plot for rearrangement of **21a** and **21b** in 20 vol% TFA at 5 °C shows the faster rate of reaction for *exo*-pyrroloindoline **21b**. From Eyring analysis, the free energy of activation was 1.9 kcal•mol^{-1} higher for *exo*-**21b** relative to *endo*-**21a**. **B.** DFT calculations indicate that *endo*-pyrroloindoline **21a** is the thermodynamically more stable than *exo*-**21b**. Cinnamyl 1,2-shift is rate limiting in both cases, and the reaction of *exo*-**21b** proceeds via a lower kinetic barrier. Note: All free energies are in kcal•mol^{-1}.

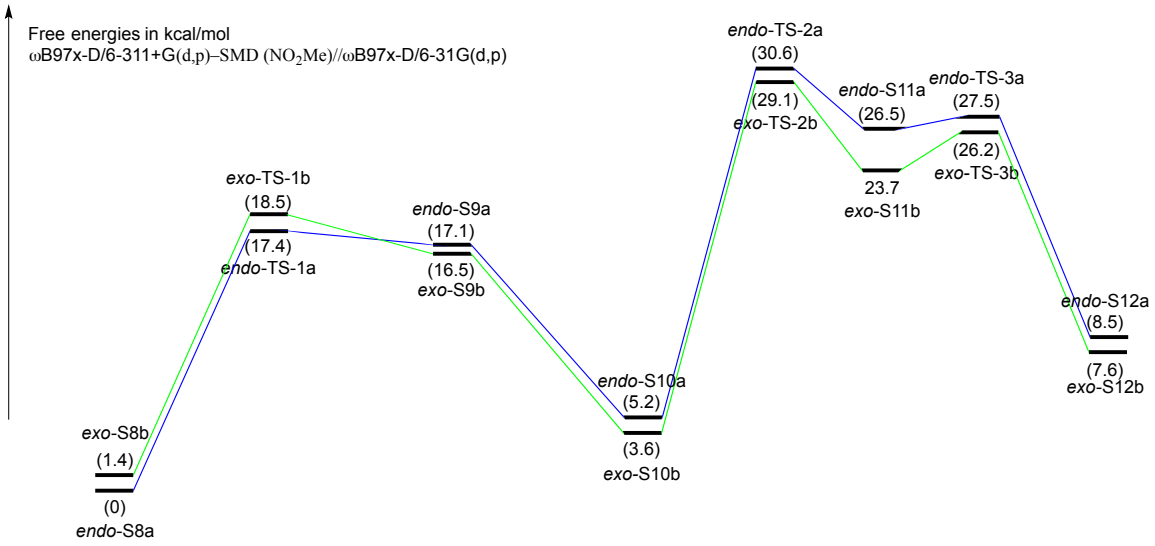

Fig. 4.4. Free energy profile for the 1,2-rearrangement of *exo*- and *endo*-pyrroloindolines shown in Figure 3 (where R=Me). (ωB97x-D/6-311+G(d,p)–SMD (nitromethane) // ωB97x-D/6-31G(d,p)) The relative free energies are compared with *endo*-**S8a** and are reported in kcal/mol. The blue pathway represents the *endo* reaction profile, and the green pathway represents the *exo* reaction profile.

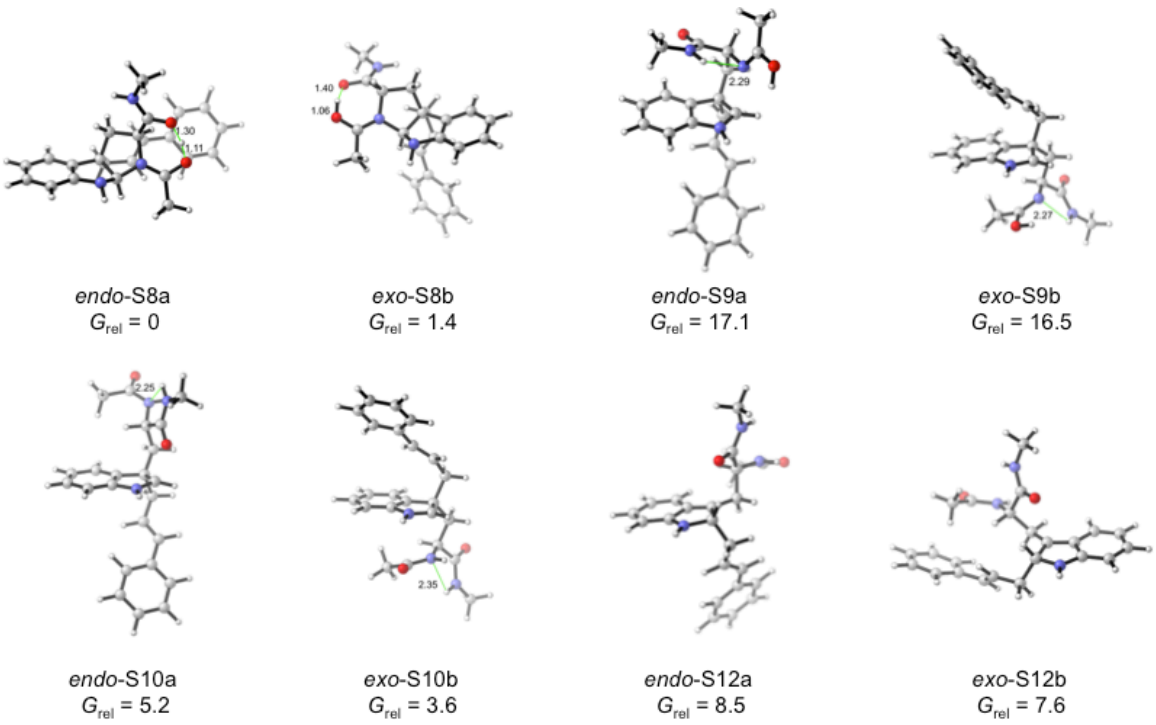

Fig. 4.5. Lowest-energy intermediates S8-S10, and S12 for the free energy profile in Fig. 4.4. (ωB97x-D/6-311+G(d,p)–SMD (nitromethane) // ωB97x-D/6-31G(d,p)). The relative free energies are compared with *endo*-**S8a** and are reported in kcal/mol.

The Friedel-Crafts macrocyclizations under study generate collections of macrocycle isomers that would be time- consuming to prepare individually. Exploring ring diversity in this manner is our approach to refining biological activity. Importantly, isomers of particular interest may also be synthesized by convergent means. This has been demonstrated by a selective synthesis of fluorinated pyrroloindoline **9d** (Scheme 4.4). Starting from 5-fluoro-L-tryptophan methyl ester and cinnamyl alcohol **24**, a derivative of template **1**, intermolecular Pd^0-catalyzed allylation promoted by Et_3B led to selective C3 cinnamylation and afforded *endo*-pyrroloindoline **26** in 80% yield as a single diastereomer.[20] The remaining two amino acids were then introduced by first amidation of **26** with *N*-Boc-L-phenylalanine, then saponification of the methyl ester and coupling

of the resulting carboxylate to L-threonine amide to give **27**. Deprotection of the *N*-Boc and *tert*-butyl groups with TFA:DCM (1:1) at 0 °C minimized C3–C2 rearrangement, and lactamization of this *seco* acid with HBTU completed bridged pyrroloindoline **9d**. This material was spectroscopically identical to that obtained by the acidolysis of **7** (see annotations Scheme 4.4). Convergent routes such as this are useful for preparing larger quantities of material, whereas Friedel-Crafts cyclization forms pyrroloindolines and additional macrocycle isomers rapidly and directly.

Scheme 4.4. Selective synthesis of pyrroloindoline 9d. Bimolecular Pd^0-catalyzed C3-selective cinnamylation of 5-fluoro-L-tryptophan promoted by Et_3B sets up to form the bridging 15-membered ring by lactamization. ^1H NMR spectra (500 MHz, DMSO-d_6) of **9d** obtained by this route match that of material isolated from the acid-promoted cyclization. Key resonance annotations in blue. * Denotes contaminant signals.

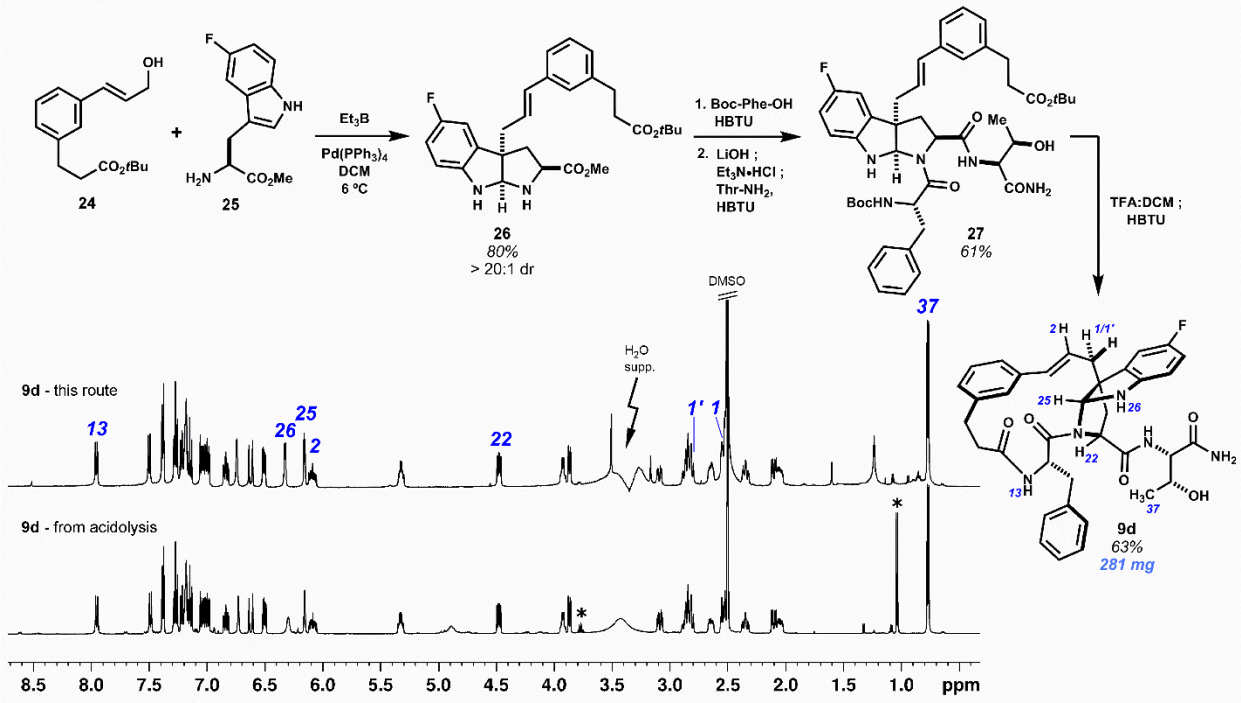

Internal alkylations using simple template **1** form large rings with broad functional group tolerance and procedural ease. Creative opportunity exists to combine macrocyclizations of this type with additional template reactivity to further stabilize the peptide domain by rigidifying product structures. For example, variant **28** additionally bears a latent aldehyde designed to initiate *N*-acyliminium ion cyclizations (e.g. **29**, Scheme 4.5), the results of which depend on the nature of the P1 side chain.[21] Extensive investigations of this reaction by the Meldal laboratory demonstrate flexibility and generally high diastereoselectivity.[22] In direct comparison to template **1**, we examined the performance of trifunctional **28** using prototypical tryptophan-containing oligomer Trp-Trp-Tyr.[9,22] Acylation of the N-terminus and treatment with aqueous acetic acid promoted diastereoselective Pictet-Spengler cyclization of Trp1 to give intermediate fused tryptoline **30** in 88% yield. When treated with Tf_2NH (3 eq.) in $MeNO_2$, this material was cleanly transformed to isomeric products **31a**–**f** resulting exclusively from alkylation of Trp2 with the major product arising from substitution at indole C5, as expected. Alkylation *ortho* to the phenol of tyrosine, anticipated from previous studies of analogous substrate **2**, was not oserved.[23] Alkylation of the P1 tryptoline moiety was also not observed, presumably due to strain associated with annulation of this rigid ring system. These results anticipate that templates **1** and **28** will exhibit subtly different regioselectivity in large ring-forming reactions. That said, we were pleased to find polycyclic pyrroloindoline **31e**, despite these differences. This product possesses nine fused rings and a mere five rotatable bonds, whereas Trp-Trp-Tyr itself possesses eleven such bonds. Additionally, **31e** bears less polar surface area (161 $Å^2$) than the starting peptide (181 $Å^2$), with only non-polar surface area introduced by the template. These alterations tend towards molecular properties advocated for the design of orally bioavailable drugs.[11c,24] Though **31e** has not yet been evaluated for biological activity, this outcome exemplifies marked structural alterations that can

be quickly achieved. The pharmacological properties of such structures will almost assuredly improve relative to the starting peptide.

Scheme 4.5. Combining trifunctional template 28 with Trp-Trp-Tyr rapidly forms complex polycycles. Initial amidation and Pictet-Spengler cyclization of Trp1 (i.e. **29**) followed by acid-promoted cyclization leads to macrocycle isomers **31a**–**f** substituting the periphery of Trp2. Polycycle **31e**, results from indole C3 alkylation and cyclization to the *endo*-pyrroloindoline, analogously to related products obtained from template 1. *Note: Peak **31d** contained two product isomers that were not identified.

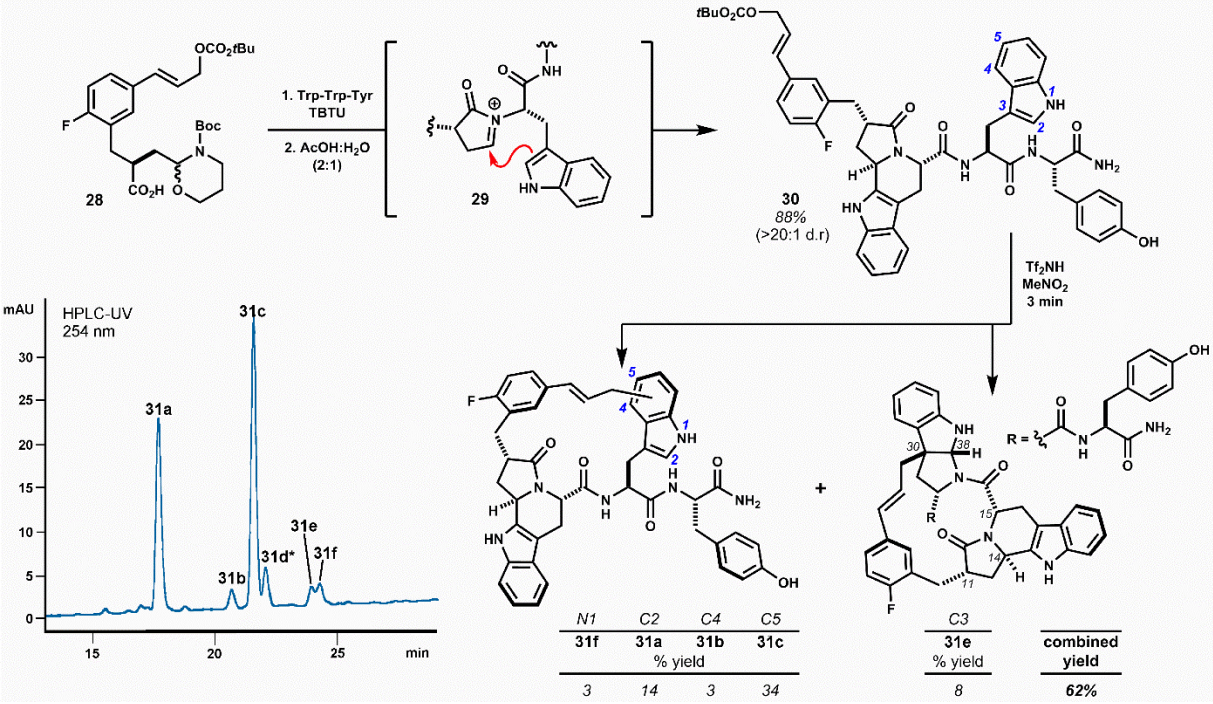

4.5 Conclusions

Regiodivergent internal alkylations of tryptophan create macrocycles of varying connectivity in two or three steps from linear peptides. Macrocyclic products bearing embedded

endo-pyrroloindolines are a valuable facet of this chemistry. The simplicity of the acidolysis method permits even minor constituents to be isolated, screened for function, and characterized with relative ease. In this regard, the general presence of pyrroloindolines and predictability of regiochemical outcomes are more important than the abundance of any one product. For structures of particular interest, convergent target-oriented synthesis is always an option, as we demonstrate. These more step-intensive routes offer scalable access when refined medicinal chemistry is appropriate. Finally, methods combining large ring-formations with additional template-initiated annulation, such as in reactions of **28**, hold unique potential to quickly build peptidomimetics of unprecedented structural complexity.

4.6 References

(1) Ruiz-Sanchis, P.; Savina, S. A.; Albericio, F.; Álvarez, M. *Chem. Eur. J.* **2011**, *17*, 1388.

(2) (a) Spande, T. F.; Wilchek, M.; Witkop, B. *J. Am. Chem. Soc.* **1968**, *90*, 3256. (b) Mcfarland, B. G.; Inoue, Y.; Nakanishi, K. *Tetrahedron Lett.* **1969**, *10*, 857. (c) Loudon, G. M.; Portsmouth, D.; Lukton , A.; Koshland, D. E. J. *J. Am. Chem. Soc.* **1969**, *91*, 2792. (d) Baran, P. S.; Guerrero, C. A.; Corey, E. J. *Org. Lett.* **2003**, *5*, 1999.

(3) (a) López, C. S.; Pérez-Balado, C.; Rodríguez-Graña, P.; De Lera, Á. R. *Org. Lett.* **2008**, *10*, 77. (b) Crich, D.; Huang, X. *J. Org. Chem.* **1999**, *64*, 7218.

(4) (a) Crich, D.; Banerjee, A. *Acc. Chem. Res.* **2007**, *40*, 151. (b) Newhouse, T.; Lewis, C. A.; Eastman, K. J.; Baran, P. S. *J. Am. Chem. Soc.* **2010**, *132*, 7119. (c) Depew, K. M.; Marsden, S. P.; Zatorska, D.; Zatorski, A.; Bornmann, W. G.; Danishefsky, S. J. *J. Am. Chem. Soc.* **1999**, *121*, 11953. (d) Nakagawa, M.; Watanabe, H.; Kodato, S.; Okajima, H.; Hino, T.; Flippen, J. L.; Witkop,

B. *Proc. Natl. Acad. Sci. U. S. A.* **1977**, *74*, 4730. (e) Taniguchi, M.; Hino, T. *Tetrahedron* **1981**, *37*, 1487.

(5) (a) Nelson, H. M.; Reisberg, S. H.; Shunatona, H. P.; Patel, J. S.; Toste, F. D. *Angew. Chem., Int. Ed.* **2014**, *53*, 5600. (b) Repka, L. M.; Ni, J.; Reisman, S. E. *J. Am. Chem. Soc.* **2010**, *132*, 14418. (c) Shao, W.; Li, H.; Liu, C.; Liu, C.-J.; You, S.-L. *Angew. Chem., Int. Ed.* **2015**, *54*, 7684. (d) Lozano, O.; Blessley, G.; Martinez Del Campo, T.; Thompson, A. L.; Giuffredi, G. T.; Bettati, M.; Walker, M.; Borman, R.; Gouverneur, V. *Angew. Chem., Int. Ed.* **2011**, *50*, 8105. (e) Repka, L. M.; Reisman, S. E. *J. Org. Chem.* **2013**, *78*, 12314. (f) Austin, J. F.; Kim, S.-G.; Sinz, C. J.; Xiao, W.-J.; MacMillan, D. W. C.; *Proc. Natl. Acad. Sci. U. S. A.* **2004**, *101*, 5482. (g) Zhu, S.; MacMillan, D. W. C. *J. Am. Chem. Soc.* **2012**, *134*, 10815. (h) Wolstenhulme, J. R.; Cavell, A.; Gredičak, M.; Driver, R. W.; Smith, M. D. *Chem. Commun.* **2014**, *50*, 13585. (i) Huang, Y.; Zheng, C.; Pan, L.; Jin, Q.; Zhao, G. *J. Org. Chem.* **2015**, *80*, 10710.

(6) Zhang, X.; Liu, W.-B.; Tu, H.-F.; You, S.-L. *Chem. Sci.* **2015**, *6*, 4525.

(7) Li, G.; Li, B.; Yang, T.; Yan, J.; Liu, G.; Zhang, G. *J. Nat. Prod.* **2006**, *69*, 1374.

(8) Raju, R.; Piggott, A. M.; Huang, X. C.; Capon, R. J. *Org. Lett.* **2011**, *13*, 2770.

(9) Lawson, K. V.; Rose, T. E.; Harran, P. G. *Tetrahedron* **2013**, *69*, 7683.

(10) Hino, T.; Taniguchi, M. *J. Am. Chem. Soc.* **1978**, *100*, 5564.

(11) (a) Goetz, G. H.; Philippe, L.; Shapiro, M. J. *ACS Med. Chem. Lett.* **2014**, *5*, 1167. (b) Bockus, A. T.; Lexa, K. W.; Pye, C. R.; Kalgutkar, A. S.; Gardner, J. W.; Hund, K. C. R.; Hewitt, W. M.; Schwochert, J. A.; Glassey, E.; Price, D. A.; Mathiowetz, A. M.; Liras, S.; Jacobson, M. P.; Lokey, R. S. *J. Med. Chem.* **2015**, *58*, 4581. (c) Bockus, A. T.; McEwen, C. M.; Lokey, R. S. *Curr. Top. Med. Chem.* **2013**, *13*, 821. (d) White, T. R.; Renzelman, C. M.; Rand, A. C.; Rezai, T.; McEwen, C. M.; Gelev, V. M.; Turner, R. A.; Linington, R. G.; Leung, S. S. F.; Kalgutkar, A. S.;

Bauman, J. N.; Zhang, Y.; Liras, S.; Price, D. A.; Mathiowetz, A. M.; Jacobson, M. P.; Lokey, R. S. *Nat. Chem. Biol.* **2011**, *7*, 810. (e) Tsantrizos, Y. S.; Bolger, G.; Bonneau, P.; Cameron, D. R.; Goudreau, N.; Kukolj, G.; LaPlante, S. R.; Llinàs-Brunet, M.; Nar, H.; Lamarre, D. *Angew. Chemie Int. Ed. English* **2003**, *42*, 1356. (f) Yudin, A. K. *Chem. Sci.* **2015**, *6*, 30. (g) Maianti, J. P.; McFedries, A.; Foda, Z. H.; Kleiner, R. E.; Du, X. Q.; Leissring, M. A.; Tang, W.-J.; Charron, M. J.; Seeliger, M. A.; Saghatelian, A.; Liu, D. R. *Nature* **2014**, *511*, 94. (h) Dinsmore, C. J.; Bogusky, M. J.; Culberson, J. C.; Bergman, J. M.; Homnick, C. F.; Zartman, C. B.; Mosser, S. D.; Schaber, M. D.; Robinson, R. G.; Koblan, K. S.; Huber, H. E.; Graham, S. L.; Hartman, G. D.; Huff, J. R.; Williams, T. M. *J. Am. Chem. Soc.* **2001**, *123*, 2107. (i) Cherney, R. J.; Wang, L.; Meyer, D. T.; Xue, C.-B.; Wasserman, Z. R.; Hardman, K. D.; Welch, P. K.; Covington, M. B.; Copeland, R. A.; Arner, E. C.; DeGrado, W. F.; Decicco, C. P. *J. Med. Chem.* **1998**, *41*, 1749.

(12) (a) Craik, D. J.; Fairlie, D. P.; Liras, S.; Price, D. *Chem. Biol. Drug Des.* **2013**, *81*, 136. (b) Kotz, J.; *Sci. Exch.* **2012**, *5*, 1.

(13) (a) Hill, T. A.; Lohman, R.; Hoang, H. N.; Nielsen, D. S.; Scully, C. C. G.; Kok, W. M.; Liu, L.; Lucke, A. J.; Stoermer, M. J.; Schroeder, C. I.; Chaousis, S.; Colless, B.; Bernhardt, P. V.; Edmonds, D. J.; Gri, D. A.; Rotter, C. J.; Ruggeri, R. B.; Price, D. A.; Liras, S.; Craik, D. J.; Fairlie, D. P. *ACS Med. Chem. Lett.* **2014**, *5*, 1148. (b) Wang, C. K.; Northfield, S. E.; Colless, B.; Chaousis, S.; Hamernig, I.; Lohman, R. J.; Nielsen, D. S.; Schroeder, C. I.; Liras, S.; Price, D. A.; Fairlie, D. P.; Craik, D. J. *Proc. Natl. Acad. Sci. U. S. A.* **2014**, *111*, 17504. (c) Rezai, T.; Bock, J. E.; Zhou, M. V.; Kalyanaraman, C.; Lokey, R. S.; Jacobson, M. P.; *J. Am. Chem. Soc.* **2006**, *128*, 14073.

(14) Nielsen, D. S.; Hoang, H. N.; Lohman, R.-J.; Hill, T. A.; Lucke, A. J.; Craik, D. J.; Edmonds, D. J.; Griffith, D. A.; Rotter, C. J.; Ruggeri, R. B.; Price, D. A.; Liras, S.; Fairlie, D. P. *Angew. Chemie Int. Ed.* **2014**, *53*, 12059.

(15) Mari, M.; Lucarini, S.; Bartoccini, F.; Piersanti, G.; Spadoni, G. *Beilstein J. Org. Chem.*, **2014**, *10*, 1991.

(16) (a) Jackson, A. H.; Naidoo, B.; Smith, P. *Tetrahedron* **1968**, *24*, 6119. (b) Jackson, A. H.; Smith, P. *Chem. Commun.* **1967**, 264.

(17) Rose, T. E.; Lawson, K. V.; Harran, P. G. *Chem. Sci.* **2015**, *6*, 2219.

(18) Casnati, G.; Dossena, A.; Pochini, A. *Tetrahedron Lett.* **1972**, *13*, 5277.

(19) This possibility parallels reports by Crich and co-workers wherein related tryptophan-derived C2-*exo*-pyrroloindolines were found to ring open more readily, allowing ready isolation of the C2-*endo* diastereomer. See: Crich, D.; Bruncko, M.; Natarajan, S.; Teo B.; Tocher, D. *Tetrahedron* **1995**, *51*, 2215, and reference 4a.

(20) (a) Trost, B. M.; Quancard, J. *J. Am. Chem. Soc.* **2006**, *128*, 6314. (b) Kimura, M.; Futamata, M.; Mukai, R.; Tamaru, Y. *J. Am. Chem. Soc.* **2005**, *127*, 4592.

(21) (a) Groth, T.; Meldal, M. *J. Comb. Chem.* **2001**, *3*, 34. (b) Nielsen, T. E.; Meldal, M. *J. Org. Chem.* **2004**, *69*, 3765.

(22) Zhao, H.; Negash, L.; Wei, Q.; LaCour, T. G.; Estill, S. J.; Capota, E.; Pieper, A. A.; Harran, P. G. *J. Am. Chem. Soc.* **2008**, *130*, 13864.

(23) Tyrosine *C*-alkylation could be achieved by internal Pd^0-catalyzed *O*-cinnamylation and acid-promoted $O \rightarrow C_{ortho}$ rearrangement analogously to our previous report. See reference 9.

(24) (a) Veber, D. F.; Johnson, S. R.; Cheng, H.-Y.; Smith, B. R.; Ward, K. W.; Kopple, K. D. *J. Med. Chem.* **2002**, *45*, 2615. (b) Lu, J. J.; Crimin, K.; Goodwin, J. T.; Crivori, P.; Orrenius, C.; Xing, L.; Tandler, P. J.; Vidmar, T. J.; Amore, B. M.; Wilson, A. G. E.; Stouten, P. F. W.; Burton, P. S. *J. Med. Chem.* **2004**, *47*, 6104.

Chapter 5. Arynes and Cyclic Alkynes as Synthetic Building Blocks for Stereodefined Quaternary Centers

5.1 Abstract

We report a facile method to synthesize stereodefined quaternary centers from reactions of arynes and related strained intermediates β-ketoester-derived substrates. Conversion of β-ketoesters to chiral enamines is followed by reaction with *in situ* generated strained arynes or cyclic alkynes. Hydrolytic workup provides the arylated or alkenylated products in enantiomeric ratios as high as 98:2. We also describe the one-pot conversion of a β-ketoester substrate to the corresponding enantioenriched α-arylated product. Computations show how chirality is transferred from the *N*-bound chiral auxiliary to the final products. These are the first theoretical studies of aryne trapping by chiral nucleophiles to set new stereocenters. Our approach provides the most general known solution to the challenging problem of stereoselective β-ketoester arylation/alkenylation, with formation of a quaternary center.

5.2 Introduction

Arynes have historically been avoided as synthetic intermediates as a result of their high reactivity[1,2] However, recent studies have demonstrated that arynes can be generated under mild reaction conditions,[3] trapped regioselectively using predictive models,[4] and employed in a host of synthetic applications. The utility of arynes is evident, as they have now been used to synthesize natural products, ligands, materials, agrochemicals, and pharmaceutical agents (e.g., **1**–**3**, Figure 5.1a).**Error! Bookmark not defined.**,[5]

The majority of reported synthetic applications of arynes are intermolecular reactions that lead to achiral or racemic products.[6] We questioned if arynes and related strained intermediates

could instead serve as building blocks to generate enantioenriched products bearing quaternary centers. Only two methodologies leading to intermolecular, stereoselective aryne trappings have been reported and are limited to the synthesis of tertiary stereocenters.[7,8]

We considered the reaction manifold in which β-ketoesters **4**[9] would be trapped with strained alkynes **5**, to give their corresponding α-arylated products **6** with formation of a quaternary stereocenter (Figure 4.1b).[10] As prior efforts to achieve this direct functionalization in a racemic sense were accompanied by an undesired C–C bond fragmentation,[11] we considered a two-step, alternative approach. First, β-ketoesters **4** would be treated with amines **7** to afford the corresponding enamines **8**.[12] Trapping of the enamines **8** with in situ-generated arynes (or strained cyclic alkynes) would give the α-arylated or alkenylated products **6** after hydrolysis in the same pot.[13] The use of a chiral amine (i.e., **7**) in this process would ultimately give rise to enantioenriched products **6** bearing quaternary stereocenters.**Error! Bookmark not defined.** It should be n oted that the enantioselective α-arylation of β-ketoesters has remained a challenging synthetic problem.[14] Promising developments include the use of hypervalent iodine reagents (racemic or modest enantioenrichment),[15] the Cu-catalyzed, enantioselective coupling of 2-methylacetates with 2-iodotrifluoroacetanilides,[16] and the Pd-catalyzed α-arylation of malonates and cyanoacetates (racemic).[17] A general method for the stereocontrolled α-arylation or -alkenylation of β-ketoesters has not been disclosed.

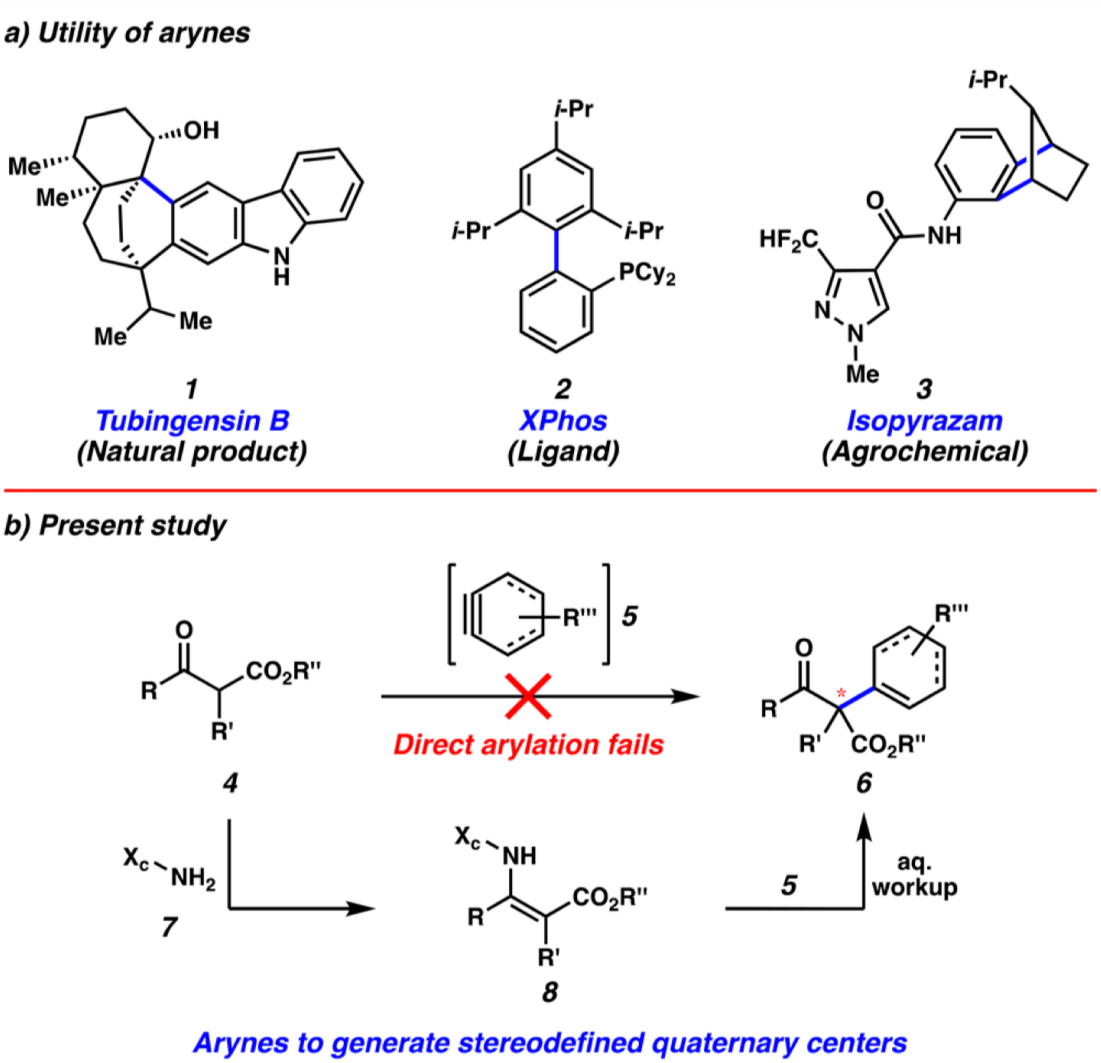

Figure 5.1. Synthetic applications of arynes and strategy for the stereoselective arylation of β-ketoesters.

We report the development of the synthetic sequence shown in Figure 5.1b, which provides a facile method to achieve the stereoselective α-arylation/alkenylation of β-ketoesters.[Error! Bookmark not defined.] In addition to providing access to adducts bearing stereodefined quaternary centers, this methodology demonstrates that highly reactive arynes and related intermediates can serve as

building blocks to access enantioenriched products by intermolecular trapping. In addition, the origins of stereoselectivity have been revealed by a computational investigation of these reactions.

5.3 Computational Methods

All quantum chemical calculations were performed with Gaussian 09. Geometry optimizations and frequencies were calculated with the B3LYP (in vacuo) density functional with the 6-31+G(d,p) basis set. Optimized geometries were verified by frequency calculations as minima (zero imaginary frequencies) or transition structures (a single imaginary frequency). Free energy corrections were determined using unscaled B3LYP/6-31+G(d,p) vibrational frequencies assuming a standard state of 1 atm and 298.15 K. Errors in the treatment of low modes as harmonic oscillations were mitigated by use of the quasiharmonic approximation proposed by Truhlar and coworkers. Single point energy calculations were performed on optimized geometries with the M06-2X functional and def2-TZVPP[5] basis set in conjunction with the SMD implicit solvation model. The free energies reported herein were determined by adding zero-point energy and thermal correction determined using B3LYP/6-31+G(d,p) to electronic energies computed at the M06-2X/def2-TZVPP–SMD level of theory. Transition structures were also optimized at the B3LYP level of theory with the implicit SMD solvation method, which provided similar energies but yielded poor TS geometries. Transition structures optimized with M06-2X had convergence issues and often failed to locate a TS. This has been found in similar computational studies involving aryne intermediates. The B3LYP functional has been shown to have better convergence on transition structures for these reactions. We selected the M06-2X/def2-TZVPP–SMD//B3LYP/6-31+G(d,p) level of theory due to providing a combination of accurate geometries and energies for these reactions, in addition to the examples provided by Goodman and our group.

Monte Carlo conformational searches were performed on the reactive complexes using the OPLS3 force field in Maestro/Macromodel. Reactive conformations with the distance between the bond-forming atoms shorter than 4.0 Å were used as input geometries for transition structure optimizations. Molecular graphics were generated using CYLView.

5.4 Results and Discussion

Development of a Racemic and Stereospecific Reaction to Generate Quaternary Centers. To commence our studies, we selected β-ketoester **9** as an initial substrate for the two-step arylation procedure (Figure 5.2). As the use of enamines and arynes to construct quaternary stereocenters was unknown, we first pursued a racemic transformation. Benzylamine was condensed with ketoester **9** to yield enamine **10** quantitatively. Next, enamine **10** was used to trap benzyne, which was generated in situ from silyl triflate **11** (1.5 equiv) in DME at 30 °C (6 h). After quenching with 1 M $HCl_{(aq)}$, we were delighted to obtain the desired α-arylated product **12** in 92% yield with introduction of a quaternary center. Furthermore, we surveyed several other highly reactive intermediates to gauge the possibility of utilizing substituted benzynes and cyclic alkynes. The use of fused arynes 2,3-naphthalyne and *N*-Boc-4,5-indolyne provided arylated products **13** and **14**, respectively.[18] In addition, trapping with known heterocyclic alkynes[19] delivered tetrahydropyridine **15** and dihydropyran **16** in 67% and 74% yields, respectively. These results represent a facile means to install aryl and vinyl moieties onto a cyclic β-ketoester with quaternary center formation.

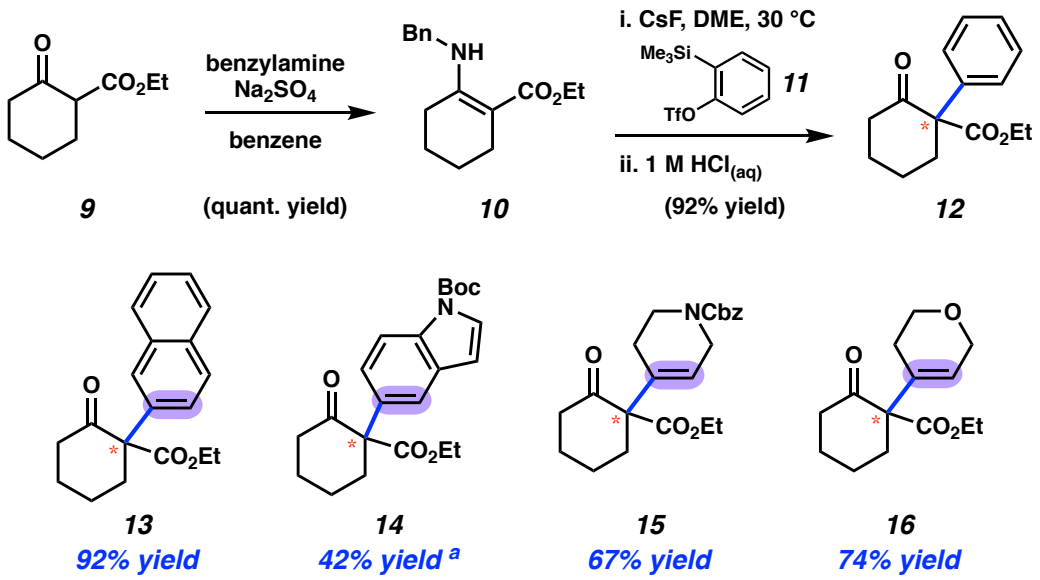

Figure 5.2. Discovery of methodology for the arylation/vinylation of β-ketoesters in racemic fashion. Conditions for enamine formation: ketoester **9** (1.0 equiv), benzylamine (1.5 equiv), Na_2SO_4 (5:1 by wt.), benzene (0.7 M), 80 °C, 16 h. Conditions for arylation/alkenylation unless otherwise stated: i. enamine **10** (1.0 equiv), silyl triflate **11** (1.5 equiv), CsF (7.5 equiv), DME (0.1 M), 30 °C, 6 h; ii. 1 M $HCl_{(aq)}$, 23 °C, 30 min. Yields reflect the average of two isolation experiments. [a] Aryne trapping performed for 3 h.

Having developed the racemic arylation/alkenylation reaction, we turned our attention to the discovery of a diastereoselective variant to access enantioenriched products (Table 1).[20] Thus, a series of enantioenriched chiral amines, readily prepared using Ellman auxiliary chemistry (i.e., **18**–**24**),[21,22] were condensed with ketoester **9** to access enamines **17**. Subsequent arylation under the conditions depicted in Figure 5.2 furnished **12** in enantioenriched form. Utilization of phenyl derivative **18** resulted in the formation of **12** in good yield and 87:13 enantiomeric ratio (er) (entry 1). Employing amine **19**, bearing a cyclohexyl moiety, gave the desired product in a lower er of 65:35 (entry 2). Recognizing the importance of the aryl fragment, we examined 1- and 2-naphthyl

derived amines **20** and **21**, which provided **12** in 90:10 and 78:22 er (entries 3 and 4, respectively). With improved results in the case of **20**, we examined anthracenyl amines **22**–**24** (entries 5–7). As the use of ethyl derivative **23** furnished **12** with the best combination of yield and er (entry 6), **23** was selected for subsequent studies. It should be noted that the Ellman-approach provides both enantiomers of **23**, which, in turn, permits access to each enantiomer of the products depicted subsequently.[23,24]

Table 5.1 Survey of chiral auxiliaries to give optically enriched ketone **12**.[a]

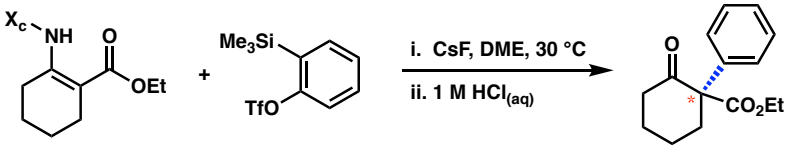

17 *11* *12*

Entry	X_c–NH_2	Yield	er	Entry	X_c–NH_2	Yield	er
1	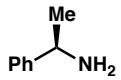 *18*	87%	87:13	5	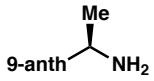 *22*	71%	97:3
2	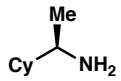 *19*	64%	65:35	6	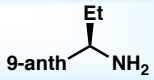 *23*	96%	92:8
3	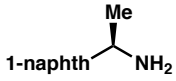 *20*	72%	90:10	7	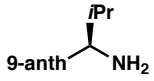 *24*	100%	83:17
4	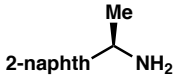 *21*	79%	78:22				

[a] Reaction conditions: i. enamine **17** (1.0 equiv), silyl triflate **11** (1.5 equiv), CsF (7.5 equiv), DME (0.1 M), 30 °C, 6 h; ii. 1 M $HCl_{(aq)}$, 23 °C, 30 min.

Scope of Methodology. With a suitable chiral amine identified, we evaluated several cyclic alkynes in the stereoselective arylation/alkenylation reaction to form quaternary stereocenters (Figure 5.3). The reaction was tolerant of substituted benzyne intermediates and extended aryl units, giving rise to arylated products **28** and **13**, respectively. Moreover, trapping of an indolyne intermediate delivered heterocycle-containing product **14**. When applied to non-aromatic, strained alkynes, the methodology provided alkenylated products in good yields and stereoselectivities. For example, trapping of cyclohexyne provided cyclohexene derivative **29** in good yield and 93:7 er. Additionally, by employing heterocyclic alkynes, products **15** and **16** were obtained in excellent yields and comparable stereoselectivities.

As shown in Figure 5.4, the methodology is also tolerant of variation in the nucleophilic component. For example, replacement of the ethyl ester with a benzyl ester in the parent substrate gave rise to arylated product **32** in 71% yield and 93:7 er. Furthermore, piperidinone and tetrahydropyranone derivatives could be employed to access heterocyclic products (i.e., **33**–**35**). Enamines derived from 7-membered ring β-ketoesters could also be utilized, as shown by the formation of arylated products **36** and **37** with excellent stereoselectivity. Lastly, the formation of ketoester **38** demonstrates the viability of utilizing this methodology for the α-arylation of acyclic β-ketoesters.

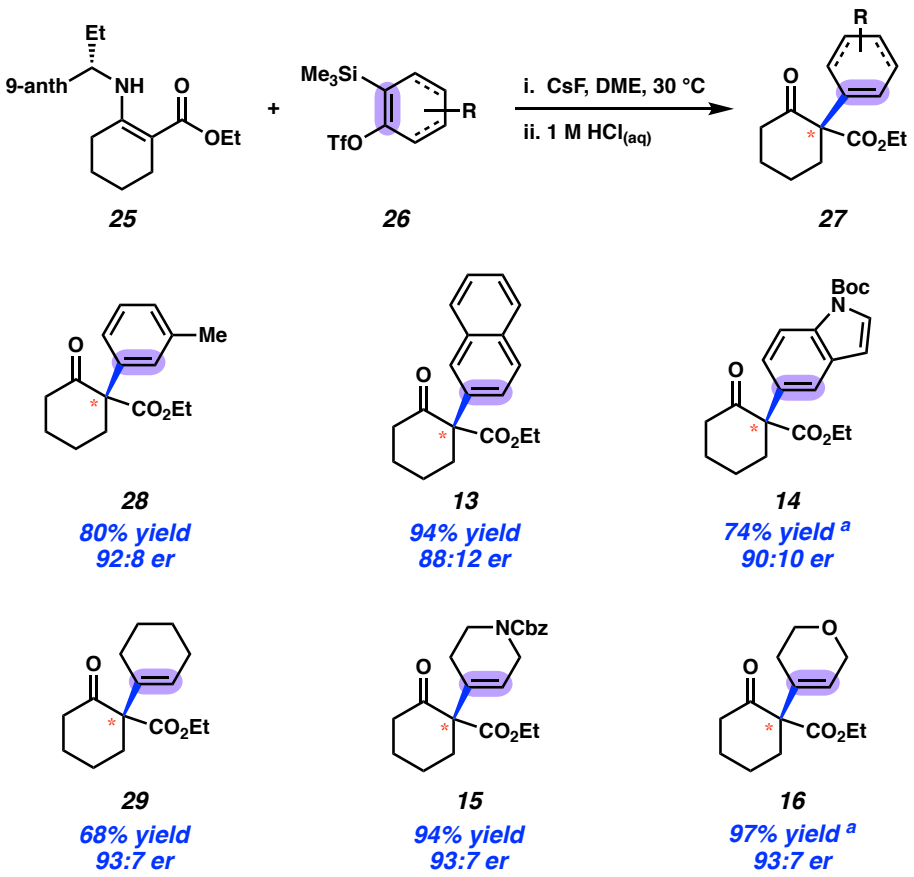

Figure 5.3. Variation of the electrophile. Conditions unless otherwise stated: i. enamine **25** (1.0 equiv), silyl triflate **26** (1.5 equiv), CsF (7.5 equiv), DME (0.1 M), 30 °C, 6 h; ii. 1 M $HCl_{(aq)}$, 23 °C, 30 min. Yields reflect the average of two isolation experiments. [a] Aryne or cyclic alkyne trapping performed for 3 h.

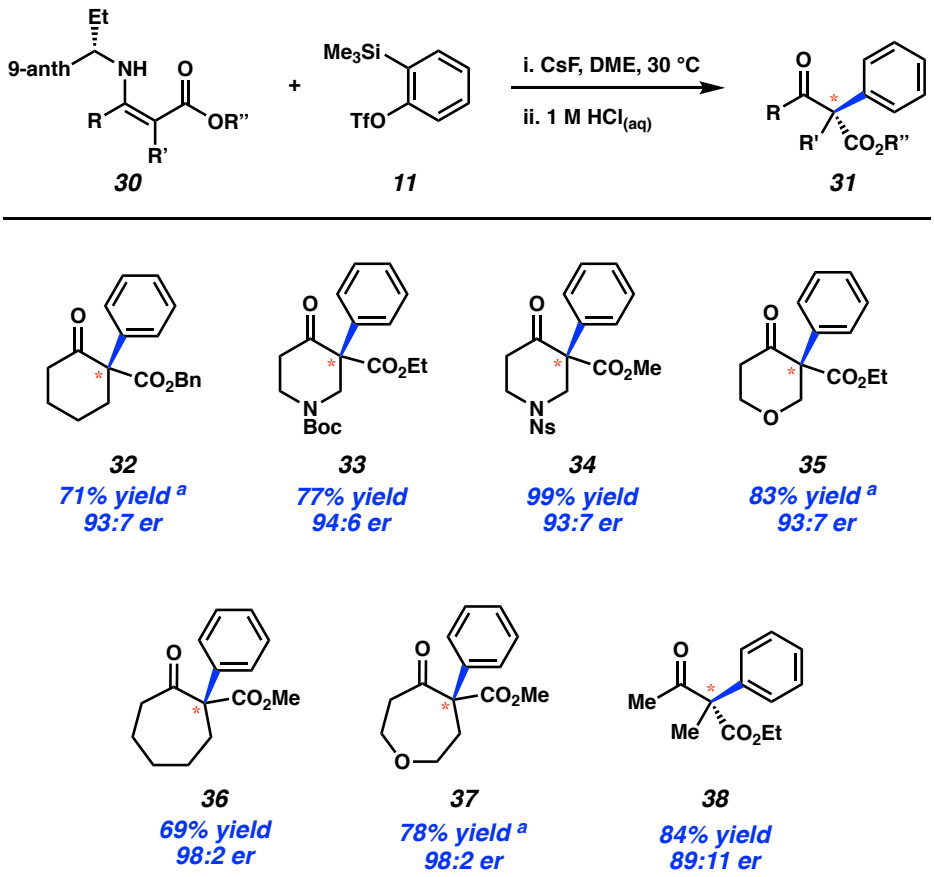

Figure 5.4. Variation of the nucleophilic component **30** in the trapping with **11**. Conditions unless otherwise stated: i. enamine **30** (1.0 equiv), silyl triflate **11** (1.5 equiv), CsF (7.5 equiv), DME (0.1 M), 30 °C, 3 h; ii. 1 M $HCl_{(aq)}$, 23 °C, 30 min. Yields reflect the average of two isolation experiments. [a] Aryne trapping performed for 6 h.

One-pot, Stereoselective Arylation. As one final application of this methodology, we developed a one-pot variant of the methodology to convert ketoester substrate **39** to α-arylated product **36**, with recovery of the chiral auxiliary (Figure 5.5). β-Ketoester **39** was reacted with amine **23** to generate enamine **40** in situ. Addition of CsF and silyl triflate **11**, followed by stirring at 30 °C for 6 h, and subsequent acid-mediated hydrolysis yielded the desired α-arylated product **36**. When performed on mmol scale, the reaction gave **36** in 68% yield and 96:4 er, in addition to

67% recovered amine **23**. This protocol provides a promising means to achieve the direct, asymmetric α-arylation of β-ketoesters.

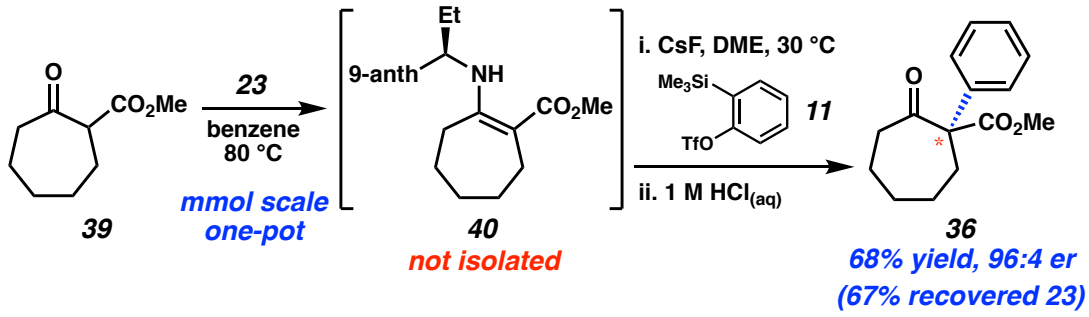

Figure 5.5. One-pot, mmol-scale arylation reaction to furnish **36**. Conditions for enamine formation: ketoester **39** (1.0 equiv), amine **23** (1.0 equiv), benzene (0.7 M), 80 °C, 16 h, followed by evaporation of benzene solvent. Conditions for arylation: i. silyl triflate **11** (1.5 equiv), CsF (7.5 equiv), DME (0.1 M), 30 °C, 6 h; ii. 1 M $HCl_{(aq)}$, 23 °C, 12 h.

Computational Analysis of Chirality Transfer. Density functional theory (DFT) calculations were performed to understand how stereochemical information is transferred from the chiral auxiliary to the newly formed quaternary stereocenter. Our laboratories have studied reactions of arynes in nucleophilic additions using computations,[Error! Bookmark not defined.] but no t heoretical studies of aryne trapping by chiral nucleophiles to set new stereocenters have been reported. All calculations described here utilize the M06-2X[25]/def2-TZVPP–SMD[26] (diethyl ether)//B3LYP[27]/6-31+G(d,p) level of theory.

We first calculated the stereo-controlling transition structures for the reaction of benzyne and the *S* enantiomer of the chiral enamine derived from amine **20**, which possesses the 1-naphthyl group at the chiral center. The stereochemistry-controlling transition structures are shown in Figure 5.6. Each pathway has a low barrier ($\Delta G^{\ddagger}$ = 9.6 and 11.6 kcal/mol, respectively). **TS1** leads to the experimentally preferred stereoisomer, **(*S*)-12**, whereas **TS2** yields the minor enantiomer, **(*R*)-12**.

The difference in free energy of activation ($\Delta\Delta G^{\ddagger}$) is 2.0 kcal/mol, within error of the experimentally observed selectivity of 90:10 ($\Delta\Delta G^{\ddagger}$ = 1.3 kcal/mol). In both **TS1** and **TS2**, an intramolecular hydrogen bond between the NH and ester carbonyl is present. Axial-attack by benzyne occurs in both cases, as expected from the preference the forming bond to be staggered with respect to the allylic CH bonds (known previously as the Fürst-Plattner rule).[28] While attack is axial in both cases, and the chiral group is in its favored conformation, the interaction of the CH at the stereogenic center is disfavorable in the minor TS.

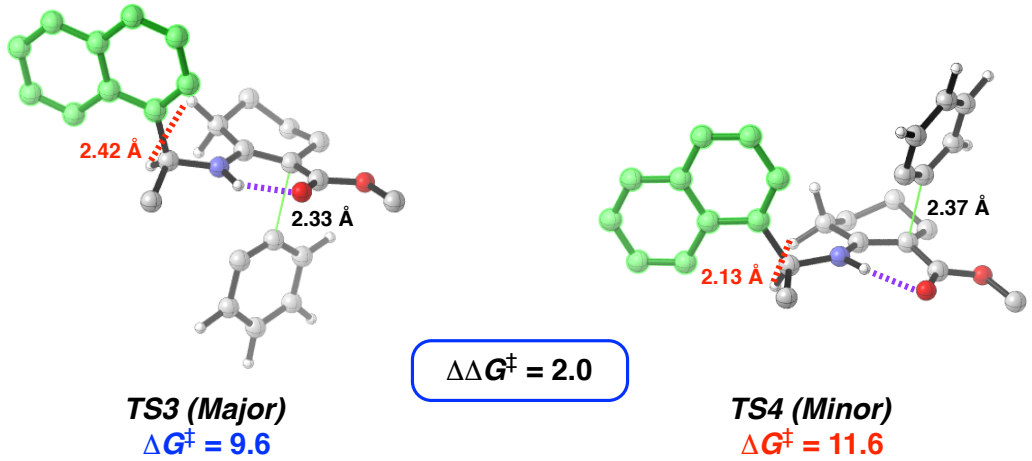

Figure 5.6. Lowest-energy transition structures **TS1** and **TS2** for the addition of benzyne and the chiral enamine derived from amine **20** (M06-2X/def2-TZVPP–SMD (diethylether)//B3LYP/6-31+G(d,p)). Free energy activation barriers ($\Delta G^{\ddagger}$) are compared to separated intermediates. The difference in free energies of activation ($\Delta\Delta G^{\ddagger}$), relative to **TS1**, are reported in kcal/mol.

In **TS2**, there is a close-contact H–H interaction of 2.1 Å between the chiral center of the enamine and methylene of the six-membered ring. This contact is alleviated in **TS1**, with an H–H interaction distance of 2.4 Å. Our laboratory has previously examined the transmission of chirality in the reaction of a similar chiral enamine with acrylonitrile, which similarly revealed the importance of torsional interactions between forming bonds and allylic bonds.[29] In that case, the

same conformations and their energies were found for the chiral enamine with a phenyl ring instead of naphthyl. Torsional strain[30] controls the stereoselectivity of this reaction, where the enamine conformations remain the same for both stereoisomeric transition states. One might expect that the stereoselectivity cannot be modulated by the size of the substituent, but as found here, enamine **25** has improved enantioselectivity with the larger 9-anthracenyl substituent.

We calculated the stereochemistry-controlling transition structures for the reaction of chiral enamine **25** and benzyne using methyl groups in place of ethyl groups to simplify computations. **Figure 5.7.** Lowest-energy transition structures **TS3** and **TS4** for the addition of benzyne and chiral enamine **25** (M06-2X/def2-TZVPP–SMD (diethylether)//B3LYP/6-31+G(d,p)). Free energy activation barriers ($\Delta G^{\ddagger}$) are compared to separated intermediates. The difference in free energies of activation ($\Delta\Delta G^{\ddagger}$), relative to **TS1**, are reported in kcal/mol.[31] The two lowest-energy transition structures leading to the major and minor stereoisomers are shown in Figure 5.7. **TS3** leads to the experimentally preferred stereoisomer, **(*S*)-12**, whereas **TS4** yields the minor enantiomer. The difference in free energy of activation ($\Delta\Delta G^{\ddagger}$) is 2.5 kcal/mol, within error of the experimentally observed selectivity of 92:8 ($\Delta\Delta G^{\ddagger}$ = 1.5 kcal/mol) and 0.5 kcal/mol higher than observed with **20**. Axial-attack by benzyne again occurs the two half-chair conformers of the cyclohexene. However, here the conformation of the enamine stereogenic group differs between the stereoisomeric transition structures. While, the conformation of **TS3** is analogous to that in **TS1**, the enamine in **TS4** is in a higher-energy conformation because the face being blocked to form the **(*R*)-**isomer is blocked by the anthracene group. This conformation yields a higher-energy penalty than the torsional strain found in **TS2**, which enables an increase in enantioselectivity.

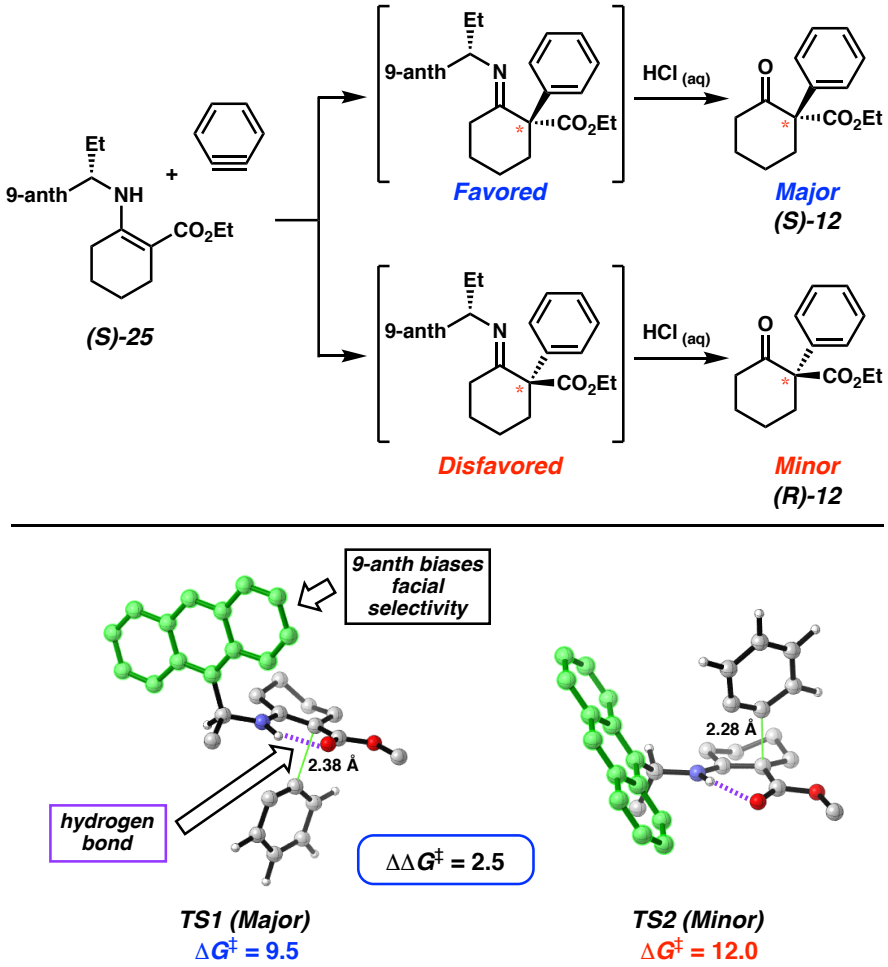

Figure 5.7. Lowest-energy transition structures **TS3** and **TS4** for the addition of benzyne and chiral enamine **25** (M06-2X/def2-TZVPP–SMD (diethylether)//B3LYP/6-31+G(d,p)). Free energy activation barriers ($\Delta G^{\ddagger}$) are compared to separated intermediates. The difference in free energies of activation ($\Delta\Delta G^{\ddagger}$), relative to **TS1**, are reported in kcal/mol.

5.5 Conclusions

We have developed the first methodology that allows for arynes and related strained intermediates to be trapped intermolecularly for the formation of stereodefined quaternary centers. The strategy relies on the facile conversion of β-ketoesters to chiral enamines, which undergo nucleophilic trapping of in situ generated strained arynes or cyclic alkynes. Hydrolysis in the same

pot provides the arylated products in good to excellent enantiomeric ratios (up to 98:2 er). This strategy circumvents a previously known undesired C–C bond fragmentation, while providing the most general solution to the challenging problem of stereoselective β-ketoester arylation/alkenylation, with formation of a quaternary center. In addition, a one-pot procedure for the conversion of a β-ketoester substrate to the corresponding enantioenriched α-arylated product was developed. Finally, computations show how chirality transfer is achieved from the chiral auxiliary to the final products, a type of conformational transmission operating in the trapping of arynes by chiral nucleophiles. We expect these studies will enable further developments of intermolecular, stereoselective reactions of highly reactive aryne and cyclic alkyne intermediates.

5.6 References

(1) For reviews regarding benzyne and related reactive intermediates, see: a) Pellissier, H.; Santelli, M. *Tetrahedron* **2003**, *59*, 701–730. b) Wenk, H. H.; Winkler, M.; Sander, W. *Angew. Chem., Int. Ed.* **2003**, *42*, 502–528. c) Sanz, R. *Org. Prep. Proced. Int.* **2008**, *40*, 215–291. d) Bronner, S. M.; Goetz, A. E.; Garg, N. K. *Synlett* **2011**, 2599–2604. e) Tadross, P. M.; Stoltz, B. M. *Chem. Rev.* **2012**, *112*, 3550–3557. f) Gampe, C. M.; Carreira, E. M. *Angew. Chem., Int. Ed.* **2012**, *51*, 3766–3778. g) Bhunia, A.; Yetra, S. R.; Biju, A. T. *Chem. Soc. Rev.* **2012**, *41*, 3140–3152. h) Yoshida, H.; Takaki, K. *Synlett* **2012**, 1725–1732. i) Dubrovskiy, A. V.; Markina, N. A.; Larock, R. C. *Org. Biomol. Chem.* **2013**, *11*, 191–218. j) Wu, C.; Shi, F. *Asian J. Org. Chem.* **2013**, *2*, 116–125. k) Hoffmann, R. W.; Suzuki, K. *Angew. Chem., Int. Ed.* **2013**, *52*, 2655–2656. l) Goetz, A. E.; Garg, N. K. *J. Org. Chem.* **2014**, *79*, 846–851. m) Goetz, A. E.; Shah, T. K.; Garg, N. K. *Chem. Commun*. **2015**, *51*, 34–45. n) Yoshida, S.; Hosoya, T. *Chem. Lett.* **2015**, *44*, 1450–1460. o) Bhojgude, Sachin Suresh; Bhunia, A.; Biju, A. T. *Acc. Chem. Res.* **2016**, *49*, 1658–1670.

(2) For the quantification of benzyne's high electrophilicity, see: Fine Nathel, N. F.; Morrill, L. A.; Mayr, H.; Garg, N. K. *J. Am. Chem. Soc.* **2016**, *138*, 10402–10405.

(3) For Kobayashi's generation of arynes from *o*-silyltriflate precursors, see: Himeshima, Y.; Sonoda, T.; Kobayashi, H. *Chem. Lett.* **1983**, 1211–1214.

(4) For the aryne distortion/interaction model, see: a) Cheong, P. H.-Y.; Paton, R. S.; Bronner, S. M.; Im, G.-Y. J.; Garg, N. K.; Houk, K. N. *J. Am. Chem. Soc.* **2010**, *132*, 1267–1269. b) Im, G.-Y. J., Bronner, S. M.; Goetz, A. E.; Paton, R. S.; Cheong, P. H.-Y.; Houk, K. N.; Garg, N. K. *J. Am. Chem. Soc.* **2010**, *132*, 17933–17944. c) Goetz, A. E.; Bronner, S. M.; Cisneros, J. D.; Melamed, J. M.; Paton, R. S.; Houk, K. N.; Garg, N. K. *Angew. Chem., Int. Ed.* **2012**, *51*, 2758–2762. d) Bronner, S. M.; Mackey, J. L.; Houk, K. N.; Garg, N. K. *J. Am. Chem. Soc.* **2012**, *134*, 13966–13969. e) Medina, J. M.; Mackey, J. L.; Garg, N. K.; Houk, K. H. *J. Am. Chem. Soc.* **2014**, *136*, 15798–15805. f) Picazo, E.; Houk, K. N.; Garg, N. K. *Tetrahedron Lett.* **2015**, *56*, 3511–3514.

(5) For select examples of synthetic applications, see: a) Mauger, C. C.; Mignani, G. A. *Org. Proc. Res. Dev*. **2004**, *8*, 1065–1071. b) Lin, J. B.; Shah, T. K.; Goetz, A. E.; Garg, N. K.; Houk, K. N. *J. Am. Chem. Soc.* **2017**, *139*, 10447–10455. c) Surry, D. S.; Buchwald, S. L. *Angew. Chem., Int. Ed*. **2008**, *47*, 6338–6361. d) Ross, S. P.; Hoye, T. R. *Nat. Chem.* **2017**, *9*, 523–530. e) Corsello, M. A.; Kim, J.; Garg, N. K. *Nat. Chem.* **2017***, 9,* 944–949.

(6) Intramolecular aryne trappings, although less common, have been used to construct complex natural product frameworks. See references **Error! Bookmark not defined.**, **Error! Bookmark not defined.**, and the following recent examples: a) Goetz, A. E.; Silberstein, A. L.; Corsello, M. A. *J. Am. Chem. Soc.* **2014**, *136*, 3036–3039. b) Neog, K.; Borah, A.; Gogoi, P. *J. Org. Chem.* **2016**, *81*, 11971−11977. c) Corsello, M. A.; Kim, J. Garg, N. K. *Nat. Chem.* **2017**, *9*,

944–949. d) Ross, S.P.; Hoye, T.R. *Nature Chem.* **2017**, *9*, 523–530. e) Neumeyer, M.; Kopp, J.; Brückner, R. *Eur. J. Org. Chem.* **2017**, 2883 – 2915.

(7) For the intermolecular trapping of benzyne with dienes bearing the Oppolzer sultam (with later cleavage of the auxiliary) to generate tertiary stereocenters, see: a) Dockendorff, C.; Sahli, S.; Olsen, M.; Milhau, L.; Lautens, M. *J. Am. Chem. Soc.* **2005**, *127*, 15028–15029. b) Webster, R.; Lautens, M. *Org Lett.* **2009**, *11*, 4688–4691.

(8) For the intermolecular trapping of arynes with Schöllkopf reagents (with later hydrolysis) to generate tertiary stereocenters, see: a) Jones, E. P.; Jones, P.; Barrett, A. G. M. *Org. Lett.* **2011**, *13*, 1012–1015. b) Jones, E. P.; Jones, P.; White, A. J. P.; Barrett, A. G. M. *Beilstein J. Org. Chem.* **2011**, *7*, 1570–1576.

(9) β-keto esters are commonly seen in bioactive molecules, so methods to synthesize functionalized derivatives are valuable. A Reaxys search reveals there are 53,683 known □-keto esters with biological activity. January 24, 2018.

(10) Methodologies to generate quaternary stereocenters, especially with control of absolute stereochemistry, remain highly sought after. For pertinent reviews, see: a) Quasdorf, K. W.; Overman, L. E. *Nature* **2014**, *516*, 181–191. b) Liu, Y.; Han, S.-J.; Liu, W.-B.; Stoltz, B. M. *Acc. Chem. Res.* **2015**, *48*, 740–751. c) Schockley, S. E.; Holder, J. C.; Stoltz, B. M. *Org. Process Res. Dev.* **2015**, *19*, 974–981. d) Zeng, X.-P.; Cao, Z-Y.; Wang, Y-H.; Zhou, F.; Zhou, J. *Chem. Rev.* **2016**, *116*, 7330–7396.

(11) For the α-arylation of β-ketoesters, with concomitant C–C bond fragmentation, see: Tambar, U. K.; Stoltz, B. M. *J. Am. Chem. Soc.* **2005**, *127*, 5340–5341.

(12) Enamines derived from β-ketoesters were considered well suited, as they are stable on neutral alumina and can be purified prior to use.

(13) For the α-arylation of enamines with arynes to give functionalized achiral enamines, see: a) Ramtohul, Y. K.; Chartrand, A. *Org. Lett.* **2007**, *9*, 1029–1032. b) Li, R.; Wang, X.; Wei, Z.; Wu, C.; Shi, F. *Org. Lett.* **2013**, *15*, 4366–4369.

(14) A related breakthrough, albeit not using β-ketoesters, is the α-arylation of oxindoles using Pd catalysis; see: a) Altman, R. A.; Hyde, A. M.; Huang, X.; Buchwald, S. L. *J. Am. Chem. Soc.* **2008**, *130*, 9613–9620. b) Taylor, A. M.; Altman, R. A.; Buchwald, S. L. *J. Am. Chem. Soc.* **2009**, *131*, 9900–9901. c) Li, P.-F.; Buchwald, S. L. *Angew. Chem., Int. Ed.* **2011**, *50*, 6396–6400.

(15) a) Beringer, F. M.; Forgione, P. S.; Yudis, M. D. *Tetrahedron* **1960**, *8*, 49–63. b) Ochiai, M.; Kitagawa, Y.; Takayama, N.; Takaoka, Y.; Shiro, M. *J. Am. Chem. Soc.* **1999**, *121*, 9233–9234. c) Oh, C. H.; Kim, J. S.; Jung, H. H. *J. Org. Chem.* **1999**, *64*, 1338–1340.

(16) Xie, X.; Chen. Y.; Ma. D. *J. Am. Chem. Soc.* **2006**, *128*, 16050–16051.

(17) For the Pd-catalyzed α-arylation of malonates, see: Beare, M. A.; Hartwig, J. F. *J. Org. Chem.* **2002**, *67*, 541–555.

(18) For reasons not fully understood, the racemic arylation of indolyne was lower yielding than the corresponding stereoselective arylation reaction.

(19) a) McMahon, T. C.; Medina, J. M.; Yang, Y.-F.; Simmons, B. J.; Houk, K. N.; Garg, N. K. *J. Am. Chem. Soc.* **2015***, 137*, 4082–4085. b) Shah, T. K.; Medina, J. M.; Garg, N. K. *J. Am. Chem. Soc.* **2016***, 138*, 4948–4954.

(20) Other strategies for this transformation were pursued, such as the use of Cu/BOX as a catalyst for the arylation reaction. Additionally, many other classes of amines, such as amino acids and amino acid derivatives were examined in the arylation reaction, but led to either poor yields and/or poor stereochemical outcomes.

(21) For a review on Ellman's chiral sulfinamides, see: Ellman, J. A.; Owens, T. D.; Tang, T. P. *Acc. Chem. Res.* **2002**, 35, 984. Procedure followed to synthesize chiral anthracenyl amines: Rodriguez–Hernandez, R.; Hernandez–Castillo, T.; Huizar–Trejo, K. E. *Synthesis* **2011**, *17*, 2817–2821.

(22) Chiral auxiliaries have seen widespread use to install important stereocenters in drugs and complex targets. For a recent review, see: Farina, V.; Reeves, J. T.; Senanayake, C. H.; Song, J. J. *Chem. Rev.* **2006**, *106*, 2734–2793. For examples using chiral sulfinamides, see: a) Pflum, D. A.; Krishnamurthy, D.; Han, Z.; Wald, S. A.; Senanayake, C. H. *Tetrahedron Lett.* **2002**, *43*, 923–926. b) Han, Z. S.; Herbage, M. A.; Mangunuru, H. P. R.; Xu, Y.; Zhang, L.; Reeves, J. T.; Sieber, J. D.; Li, Z.; DeCroos, P.; Zhang, Y.; Li, G.; Li, N.; Ma, S.; Frinberg, N.; Wang, X.; Goyal, N.; Krishnamurthy, D.; Lu, B.; Song, J. J.; Wang, G.; Senanayake, C. H. *Angew. Chem., Int. Ed.* **2013**, *52*, 6713–6717. For examples of chiral auxiliaries used in drug development see: Zhang, W.-Y.; Sun, C.; Hunt, D.; He, M.; Deng, Y.; Zhu, Z.; Chen, C.-L.; Katz, C. E.; Niu, J.; Hogan, P. C.; Xiao, X.-Y.; Dunwoody, N.; Ronn, M. *Org. Process Res. Dev.* **2016**, *20*, 284–296.

(23) For the crystallographic data used to assign the absolute stereochemistry of amine **23** and its enantiomer, see the SI.

(24) The choice of enantiomer of **23** used in subsequent experiments was made arbitrarily, as both were prepared in gram quantities.

(25) Zhao, Y.; Truhlar, D. G. *Theor. Chem. Acc.* **2008**, *120*, 215−241.

(26) Marenich, A. V.; Cramer, C. J.; Truhlar, D. G. *J. Phys. Chem. B* **2009**, *113*, 6378–6396.

(27) P. S. a) Vosko, S. H.; Wilk, L.; Nusair, M. *Can. J. Phys*. **1980**, *58*, 1200−1211. b) Lee, C.; Yang, W.; Parr, R. G. *Phys. Rev. B*: *Condens. Matter Mater. Phys*. **1988**, *37*, 785−789. c) Becke,

A. D. *J. Chem. Phys.* **1993**, *98*, 5648−5652. d) Stephens, P. J.; Devlin, F. J.; Chabalowski, C. F.; Frisch, M. J. *J. Phys. Chem.* **1994**, *98*, 11623−11627.

(28) Lucero, M. J.; Houk, K. N. *J. Am. Chem. Soc.* **1997**, *119*, 826–827.

(29) Lucero, M. J.; Houk, K. N. *J. Am. Chem. Soc.* **1997**, *119*, 826–827.

(30) Wu, Y. D.; Houk, K. N.; Paddon-Row, M. N. *Angew. Chem., Int. Ed. Engl*. **1992**, *31*, 1019–1021.

(31) From the results provided in Table 1, entries 5 and 6, the use of methyl vs ethyl has a negligible impact on stereoselectivity.

Chapter 6. Catalytic Enantioselective Hetero-[6+4] and [6+2] Cycloadditions of Heteroaromatic Compounds

6.1 Abstract

The development of the first chemo-, regio- and stereoselective hetero-[6+4] and [6+2] cycloadditions of heteroaromatic compounds is presented. The concept is based on activation of pyrroles, imidazoles and pyrazoles by an aldehyde handle, which by reaction with an organocatalyst generates an electron-rich hetero-6π-component that reacts in a chemo-, regio- and stereoselective manner with electron-deficient dienes and olefins. For the hetero-[6+4] cycloaddition of the pyrrole system with electron-deficient dienes, a wide variation of both reaction partners are possible providing attractive pyrrolo-azepine products in high yields and excellent enantioselectivities (up to 99% ee). The hetero-[6+4]-cycloaddition reaction concept is extended to include imidazoles and pyrazoles giving imidazolo- and pyrazolo-azepines. The same concept is successfully employed to include hetero-[6+2] cycloadditions of the pyrrole system with nitroolefins giving important pyrrolizidine alkaloid scaffolds. Experimental NMR and mechanistic studies show that the first step of the reaction is rapid formation of an iminium-ion, which by treatment with a base generates two hetero-6π-intermediates. Density functional theory calculations were used to determine the mechanism and sources of asymmetric induction in the hetero-[6+4] and [6+2] cycloadditions. After forming the reactive hetero-6π-components, a stepwise addition occurs with the diene or olefin leading to a zwitterionic intermediate which undergoes cyclization to afford the cycloadducts, followed by catalyst release. The stereoselectivity is controlled by the second step, and computations elaborate on the various substrate and catalyst effects that alter the experimentally observed enantioselectivity. The

computational studies provided a basis for improving the enantioselectivity of the hetero-[6+2] cycloaddition.

6.2 Introduction

Moving the borders of reactivity can pave avenues for novel methodologies in organic synthesis. An important challenge for such new developments is to provide methodologies where basic organic molecules are employed in combination with diverse reaction partners. Furthermore, combining experimental and computational investigations might provide deeper mechanistic understandings for expanding reactivity into new chemical spaces. In the following, we present the unprecedented catalytic chemo-, regio-, and enantioselective hetero-[6+4] and [6+2] cycloaddition reactions of heteroaromatic compounds. Mechanistic studies allow for identification of reactive intermediates in the catalytic cycle. Computational studies afford important insights into the mechanism and stereoselectivity of these cycloaddition reactions and allow for improvement of enantioselecivity.

Heterocyclic compounds, such as pyrroles, imidazoles and pyrazoles are fundamental scaffolds in chemistry. Their functionalization has been the center of numerous synthetic efforts, due to their presence in *e.g.* biologically relevant compounds[1-5] and materials.[6-9] For these heterocyclic compounds a large number of especially electrophilic C-functionalization are well-established methodologies.[10] Besides classical electrophilic aromatic substitution chemistry, such as halogenation, nitration, sulfonation, acylation and Vilsemeir-Haack formilation, asymmetric functionalization of pyrrole derivatives is mainly carried out under Friedel-Crafts conditions[11,12] or following C-H functionalization methodologies[13] (Scheme 6.1, top). On the other hand, their

employment as *N*-centered nucleophiles is much less explored, although *N*-fused bicycles are key backbones of many important products.[14-19]

Scheme 6.1. *N*- versus *C*- asymmetric functionalization of pyrrole derivatives.

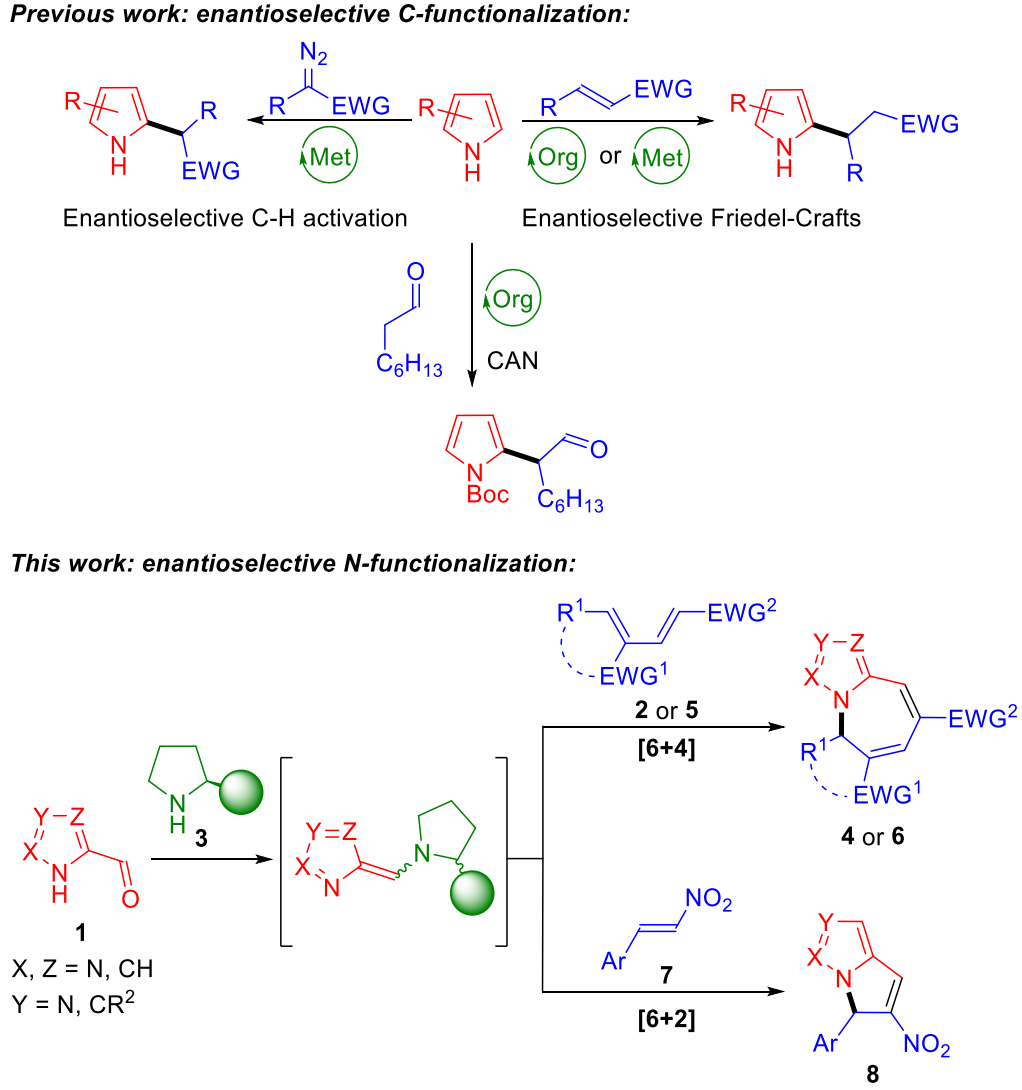

In the present work, we disclose novel direct strategies for enantioselective functionalization of pyrroles, imidazoles and pyrazoles based on unprecedented catalytic enantioselective hetero-[6+4] and [6+2] cycloaddition reaction (Scheme 6.1, bottom).

Recently, the first intermolecular organocatalytic enantioselective [6+4],[20] [8+2][21,22] and [10+4] cycloadditions[23] were disclosed. In addition, Hayashi has reported a [6+2] intramolecular cycloaddition of a fulvene moiety with a catalytically generated enamine.[24] Hong has explored stoichiometric amounts of 6-aminofulvenes for intermolecular [6+2],[25] [6+3][26] and [6+4] cycloadditions.[27] Furthermore, Chen developed an organocatalyzed enantioselective [6+2] cycloaddition where a 4-aminofulvene intermediate is produced *in situ* in catalytic quantities.[28]

Pyrroles, imidazoles and pyrazoles, substituted with an aldehyde are stable aromatic species which, upon condensation with an aminocatalyst, can render aminoazafulvenes. These 6π-components can be expected prone to participate in cycloadditions. Stable 6-aminoazafulvenes were first reported in 1975 by Kanemasa,[29] and later 6-amino-1,4-diazafulvene was shown to react as a 6π-component in thermal[30] and metal-promoted[31] cycloadditions.

To the best of our knowledge pyrrole-, imidazole- and pyrazoles-derivatives have never been demonstrated to participate in enantioselective hetero-[6+4] cycloadditions, and only few examples of racemic hetero-[6+2] cycloadditions have been disclosed.[16-18] The nitrogen-containing bicyclic compounds obtained in Scheme 6.1, bottom, include pyrrolo[1,2-a]azepines **4** or **6**, and pyrrolizine derivatives **8**. The former is a scaffold in the family of Stemona alkaloids, like Parvistemonine A **A**,[32] and cephalotaxine alkaloids **B**.[33] Furthermore, Midazolam **C** and related imidazopyrrolobenzodiazepines-based anti-anxiety drugs,[34] present a similar backbone built on a diazole moiety. Compounds **8** contain a skeleton shared between a family of recurring natural pyrrolizidine alkaloids **D** exhibiting cytotoxicity.[35] In addition, this motif is present in Ketorolac, a non-steroidal anti-inflammatory drug **E** (Scheme 6.2).[36]

Scheme 6.2. Biologically-relevant scaffolds A-E based on products 4, 6 and 8 in Scheme 7.1

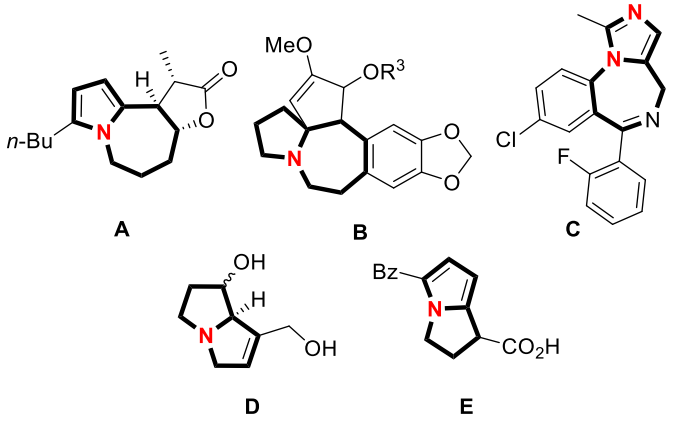

6.3 Computational Methods

All quantum chemical calculations were performed with Gaussian 09. Geometry optimizations and frequencies were calculated with the B3LYP density functional with the 6-31G(d) basis set in conjunction with the SMD implicit solvation model (chloroform). Optimized geometries were verified by frequency calculations as minima (zero imaginary frequencies) or transition structures (a single imaginary frequency). Free energy corrections were determined using unscaled B3LYP/6-31G(d) vibrational frequencies assuming a standard state of 1 atm and 298.15 K. Errors in the treatment of low modes as harmonic oscillations were mitigated by use of the quasiharmonic approximation proposed by Truhlar and coworkers. Single point energy calculations were performed on optimized geometries with M06-2X/def2-TZVPP with the implicit solvation model SMD (chloroform). The free energies reported herein were determined by adding zero-point energy and thermal correction determined using B3LYP/6-31G(d)–SMD to electronic energies computed at the M06-2X/def2-TZVPP-SMD level of theory.

Monte Carlo conformational searches were performed on the intermediates using the OPLS3 force field in Maestro/Macromodel. Transition structure input geometries were generated

by performing scans for the N–C or C–C addition at the B3LYP/6-31G(d) level of theory on the located minima (reactive intermediates).

6.4 Results and Discussion

Screening of reaction conditions for hetero-[6+4] cycloadditions. We started our investigation by treating pyrrole-2-carbaldehyde **1a** with secondary aminocatalysts **3** to provide the desired transient electron-rich 6-aminoazafulvene which was captured by electron-deficient diene **2a** in a hetero-[6+4] cycloaddition, rendering the tricyclic compound **4aa** after catalyst release. The most commonly employed aminocatalyst **3a**[37] combined with benzoic acid and molecular sieves (MS) as additives in dry $CDCl_3$ at room temperature delivered **4aa** in trace amounts, but with an excellent degree of enantioselectivity (99% ee, Table 6.1, entry 1). Changing for a less bulky fluorine substituted catalyst **3b**[38,39] improved the yield to 40% maintaining the enantioselectivity (entry 2), while catalyst **3c** afforded **4aa** with improved yield but slightly diminished enantioselectivity (entry 3). The most stereoselective catalyst was selected and, in order to overcome the poor reactivity, other reaction parameters were evaluated. Notably, to achieve a decent degree of conversion, both benzoic acid and MS had to be applied as additives (entries 4,5). Performing the reaction at 40 °C resulted in diminished yield due to rapid decomposition of **2a** (entry 6). However, employing an excess of **2a** improved the yield slightly (entry 7). Finally, after additional screening, we found that *p*MeOBzOH along with more concentrated reaction medium and a reaction time of 2 d afforded **4aa** in 73% yield and 99% ee (entry 8).

Table 6.1. Optimization of the hetero-[6+4] cycloaddition.[a]

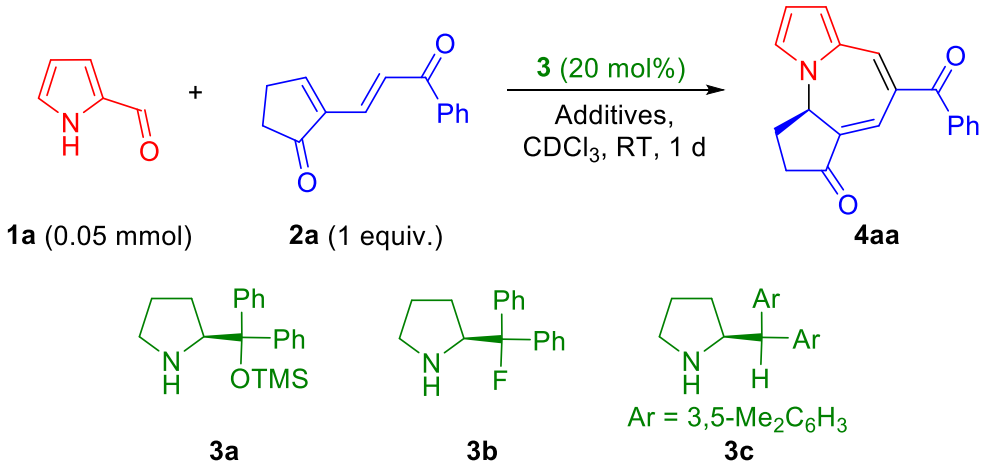

Entry	Cat **3**	Additive[b]	Yield (%)[c]	ee (%)[d]
1	3a	BzOH, MS	5	99
2	3b	BzOH, MS	40	99
3	3c	BzOH, MS	65	95
4	3b	MS	12	n.d.
5	3b	BzOH	10	n.d.
6[e]	3b	BzOH, MS	20	96
7[f]	3b	BzOH, MS	46	99
8[f]	3b	*p*MeOBzOH, MS	75(73)[g]	99

[a] Reaction conditions: Supporting Information. [b] 20 mol% acid used. [c] Yield measured by NMR of the crude reaction mixture with Et_4Si as internal standard. [d] Determined by chiral stationary phase UPCC. [e] Reaction at 40 °C. [f] Reaction conditions: **1a** (0.1 mmol), **2a** (0.15 mmol), 2 d. [g] Isolated yield.

Scope of hetero-[6+4] cycloadditions for pyrroles. First, variations of substituents in the 4-position of the pyrrole ring were employed. The introduction of heteroatoms such as bromine (**1b**), silicon (**1c**) and sulfur (**1d**) provided the products **4ba-da** in 68-90% yield and 99% ee (Table 6.2, entries 2-4). The absolute configuration of **4da** was assigned by single crystal X-ray analysis and extended by analogy to products **4** and **6** (*vide infra*). An aromatic substituent (aldehydes **1e** and **1f**) gave **4ea** and **4fa** with similarly high yields and excellent stereoselectivities (entries 5,6). Modifications on the electron-withdrawing group of **2** were then explored, finding that different

aromatic ketones (**2b-d**) and esters (**2e**,**f**) allowed the synthesis of **4ab-af** in 54-88% yield and 99% ee (entries 7-11).

Table 6.2. Reaction scope of the hetero-[6+4] cycloaddition: variation of aldehydes 1 and electron-poor dienes 2[a]

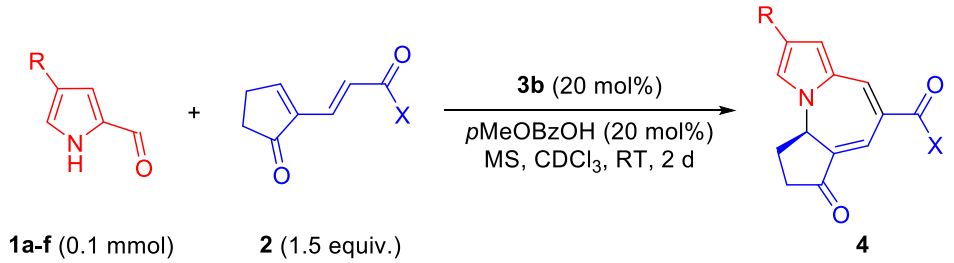

1a-f (0.1 mmol) **2** (1.5 equiv.) **4**

Entry	1, R	**2**, X	Yield (%)[b]	ee (%)[c]
1	**1a**, H	**2a**, Ph	**4aa** 73	99
2	**1b**, Br	**2a**, Ph	**4ba** 68	99
3	**1c**, Si(*i*Pr)$_3$	**2a**, Ph	**4ca** 90	99
4	**1d**, SPh	**2a**, Ph	**4da** 70	99
5	**1e**, Ph	**2a**, Ph	**4ea** 65	99
6	**1f**, *p*MeOC$_6$H$_4$	**2a**, Ph	**4fa** 52	99
7	**1a**, H	**2b**, *p*BrC$_6$H$_4$	**4ab** 87	99
8	**1a**, H	**2c**, *p*MeOC$_6$H$_4$	**4ac** 54	99
9	**1a**, H	**2d**, *p*NO$_2$C$_6$H$_4$	**4ad** 67	99
10	**1a**, H	**2e**, OEt	**4ae** 60	99
11	**1a**, H	**2f**, OPh	**4af** 88	99

[a] Reaction conditions: Supporting Information. [b] Isolated yield. [c] Determined by chiral stationary phase UPCC.

Scope of hetero-[6+4]-cycloadditions for imidazoles and pyrazoles. Gratifyingly, the described hetero-[6+4] cycloaddition strategy could be extended to imidazoles (**1g**,**h**) and pyrazoles (**1i**), applying only some minor modifications of the reaction conditions. The scope of the reaction of **1g-i** was demonstrated by reaction with four electron-poor dienes **2** (Scheme 6.3). Imidazole-2-carbaldehyde **1g**, as well as imidazole-4-carbaldehyde **1h**, required in most of the

cases milder reaction conditions (10 mol% catalyst and additive and higher dilution) due to some instability of the respective products in the reaction mixtures. The hetero-[6+4] cycloadducts **4ga**, **4gd** and **4ge** were obtained in moderate to good yields (46-69%) and high enantioselectivities (84-95% ee). In comparison, similar high enantiomeric excesses, but lower yields were obtained for **4ha**, **4hb** and **4he**, probably due to enhanced instability of these products. Finally, pyrazole-5-carbaldehyde **1i** turned out to be the least reactive heterocycle investigated; however, we were pleased to obtain **4ia** and **4ib** in 31% and 38% yield, and 87% and 90% ee, respectively.

Scheme 6.3. Scope of the hetero-[6+4] cycloaddition of imidazoles and pyrazole 1g-i with electron-deficient dienes 2[a]

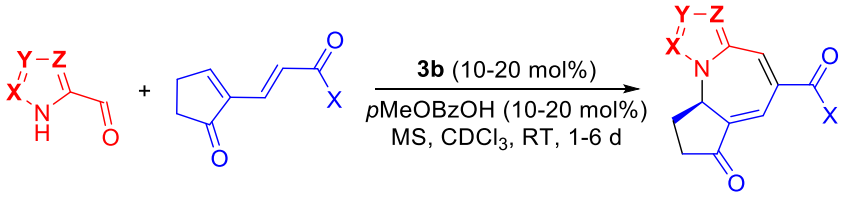

1g-i (2 equiv.) **2** (0.1 mmol) **4**: Yield[b], ee[c]

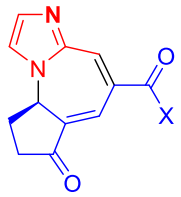

4ga, X = Ph: 69%, 93% ee
4gd[d], X = *p*$NO_2C_6H_4$: 46%, 89% ee
4ge, X = OEt: 62%, 95% ee

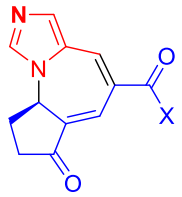

4ha, X = Ph: 34%, 94% ee
4hb, X = *p*BrC_6H_4: 20%, 95% ee
4he[e], X = OEt: 54%, 96% ee

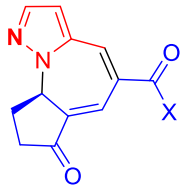

4ia[d,f], X = Ph: 31%, 87% ee
4ib[d,f], X = *p*BrC_6H_4: 38%, 90% ee

[a] Reaction conditions: Supporting Information. Unless otherwise stated, 10 mol% **3b** and 10 mol% *p*MeOBzOH were employed; reaction time: 1 d. [b] Isolated yield. [c] Determined by chiral stationary phase UPCC. [d] **3b** (20 mol%), *p*MeOBzOH (20 mol%) [e] Reaction time: 2 d. [f] Reaction time: 6 d.

In addition, a different class of electron-deficient dienes **5** based on an acyclic, and less conformationally restricted scaffold reacted with pyrrole **1a** and imidazole **1g** as well, although requiring an increased catalyst and additive loading (40 mol%), and a longer reaction time (4 d). Both an electron-neutral aryl substituent (**5a**) and an electron-poor one (**5b**) were tolerated (Scheme 6.4). Products **6aa** and **6ab**, displaying a different decoration of the seven-membered ring with respect to cycloadducts **4**, were obtained in good yields and excellent enantioselectivities. Imidazole **1g** also reacted with **5a**, affording **6ga** in moderate yield and slightly diminished enantioselectivity. However, the reaction with ester **5c** was found to give rise to **6gc** in only 10% yield and 51% ee. These examples demonstrate the broad applicability of the methodology for the construction of structurally diverse hetero-[6+4]-cycloadducts.

Scheme 6.4. Scope of the hetero-[6+4] cycloaddition of pyrrole and imidazole with electron-deficient dienes 5[a]

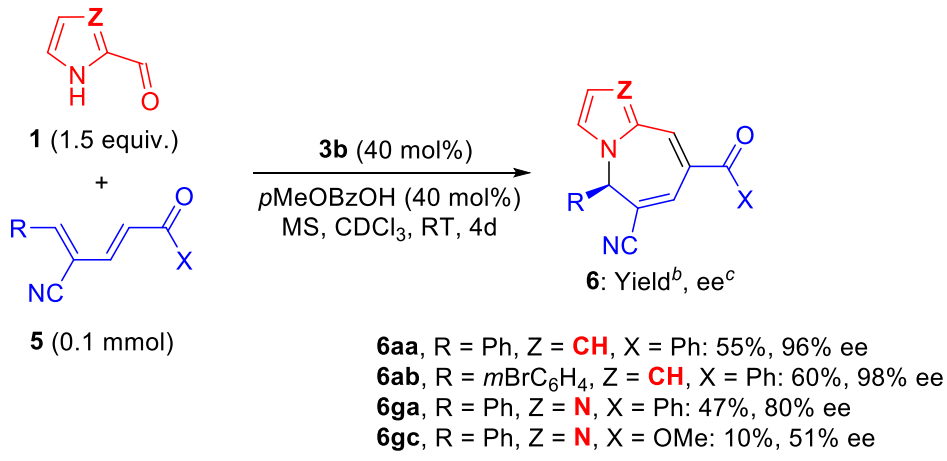

[a] Reaction conditions: Supporting Information. [b] Isolated yield. [c] Determined by chiral stationary phase UPCC.

Transformation of hetero-[6+4] cycloadducts. Having explored the reactivity of various substrates towards the hetero-[6+4]-cycloaddition reaction, we decided to illustrate the bicyclic system as intermediate in the synthesis of more functionalized compounds. The reaction of **4aa** with BnSH in presence of a catalytic amount of Et_3N afforded compound **9**, bearing 3 consecutive stereocenters, as a single diastereomer in 57% yield and 99% ee (Scheme 6.5).

Scheme 6.5. Transformation of [6+4]-cycloadduct[a]

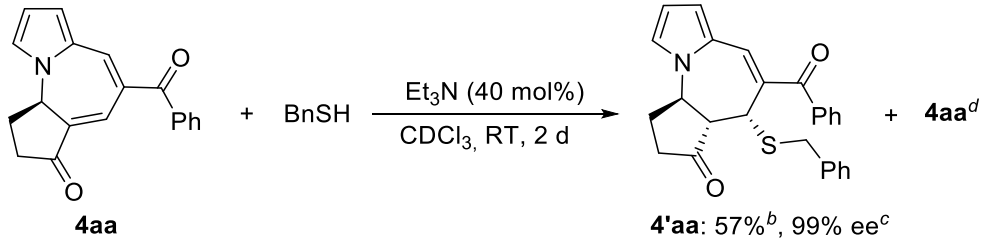

[a] Reaction conditions: Supporting Information. [b] Isolated yield. [c] Determined by chiral stationary phase UPCC. [d] 38% recovered starting material (**4aa**).

Screening of reaction conditions for hetero-[6+2] cycloadditions. We then envisioned to extend this strategy to enantioselective hetero-[6+2] cycloadditions.[40,41] We initially found that pyrrole-2-carbaldehyde **1a** reacted with 1.5 equiv. of *trans*-β-nitrostyrene **7a** in presence of catalyst ***ent*-3a** (20 mol%) in $CDCl_3$ at room temperature to produce cycloadduct **8aa** in 40% yield and 66% ee after 48 h (Table 6.3, entry 1). The addition of benzoic acid (20 mol%) increased the enantioselectivity (entry 2) and performing the reaction in the presence of MS allowed to reach the same yield in 24 h (entry 3). Employing catalyst **3b**, which was highly stereoselective in the hetero-

[6+4] cycloaddition, resulted in slightly improved yield and similar enantioselectivity (entry 4). Bulkier catalyst **3d** improved the enantioselectivity to 82% ee, without significantly lowering the conversion (entries 5,6). To ease the purification, we inverted the **1a**/**7a** ratio, affording full consumption of **7a**. During this experiment we noticed that compound **8aa** was prone to double bond shift in the reaction mixture, leading to isomer **8'aa**. We hypothesized that this shift was acid promoted, leading us to lower its amount to 10 mol%. Even so, we found that this side reaction still occurred, but only when the nitroolefin was consumed (entries 7,8). Therefore, an excess of nitroolefin was reapplied to disfavour the isomerization, thus delivering the optimal conditions (entry 9). Unfortunately, we observed both isomerization and decomposition of **8aa** as isolated compound. At present time we did not elucidate the pathway of this double bond shift. However, we exclude an equilibration between the two isomers, since recovered **8aa** showed only slightly diminished enantiomeric excess instead of displaying complete racemization. Nonetheless, we surmised that exploiting the reactivity of the electrophilic double bond, might circumvent this issue and at the same time bring diversity to the methodology. We therefore conceived a two-step one-pot strategy consisting in the addition of a nucleophile to the reaction mixture at the end of the hetero-[6+2] cycloaddition step.

Table 6.3. Optimization of the hetero-[6+2] cycloaddition.[a]

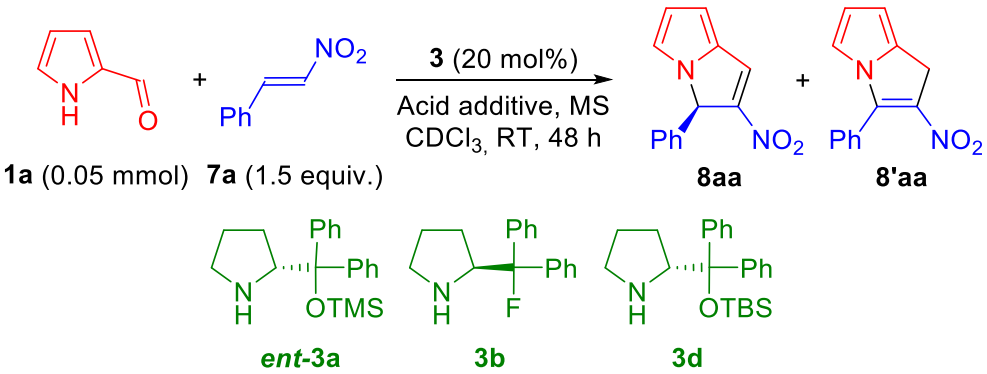

Entry	**3**	Addi-tive	Yield (conv. of **7a**, %)[b,c]	Ratio **8aa**/ **8'aa**[b]	ee (%)[d]
1	***ent*-3a**	-[e]	40 (50)	>20:1	66
2	***ent*-3a**	BzOH[h,e]	40 (48)	>20:1	76
3[f]	***ent*-3a**	BzOH[h]	41 (52)	>20:1	76
4	**3b**	BzOH[h]	49 (59)	>20:1	-77
5[f]	**3d**	BzOH[h]	35 (30)	>20:1	82
6	**3d**	BzOH[h]	50 (65)	18:1	82
7[f,g]	**3d**	BzOH[i]	40 (80)	13:1	81
8[g]	**3d**	BzOH[i]	41 (>99)	2.5:1	76
9	**3d**	BzOH[i]	62 (65)	>20:1	82

[a] Reaction conditions: Supporting Information. [b] Measured by NMR of the crude reaction mixture with Et_4Si as internal standard. [c] Amount of **7a** present in the reaction mixture divided by initial amount. [d] Determined by chiral stationary phase UPCC. [e] No MS added. [f] Reaction time: 24 h. [g] In this case, the reaction was carried out with an inverted ratio of 1.5 equiv. of aldehyde. [h] 20 mol% of BzOH used. [i] 10 mol% of BzOH used.

Scope and transformations of hetero-[6+2] cycloadducts of pyrroles. It was found that aryl groups on the pyrrole ring would lead to stable hetero-[6+2] adducts and **8ea** and **8fa**, derived from pyrrole-2-carbaldehydes **1e** and **1f** reacting with *trans*-β-nitrostyrene **7a**, were directly isolated in good yields and enantioselectivities (Scheme 6.6).

Scheme 6.6. Scope of the hetero-[6+2] cycloaddition of pyrrole-2-carbaldehydes 1 with nitroolefins 7[a]

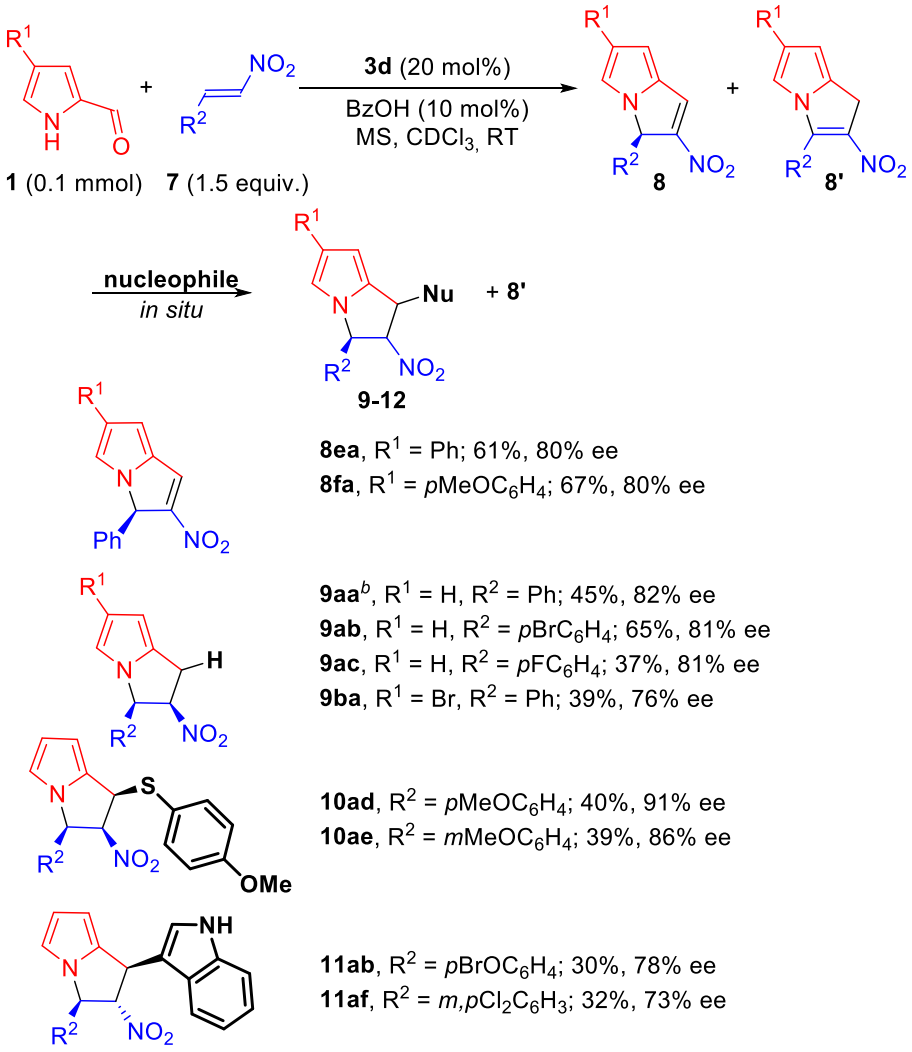

[a] Reaction conditions: Supporting Information. Isolated yields. Enantiomeric excess determined by chiral stationary phase UPCC. [b] Reaction performed on 1 mmol scale.

In Scheme 6.6, we demonstrate the hetero-[6+2] cycloaddition of two different pyrrole-2-carbaldehydes with various nitroolefins coupled with a selective reduction with $NaBH_4$ for the preparation of dihydropyrrolizines **9**. This reaction afforded **9aa**, derived from pyrrole-2-carbaldehyde **1a** and *trans*-β-nitrostyrene **7a** in 45% overall yield and 82% ee. This protocol was also successfully applied to the hetero-[6+2] cycloaddition of **1a** with 4-bromo- and 4-fluoro substituted nitroolefins **7b** and **7c** affording **9ab** and **9ac** with similar results. The 4-bromo

substituted pyrrole-2-carbaldehyde **1b** underwent the same reaction sequence, displaying slightly diminished efficiency. 4-Methoxy- and 3-methoxy substituted nitroolefins **7d** and **7e** also participated successfully in the hetero-[6+2] cycloaddition with **1a**. Further diversity was demonstrated by addition of benzylthiol at the end of these last cycloadditions, giving **10ad** and **10ae** with moderate yields and good enantioselectivities, displaying three contiguous stereocenters, as single diastereoisomers. A neutral nucleophile such as indole was also found to be a competent reaction partner. This protocol was employed to prepare **11ab** and **11af**, obtained as single diastereoisomers. The absolute stereochemistry of compound **8ea** was determined by ECD analysis. For compounds **9**, **10** and **11**, the stereochemistry of the stereocenters created during the transformations, relative to that of the original stereocenter, was assigned by NMR spectroscopy. The disclosed one-pot hetero-[6+2] cycloaddition – nucleophilic addition sequence – was thus demonstrated to display wide applicability and synthetic utility in the rapid preparation of complex and biologically relevant structures from simple and commercially available starting materials.

MECHANISTIC INVESTIGATIONS

Experimental investigations. A series of experimental investigations were initiated to gain insight into possible intermediates and reaction pathway(s) involved in the mechanism of the hetero-[6+4]- and [6+2] cycloadditions. We started by attempting to detect the reactive intermediate(s) by means of NMR spectroscopy.[42-44] A proposed mechanism for the hetero-[6+4] cycloaddition is outlined in Scheme 6.7.

Scheme 6.7. Proposed mechanism for the formation of the hetero-[6+4] cycloadduct *via* iminium-ion I and hetero-6π-component II

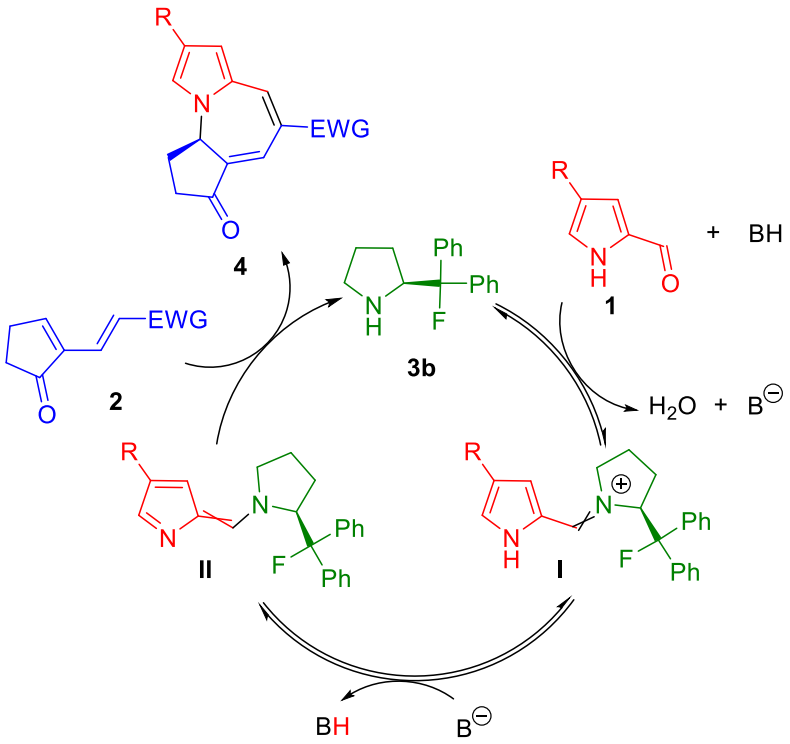

The first step of the mechanistic investigations was to identify the proposed intermediates **I** and **II** in Scheme 6.7. We started by treating pyrrole-2-carbaldehyde **1b** with a stoichiometric amount of catalyst **3b** and benzoic acid in $CDCl_3$ at room temperature over MS for 18 h (Scheme 6.8, Experiment 1). A new species was observed by ^1H NMR, assigned to be iminium-ion **I**. Isolation of **I** was impaired by its tendency to rapidly hydrolyze in air.[45] When the electron-deficient diene **2e** was added to the NMR tube, product **4be** (EWG = CO_2Et, 99% ee) was formed, and in parallel iminium-ion **I** disappeared. The absence of MS in the NMR tube considerably slowed down the regeneration of intermediate **I**, via condensation of **3b** with **1b**, resulting in increasing catalyst **3b** concentration over time. We thus proved the role of **I** as a productive intermediate for the reaction. By treatment of the intermediate **I** with a base, such as triethylamine, another species appeared, showing broad signals in ^1H NMR and two distinctive different signals in ^{19}F NMR, suggesting the presence of two isomers. These NMR signals were assigned to intermediate **II**, which was also unstable and prone to hydrolysis. Further characterization of

intermediate **II** was not possible (Scheme 6.8, Experiment 2). Then, electron-poor 4π-component **2e** was treated with preformed intermediate **II**, in the absence of MS, and formation of product **4be** was observed (^{1}H NMR), along with consumption of **II** and concomitant catalyst **3b** release (monitored by ^{19}F NMR), suggesting **II** as a second reactive intermediate in the hetero-[6+4] cycloaddition. It should be noted that under these latter stoichiometric reaction conditions and in the presence of triethylamine, performed for the mechanistic investigations, product **4be** was formed in 85% ee, which is lower than the excellent enantioselectivities obtained in the hetero-[6+4] cycloaddition under catalytic conditions.

Scheme 6.8. Experiments for the observation of intermediates I and II and their reaction with diene 2e.

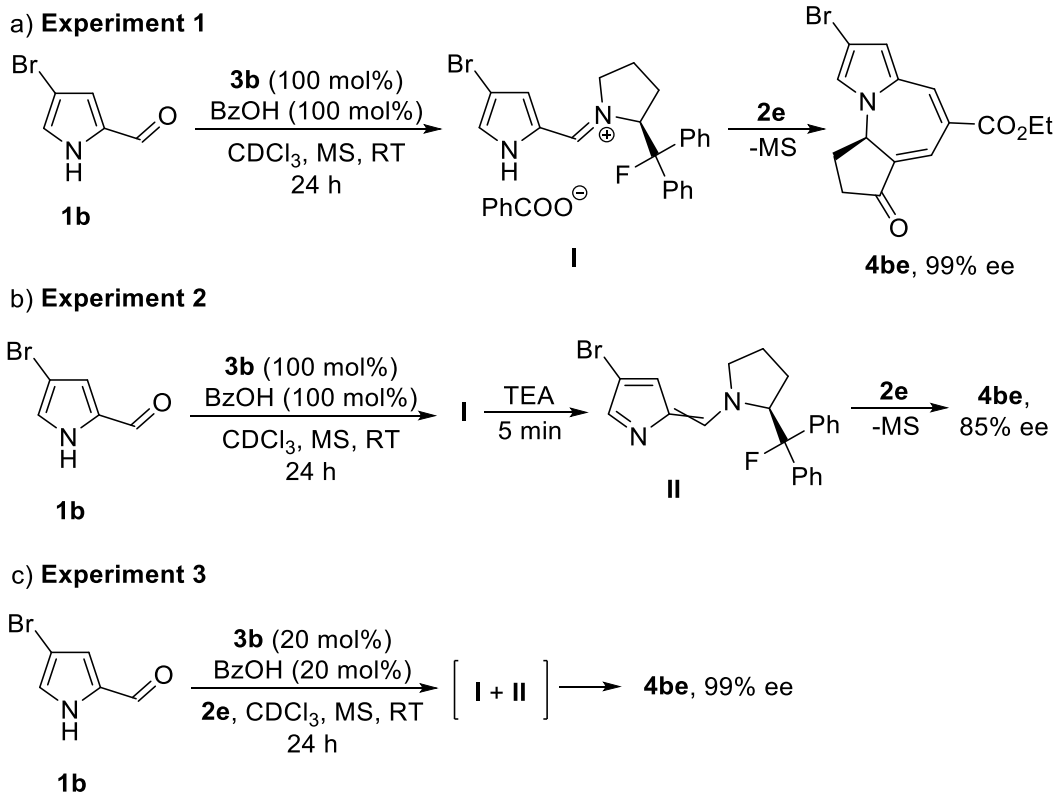

To better mimic the optimized reaction conditions, we moved to monitor the actual catalytic reaction proceedings by mean of NMR spectroscopy (Scheme 6.8, Experiment 3 and Figure 6.1). The aldehyde was continuously consumed during the reaction (graph A). The concentration of the catalyst quickly decreased at the beginning of the reaction course, and, since it was regenerated by product formation, its amount reached a steady state (graph B). Interestingly, the rapid formation of iminium-ion **I** was observed at first and ^{19}F NMR revealed the presence of intermediate **II** as well, in about 3:1 ratio in favor of **I**. Intermediate **I** reached a steady state after a rapid build-up (graph C), and remained constant for several hours, while product **4be** was slowly forming (graph D). During these investigations, intermediate **II**, appeared as two distinct signals, confirming the presence of two isomers. The importance of MS was also underlined by this experiment, as they allowed constant replacement of the reacted intermediates by facilitating the condensation of catalyst **3b** and **1b**. Observability of intermediates **I** and **II** in the experiment under the real optimized reaction conditions (*i.e.* their formation was not forced), indicates compelling evidence of these species being reactive intermediates in the hetero-[6+4] cycloaddition.

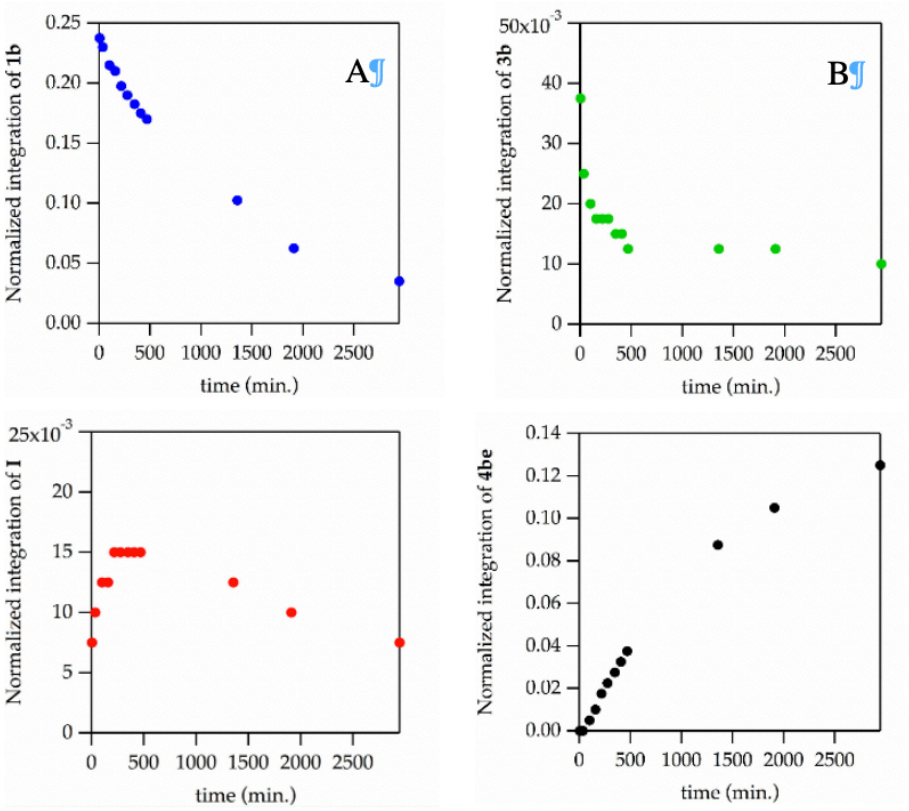

Figure 6.1. Consumption of pyrrole **1b** (graph A); amount of catalyst **3b** over time (graph B); the development of iminium-ion **I** over time (graph C) and cycloadduct **4be** formation (graph D) as a function of time. Reaction conditions: Pyrrole **1b** (1 equiv.), electron-deficient diene **2e** (1 equiv.), catalyst **3b** (20 mol%) and benzoic acid (20 mol%) in $CDCl_3$ (0.17 M), in the presence of MS. Integrations have been normalized towards TES as internal standard.

Computational investigations. The energetic preferences of iminium-ion **I** and intermediate **II** were investigated with density functional theory. Computations were performed with M06-2X[46]/def2-TZVPP[47] corrected energies with the SMD[48] ($CHCl_3$) solvation model on B3LYP[49]/6-31G(d) calculated geometries.

Intermediate structures. The lowest-energy conformations for the *trans*- and *cis*-iminium-ion are shown in Figure 6.2. Their difference in free energy is 3.2 kcal/mol, in favor of the *trans*-

iminium-ion. The *cis*-iminium-ion acquires a disfavored conformation of the catalyst to accommodate the pyrrole substituent (the high-energy catalyst is shown in Figure 6.2). This corroborates well with the NMR observation of one signal for iminium-ion **I**. The *cis*- and *trans*-6π-components were also calculated. We found that their difference in free energy was 1.1 kcal/mol in favor of the *cis*-6π-component. This also agrees with the observation of two signals for intermediate **II**, where both *cis*- and *trans*-6π-components are observable by NMR spectroscopy.

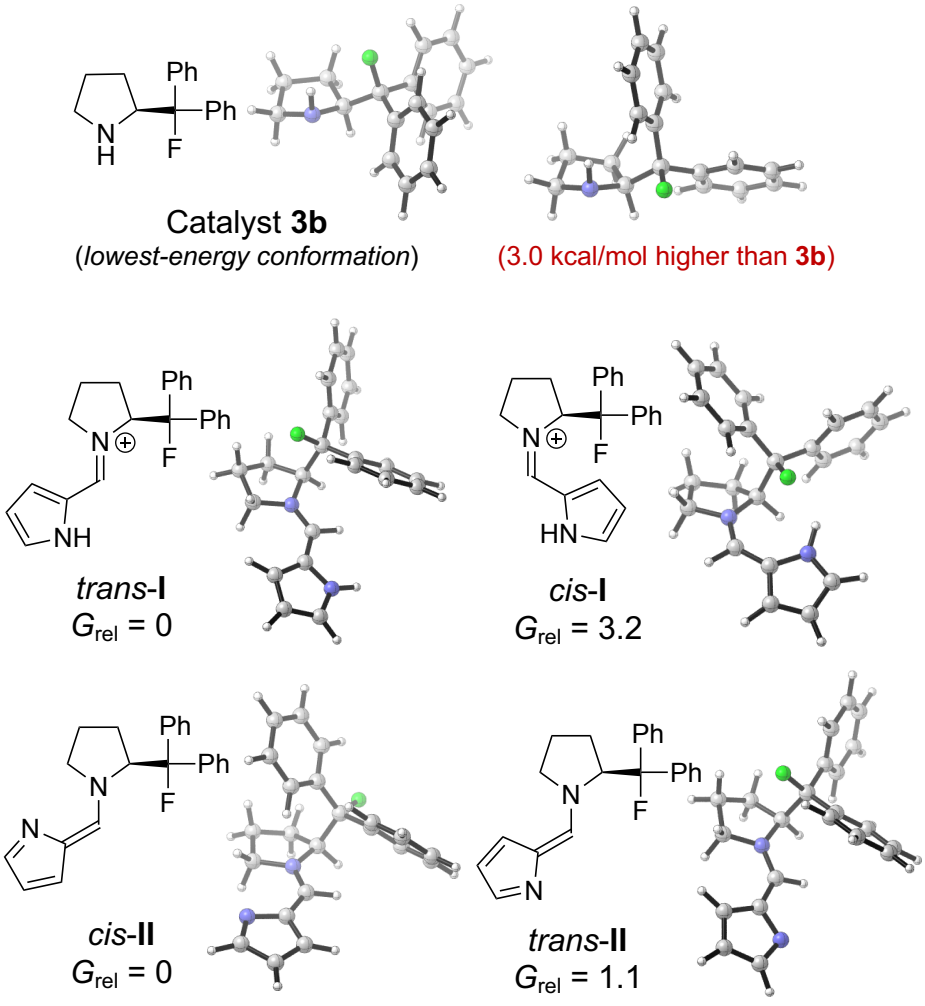

Figure 6.2. Optimized ground-state structures for two conformations of the catalyst and lowest-energy conformations for the *cis*- and *trans*-arrangements of intermediates **I** and **II** (M06-2X/def2-TZVPP–SMD//B3LYP/6-31G(d)–SMD ($CHCl_3$).

Calculation of the enantioselective hetero-[6+4] cycloaddition pathway. To probe the mechanism of the hetero-[6+4] cycloadditions, DFT calculations were performed to locate the transition states of the reaction of the 6π-components **II** and a slightly truncated model of substrate **2**. This truncation modified the aryl group or ester on the terminal ketone to a methyl to avoid conformational flexibility. The concerted cycloaddition transition structures were exhaustively searched, but only revealed step-wise pathways.

We computed the free energy profile for the reaction mechanism after the hetero-6π-components **II** are formed (Figure 6.3). The zero-energy refers to the separated hetero-6π-components **II** and substrate **2**. The first step involves nucleophilic addition of the pyrrole nitrogen to the electrophilic β-position of the cyclic enone. The two lowest-energy transition structures leading to the two stereoisomers are **TS-Ia** and **TS-Ib**. Transition structure **TS-Ia** provides the (*R*)-zwitterionic intermediate (*R*)-**int-Ia** which leads to the observed stereoisomer with a free energy of activation barrier of 23.4 kcal/mol. Transition structure **TS-Ib** yields the corresponding (*S*)-intermediate and minor stereoisomer with a free energy of activation barrier of 22.8 kcal/mol. Interestingly, both low-energy TSs are nucleophilic additions via the pyrrole nitrogen lone pair instead of the π-system. Both transition structures arise from the *trans*-**II** hetero-6π-component. All transition structures from *cis*-**II** were at least 3.0 kcal/mol higher in energy. We found the difference in energy between **TS-Ia** and **TS-Ib** to be 0.6 kcal/mol, in favor of **TS-Ib**. We predict the two zwitterions, (*R*)-**int-Ia** and (*S*)-**int-Ib**, form in approximately a 74:26 ratio. The zwitterions

are 8.0 and 9.5 kcal/mol higher in energy than the separated (*R*)- and (*S*)-intermediates, respectively.

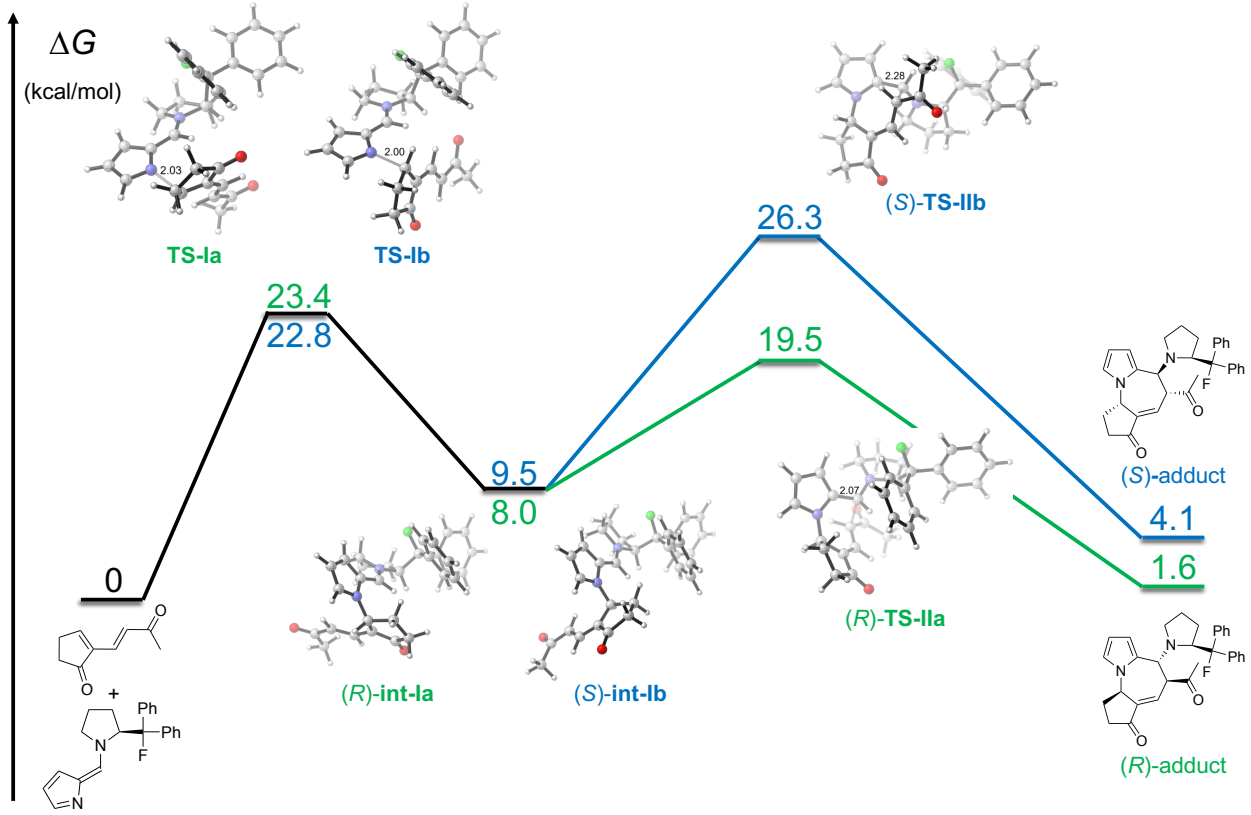

Figure 6.3. Computed free energy reaction pathway profile for the hetero-[6+4] cycloaddition involving hetero-6-π-intermediate *trans*-**II** derived from catalyst **3b** and model of substrate **2** (M06-2X/def2-TZVPP–SMD//B3LYP/6-31G(d)–SMD ($CHCl_3$). The starting point is the computed free energy of the separated *trans*-**II** and substrate and all following energies are compared to them. All structures are lowest-energy conformations of transition states or ground states.

From the zwitterionic intermediate, the cyclization via C–C bond formation occurs by addition of the conjugated enolate to the carbon of the iminium-ion. The lowest-energy transition structures for the cyclization of the major and minor stereoisomers are shown in Figure 6.3. The

lowest-energy TS, (*R*)-**TS-IIa** leads to the observed adduct with a free energy of activation barrier of 19.5 kcal/mol, which eliminates to the product (not computed). The lowest-energy TS leading to the minor stereoisomer, (*S*)-**TS-IIb**, has a free energy of activation barrier of 26.3 kcal/mol. Transition structure (*S*)-**TS-IIb** is disfavored due to the *s-cis* arrangement of the iminium-ion and high-energy conformation of the pyrrolidine catalyst (see high-energy catalyst conformation in Figure 6.2). The source of these unstable interactions arises from the ketone position in the C–C bond TS. In (*R*)-**TS-IIa**, the ketone is on the opposite side of the bulky pyrrolidine substituent, whereas in (*S*)-**TS-IIb** the ketone points directly at the diphenyl fluoro group, forcing the conformational changes. In summary, the stereoselectivity is controlled by the C–C bond forming step - the second step in the step-wise mechanism. The N–C bond forming step yields both (*R*)- and (*S*)-intermediates, however only (*R*)-**int-Ia** cyclizes readily to the adduct. The barrier for cyclization for (*S*)-**TS-IIb** is significantly higher than the reverse reaction back to the reactants ($\Delta\Delta G^{\ddagger}$ = 3.5 kcal/mol), which causes (*S*)-**int-Ib** to reverse until it is completely consumed and converted to the (*R*)-adduct. This corroborates with the experimental results where only the (*R*)-product is observed. Calculations using catalyst **3c** reveal a decreased difference in the free energy barriers between forward cyclization and reverse for the zwitterionic intermediate leading to the minor enantiomer ($\Delta\Delta G^{\ddagger}$ = 2.8 kcal/mol) in agreement with the 95% ee (Table 6.1, entry 3). This is due to removing the disfavoured F•••O interaction found in (*S*)-**TS-IIb**.

Calculation of the enantioselective hetero-[6+2] cycloaddition pathway. While the hetero-[6+4] cycloadditions are practically stereospecific for the reactions with the electron-deficient dienes **4**, the hetero-[6+2] cycloaddition variant is modest in enantioselectivity. We examined the example in Table 6.3, entry 4, due to its close similarity with the hetero-[6+4] cycloaddition system to determine the drop in enantioselectivity to 77% ee. We performed exhaustive computational

modelling of the mechanism, and show the free energy profile for lowest-energy TSs and intermediates in Figure 6.4. The two lowest-energy transition structures for the first N–C bond forming step, **TS-IIIa** and **TS-IIIb**, are within 0.2 kcal/mol, similar to the hetero-[6+4] cycloaddition. They have a free energy of activation barriers of 23.8 and 24.0 kcal/mol for the (*R*)- and (*S*)-pathways, respectively. The two stereoisomeric intermediates, (*S*)-**int-IIIa** and (*R*)-**int-IIIb**, are formed. In this case, (*S*)-**int-IIIa** cyclizes readily with a free energy of activation barrier of 14.7 kcal/mol compared to the separated reactants (2.6 kcal/mol from the intermediate) to form the (*S*)-adduct. In contrast, the barrier for cyclization to form the (*R*)-adduct is 23.8 kcal/mol *via* (*R*)-**TS-IVb**, equivalent to the N–C bond forming barrier for the (*R*)-pathway. This TS is unfavourable due to the steric interaction between the nitro group and the phenyl of the pyrrolidine.

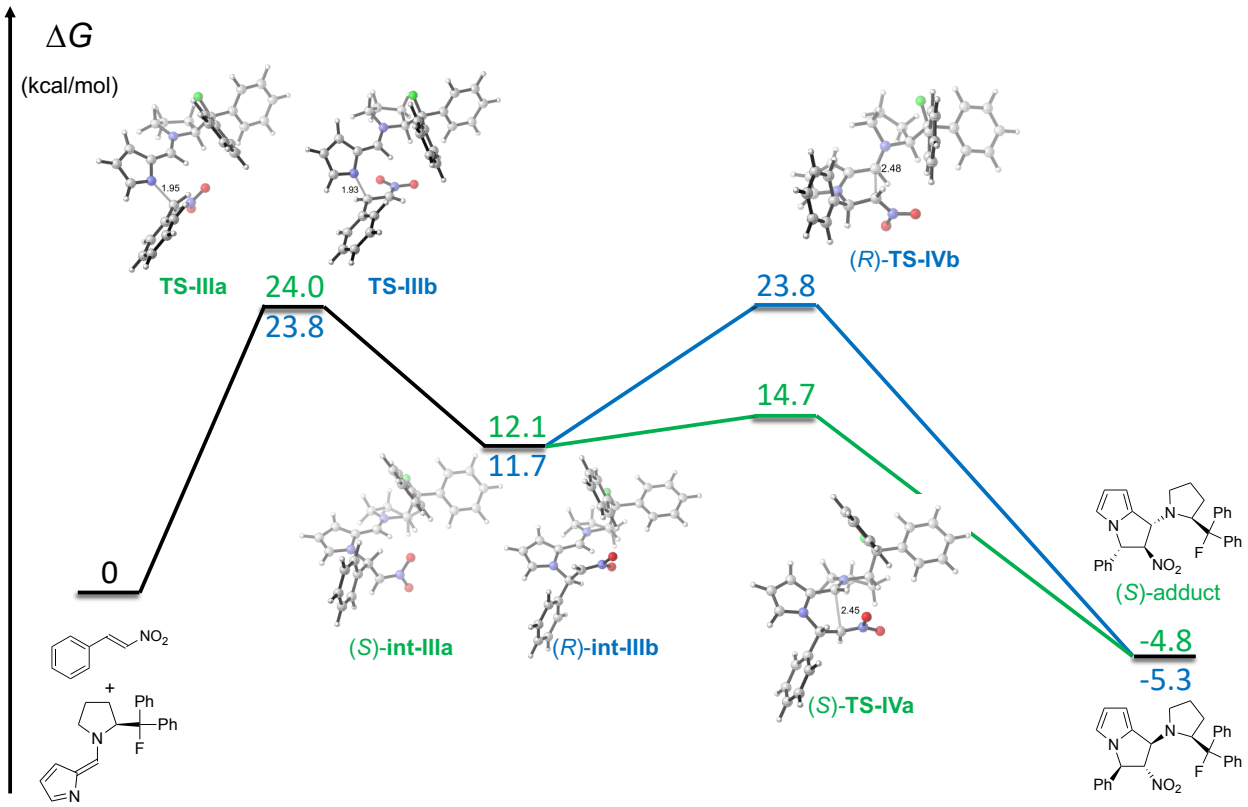

Figure 6.4. Computed free energy reaction pathway profile for the hetero-[6+2] cycloaddition involving hetero-6-π-intermediate *trans*-**II** derived from catalyst **3b** and model of substrate **7**

(M06-2X/def2-TZVPP–SMD//B3LYP/6-31G(d)–SMD ($CHCl_3$). The starting point is the computed free energy of the separated *trans*-**II** and substrate and all following energies are compared to them. All structures are lowest-energy conformations of transition states or ground states.

Unlike the [6+4] cycloaddition, the nitro group is small enough not to force a conformational change in the catalyst in the [6+2] cycloaddition, and thus the destabilization of (*R*)-**TS-IVb** is not as pronounced as (*S*)-**TS-IIb**. The free energy barrier for (*R*)-**TS-IVb** is equal to the N–C bond-forming step for the (*R*)-pathway. To summarize, the N–C bond formation occurs without stereoselectivity and yields both zwitterionic intermediates. The (*S*)-adduct forms rapidly, whereas the (*R*)-intermediate (*R*)-**int-IIIb** has equal barriers to form the adduct or reverse to the reactants, leading to a 2:1 ratio of (*R*)- to (*S*)-stereoisomers. In comparison to the hetero-[6+4] cycloaddition with the electron-deficient diene **2**, which is stereospecific, the hetero-[6+2] cycloaddition achieves modest enantioselectivity due to the smaller size of the substrate **7** in the C–C transition state.

Based on these computational results, we anticipated that destabilizing the minor pathway transition structure for the C–C bond (*R*)-**TS-IVb** would improve the enantioselectivity. We predicted that substitution at the 3,5-positions of the pyrrolidine phenyl groups could provide an unfavourable steric environment around the nitro group in (*R*)-**TS-IVb**. This substitution would not interfere with the other stereoisomeric C–C bond-forming TS (*S*)-**TS-IVa**, as well as both the N–C bond forming TSs. A 3,5-Me_2Ph substituted pyrrolidine, catalyst **3j**, was synthesized to test the prediction (Scheme 6.8). The reaction of **1a** and nitrostyrene **7a** with catalyst **3j** afforded the corresponding cycloadduct ***ent*-8aa** with improved enantioselectivity of 85% ee (Scheme 6.8),

supporting the computational prediction. The transition structure for the disfavoured C–C forming bond transition structure **TS-3j-a** is also shown in Scheme 8 with a free energy barrier of 25.0 kcal/mol, showing the increased steric repulsion between the nitro group the methyl substituent introduced in catalyst **3j**.

Scheme 6.8. Experiments for the predicted catalyst **3j** and calculated transition structure.

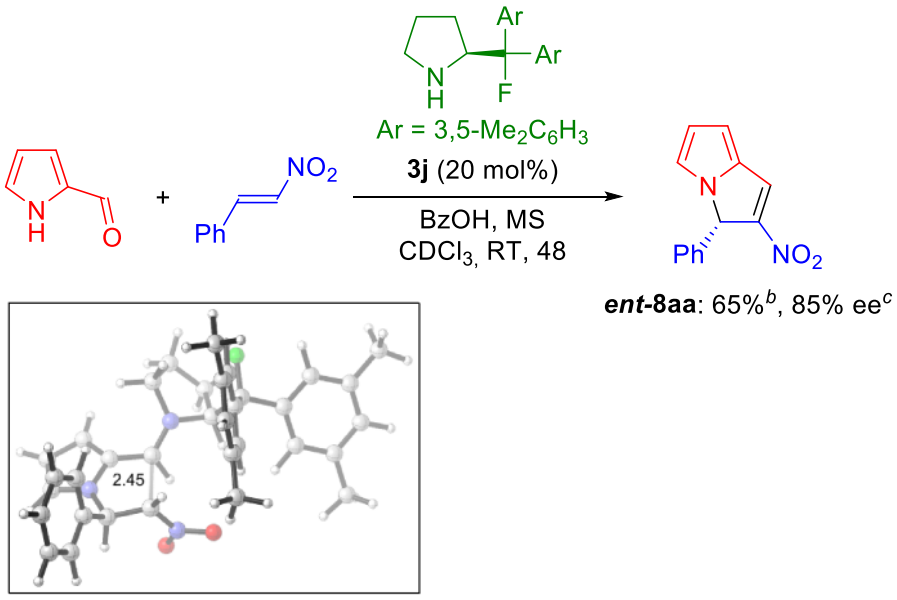

6.5 Conclusions

In conclusion, we have developed a novel concept for catalytic enantioselective activation of heteroaromatic compounds, such as pyrroles, imidazoles and pyrazoles by organocatalysis by generating electron-rich hetero-6π-intermediates acting as a nucleophile. This intermediate reacts in a highly chemo-, regio- and stereoselective manner with various types of electron-deficient dienes and olefins, in [6+4]- and [6+2] cycloaddition reactions, respectively. The reaction of pyrroles provide bio-attractive pyrrolo-azepine scaffolds by a [6+4] cycloaddition reaction with

dienes in high yields and enantioselectivities up to 99% ee. Imidazolo- and pyrazolo-azepines are formed in a similar [6+4] cycloaddition by reaction of imidazoles and pyrazoles with dienes. The activation concept for pyrroles has been extended to enantioselective [6+2] cycloaddition reactions with nitroolefins affording pyrralizidines alkaloid scaffolds which are demonstrated to undergo further reactions. By NMR investigations, we have been able to identify two different types of intermediates in the catalytic cycle. First, an iminium-ion intermediate is formed; then deprotonation of the heteroaromatic N–H leads to the reactive electron-rich hetero-6□-intermediate formed in two isomeric forms, of which only one reacts with the diene and olefin in the [6+4] and [6+2] cycloadditions, respectively. The methodology developments, scope of the two different cycloaddition reactions and mechanistic investigations allowing for the identification of reactive intermediates have been coupled with extensive computational studies. Based on these computational studies, we have shown that these hetero-[6+4] and [6+2] cycloadditions occur via step-wise mechanisms. The stereocontrol occurs at the second C–C bond forming step, rather than the N–C bond forming transition state. The source of stereoselectivity is the difference in free energy of activation barriers between the C–C and N–C TS for the minor stereoisomer, rather than the traditional comparison between two stereoisomeric transition structures. In the case of the hetero-[6+4] cycloaddition, high stereoselectivity is achieved due to the bulky 4π substrate which interacts strongly with the substituent of the pyrrolidine catalyst. For the hetero-[6+2] cycloaddition system, the nitro-vinyl substrate is naturally smaller and does not cause large steric effects at the pyrrolidine catalyst, which lowers the C–C bond forming TS and thus achieves worse stereoselectivity. These computational investigations have predicted that catalyst modification might improve the enantioselectivity. [6+2] Cycloadditions applying a catalyst based on these predictions shows increased enantioselectivity from 77% to 85% ee.

6.6 References

(1) Bhardwaj, V.; Gumber, D.; Abbot, V.; Dhiman, S.; Sharma, P. Pyrrole: A Resourceful Small Molecule in Key Medicinal Hetero-aromatics. *RSC Adv.* **2015**, 5, 15233-15266.

(2) Baltazzi, E.; Krimen, L. I. Recent Advances in the Chemistry of Pyrrole. *Chem. Rev.* **1963**, *63*, 511-556.

(3) Estèvez, V.; Villacampa, M.; Menèndez, J. C. Recent advances in the synthesis of pyrroles by multicomponent reactions. *Chem Soc. Rev.* **2014**, *43*, 4633-4657

(4) Walsh, C. T.; Garneau-Tsodikova, S.; Howard-Jones, A. R. Biological formation of pyrroles: Nature's logic and enzymatic machinery. *Nat. Prod. Rep.* **2006**, *23*, 517-531.

(5) Mal, D.; Shome, B.; Dinda, B. K. Pyrrole and its Derivatives. In *Heterocycles in Natural Product Synthesis*; Majumdar, K. C.; Chattopadhyay, S. K. Wiley-VCH: New York, 2011; pp 313-544.

(6) McNeill, R.; Siudak, R.; Wardlaw, J. H.; Weiss, D. E. Electronic Conduction in Polymers. I. The Chemical Structure of Polypyrrole. *Aust. J. Chem.* **1963**, *16*, 1056-1075.

(7) MacDiarmid, A. G. "Synthetic Metals": A Novel Role for Organic Polymers (Nobel Lecture). *Angew. Chem. Int. Ed.* **2001**, *40*, 2581-2590.

(8) Janata, J.; Josowicz, M. Conducting Polymers in Electronic Chemical Sensors. *Nat. Mater.* **2003**, *2*, 19-24.

(9) Liang, X.; Li, Y.; Li, X.; Jing, L.; Deng, Z.; Yue, X.; Li, C; Dai, Z. PEGylated Polypyrrole Nanoparticles Conjugating Gadolinium Chelates for Dual-Modal MRI/Photoacoustic Imaging Guided Photothermal Therapy of Cancer. *Adv. Funct. Mater.* **2015**, *25*, 1451-1462.

(10) Katritzky, A. R.; Ramsden, C. A.; Joule, J. A.; Zhdankin, V. V., Reactivity of Five-Membered Rings with One Heteroatom, *Handbook of Heterocyclic Chemistry*, **2010**, 383-472.

(11) Paras, N. A.; MacMillan, D. W. C. New Strategies in Organic Catalysis: The First Enantioselective Organocatalytic Friedel−Crafts Alkylation. *J. Am. Chem. Soc.* **2001**, *123*, 4370-4371.

(12) Trost, B.M.; Müller, C. Asymmetric Friedel−Crafts Alkylation of Pyrroles with Nitroalkenes Using a Dinuclear Zinc Catalyst. *J. Am. Chem. Soc.* **2008**, *130*, 2438-2439.

(13) Zhang, D.; Qiu, H.; Jiang, L.; Lv, F.; Ma, C.; Hu, W. Enantioselective Palladium(II) Phosphate Catalyzed Three-Component Reactions of Pyrrole, Diazoesters, and Imines. *Angew. Chem. Int. Ed.* **2013**, *52*, 13356-13360.

(14) Lee, H.-J.; Cho, C.-W. Cinchona-Based Primary Amine-Catalyzed Asymmetric Cascade Aza-Michael–Aldol Reactions of Enones with 2-(1*H*-Pyrrol-2-yl)-2-oxoacetates: Synthesis of Chiral Pyrrolizines with Multistereocenters. *J. Org. Chem.* **2013**, *78*, 3306-3312.

(15) Bae, J.-Y.; Lee, H.-J.; Youn, S.-H.; Kwon, S.-H.; Cho, C.-W. Organocatalytic Asymmetric Synthesis of Chiral Pyrrolizines by Cascade Conjugate Addition−Aldol Reactions. *Org. Lett.* **2010**, *12*, 4352-4355.

(16) Lee, H.-J.; Cho, C.-W. Asymmetric Synthesis of Chiral Pyrrolizine-Based Triheterocycles by Organocatalytic Cascade Aza-Michael–Aldol Reactions. *Eur. J. Org. Chem.* **2014**, 2014, 387-394.

(17) Li, P.; Fang, F.; Chen, J.; Wang, J. Organocatalytic Asymmetric Aza-Michael Addition of Pyrazole to Chalcone. *Tetrahedron: Asymmetry* **2014**, *25*, 98-101.

(18) Fu, N.; Zhang, L.; Luo, S.; Cheng, J.-P. Chiral Primary Amine Catalysed Asymmetric Conjugate Addition of Azoles to α-Substituted Vinyl Ketones. *Org. Chem. Front.* **2014**, *1*, 68-72.

(19) Zhang, J.; Zhang, Y.; Liu, X.; Guo, J.; Cao, W.; Lin, L.; Feng, X. Enantioselective Protonation by Aza-Michael Reaction between Pyrazoles and α-Substituted Vinyl Ketones. *Adv. Synth. Catal.* **2014**, 356, 3545-3550.

(20) Mose, R.; Preegel, G.; Larsen, J.; Jakobsen, S.; Iversen, E. H.; Jørgensen, K. A. Organocatalytic Stereoselective [8+2] and [6+4] Cycloadditions. *Nat. Chem.* **2017**, *9*, 487-492.

(21) Donslund, B. S.; Monleón, A.; Palazzo, T. A.; Christensen, M. L.; Dahlgaard, A.; Erickson, J. D.; Jørgensen, K. A. Organocatalytic Enantioselective Higher-Order Cycloadditions of In Situ Generated Amino Isobenzofulvenes. *Angew. Chem. Int. Ed.* **2018**, *57*, 1246-1250.

(22) Wang, S.; Rodríguez-Escrich, C.; Pericàs, M. A. Catalytic Asymmetric [8+2] Annulation Reactions Promoted by a Recyclable Immobilized Isothiourea. *Angew. Chem. Int. Ed.* **2017**, *56*, 15068-15072.

(23) Donslund, B.; Jessen, N. I.; Bertuzzi, G.; Giardinetti, M.; Palazzo, T. A.; Christensen, M. L.; Jørgensen, K. A. Catalytic Enantioselective [10+4] Cycloadditions. *Angew. Chem. Int. Ed.* **2018**, *57*, 13182-13186.

(24) Hayashi, Y.; Gotoh, H.; Honma, M.; Sankar, K.; Kumar, I.; Ishikawa, H.; Konno, K.; Yui, H.; Tsuzuki, S.; Uchimaru, T. Organocatalytic, Enantioselective Intramolecular [6 + 2] Cycloaddition Reaction for the Formation of Tricyclopentanoids and Insight on Its Mechanism from a Computational Study. *J. Am. Chem. Soc.* **2011**, *133*, 20175-20185.

(25) Hong, B.-C.; Shr, Y.-J.; Wu, J.-L.; Gupta, A. K.; Lin, K.-J. Novel [6 + 2] Cycloaddition of Fulvenes with Alkenes: A Facile Synthesis of the Anislactone and Hirsutane Framework. *Org. Lett.* **2002**, 4, 2249-2252.

(26) Hong, B.-C.; Sun, H.-I; Chen, Z.-Y. Unprecedented and Novel Hetero [6+3] Cycloadditions of Fulvene: A Facile Synthesis of the 11-Oxasteroid Framework. *Chem. Commun*. **1999**, 2125-2126.

(27) Hong, B.-C.; Jiang, Y.-F.; Kumar, E. S. Microwave-assisted [6+4]-Cycloaddition of Fulvenes and α-Pyrones to Azulene–indoles: Facile syntheses of Novel Antineoplastic Agents. *Bioorg. Med. Chem. Lett.* **2001**, 11, 1981-1984.

(28) Zhou, Z.; Wang, Z.-X.; Zhou, Y.-C.; Xiao, W.; Ouyang, Q.; Du, W.; Chen, Y.-C. Switchable Regioselectivity in Amine-catalysed Asymmetric Cycloadditions. *Nat. Chem.* **2017**, *9*, 590-594.

(29) Watanabe, M.; Kobayashi, T.; Kajigaeshi, S.; Kanemasa, S. Azafulvenes 1. A novel Generative Method of 6-Amino-1-Azafulvene and its Cycloaddition Reaction with Isothiocyanate. *Chem. Lett.* **1975**, *4*, 607-610.

(30) Galeazzi, E.; Guzman, A.; Rodriguez, G.; Muchowski, J. M. Generation and Lithiation of the Dimers of 6-(Dimethylamino)-1,4-diazafulvene. A Novel Synthesis of 2-Alkanoylimidazoles. *J. Org. Chem.* **1993**, *58*, 974-976.

(31) Barluenga, J.; García-Rodríguez, J.; Martínez, S.; Suárez-Sobrino, A. L.; Tomás, M. Facile and Versatile Annulation of the Imidazole Ring: Single and Sequential Cyclization Reactions of Fischer Carbene Complexes with 1,4-Diazafulvenes. *Chem. Eur. J.* **2006**, *12*, 3201-3210.

(32) Huang, S.-Z.; Kong, F.-D.; Ma, Q.-Y.; Guo, Z.-K.; Zhou, L.-M.; Wang, Q.; Dai, H.-F.; Zhao, Y.-X. Nematicidal Stemona Alkaloids from Stemona Parviflora. *J. Nat. Prod.* **2016**, *79*, 2599-2605.

(33) Paudler, W. W.; Kerley, G. I.; McKay, J. The Alkaloids of Cephalotaxus drupacea and Cephalotaxus Fortunei. *J. Org. Chem.* **1963**, *28*, 2194-2197.

(34) Walser, A.; Fryer, R. I. Imidazodiazepines and Processes Therefor. US4280957 (A), July 28, **1981**.

(35) Rizk, A.-F. *Naturally Occurring Pyrrolizidine Alkaloids*; CRC Press: Boca Raton, FL, USA, **1990**.

(36) Harrington, P. J.; Khatri, H. N.; Schloemer, G. C. Preparation of Ketorolac. US6323344 (B1), November 27, **2001**.

(37) Marigo, M.; Wabnitz, T. C.; Fielenbach, D.; Jørgensen, K. A. Enantioselective Organocatalyzed □-Sulfenylation of Aldehydes. *Angew. Chem. Int. Ed.* **2005**, *44*, 794-797.

(38) Ho, C.-Y.; Chen, Y.-C.; Wong, M.-K.; Yang, D. Fluorinated Chiral Secondary Amines as Catalysts for Epoxidation of Olefins with Oxone. *J. Org. Chem.* **2005**, *70*, 898-906.

(39) Sparr, C.; Schweizer, B.; Senn, H. M.; Gilmour, R. The Fluorine-Iminium Ion *Gauche* Effect: Proof of Principle and Application to Asymmetric Organocatalysis. *Angew. Chem. Int. Ed.* **2009**, *48*, 3065-3068.

(40) Takaoka, K.; Aoyama, T.; Shioiri, T. Cycloaddition Reactions of Trimethylsilylketene with 8-Azaheptafulvenes and 6-Amino-1-azafulvenes. *Heterocycles* **2001**, *54*, 209-215.

(41) For a very low enantioselectivity seminal work, see: Yin, G.; Zhei, R.; Li, L.; Tian, J.; Chen, L. One-Pot Enantioselective Synthesis of 3-Nitro-2*H*-chromenes Catalyzed by a Simple 4-Hydroxyprolinamide with 4-Nitrophenol as Cocatalyst. *Eur. J. Org. Chem.* **2013**, *2013*, 5431-5438.

(42) Sonnet, P. E. Synthesis of β-Substituted Pyrroles *via* 1-(Pyrrol-2-ylmethylene)pyrrolidinium Salts. *J. Org. Chem.* **1971**, *36*, 1005-1007.

(43) Berthiaume, S. L.; Bray, B. L.; Hess, P.; Liu, Y.; Maddox, M. L.; Muchowski, J. M.; Scheller, M. E. Synthesis of 5-substituted Pyrrole-2-carboxaldehydes. Part I. Generation of Formal

5-Lithiopyrrole-2-carboxaldehyde Equivalents by Bromine-lithium Exchange of 2-Bromo-6-(diisopropylamino)-1-azafulvene Derivatives. *Can. J. Chem.* **1995**, *73*, 675-684.

(44) Sonnet, P. E.; Flippen, J. L.; Gilardi, R. D. Substituted 1-(Pyrrol-2-ylmethylene)pyrrolidinium Salts a Source of Stable 2-Azafulvenamines. *J. Het. Chem.* **1974**, *11*, 811-812.

(45) Residual traces of water are responsible for partial hydrolysis of the iminium ion, explaining why we could never obtain this intermediate quantitatively.

(46) Zhao, Y.; Truhlar, D. G., The M06 suite of density functionals for main group thermochemistry, thermochemical kinetics, noncovalent interactions, excited states, and transition elements: Two new functionals and systematic testing of four M06-class functionals and 12 other functionals. *Theor. Chem. Acc.* **2008**, *120*, 215−241.

(47) Weigend, F.; Ahlrichs, R., Balanced basis sets of split valence, triple zeta valence and quadruple zeta valence quality for H to Rn: Design and assessment of accuracy. *Phys. Chem. Chem. Phys*. **2005**, *7*, 3297−3305.

(48) Marenich, A. V.; Cramer, C. J.; Truhlar, D. G., Universal solvation model based on solute electron density and on a continuum model of the solvent defined by the bulk dielectric constant and atomic surface tensions. *J. Phys. Chem. B* **2009**, *113*, 6378-6396.

(49) Vosko, S. H.; Wilk, L.; Nusair, M., Accurate spin-dependent electron liquid correlation energies for local spin density calculations: a critical analysis. *Can. J. Phys*. **1980**, *58*, 1200−1211. (b)Lee, C.; Yang, W.; Parr, R. G., Development of the Colle-Salvetti correlation-energy formula into a functional of the electron density. *Phys. Rev. B*: *Condens. Matter Mater. Phys*. **1988**, *37*, 785−789. (c) Becke, A. D., Density-functional thermochemistry. III. The role of exact exchange. *J. Chem. Phys.* **1993**, *98*, 5648−5652. (d) Stephens, P. J.; Devlin, F. J.; Chabalowski, C. F.; Frisch,

M. J., Ab initio calculation of vibrational absorption and circular dichroism spectra using density functional force fields. *J. Phys. Chem.* **1994**, *98*, 11623−11627.

Chapter 7. Demystifying the Soai Reaction

7.1 Abstract

The extraordinary Soai reaction has profoundly impacted chemists' perspective of absolute asymmetric synthesis and its role in the origin of biological homochirality. Herein, we describe the unprecedented observation of asymmetry amplifying autocatalysis in the alkylation of 5-(trimethylsilylethynyl)pyridine-3-carbaldehyde using diisopropylzinc. Kinetic studies with a "Trojan-horse" substrate and spectroscopic analysis of a series of zinc-alkoxides that incorporate specific structural mutations reveal a 'pyridine-assisted cube escape'. The new cluster functions as a catalyst that activates the aldehyde and poises a bound diisopropylzinc moiety for alkyl group transfer. Transition-state models leading to both the homochiral and heterochiral products were validated by density functional theory calculations. Our deconstruction of the Soai system contributes substantially to understanding the mechanism of this transformation that has stood as a longstanding challenge in chemistry.

7.2 Introduction

The autocatalytic, asymmetry amplifying alkylation of pyrimidine-5-carbaldehydes with diisopropylzinc, crowned as the 'Soai reaction', occupies a venerable position in organic chemistry (Figure 7.1a).[1,2] The transformation is peerless in its efficiency for asymmetric autocatalysis and sensitivity to initial chiral imbalances, making it a *sui generis* example of a reaction predisposed to evolve toward homochirality. Enantiopure products are obtained in three reaction cycles even with calculated autocatalyst e.e. as low as 5×10^{-5} %.[3] In the absence of added catalyst, symmetry breaking can yield non-racemic products,[4-7] thus categorizing the transformation as an example of absolute asymmetric synthesis.[8] A large variety of chiral additives[1,9-15] and even circularly

polarized light[16] and isotopic chirality[17-19] can influence the outcome of the reaction by biasing an initial imbalance toward one of the enantiomers. Soai's seminal discoveries have received widespread attention in diverse chemical fields and have revived discussions regarding absolute asymmetric synthesis, chiral symmetry breaking, and the origin of biological homochirality.[20-23]

Since the discovery of the reaction in 1995, the groups of Soai, Blackmond and Brown have spearheaded efforts to provide a mechanistic explanation (Figure 7.1b). Initial kinetic studies suggested a dimeric[24] or trimeric[25] alkoxide aggregate as the catalyst. A revised proposal[26] invoking a dimeric alkoxide catalyst and two substrate molecules leading to a tetrameric transition state was successfully modeled with DFT calculations.[27] Reaction simulations by Buhse demonstrated compatibility with both monomeric and dimeric catalysts, suggesting inherent limitations of kinetic analysis.[28,29] The first spectroscopic studies on the zinc alkoxide were consistent with a dimeric structure but were limited in scope because of the challenges associated with solubility and peak broadening in toluene, which is the reaction solvent.[30] For the first time in 2007, Klankermayer *et.al.* suggested a square-macrocycle-square (SMS) tetramer as a possible end product species.[31] In 2010, Brown and Blackmond reported an intriguing inverse dependence of reaction rate on temperature and provided further support for the SMS tetramer as a promising species in the reaction cycle on the basis of further kinetic and spectroscopic investigations[32] as well as a DFT study on these tetramers by Gridnev.[33] Finally in 2015, Soai disclosed the first X-ray crystal structures of the enantiopure and racemic alkoxides which exist as tetramers or oligomers depending on crystallization conditions (Figure 7.1b).[34]

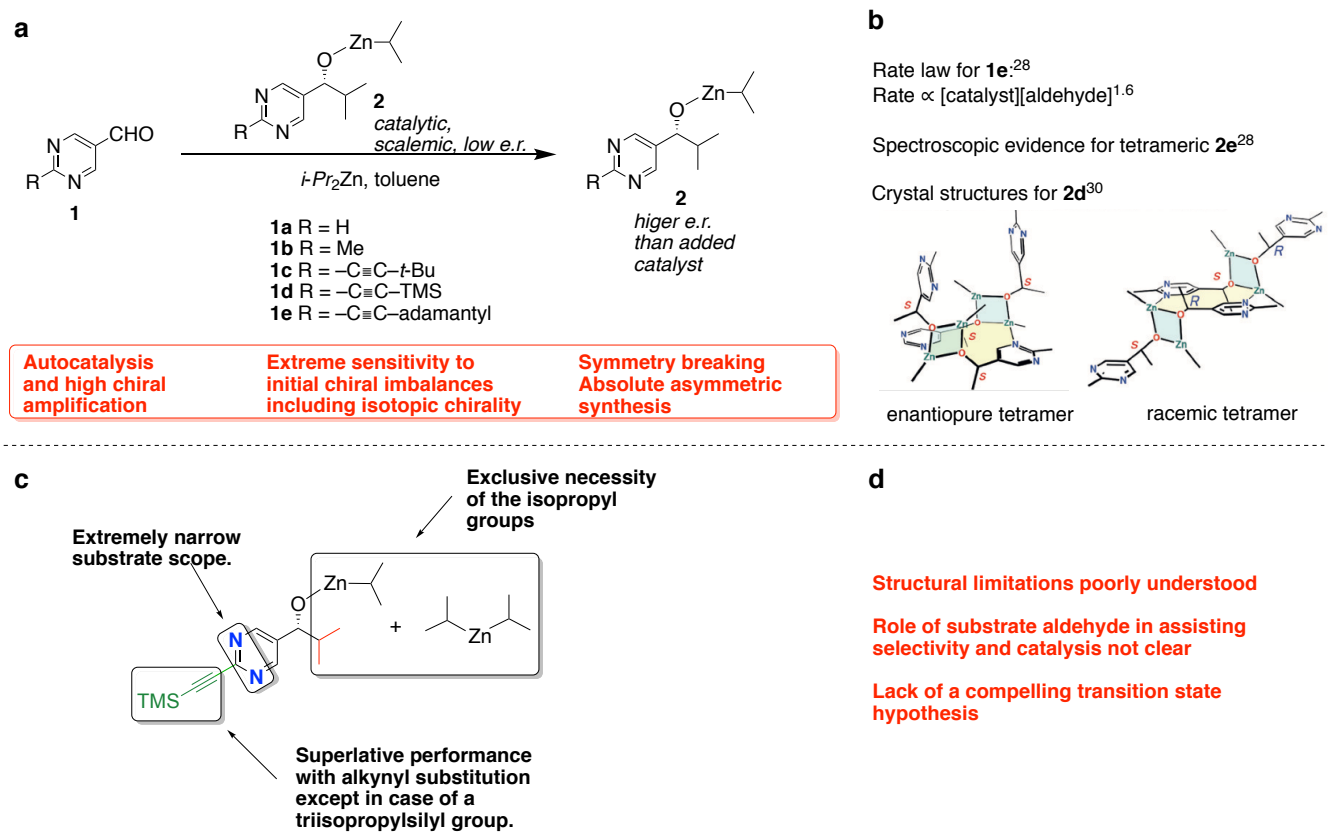

Figure 7.1: a. The Soai reaction system. **b.** Current state of structural and mechanistic understanding. **c.** Structural idiosyncrasies. **d.** Unsolved challenges and open questions.

The remarkable robustness of the Soai reaction is rivaled by the severe structural constraints on the reactants for successful asymmetric autocatalysis (Figure 7.1c).[35] Although systematic studies with other dialkylzinc reagents are lacking, asymmetric amplification is observed exclusively with diisopropylzinc. 2-Alkynylpyrimidine-5-carbaldehydes[36] remain the workhorse substrates and only scant reports with other competent aldehydes have been presented.[37,38] An inspection of the proposed tetrameric catalyst structure does not reveal a role for the second nitrogen in the pyrimidine ring nor the defining contributions from the alkyl groups toward catalyst aggregation. Moreover, the reasons for superlative performance of the alkynyl-substituted substrates remain unclear. Another idiosyncrasy is the bewildering failure of 2-

(triisopropylsilylethynyl)pyrimidine-5-carbaldehyde to display amplifying autocatalysis.[36] For a reaction demonstrating such striking characteristics, the extremely narrow substrate scope is perhaps unsurprising. Nevertheless, a fundamental rationalization of these structural constraints that allow exclusive access to the requisite catalytic intermediates remains obscure highlighting our lack of understanding of this reaction. Although the current consensus of a tetrameric alkoxide catalyst represents a significant milestone in the identification of product aggregation, this knowledge has not enabled the formulation of a compelling transition state hypothesis nor provided deeper insights into the structural contributions from various parts of the molecule that give rise to asymmetric autocatalysis. Two decades since Soai's pioneering publication, a holistic understanding of the reaction remains an open challenge with fundamental implications on our understanding of chiral symmetry breaking and absolute asymmetric synthesis.

7.3 Computational Methods

All quantum chemical calculations were performed with Gaussian 09. Geometry optimizations and frequencies were calculated with the B3LYP (*in vacuo*) density functional with the 6-31G(d) basis set. Optimized geometries were verified by frequency calculations as minima (zero imaginary frequencies) or transition structures (a single imaginary frequency). Free energy corrections were determined using unscaled B3LYP/6-31G(d) vibrational frequencies assuming a standard state of 1 atm and 298.15 K. Errors in the treatment of low modes as harmonic oscillations were mitigated by use of the quasiharmonic approximation proposed by Truhlar and coworkers. Single point energy calculations were performed on optimized geometries with M06-2X/def2-TZVPP in conjunction with the SMD implicit solvation model for the experimental solvent used (toluene). The free energies reported herein were determined by adding zero-point energy and

thermal correction determined using B3LYP/6-31G(d) to electronic energies computed at the M06-2X/def2-TZVPP-SMD level of theory.

The tetramer input geometry was obtained from the crystal structure by Soai, and then manually modified for our computational models. Monte Carlo conformational searches were performed on the intermediates using the OPLS3 force field in Maestro/Macromodel. Transition structure input geometries were generated by performing scans for the alkylation at the B3LYP/6-31G(d) level of theory on the located minima.

7.4 Results and Discussion

The first stage of our investigation was to deconstruct the Soai system and understand the contributions to catalysis and asymmetric amplification from its various components: (1) the dialkylzinc reagent, (2) the carbinol substituent, (3) the aromatic core and (4) the alkynyl substituent. Orienting studies began with the well-known pyrimidine-5-carbaldehyde **1d** and different dialkylzinc reagents.[39] The next series of experiments probed the role of the aromatic core, which led us to the startling discovery that *5-(trimethylsilylethynyl)pyridine-3-carbaldehyde **(3)** displayed efficient amplifying asymmetric autocatalysis in the reaction with diisopropylzinc* (Figure 6.2a). Product carbinol **4**, when included in this reaction as a scalemic catalyst, afforded newly-generated product with higher enantioenrichment.[40,41] The reaction is homogenous even at high concentrations and is conveniently monitored by tracking aldehyde consumption using *in-situ* IR spectroscopy (Figure 7.2). The transformation displays all the characteristics of an amplifying autocatalytic process (Figure 7.2b). Without added catalyst, sigmoidal aldehyde consumption, with an initial induction period, followed by a rapid reaction is observed, characteristic of autocatalysis (entry 1, blue dashed curve). Inclusion of scalemic product carbinol

(4) eliminates the induction period, leading to the rapid production of product with higher enantioenrichment than the initially added autocatalyst (entry 2, red dashed curve). At lower concentrations, the background reaction without added product is sluggish and inefficient (entry 3, solid blue curve). However, inclusion of either enantioenriched (entry 4, solid red curve) or racemic (entry 5, solid green curve) carbinol (**4**) results in accelerated reactions and efficient product generation. In case of the enantioenriched autocatalyst (entry 4), highly enantioenriched product is obtained whereas the racemic autocatalyst (entry 5) yields racemic product. Crucially, the latter reaction is much slower than the former indicating the lower catalytic activity of the racemic autocatalyst species, further highlighting the non-linear effect. These observations establish that just as is the case in the iconic Soai pyrimidine-system, non-linear amplifying autocatalysis is also operative in the reaction of **3** and diisopropylzinc.

a

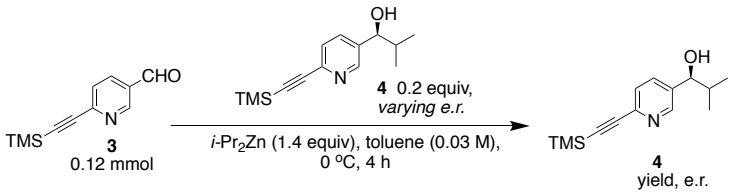

entry	**4** cat e.r.	yield* (%)	product e.r.**
1	55:45	77	92:8
2	60:40	87	96:4
3	70:30	90	98:2
4	80:20	90	98:2
5	90:10	87	99:1

* yield of isolated, newly formed product
** e.r. of newly formed product excluding initial catalyst

b

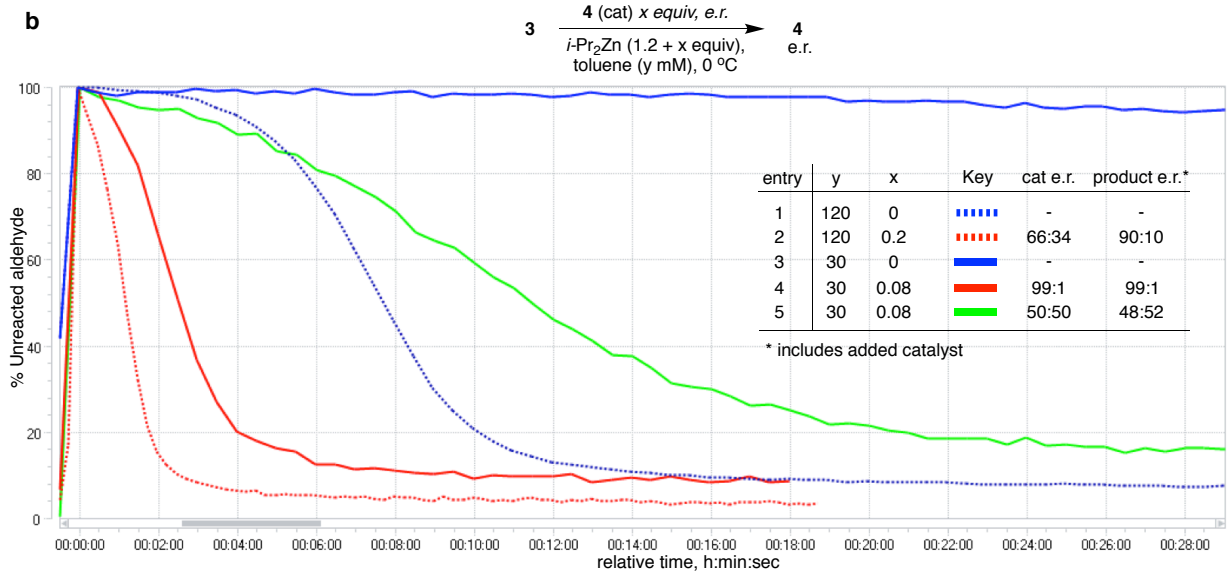

entry	y	x	Key	cat e.r.	product e.r.*
1	120	0		-	-
2	120	0.2		66:34	90:10
3	30	0		-	-
4	30	0.08		99:1	99:1
5	30	0.08		50:50	48:52

* includes added catalyst

c

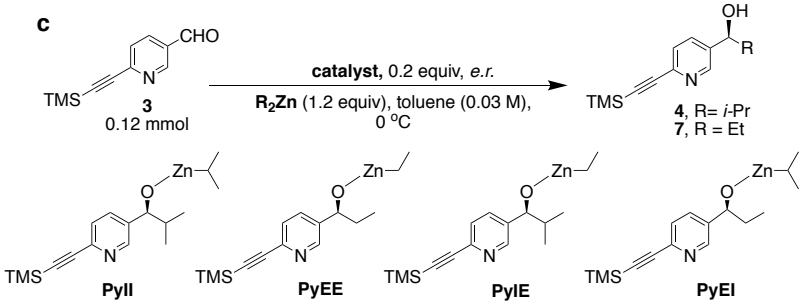

entry	R	catalyst	Key	cat e.r.	product e.r.*
1	***i*-Pr**	none		-	-
2	***i*-Pr**	PyII		62:38	92:8 (75)**
3	***i*-Pr**	PyEI		70:30	98:2 (65)
4	**Et**	none		-	-
5	**Et**	PyEE		72:28	68:32 (15)**
6	**Et**	PyIE		70:30	74:26 (28)

* at specified conversion in parenthesis
** includes added catalyst

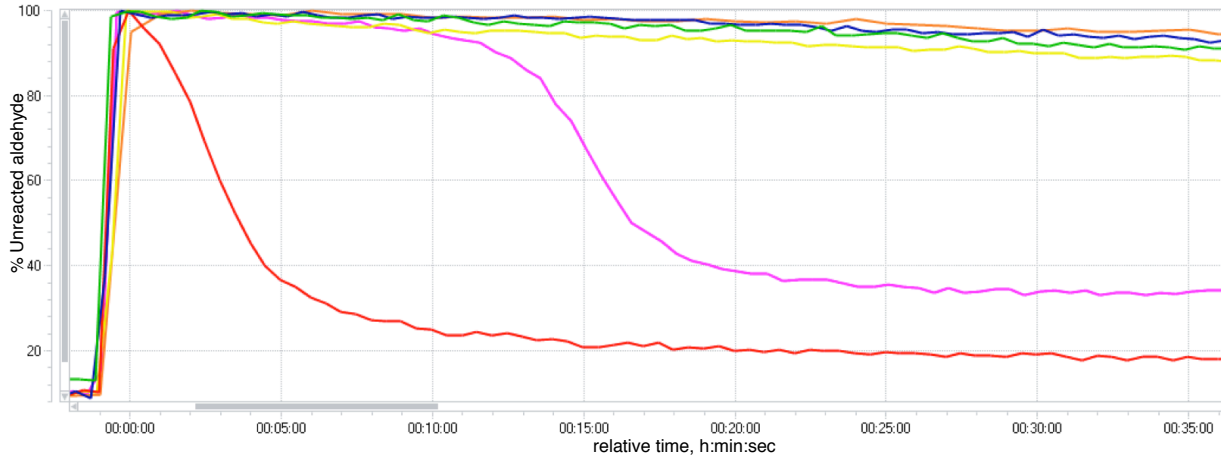

Figure 7.2: a. Asymmetric autocatalysis with chiral amplification in alkylation of **3** with diisopropylzinc. **b.** Observation of sigmoidal aldehyde consumption profiles and non-linear autocatalysis upon monitoring aldehyde consumption by *in-situ* IR spectroscopy **c** Qualitative comparison of catalytic activities and non-linear effect of alkoxides **Py*XX*** in dialkylzinc addition to **3** by ReactIR monitoring of aldehyde consumption.

The new system also shares the other non-obvious, idiosyncratic characteristics typical to the Soai reaction. In the new pyridine system, an inverse rate profile with respect to temperature was noted, with a rate maximum at ~0^{o} C. The analogous reaction of **3** with diethylzinc did not result in asymmetric amplification or rate enhancement (Figure 7.2c, entries 4 and 5). Remarkably, the reaction of diisopropylzinc with 5-(triisopropylsilylethynyl)pyridine-3-carbaldehyde was sluggish and demonstrated neither asymmetric amplification nor autocatalytic rate enhancement. Such striking similarities of the two systems clearly demonstrate that one of the nitrogen atoms in the pyrimidine ring is dispensable in the Soai system.

To evaluate contributions of the alkyl group on the carbinol center in the catalyst and the O-Zn-alkyl group, a qualitative comparison of catalysis by four different zinc alkoxides (**PyII, PyEE, PyIE** and **PyEI)** was made by *in-situ* IR monitoring of dialkylzinc additions to **3** in catalyzed and uncatalyzed reactions (Figure 7.2c) (nomenclature: *Py/Ph* = pyridine/phenyl indicating the aromatic core, *I/E* = isopropyl/ethyl indicating the carbinol alkyl group and *I/E* = isopropyl/ethyl indicating the alkylzinc group). In all cases, the corresponding scalemic carbinols were used for generating the zinc alkoxides and the product enantiomeric composition was analyzed to assess any non-linear effects. Under these conditions, the uncatalyzed reactions (entries 1 and 4) are sluggish, show low conversion and ultimately stall. Inclusion of either **PyEE**

(entry 5) or **PyIE** (entry 6) shows no appreciable rate enhancement. In the case of **PyEE**, the product carbinol has a lower e.r. than the added catalyst whereas a minor positive non-linear effect is seen in case of **PyIE**. Entry 2 represents the autocatalytic reaction with diisopropylzinc and reiterates the high catalytic efficiency and strong non-linear behavior of catalyst **PyII**. Finally, with alkoxide **PyEI** (entry 3), a sigmoidal aldehyde decay with high final product e.r. is achieved. The absence of an initial rate enhancement is noteworthy. This behavior is interpreted to arise from a low catalytic activity of **PyEI** giving rise to an initial production of **PyII** followed by strong asymmetric autocatalysis from a buildup of **PyII**. Taken together, these observations indicate that in this alkoxide series, only **PyII** possesses the requisite structural requirements for efficient, amplifying catalysis and replacement of either or both isopropyl groups results in alkoxides (**PyEE, PyIE** and **PyEI**) that possess markedly inferior catalytic efficiencies.

To gain insights into the structural requirements for efficient catalysis, a spectroscopic study to characterize the solution state structures of phenyl (**PhEE, PhEI, PhIE** and **PhII**) and pyridyl (**PyEE, PyEI, PyIE** and **PyII**) zinc alkoxides in toluene was initiated (Figure 7.3). The high solubility of these species along with their stability in toluene for extended periods represented a significant advantage over their pyrimidine analogs and facilitated detailed 1D and 2D NMR spectroscopic characterization.

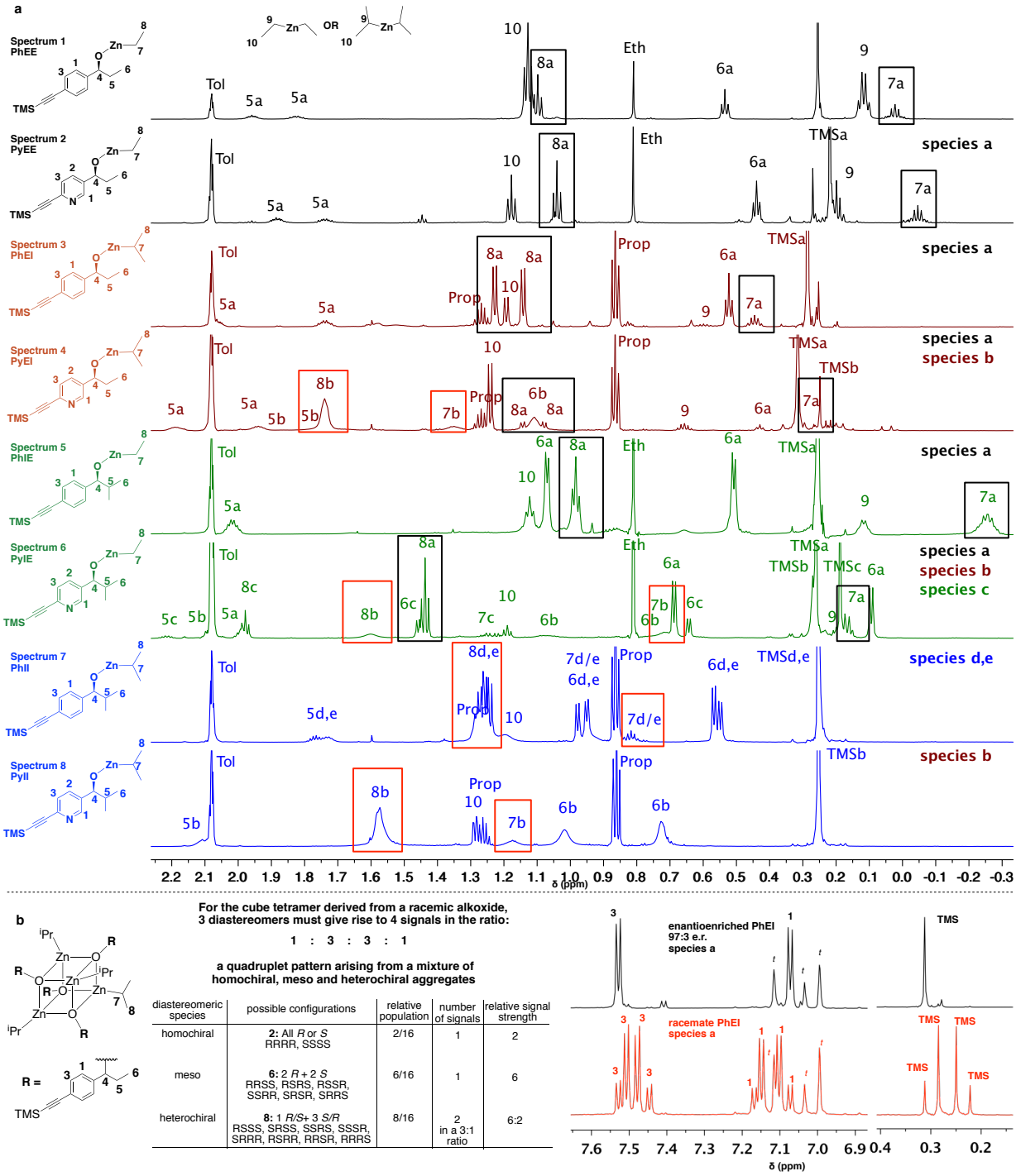

diastereomeric species	possible configurations	relative population	number of signals	relative signal strength
homochiral	**2:** All *R* or *S* RRRR, SSSS	2/16	1	2
meso	**6:** 2 *R* + 2 *S* RRSS, RSRS, RSSR, SSRR, SRSR, SRRS	6/16	1	6
heterochiral	**8:** 1 *R*/*S*+ 3 *S*/*R* RSSS, SRSS, SSRS, SSSR, SRRR, RSRR, RRSR, RRRS	8/16	2 in a 3:1 ratio	6:2

Figure 7.3: Partial ^{1}H-NMR spectra (750 MHz) of zinc alkoxides in toluene-d_8 at 23 ^{0}C. *tol* = residual toluene, *prop* = propane, *eth* = ethane. **a.** Enantioenriched zinc alkoxides with signature chemical shifts for species **a** (black boxed) and species **b-d** (red boxed) **b.** Diastereomeric species

possible in a racemic cubic tetramer with their relative peak distributions. ^{1}H NMR of the aryl and TMS region for racemic **PhEI** displays this predicted quadruplet pattern.

In general, for all alkoxides, spectra obtained from racemic samples showed greater multiplicity of signals and additional peaks compared to spectra obtained from enantioenriched samples, proving that none of these alkoxides exist as monomers. Figure 7.3a presents the upfield region of the eight, enantioenriched alkoxides to allow comparison of important spectral characteristics. To assist this comparison, alkoxides differing by only a nitrogen atom in the aromatic core are assigned the same color and are arranged successively. Different colors highlight four possible combinations of the carbinol-alkyl and O-Zn-alkyl groups. For the enantioenriched phenyl alkoxides **PhEE** (spectrum 1), **PhEI** (spectrum 3) and **PhIE** (spectrum 5), a single set of peaks corresponding to a predominant species was observed. The signature characteristics of this species are the sharp, clearly resolved peaks with only minor perturbation over a wide temperature range (-20 – 50 ^{o}C) and the atypical *upfield* chemical shifts of the alkylzinc protons H(7) and H(8) (Figure 7.3a, black boxes) in comparison to the free dialkylzinc protons H(9) and H(10)

For alkoxide **PhEI**, a remarkable quadruplet splitting pattern in the racemic aggregate is observed in comparison to the enantiopure aggregate (Figure 7.3b). Such a pattern is consistent with a symmetric, cubic tetramer structure, which finds ample precedent.[42,43] The racemic cubic tetramer can exist as a mixture of three diastereomers depending on the configurations at the four constituent alkoxide stereogenic centers: (1) homochiral (D_2), (2) meso (S_4) and (3) heterochiral (C_1) (Figure 7.3b). The symmetry of the cube renders many combinations degenerate, for example, all six possibilities in the meso case represent a single, equivalent structure whereas in the heterochiral diastereomer, the eight possibilities represent two enantiomorphs (*c.f.* RSSS, SRSS,

SSRS, SSSR are all equivalent structures representing one of the enantiomorphs). The heterochiral cubic tetramer contains two sets of diastereotopic protons (arising from the minor and major enantiomers in an individual cube) and is expected to give rise to two signals in a 3:1 ratio. Thus, an overall 1:3:3:1 peak pattern is ideally expected in the spectrum of the racemic cubic tetramer. The atypical upfield shift of the alkylzinc protons is believed to arise from shielding by the aryl groups and is also observed in the ethylzinc alkoxide of (*S*)-1-phenylethanol, the methylzinc alkoxide of which has been proposed to form a cubic tetramer.[44] On the basis of these observations, species **PhEE, PhEI** and **PhIE** are believed to form cubic tetramers (species **a**, Figure 7.3a) in solution and the upfield chemical shifts of protons H(7) and H(8) (black boxes) are a diagnostic feature of this structure.

The spectrum of pyridylzinc alkoxide **PyEE** (spectrum 2) shows a predominant species matching the spectral characteristics of a cubic tetramer. Clearly, presence of the pyridine nitrogen in **PyEE** does not disrupt the natural preference to form a cubic tetramer. Increasing the bulk of the alkyl groups in the pyridyl series in species **PyEI** (spectrum 4) and **PyIE** (spectrum 6) still maintained the cubic tetramer assembly (species **a**, black boxed diagnostic peaks) but also showed the presence of other species (species **b**, **c**), the peaks of which are labeled with the suffix '**b**' or '**c**' in Figure 7.3a (*c.f.* H(**7b**), H(**6c**)). Broad peaks with *downfield* shifts of protons H(7) and H(8) (red boxes) characterize species **b**. A third species (**c**) with sharp peaks and downfield alkylzinc protons can be identified in the spectrum of **PyIE** (spectrum 6). In the spectra for the bulkiest derivatives of both phenyl and pyridyl complexes **PhII** (spectrum 7) and **PyII** (spectrum 8) respectively, diagnostic peaks for the cubic tetramer are completely absent. Two components can be detected in the spectrum of **PhII** (species **d**, **e**) whereas the single species with broad peaks seen in the spectrum of **PyII** resembles species **b** (in the spectra of **PyEI** and **PyIE**) in chemical shift patterns

(red boxed). Species **b** and **c** also show diagnostic peak differences in the aryl region in comparison to species **a**.

Diffusion Ordered Spectroscopy (DOSY) studies of the alkoxides for molecular weight estimations established that all of these compounds except **PhII** are tetrameric and are unchanged over a temperature range of 0 to 50 ^{0} C, highlighting the stability of these aggregates. DOSY analysis showed that **PhII** exists as a mixture of trimers. This evidence provides further support to the hypothesis that species **a** are cubic tetramers and reveals that species **b** and **c** represent distinct aggregate structures that are also tetrameric.

Rationalizing the effect of structure on alkoxide aggregation (Figure 7.4) begins with the assumption that a cubic tetramer is the preferred constitution for these alkylzinc alkoxides. However, replacement of ethyl groups around the cube core by bulkier isopropyl groups results in destabilization of the cube structure by steric repulsion to the point at which the cube is no longer viable as in cases of **PhII** and **PyII**. A weakened cube can be further disrupted by a pyridine nitrogen through coordination to the zinc alkyls to assist in the formation of alternative tetrameric aggregates. Indeed, addition of pyridine to solutions of **PhEI, PhIE** and **PhII** results in disruption of the aggregate structure whereas **PhEE** remains unaffected (Figure 7.4a). With a pyridine nitrogen available for coordination to zinc, alkoxides **PyEE, PyEI, PyIE** and **PyII** are poised to *escape the cube* only if the core is sufficiently weakened. The resulting continuum of structures displayed by these alkoxides represents this phenomenon. Whereas **PyEE** maintains a cubic tetramer constitution because its core is sufficiently stable to resist pyridine disruption, **PyEI** and **PyIE** exhibit formation of other tetrameric species owing to partial cube escape facilitated by nitrogen coordination. Finally, zinc alkoxide **PyII** represents the end point with complete cube escape and access to an exclusive, alternative tetrameric aggregate structure. The most simple way

in which such a cube-escape can occur is an intramolecular coordination of the pyridyl nitrogen to *expand* the cube to a square-macrocycle-square (SMS) connectivity (Figure 7.4b). This connectivity is identical to the crystal structure described by Soai. Clearly, only a single nitrogen is required in the aromatic core to build this tetramer.

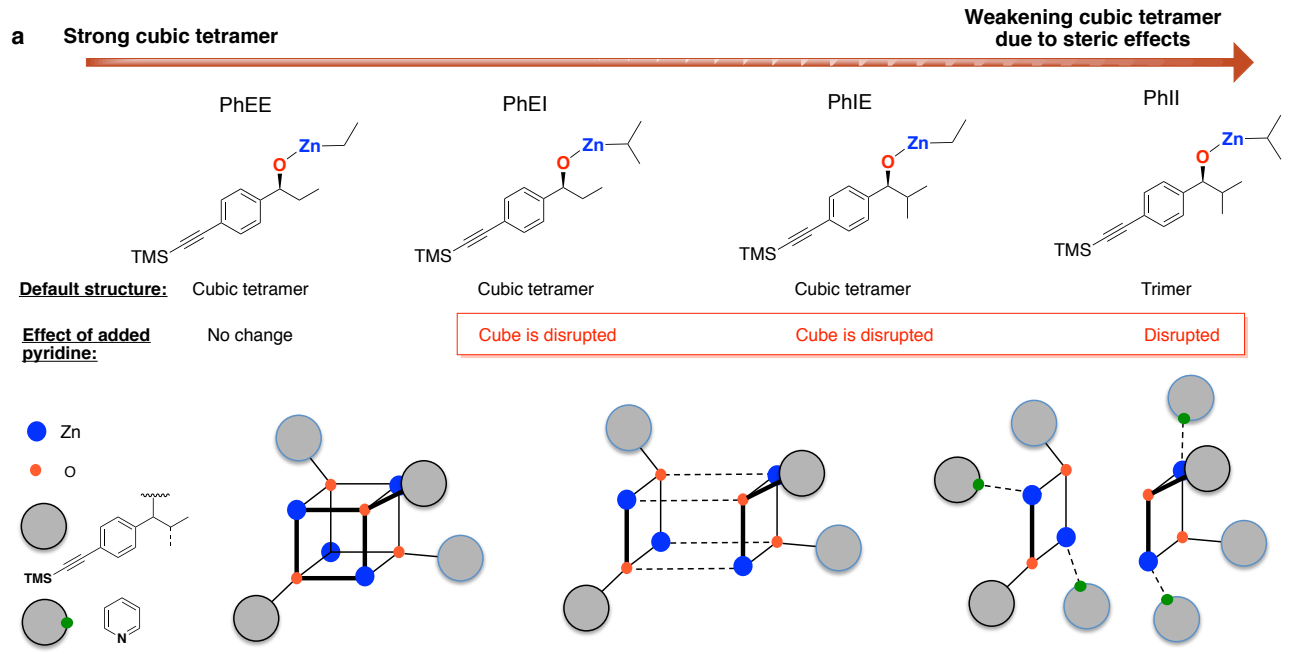

A sterically compromised cubic tetramer is disrupted by pyridine coordination

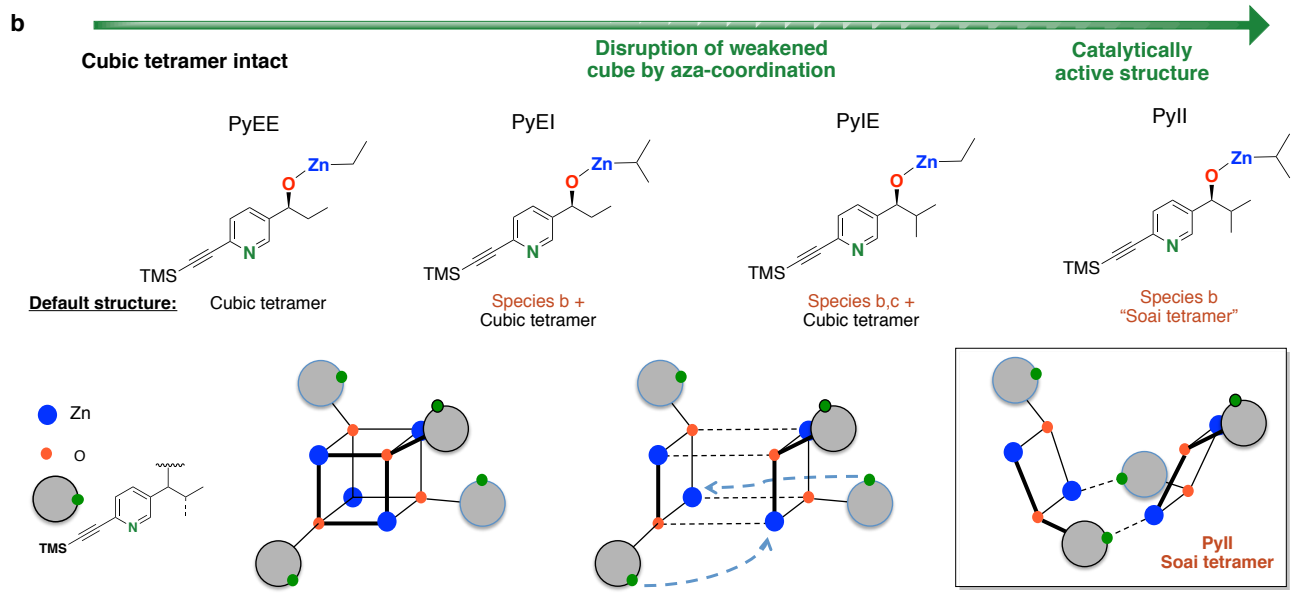

A sterically compromised cubic tetramer is *disrupted* by *intramolecular* pyridine coordination to yield the Soai tetramer

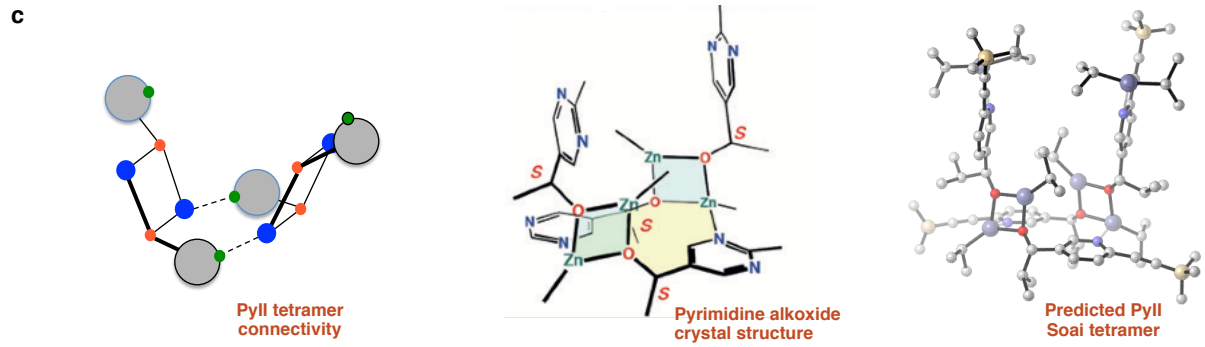

Figure 7.4: a. Sterically weakened PhXX cubic tetramers are disrupted by pyridine. **b.** A conceptually similar 'cube escape' occurs in the PyXX alkoxides with intramolecular pyridine coordination yielding the Soai tetramer. **c.** The predicted identity of the cube-escaped PyII Soai tetramer based on analogy with Soai's crystal structure.

In light of the striking similarity of **PyII** to the structure and properties of the original Soai system **2d**, as well as the rationale for the assembly of the SMS tetramer, the proposal that its identity is analogous to that found in the recently disclosed X-ray crystal structure of **2c** (the 'Soai tetramer') seems compelling (Figure 7.4c).

Investigation of the properties of autocatalytically competent **PyII** would be simplified by the identification of a competent substrate that would give rise to a non-autocatalytically competent product. Previous studies had established that the reaction of pyridine-3-carbaldehyde (**5**) with diisopropylzinc does not display amplifying autocatalysis[45] and this behavior was confirmed in our own studies. We thus envisaged using this aldehyde as a non-autocatalytically competent substrate for catalyst **PyII**.

The alkylation of **5** with diisopropylzinc in presence of scalemic **PyII** (67:33 e.r.) displayed marked rate enhancement in comparison to the uncatalyzed reaction (Figure 7.5a, entries 1 and 2). Crucially, a positive non-linear effect is also observed such that the product carbinol **6** possessed a higher e.r. (87:13) than the catalyst and of the same absolute configuration (*S*). Clearly, the attributes enabling **PyII** to function as an autocatalyst with aldehyde **3**, namely, enantioselective catalysis and a positive non-linear effect, are also operational in the non-autocatalytic reaction with **5**. However, the aldehyde decay profile is reminiscent of a conventional catalyst-substrate reaction because the newly formed product contributes minimally to catalysis. This reaction is thus

representative of the alkyl transfer step in the autocatalytic reaction. A significant observation which highlights the substrate specificity of the **PyII** catalyst was the poor reactivity of benzaldehyde **8** and 4-(trimethylsilylethynyl)benzaldehyde **10** under identical catalytic conditions (entries 3 and 4).

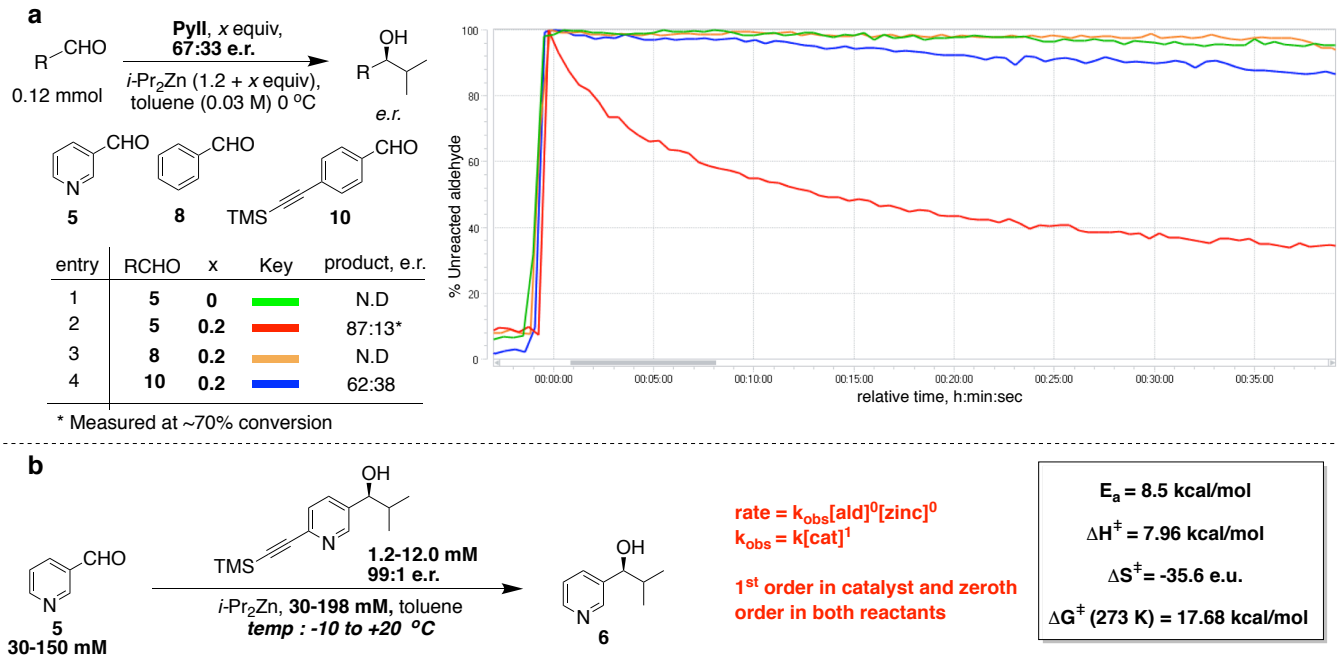

Figure 7.5: a. *In-situ* IR profiles for aldehyde consumption in diisopropylzinc alkylations catalyzed by scalemic **PyII. b.** Rate law and thermodynamic parameters for the non-autocatalytic reaction as measured using initial rate kinetic analysis.

In-situ IR monitoring of aldehyde consumption was employed for a comprehensive initial rate kinetic analysis of the diisopropylzinc alkylation of **5** catalyzed by **PyII** (Figure 7.5b). The initial rate displayed a first order dependence on catalyst concentration and zeroth order dependence on both **5** and diisopropylzinc, indicating that saturation binding of both reactants to the catalyst aggregate precedes the rate limiting alkyl transfer. We believe that the decrease in conversion rate over time arises from catalyst poisoning and/or product inhibition by the product

alkoxide that can mimic the **PyII** monomer and incorporate into the **PyII** aggregate. Arrhenius activation parameters were determined assuming a tetrameric catalyst aggregate. The alternative assumptions of monomeric, dimeric or trimeric catalyst aggregates resulted in only a minor variation in calculated values of $\Delta S^{\ddagger}$ and $\Delta G^{\ddagger}$. The reaction shows conventional Arrhenius behavior with a lowering of initial rate upon decreasing temperature. These studies with "Trojan-horse" substrate **5** thus provide insights into the mode of action of the **PyII** catalyst.

For the hypothesis that **PyII** emulates the 'Soai tetramer' to be valid, it must also provide a clear explanation for the observed saturation kinetic behavior (with **5**) and production of homochiral products from both **3** and **5**. Catalysis must be facilitated by a reactant-binding model that would account for activation of the carbonyl group as well as an incoming diisopropylzinc prior to alkyl transfer. The critical demonstration of poor reactivity of aldehydes **8** and **10** (Figure 7.5a) indicates that pyridine-3-carbaldehydes are a privileged substrate class for the Soai tetramer owing to nitrogen coordination to a favorable site on the catalyst. Independent spectroscopic studies revealed that: (1) the dialkylzinc binds to the pyridine nitrogens of **PyII** as well as substrates **3** and **5**, (2) the carbonyl group in **5** has an inherently poor affinity to diisopropylzinc and binding is exclusive to the ring nitrogen with diagnostic chemical shift changes and, (3) the carbonyl group in **5** *can* coordinate to an unsaturated zinc in the alkoxide core. In light of these considerations, two possible models for reactant docking prior to the alkyl transfer are proposed. Common to both models is carbonyl coordination to an unsaturated O–Zn center and diisopropylzinc binding to the two 'pyridyl arms' of the Soai tetramer. Further, the pyridyl nitrogen of the substrate can be bound either to the remaining unsaturated Zn–O center or to a diisopropylzinc bound to one of the arms of the tetramer. These two options give rise to the *floor-to-floor* (Figure 7..6) or the *floor-to-arm* models, respectively. In both cases, a bound

diisopropylzinc on the catalyst arm appears to be stereoelectronically predisposed to react with an activated carbonyl group arising from two-point substrate docking to the catalyst.

The energetic preferences of the *floor-to-floor* and *floor-to-arm* binding modes were interrogated with density functional theory. Soai's crystal structure for **2e** was employed as the starting geometry for the **PyII** tetramer after the replacement of pyrimidine cores and *tert*-butyl groups by pyridines and trimethylsilyl groups, respectively. Computations of the aldehyde **5** bound to tetramer **PyII** using M06-2X/def2-TZVPP single-point energies with the SMD (toluene) solvation model on B3LYP/6-31G(d) calculated geometries reveal a preference for the *floor-to-floor* model (**int-5a**, Figure 7.6). Alkyl group transfer by diisopropylzinc is primed for delivery to the *Si* face of the aldehyde in **int-5a**, which would lead to the (*S*) stereoisomer. However, the *Re* face of the substrate is inaccessible in **int-5a.** To bring a bound diisopropylzinc in proximity to the *Re* face requires rotation of both the substrate and one arm of the tetramer as shown in **int-5b**. This species, which is unfavorable by 5.9 kcal/mol, would lead to the (*R*) stereoisomer. The stereocontrolling transition structures **TS-5a** and **TS-5b** arising from **int-5a** and **int-5b**, respectively, are shown in Figure 7.5. **TS-5a** is the lowest-energy transition structure and leads to the observed alcohol (*S*)-**6** with an activation free energy barrier of 12.5 kcal/mol. **TS-5b** is 2.2 kcal/mol higher in energy compared to **TS-5a** and yields the (*R*) stereoisomer. This energy difference is in agreement with the observed stereoselectivity of **PyII** with pyridine-3-carbaldehyde **5** (95:5 e.r., $\Delta\Delta G^{\ddagger}$ = 1.7 kcal/mol). The difference in energy arises from the geometric distortion of the tetramer required to accommodate the diisopropylzinc alkylation on the *Re* face of aldehyde **5** (similar to the energetic difference between **int-5a** and **int-5b**).[47] Although of no direct stereochemical consequence, it is interesting to note that the isopropyl group transfers (S_E2 reactions) occur with "inversion of configuration" at the methine carbon (*vide infra*).

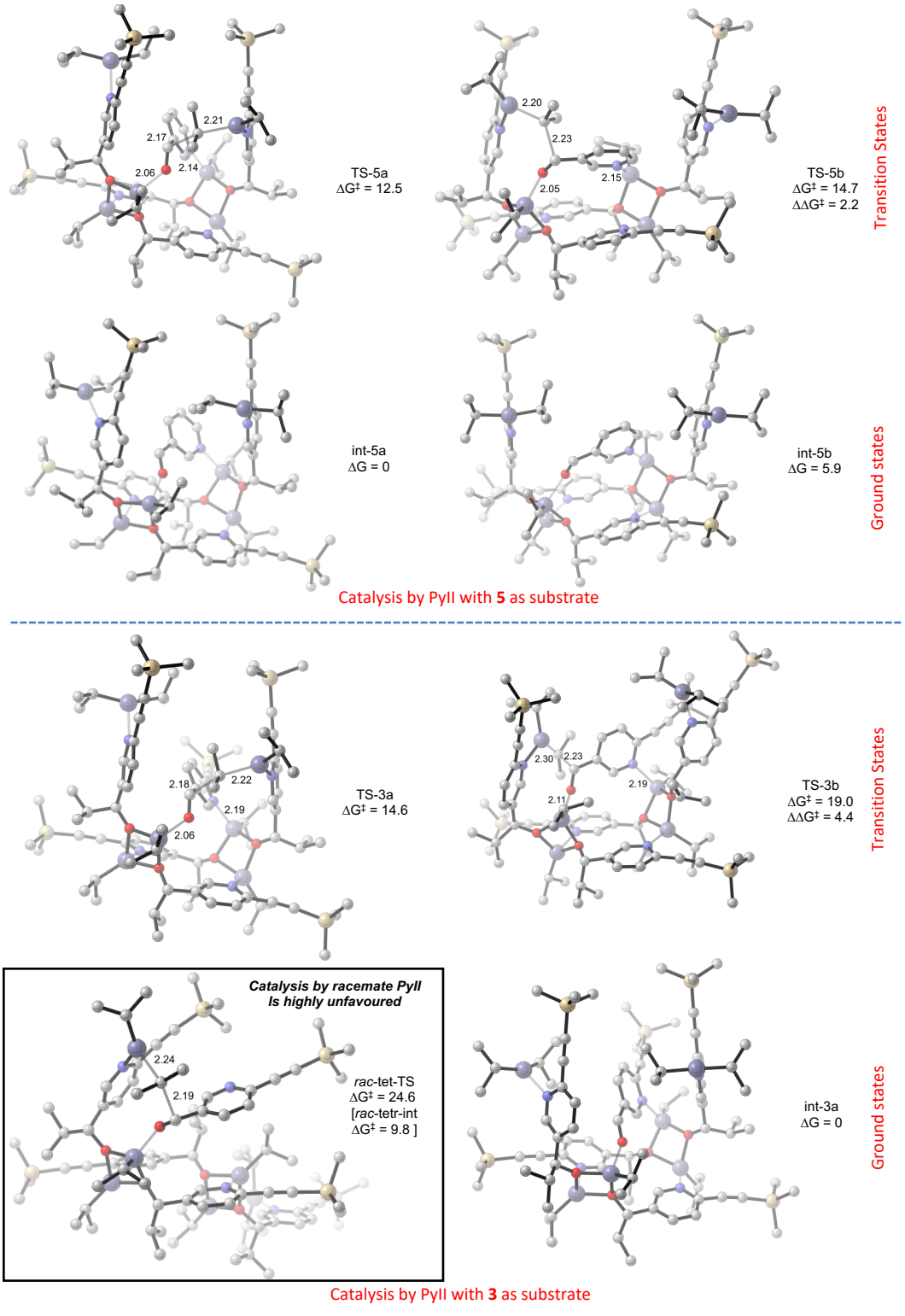

Figure 7.6: DFT studies for floor-to-floor substrate docking and alkyl transfer by the **PyII** tetramer. Transition structures **TS-3a–3b** and **TS-5a–5b**, and optimized minima **int-3a** and **int-5a–5b**

calculated at the M06-2X/def2-TZVPP–SMD (toluene)//B3LYP/6-31G(d) level of theory. Energies reported in kcal/mol. Purple, zinc; yellow, silicon; red, oxygen; blue, nitrogen; gray, carbon. Hydrogens are hidden for clarity. ΔG, free energy of activation. $\Delta\Delta G^{\ddagger}$, relative free energy activation barrier.

The transition structures and minima for the autocatalytic reaction of aldehyde **3** and tetramer **PyII** were also investigated computationally. The ground state geometry **int-3a** is quite similar to **int-5a**, N.B. the bulky aldehyde **3** is conformationally restricted in the tetramer. The lowest-energy transition structure **TS-3a** leads to the alcohol (*S*)-**4**, and the next higher energy transition structure **TS-3b** (4.4 kcal/mol) leads to the (*R*)-**4** product. This large difference in energy comports with an enantioselective autocatalytic mechanism. **TS-3a** is analogous to **TS-5a**, in which facile alkyl transfer (with "inversion") takes place from diisopropylzinc in the ground state geometry **int-3a**. Contrariwise, **TS-3b**, represents an S_E2-type mechanism with "retention of configuration" at the methine of the transferring isopropyl group. This higher-energy pathway occurs because the left arm of the tetramer does not rotate for alkyl transfer to the *Re*-face of the aldehyde as in **int-5b**. This conformation is inaccessible for aldehyde **3** because to arrange this substrate to receive the isopropyl group would require that the trimethylsilylethynyl substituent be in the same space as the opposite arm (N.B., the C5 position of aldehyde **5** in both **int-5b** and **TS-5b**, which corresponds to the trimethylsilylethynyl-substituted position of **3**). A similar type of transition structure was located for aldehyde **5**, i.e. without the trimethylsilylethynyl group (**TS-5e**), which was 5.2 kcal/mol higher in energy. This observation reveals that the constrained S_E2 substitution with retention of configuration (**TS-3b** and **TS-5e**) is highly disfavored compared to the invertive S_E2 pathway seen in **TS-5a** and **TS-3a**. Thus, the stereoselectivity arises from the

steric environment of the chiral tetramer, which favors *Si*-face addition to the aldehyde when bound in the preferred *floor-to-floor* conformation.

Finally, the catalytic competence of the racemate (heterochiral) tetramer was computationally investigated. The heterochiral aggregate was modeled according to Soai's racemate crystal structure for **2c** (Figure 7.1). The heterochiral geometry was found to be preferred to the homochiral **PyII** geometry by 2.1 kcal/mol. At the outset, a two point *floor-to-floor* substrate binding to the racemate tetramer appears impossible since the analogous unsaturated zinc atoms are positioned on opposite sides of the macrocycle. Indeed, a located single point carbonyl binding mode was found to be disfavored by 9.8 kcal in comparison to **int-3a**. The transition state arising from such a binding, **rac-tet-TS**, (Figure 7.6) has a free energy of 24.6 kcal/mol and is hence, highly disfavoured. Thus, the racemate **PyII** tetramer is catalytically incompetent as well as energetically preferred, providing a mechanism for non-linearity in the asymmetric autocatalytic action of the homochiral **PyII** Soai tetramer.

7.5 Conclusions

The Soai reaction represents a fortuitous confluence of three phenomena in catalysis: autocatalysis, enantioselective catalysis and non-linear effects (asymmetric amplification). The pyridine-based autocatalytic system **3** displays these phenomena and mirrors all reported aspects of the classical pyrimidine system. Mechanistically, this achieves a structural simplification of Soai system because the omission of a nitrogen atom in the aromatic core of the pyrimidine system in turn translates to four fewer coordinating sites on the Soai tetramer. In addition, we studied the activity of related catalysts with careful structural mutations to elucidate the constraints on the catalyst structure. Armed with this set of empirical structure-activity relationships of various

catalysts, characterization of these catalyst aggregates by detailed NMR spectroscopic analysis revealed the logical correlation of catalytic activity to molecular structure. The pyridine coordination assisted 'cube escape' model provides a hypothesis as to how the SMS macrocycle tetramer is a natural evolutionary endpoint of the pyridinyl (and presumably pyrimidyl) alkoxides.

Studies with substrates **5**, **8** and **10** revealed that the **PyII** catalyst prefers the pyridine-3-aldehyde scaffold. This is likely due to the substrate pyridyl nitrogen binding at a strategic location on the tetramer to promote catalysis. The autocatalytic reaction is a combination of two conceptually distinct steps: alkyl transfer from a dialkylzinc to the substrate aldehyde *followed by* reconstitution of the active catalyst from the newly formed product. The competency of substrate **5** provided an opportunity to decouple these two steps and study in isolation, the alkyl transfer step that reflects the key attributes of rate enhancement, selectivity and non-linearity as a means to scrutinize catalyst properties. This disconnection is achieved by combining an autocatalyst together with a competent substrate (**5**) whose product is catalytically incompetent. Such a strategy enabled us to sidestep the challenging kinetic analysis of autocatalytic reactions and employ classical initial rate measurements to indirectly interrogate catalysis by the Soai tetramer.

The structural simplification resulting from the pyridine-system and, the substrate specificity of **PyII** with the surrogate pyridine-3-carbaldehyde directly enabled suggestions of possible transition state models by minimizing choices for substrate and reagent binding sites on the tetrameric catalyst. Gratifyingly, computational studies corroborated the hypothesis that TS models of the surrogate substrate **5** are reflective of, and can be extended to, the reaction with substrate **3**, which switches enantioselective catalysis by **PyII** into an asymmetric, autocatalytic transformation and imparts improved selectivity by virtue of the conformationally restrictive trimethylsilyl-alkynyl substitution. The geometry of the heterochiral racemic tetramer precludes

floor-to-floor binding of the substrate, thus suggesting a simple resolution for the origin of non-linearity. Computational studies motivated by such a suggestion confirmed the catalytic incompetence of the energetically favoured racemic tetramer.

The uniqueness of diisopropylzinc in eliciting amplifying autocatalysis can be ascribed to the ability of the resulting product alkoxides to achieve 'cube escape'. Conversely, the reaction of diethylzinc generates a catalytically inactive cubic tetramer product and fails to display asymmetric autocatalysis. The ring nitrogen atom with a 1,3-relationship to the alkoxide oxygen is indispensable for the assembly of the catalyst by bridging two dimeric units and providing binding sites for reactants on the catalyst arms. Complementarily, this 1,3-relationship in the substrate facilitates a two-point binding mode for aldehyde activation. In other words, we suggest that the Soai tetramer allows catalysis with an 'expansion' of the cubic tetramer, made possible by replacing two Zn-O cube bonds by the aromatic pyridine linker (Figure 7.4). Such a structural change provides two unsaturated Zinc atoms for reactant coordination, at a distance defined by the aromatic pyridine linkers, hence providing the required dimensions for pyridine-3-aldehyde substrate binding!

Anecdotal claims by Brown et al. that reactions of dicyclopropylzinc, di-*tert*-butylzinc and dicyclopentylzinc with **1d** do not provide amplifying autocatalysis[47] suggests that in spite of cube escape, unfavorable interactions may preclude assembly or activity of the Soai tetramer in these cases (in case of dicyclopentylzinc, the hydride reduction product is obtained[31]). The increased Lewis basicity of the nitrogen in a pyridine when compared to a pyrimidine is expected to result in a stronger binding of the dialkylzinc reagent in this system.[48] Indeed, a number of pyridyl complexes of dialkylzincs have been previously described and our assignments of diagnostic chemical shift difference patterns between bound and unbound species are consistent with these

reports.[49,50] The stronger association is a likely reason for the saturation kinetics seen in our system (with substrate **5**) in contrast to the studies with substrate **1e**, which show an order of 1.6 in aldehyde.

Although causes for the structural idiosyncrasies of the Soai system have been commented upon earlier, this study provides the first, definitive experimental rationalization that provides an understanding of the fundamental basis of these structural requirements. The unprecedented observation of efficient amplifying autocatalysis with **3**, along with the attendant mechanistic insights provides an opportunity to further broaden the reaction scope to other substituted pyridine-3-carbaldehydes. These results contribute to addressing longstanding mechanistic questions regarding the extraordinary Soai reaction and will serve as a platform for further studies and explorations in the fascinating area of asymmetric autocatalysis.

7.6 References

1. K. Soai, T. Kawasaki, A. Matsumoto, Asymmetric Autocatalysis of Pyrimidyl Alkanol and Its Application to the Study on the Origin of Homochirality. *Acc. Chem. Res.* **47**, 3643-3654 (2014).
2. K. Soai, T. Shibata, H. Morioka, K. Choji, Asymmetric autocatalysis and amplification of enantiomeric excess of a chiral molecule. *Nature* **378**, 767-768 (1995).
3. I. Sato, H. Urabe, S. Ishiguro, T. Shibata, K. Soai, Amplification of Chirality from Extremely Low to Greater than 99.5 % ee by Asymmetric Autocatalysis. *Angewandte Chemie International Edition* **42**, 315-317 (2003).
4. K. Soai *et al.*, Asymmetric synthesis of pyrimidyl alkanol without adding chiral substances by the addition of diisopropylzinc to pyrimidine-5-carbaldehyde in conjunction with asymmetric autocatalysis. *Tetrahedron: Asymmetry* **14**, 185-188 (2003).

5. D. A. Singleton, L. K. Vo, Enantioselective Synthesis without Discrete Optically Active Additives. *J. Am. Chem. Soc.* **124**, 10010-10011 (2002).

6. D. A. Singleton, L. K. Vo, A Few Molecules Can Control the Enantiomeric Outcome. Evidence Supporting Absolute Asymmetric Synthesis Using the Soai Asymmetric Autocatalysis. *Org. Lett.* **5**, 4337-4339 (2003).

7. Soai K., Shibata T., Kowata Y.: Japan Kokai Tokkyo Koho JP 1997 9-268179. Application date: February 1 and April 18, 1996.

8. K. Mislow, Absolute Asymmetric Synthesis: A Commentary. *Collect. Czech. Chem. Commun.* **68**, 849-864 (2003).

9. I. Sato *et al.*, Highly enantioselective synthesis of organic compound using right- and left-handed helical silica. *Tetrahedron Lett.* **44**, 721-724 (2003).

10. F. Lutz, I. Sato, K. Soai, The Asymmetric Power of Chiral Ligands Determined by Competitive Asymmetric Autocatalysis. *Org. Lett.* **6**, 1613-1616 (2004).

11. T. Kawasaki *et al.*, Highly enantioselective asymmetric autocatalysis using chiral ruthenium complex-ion-exchanged synthetic hectorite as a chiral initiator. *Organic & Biomolecular Chemistry* **7**, 1073-1075 (2009).

12. I. Sato *et al.*, Determination of absolute configurations of amino acids by asymmetric autocatalysis of 2-alkynylpyrimidyl alkanol as a chiral sensor. *J. Organomet. Chem.* **692**, 1783-1787 (2007).

13. T. Kawasaki *et al.*, Asymmetric Amplification Using Chiral Cocrystals Formed from Achiral Organic Molecules by Asymmetric Autocatalysis. *Angew. Chem. Int. Ed.* **44**, 2774-2777 (2005).

14. I. Sato *et al.*, Asymmetric Induction by Helical Hydrocarbons: [6]- and [5]Helicenes. *Angew. Chem. Int. Ed.* **40**, 1096-1098 (2001).

15. T. Kawasaki *et al.*, Chiral Discrimination of Cryptochiral Saturated Quaternary and Tertiary Hydrocarbons by Asymmetric Autocatalysis. *J. Am. Chem. Soc.* **128**, 6032-6033 (2006).

16. T. Kawasaki *et al.*, Enantioselective Synthesis of Near Enantiopure Compound by Asymmetric Autocatalysis Triggered by Asymmetric Photolysis with Circularly Polarized Light. *J. Am. Chem. Soc.* **127**, 3274-3275 (2005).

17. T. Kawasaki *et al.*, Autocatalysis Triggered by Carbon Isotope (13C/12C) Chirality. *Science* **324**, 492-495 (2009).

18. T. Kawasaki *et al.*, Asymmetric Autocatalysis: Triggered by Chiral Isotopomer Arising from Oxygen Isotope Substitution. *Angew. Chem. Int. Ed.* **50**, 8131-8133 (2011).

19. A. Matsumoto *et al.*, Asymmetric Induction by a Nitrogen 14N/15N Isotopomer in Conjunction with Asymmetric Autocatalysis. *Angew. Chem. Int. Ed.* **55**, 15246-15249 (2016).

20. D. G. Blackmond, The Origin of Biological Homochirality. *Cold Spring Harbor Perspectives in Biology* **2**, a002147 (2010).

21. R. M. Flügel, *Chirality and Life: A Short Introduction to the Early Phases of Chemical Evolution*. (Springer-Verlag Berlin Heidelberg, ed. 1, 2011).

22. I. Weissbuch, M. Lahav, Crystalline Architectures as Templates of Relevance to the Origins of Homochirality. *Chem. Rev.* **111**, 3236-3267 (2011).

23. P. Cintas, Ed., *Biochirality: Origins, Evolution and Molecular Recognition.*, (Springer-Verlag Berlin Heidelberg, 2013).

24. D. G. Blackmond, C. R. McMillan, S. Ramdeehul, A. Schorm, J. M. Brown, Origins of Asymmetric Amplification in Autocatalytic Alkylzinc Additions. *J. Am. Chem. Soc.* **123**, 10103-10104 (2001).

25. I. Sato *et al.*, Relationship between the time, yield, and enantiomeric excess of asymmetric autocatalysis of chiral 2-alkynyl-5-pyrimidyl alkanol with amplification of enantiomeric excess. *Tetrahedron: Asymmetry* **14**, 975-979 (2003).

26. F. G. Buono, D. G. Blackmond, Kinetic Evidence for a Tetrameric Transition State in the Asymmetric Autocatalytic Alkylation of Pyrimidyl Aldehydes. *J. Am. Chem. Soc.* **125**, 8978-8979 (2003).

27. G. Ercolani, L. Schiaffino, Putting the Mechanism of the Soai Reaction to the Test: DFT Study of the Role of Aldehyde and Dialkylzinc Structure. *The Journal of Organic Chemistry* **76**, 2619-2626 (2011).

28. J. R. Islas *et al.*, Mirror-symmetry breaking in the Soai reaction: A kinetic understanding. *Proceedings of the National Academy of Sciences of the United States of America* **102**, 13743-13748 (2005).

29. T. Buhse, M. E. Noble-Terán, J.-M. Cruz, J.-C. Micheau, C. Coudret, in *Advances in Asymmetric Autocatalysis and Related Topics,* G. Pályi, R. Kurdi, C. Zucchi, Eds. (Academic Press, 2017), pp. 71-110.

30. I. D. Gridnev, J. M. Serafimov, J. M. Brown, Solution Structure and Reagent Binding of the Zinc Alkoxide Catalyst in the Soai Asymmetric Autocatalytic Reaction. *Angew. Chem. Int. Ed.* **43**, 4884-4887 (2004).

31. J. Klankermayer, I. D. Gridnev, J. M. Brown, Role of the isopropyl group in asymmetric autocatalytic zinc alkylations. *Chem. Commun.*, 3151-3153 (2007).

32. M. Quaranta, T. Gehring, B. Odell, J. M. Brown, D. G. Blackmond, Unusual Inverse Temperature Dependence on Reaction Rate in the Asymmetric Autocatalytic Alkylation of Pyrimidyl Aldehydes. *J. Am. Chem. Soc.* **132**, 15104-15107 (2010).

33. I. D. Gridnev, A. K. Vorobiev, Quantification of Sophisticated Equilibria in the Reaction Pool and Amplifying Catalytic Cycle of the Soai Reaction. *ACS Catalysis* **2**, 2137-2149 (2012).

34. A. Matsumoto *et al.*, Crystal Structure of the Isopropylzinc Alkoxide of Pyrimidyl Alkanol: Mechanistic Insights for Asymmetric Autocatalysis with Amplification of Enantiomeric Excess. *Angew. Chem. Int. Ed.* **54**, 15218-15221 (2015).

35. T. Gehring, M. Busch, M. Schlageter, D. Weingand, A concise summary of experimental facts about the Soai reaction. *Chirality* **22**, E173-E182 (2010).

36. T. Shibata, S. Yonekubo, K. Soai, Practically Perfect Asymmetric Autocatalysis with (2-Alkynyl-5-pyrimidyl)alkanols. *Angew. Chem. Int. Ed.* **38**, 659-661 (1999).

37. S. Tanji *et al.*, Asymmetric autocatalysis of 5-carbamoyl-3-pyridyl alkanols with amplification of enantiomeric excess. *Tetrahedron: Asymmetry* **11**, 4249-4253 (2000).

38. T. Shibata, K. Choji, T. Hayase, Y. Aizu, K. Soai, Asymmetric autocatalytic reaction of 3-quinolylalkanol with amplification of enantiomeric excess. *Chem. Commun.*, 1235-1236 (1996).

39. These results will be disclosed in a full account of this work.

40. C. Romagnoli, B. Sieng, M. Amedjkouh, Asymmetric Amplification Coupling Enantioselective Autocatalysis and Asymmetric Induction for Alkylation of Azaaryl Aldehydes. *Eur. J. Org. Chem.* **2015**, 4087-4092 (2015).

41. A catalyzed diisopropylzinc addition to 3 was reported in ref. 35. This study claimed that the reaction of diisopropylzinc and 5-(t-butylylethynyl)pyridine-3-carbaldehyde showed chiral

erosion. However, under our reaction conditions, we see amplifying autocatalysis with this substrate as well.

42. J. G. Noltes, J. Boersma, Investigations on organozinc compounds IX. Coordination chemistry of organozinc compounds RZnX: organozinc derivatives of tert-butanol, some phenols, diethylhydroxylamine and some oximes. *J. Organomet. Chem.* **12**, 425-431 (1968).

43. S. Jana, R. J. F. Berger, R. Fröhlich, T. Pape, N. W. Mitzel, Oxygenation of Simple Zinc Alkyls: Surprising Dependence of Product Distributions on the Alkyl Substituents and the Presence of Water. *Inorg. Chem.* **46**, 4293-4297 (2007).

44. M. Kitamura, S. Okada, S. Suga, R. Noyori, Enantioselective addition of dialkylzincs to aldehydes promoted by chiral amino alcohols. Mechanism and nonlinear effect. *J. Am. Chem. Soc.* **111**, 4028-4036 (1989).

45. K. Soai, S. Niwa, H. Hori, Asymmetric self-catalytic reaction. Self-production of chiral 1-(3-pyridyl)alkanols as chiral self-catalysts in the enantioselective addition of dialkylzinc reagents to pyridine-3-carbaldehyde. *J. Chem. Soc., Chem. Commun.*, 982-983 (1990).

46. See the Supplementary Materials for a discussion of the located ground state conformations of 5 and PyII, as well as alternative transition structures and alkylation mechanisms.

47. I. D. Gridnev, J. M. Serafimov, H. Quiney, J. M. Brown, Reflections on spontaneous asymmetric synthesis by amplifying autocatalysis. *Organic & Biomolecular Chemistry* **1**, 3811-3819 (2003).

48. A. Albert, R. Goldacre, J. Phillips, 455. The strength of heterocyclic bases. *Journal of the Chemical Society (Resumed)*, 2240-2249 (1948).

49. S. Schulz *et al.*, Synthesis and Crystal Structures of t-Butyl-Pyridine Adducts of ZnR2 (R = Me, i-Pr, t-Bu, Cp*). *Z. Anorg. Allg. Chem.* **637**, 83-86 (2011).

50. W. Brüser *et al.*, A comparative IR/Raman, X-ray and computational study of diethylzinc pyridine complexes. *J. Organomet. Chem.* **806**, 77-82 (2016).